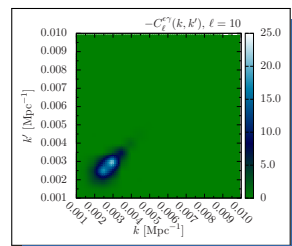
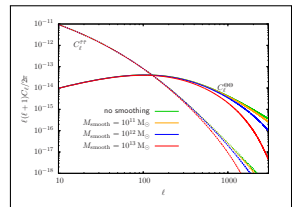
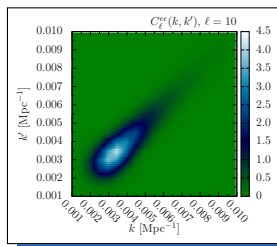
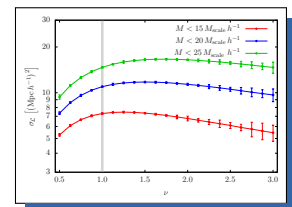
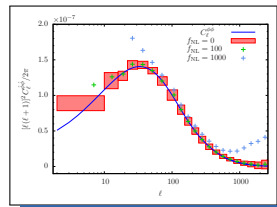
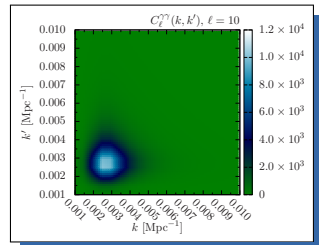


Philipp M. Merkel

Different aspects of the interplay between light and the large-scale structure of the Universe



Dissertation

submitted to the
Combined Faculties of the Natural Sciences and Mathematics
of the Ruperto-Carola-University of Heidelberg, Germany
for the degree of
Doctor of Natural Sciences

Put forward by
Philipp M. Merkel
born in Heidelberg
Oral examination: 6th November, 2013

Different aspects
of the interplay between
light and the large-scale structure
of the Universe

Referees: Prof. Dr. Björn Malte Schäfer
Prof. Dr. Volker Springel

*Ich muß mich davon überzeugen, wer recht hat,
die Gesellschaft oder ich.*

Henrik Ibsen, Nora (Ein Puppenheim)

Verschiedene Aspekte des Wechselspiels von Licht und der groß-skaligen Struktur im Universum

Die vorliegende Arbeit beschäftigt sich hauptsächlich mit dem Einfluss intrinsischer Elliptizitäts-Korrelationen auf Messungen des schwachen Gravitationslinseneffektes. Eine mögliche Ursache für diese Korrelationen sind ebensolche in den Drehimpulsen benachbarter Galaxien. Mit Hilfe eines verbesserten Ansatzes für die Drehimpuls-Korrelationen zeige ich, dass die typische Korrelationslänge von Halos von der Größe der Milchstraße ungefähr $1 \text{ Mpc } h^{-1}$ beträgt, was etwas geringer ist als von früheren Arbeiten vorhergesagt. Ich entwickle den grundlegenden Formalismus, um $3d$ -Spektren intrinsischer Elliptizitäts-Korrelationen analog zum schwachen kosmischen Linseneffekt beschreiben zu können. Damit berechne ich die Kovarianz-Matrizen für verschiedene Varianten von Elliptizitäts-Korrelationen. Im Falle eines *Euclid*-ähnlichen Surveys ist das von intrinsischen Elliptizitäts-Korrelationen stammende Signal mehr als eine Größenordnung kleiner als dasjenige des Linseneffektes. Darüber hinaus berechne ich die Parameter-Verzerrung, die aus der Außerachtlassung intrinsischer Elliptizitäts-Korrelationen in zweidimensionalen nicht-tomographischen Messungen des schwachen Gravitationslinseneffektes resultiert. Die Materiedichte Ω_m und die Normierung des linearen Materieleistungsspektrums σ_8 sind am stärksten verzerrt, falls intrinsische Elliptizitäts-Korrelationen mit Hilfe eines Drehimpuls basierten Modells beschrieben werden.

Im zweiten Teil meiner Arbeit wende ich mich sekundären Anisotropien des kosmischen Mikrowellenhintergrundes zu: dem schwachen Gravitationslinseneffekt und dem nichtlinearen integrierten Sachs-Wolfe (iSW)-Effekt. Das charakteristische Signal des Linseneffektes lässt sich ausnutzen, um das Leistungsspektrum des Linsenpotentials zu rekonstruieren. Ich zeige, wie diese Rekonstruktion durch primordiale Nicht-Gaußianitäten verzerrt wird. Für aktuelle Werte von f_{NL} ist die Verzerrung jedoch auf allen außer den größten Winkelskalen vernachlässigbar gering. Abschließend stelle ich einen neuen analytischen Zugang zur Berechnung des nichtlinearen iSW-Effektes im translinearen Bereich vor. Der Ansatz offenbart zwei unterschiedliche Beiträge: die Änderung der gravitativen Selbstenergiedichte der groß-skaligen Struktur bezüglich konformer Zeit und den Birkinshaw-Gull-Effekt.

Different aspects of the interplay between light and the large-scale structure of the Universe

The main subject of this thesis is the influence of intrinsic alignments on weak lensing measurements. One possible source of intrinsic alignments are correlations in the angular momenta of neighbouring galaxies. Employing an improved ansatz for the angular momentum correlation function I show that the typical correlation length of Milky Way-sized haloes is about $1 \text{ Mpc } h^{-1}$ which is slightly smaller than earlier work in this field suggested. Establishing the constitutive formalism to describe intrinsic alignments consistently in the framework of $3d$ cosmic shear I compute the resulting covariance matrices of different alignment types. For a *Euclid*-like survey it turns out that intrinsic alignments are more than one order of magnitude smaller than the lensing signal. In addition the parameter estimation bias in a two-dimensional non-tomographic weak lensing measurement is computed. The matter density Ω_m and the normalization of the linear matter power spectrum σ_8 are most severely biased if intrinsic alignments are described by an angular momentum based alignment model.

In the second part of my thesis I address secondary anisotropies of the cosmic microwave background: weak gravitational lensing and the nonlinear integrated Sachs-Wolfe (iSW) effect. The characteristic imprint of lensing can be used to reconstruct the lensing potential power spectrum. I show how this reconstruction is biased in the presence of primordial non-Gaussianities. For current values of f_{NL} , however, the bias is completely negligible on all but the largest angular scales. Finally, a novel analytical approach for the computation of the nonlinear iSW effect valid in the translinear regime is presented. It allows to identify two distinct contributions: the change of the gravitational self-energy density of the large-scale structure with (conformal) time and the Birkinshaw-Gull effect.

Contents

Table of Contents	ix
List of Figures	xi
List of Tables	xii
1. Introduction	1
2. Cosmology	5
2.1. The observable Universe	5
2.2. Friedmann-Lemaître-Robertson-Walker world models	6
2.3. Cosmological redshift and distances	10
2.4. Structure formation	11
3. Weak gravitational lensing	19
3.1. Jacobi equation	19
3.2. Perturbed photon propagation	20
3.3. Weak lensing power spectra	23
4. Galactic angular momenta and angular momentum couplings in the large-scale structure	27
4.1. Introduction	27
4.2. Formalism	29
4.3. Numerical results	39
4.4. Summary	42
5. Intrinsic alignments and $3d$ weak gravitational lensing	45
5.1. Introduction	45
5.2. Intrinsic galaxy ellipticity and gravitational lensing	47
5.3. $3d$ formalism	50
5.4. Numerical results	58
5.5. Summary	62
6. The impact of intrinsic alignments for cosmic shear measurements	63
6.1. Introduction	63
6.2. Intrinsic ellipticity correlations	64
6.3. Interplay with cosmic shear	67
6.4. Summary	72
7. The Cosmic Microwave Background	75
7.1. The Cosmic Microwave Background	75
7.2. The CMB power spectrum	77
7.3. CMB lensing	79
7.4. The integrated Sachs-Wolfe effect	81

8. The interplay of CMB temperature lensing power reconstruction with primordial non-Gaussianity of local type	83
8.1. Introduction	83
8.2. CMB lensing power spectrum reconstruction	84
8.3. Local non-Gaussianity	86
8.4. Power reconstruction bias	88
8.5. Summary	93
9. Contributions to the nonlinear integrated Sachs-Wolfe effect: Birkinshaw-Gull effect and gravitational self-energy density	95
9.1. Introduction	95
9.2. Nonlinear integrated Sachs-Wolfe effect	96
9.3. Contributions to the nonlinear integrated Sachs-Wolfe effect	100
9.4. Physical interpretation	103
9.5. Summary	105
10. Summary and conclusions	107
A. Mathematical details	111
A.1. Riemannian geometry	111
A.2. Statistics	113
B. Computational details	115
B.1. Derivation of the covariance matrix of the quadratic model	115
B.2. Mode coupling functions	116
B.3. Some flat-sky expressions	116
Bibliography	119
Acknowledgements	129

List of Figures

2.1.	Behaviour of a universe dominated by matter and dark energy.	8
2.2.	Visualization of the angular diameter distance.	11
2.3.	Linear and nonlinear matter power spectrum.	18
3.1.	Geodesic deviation.	20
3.2.	Illustration of the distortion caused by weak gravitational lensing.	22
3.3.	Convergence angular power spectrum.	25
4.1.	Time evolution of galactic angular momenta in different dark energy cosmologies. . .	31
4.2.	Covariance matrix of the angular momentum distribution in linear tidal torque theory.	36
4.3.	Standard deviation of the specific angular momentum as a function of halo mass. . .	41
4.4.	Standard deviation of the specific angular momentum as a function of peak height. .	41
4.5.	Angular momentum correlation function.	42
5.1.	Illustration of <i>II</i> - and <i>GI</i> -alignments.	48
5.2.	Diagonal elements of the ellipticity covariance matrix for a shallow redshift survey. .	59
5.3.	Diagonal elements of the ellipticity covariance matrix for a deep redshift survey. . .	60
5.4.	Covariance matrices for the linear alignment model.	61
6.1.	Angular power spectrum of <i>II</i> -alignments.	65
6.2.	Correlation functions of the intrinsic ellipticity field.	66
6.3.	Aperture measures of the intrinsic ellipticity field.	67
6.4.	Parameter sensitivity of the intrinsic alignment angular power spectra.	69
6.5.	Illustration of the analytical determination of the parameter estimation bias.	69
6.6.	Weak shear confidence regions and parameter estimation bias.	71
7.1.	All sky map of the CMB temperature fluctuations.	76
7.2.	CMB temperature power spectrum.	78
7.3.	Lensed and unlensed CMB temperature power spectrum.	81
8.1.	Biases involved in the reconstruction of the CMB lensing potential power spectrum. .	86
8.2.	CMB lensing power reconstruction using the quadratic estimator.	92
8.3.	Reconstruction bias associated with primordial non-Gaussianity ($f_{\text{NL}} = 100$).	92
8.4.	Reconstruction bias associated with primordial non-Gaussianity ($f_{\text{NL}} = 1000$).	93
9.1.	Growth function of the linear and nonlinear iSW effect.	98
9.2.	Weighting function of the linear and nonlinear iSW effect.	100
9.3.	Angular power spectra of the linear and nonlinear iSW effect.	100
9.4.	Contributions of different mass scales to the power spectra of the linear and nonlinear iSW effect.	101
9.5.	Three-dimensional power spectra of the different contributions to the nonlinear iSW effect.	102
9.6.	Angular power spectra of the different contributions to the nonlinear iSW effect. . . .	103
A.1.	Geometrical meaning of the Riemann curvature tensor.	112

List of Tables

2.1. Cosmological parameters.	9
A.1. Christoffel symbols of the perturbed FLRW metric.	112

1

Chapter 1

Introduction

The contemporary picture of the Universe is largely determined by the observation of light in its different wavebands. Since the speed of light is finite, photons observed today are emissaries of the Universe's past. The light of the oldest galaxies known today was emitted approximately 600 million years after the Big Bang, when the size of the Universe amounted to only about one tenth of its present value. Photons of the cosmic microwave background (CMB) are even older. They were released around 400 000 years after the Big Bang. At that time the Universe was about one thousand times smaller than it is today. Their origin from such an early stage of the Universe's evolution makes CMB photons the primary tool in the investigation of the initial conditions, from which all observable structures formed by gravitational collapse. The nowadays well established cosmological standard model, which is presented in Chapter 2, is to a major extent based on CMB observations.

However, light reaching today's observer contains not only information about its source, the emitting object, but also about the entire matter and energy distribution of the Universe between source and observer. This is an immediate consequence of General Relativity: the spacetime geometry of the Universe (and thus light paths therein) are determined by its energy content. The deflection of light by matter, or more generally by any form of energy, is known as gravitational lensing. It has become one of the most important tools in the investigation of the Cosmos and is discussed in detail in Chapter 3.

Due to its sensitivity to all forms of energy irrespective of its nature, gravitational lensing is predestined for studying the dark components of the Universe's energy budget: *dark energy* and *cold dark matter*. Both components do not form part of the standard model of particle physics and interact (almost) exclusively gravitationally. Nonetheless, they are the dominant contribution (dark energy $\sim 70\%$, cold dark matter $\sim 25\%$) to the total energy of the Universe. The fraction contributed by luminous, i.e. baryonic, matter is astonishing small. This highlights the need for the tightest possible constraints on the parameters describing the dark sector.

The mystery of dark energy and cold dark matter inspired the invention of an overwhelming variety of models of arbitrary complexity. However, there is little hope that observational data, tough their quality is permanently improving, will ever be able to discriminate between different models. It is therefore advantageous to concentrate on a general parametrization of the most important properties of the dark components. First, these are the shares of the entire Universe's energy budget which they hold, Ω_{CDM} and Ω_{DE} , respectively. While cold dark matter is assumed to be pressureless, the relation between pressure and energy density, i.e. the so-called equation of state parameter w , is of mayor interest in case of dark energy. It is the key quantity to distinguish dynamical realizations of dark energy from a static cosmological constant. One commonly parametrizes the dark energy equation of state parameter and its possible time evolution by two more parameters: its value observed today, w_0 , and its value at early times, $w_0 + w_a$, assuming that it evolves linearly with respect to the scale factor. These parameters are then accessible to cosmological observations, in particular gravitational lensing measurements.

Tight constraints on these parameters, however, require a reliable control of systematic errors. In

case of weak lensing studies the intrinsic alignment of galaxies is one of these systematics. Correlations in the intrinsic ellipticities of adjacent galaxies mimic the lensing signal. This contamination inevitably introduces a bias if cosmic shear measurements are carried out under the null hypothesis of intrinsically randomly orientated galaxy shapes. This bias is substantial in the determination of the dark energy equation of state parameter and its time evolution. Therefore, the main part of my thesis aims at a better understanding of intrinsic alignments and their interplay with weak gravitational lensing.

One possible source of intrinsic alignments are correlations in the angular momenta of neighbouring galaxies. This is a purely geometrical effect because the spin axis determines the angle under which the galactic disc is observed. Thus, correlations in the galactic angular momenta necessarily lead to correlated galaxy shapes. The correct modelling of angular momentum correlations in the cosmic large-scale structure is therefore an important step towards a better understanding of intrinsic alignments. In Chapter 4 a novel ansatz for the analytical computation of angular momentum correlations is proposed. Since galaxies form at peaks in the cosmic density field, the underlying random process is discrete in nature. My approach takes this discreteness explicitly into account. It allows to derive all dynamical fields involved from a high-dimensional correlated Gaussian random process, the covariance matrix of which is completely characterized in terms of the linear matter power spectrum. My results are therefore naturally limited to linear structure growth. This restriction, however, is compensated for by the fact that, in contrast to previous works, neither further assumptions nor new parameters have to be included.

The need for tighter and tighter parameter constraints stimulated the development of more and more advanced methods for measuring cosmic shear. In the last ten years a large variety of methods have been invented and successfully applied. Key among these is $3d$ cosmic shear. In this formalism the three-dimensional character of the observable shear field is preserved. It avoids any line-of-sight projection, making the additional information contained in the time evolution of the shear field fully accessible. It therefore improves on shear tomography, which uses binning in redshift. In contrast to the cosmic density field the weak lensing shear field is not statistically homogeneous; only statistical isotropy is maintained. Its time-resolved investigation therefore has to deal with (spatial) mode coupling increasing the numerical complexity of $3d$ cosmic shear analyses considerably. This mode coupling is further enhanced by the observational uncertainties in the galaxies' redshift. Nonetheless, the capability to follow the time evolution of the lensing signal makes $3d$ cosmic shear very well suited for the investigation of dark energy. As the quality of photometric redshift data is increasingly improving, intrinsic alignments are expected to be the most severe contamination in $3d$ weak lensing measurements. In order to remove, or at least reduce, this contamination, intrinsic alignments need to be consistently incorporated in the $3d$ cosmic shear formalism. So far, only fitting formulae derived from numerical simulations exist. In Chapter 5 I develop the constitutive formalism to describe intrinsic alignments in the language of $3d$ cosmic shear starting from physical alignment models. This purely analytical approach then allows to compute the covariance matrices of the intrinsic ellipticity field and its cross-correlation with the lensing induced one. Comparison with the $3d$ weak gravitational lensing covariance matrix yields valuable insights into the linking of intrinsic alignments to the observed three-dimensional power.

The part of my thesis which is concerned with intrinsic alignments concludes in Chapter 6. Here I return to the conventional two-dimensional weak lensing analysis without tomography. The biases, which are introduced in a minimal set of cosmological parameters, if the presence of intrinsic alignments is not accounted for, are computed. In contrast to previous studies I employ an angular momentum based model in my calculations. This model is closely related to that of Chapter 4, but appropriately simplified in order to make the computational efforts feasible. Advantageous of this approach is the fact that its free parameters may, in principle, be determined from observations other than galactic shape measurements. This avoids a marginalization over nuisance parameters which inevitably weakens the derived constraints on cosmological parameters.

In the second part of my thesis I leave intrinsic alignments behind and address the cosmic microwave background (CMB). A short overview of its most important properties is provided in Chapter 7. The effect of gravitational lensing does not only apply to light emitted by galaxies, but also to CMB photons leaving a characteristic imprint on the statistics of the CMB temperature fluctuations; it causes a secondary anisotropy. In the current era of high-precision CMB experiments this characteristic signal is exploited as a valuable source of additional information. It allows to statistically reconstruct the CMB lensing potential power spectrum, which may then be used to tighten constraints on cosmological parameters derived from the CMB. This reconstruction, however, is biased in the presence of primordial non-Gaussianity. In Chapter 8 a formulation of this bias, which takes the curvature of the sky explicitly into account and overcomes the flat-sky approximation used in previous studies, is presented. Simulating a large sample of CMB temperature maps which consistently incorporate all relevant contributions to the signal, i.e. primordial non-Gaussianity, gravitational lensing and instrumental noise, I quantify the reconstruction bias for an experiment similar to the *Planck* satellite mission.

Another secondary anisotropy of the CMB is the integrated Sachs-Wolfe (iSW) effect. While they are blueshifted on entering a potential well in the large-scale structure, CMB photons experience a redshift when they leave the potential. Due to the time variation of the potential, blue- and redshift do not compensate each other in amount, which causes an additional anisotropy in the CMB temperature. Since it is absent in a universe exclusively built up by matter, the signal of the iSW effect is highly sensitive to dark energy. Chapter 9 is devoted to the nonlinear iSW or Rees-Sciama effect, which results from inhomogeneous structure growth, i.e. nonlinearly evolving potentials. I present a new analytical derivation of this effect which is valid in the moderate nonlinear regime. It reduces the numerical costs considerably and allows for a direct physical interpretation of the individual contributions to the nonlinear iSW effect, which are concealed in earlier studies.

The main findings of my thesis are then finally summarized in Chapter 10, where I also draw some further conclusions. Two appendices provide additional material, which has been excluded from the principal part of this thesis for clarity. Appendix A contains mathematical details, primarily definitions and theorems used throughout my thesis, whereas Appendix B gathers detailed calculations and derivations the results of which are presented in the main part.

Parts of this work have been published in the following journal articles:

- **Merkel, Ph. M.** & Schäfer, B. M. (2013b): *Intrinsic alignments and 3d weak gravitational lensing*. *MNRAS*, in press.
- **Merkel, Ph. M.** & Schäfer, B. M. (2013c): *The interplay of CMB temperature lensing power reconstruction with primordial non-Gaussianity of local type*. *MNRAS*, 429, 444.
- **Merkel, Ph. M.** & Schäfer, B. M. (2013a): *Contributions to the non-linear integrated Sachs-Wolfe effect: Birkinshaw-Gull effect and gravitational self-energy density*. *MNRAS*, 431, 2433.
- Schäfer, B. M. & **Merkel, Ph. M.** (2012): *Galactic angular momenta and angular momentum couplings in the large-scale structure*. *MNRAS*, 421, 2751.
- Capranico, F., **Merkel, Ph. M.** & Schäfer, B. M. (2013): *Intrinsic ellipticity correlations of galaxies: Models, likelihoods and interplay with weak lensing*. *MNRAS*, in press.

2 Chapter 2

Cosmology

This chapter contains the most important physical concepts for a systematic study of the Universe. It is far from being complete in the sense that it does not cover all aspects of cosmology, in particular it skips the physics of the (very) early universe, including nucleosynthesis. Instead, this overview is intended to introduce and motivate all quantities and formulae used in the main part of this work in a self-consistent way. Its purpose is to make this work accessible to non-cosmologists and to ease the reading for people working in that field. The gaps which are inevitably left by my presentation might be filled by one of these excellent textbooks on cosmology: [Peacock \(2003\)](#); [Mukhanov \(2005\)](#); [Dodelson \(2007\)](#) and the more recent review by [Bartelmann \(2010a\)](#).

2.1. The observable Universe

Before I develop the theoretical foundations of modern cosmology in the following sections, I would like to summarize some well established facts of the observable Universe.

First of all, the Universe is *homogeneous* and *isotropic* on scales larger than roughly 100 Mpc. On smaller scales, however, there are well developed inhomogeneous structures. Before homogeneity and isotropy were confirmed, for example by deep galaxy surveys, cosmological physics had already postulated these properties in form of the

Cosmological Principle

- (i) *When averaged over sufficiently large scales, the observable properties of the Universe are independent of direction.*
- (ii) *There exists no preferred position in the Universe (Copernican principle).*

Obviously, a Universe which is isotropic everywhere, as required by the Copernican principle, must be homogeneous, too. It is important to note that the first assumption is not restricted to the distribution of large-scale structure at all but is much more far-reaching. It contains physical laws as a whole. The cosmological principle has proven to be one of the most powerful working assumptions of modern cosmology. It ensures that observations from one single vantage point entail information of the entire Universe.

Observationally, the cosmological principle is further supported by measurements of the *cosmic microwave background (CMB)*. The Universe is pervaded by thermal radiation with temperature $T_0 = 2.73$ K. Its fluctuations are tiny (one per cent mille) and reflect those in the Universe's energy distribution when it was about a thousand times smaller than today. The expansion of the Universe is

governed by the *Hubble law*. The receding velocity, for example of distant galaxies, from the observer is proportional to the distance to the observer.

The total energy density of the Universe is composed of three different species. Normal, i.e. baryonic, matter contributes only about five percent; the rest is constituted by a dark component, which appears to consist of *cold dark matter* with negligible pressure ($\sim 25\%$) and *dark energy* with negative pressure ($\sim 70\%$). There seems to be (almost) no interaction between dark matter, dark energy and baryonic matter besides gravity. The number of baryons is tiny in comparison to the number of photons. There are roughly 10^9 photons per baryon, whereas the energy fraction carried by radiation is negligible in the late phases of the Universe. Finally, the chemical composition of baryonic matter is about 75 per cent hydrogen, 25 per cent helium and trace amounts of heavier elements. The amount of antimatter present in the Universe is insignificant.

2.2. Friedmann-Lemaître-Robertson-Walker world models

For a consistent description of the Universe as a whole, along with its evolution, the use of General Relativity is mandatory. Cosmological physics has to deal with matter moving with relativistic velocities and having arbitrary, even negative, pressure and the distances involved are too large for neglecting retardation and curvature effects. Therefore, cosmology requires necessarily a fully relativistic theory of gravitational fields beyond Newtonian gravity.

Einstein's theory of general relativity is a *geometrical*¹ theory of gravitation (Einstein, 1915, 1916). In contrast to the Newtonian picture, the relative acceleration of particles is not due to gravitational forces but results from the curvature of spacetime the particles are moving in. Spacetime is described by a four-dimensional pseudo Riemannian manifold whose metric tensor $g_{\mu\nu}$ has Lorentzian signature $(-1, 1, 1, 1)$. The metric allows to define the infinitesimal spacetime interval between two events, i.e. two points in spacetime,

$$ds^2 \equiv g_{\mu\nu} dx^\mu dx^\nu \quad (2.1)$$

which is invariant with respect to coordinate transformations. Throughout this work I will adopt Einstein's convention for the summation over repeated indices

$$g_{\mu\nu} dx^\mu dx^\nu \equiv \sum_{\mu,\nu} g_{\mu\nu} dx^\mu dx^\nu. \quad (2.2)$$

If not stated otherwise Greek indices run from 0 to 3 (0 indicating the time-like coordinate) while Latin indices are reserved for spatial coordinates.

General relativity is a *metric* theory of gravitation. The components of the metric become dynamical fields whose evolution is determined by the *Einstein field equations*

$$R_{\mu\nu} - \frac{1}{2} R g_{\mu\nu} - \Lambda g_{\mu\nu} = \frac{8\pi G}{c^4} T_{\mu\nu} \quad (2.3)$$

(e.g. Landau & Lifšic, 1975). The left hand-side contains geometrical quantities only, while the right-hand side accounts for the Universe's matter content described by the energy momentum tensor $T_{\mu\nu}$. The Ricci tensor is obtained from the single independent contraction of the Riemann tensor, i.e. $R_{\mu\nu} = R^\alpha{}_{\mu\alpha\nu}$. Its trace yields the Ricci scalar $R = R^\mu{}_\mu$. According to Lovelock's theorem, the cosmological constant Λ may be considered as a geometrical quantity rather than as a contribution to the matter content (Lovelock, 1971, 1972). The numerical factor on the right-hand side, where G is Newton's constant and c the speed of light, ensures that Newtonian gravity is recovered in case of weak gravitational fields and non-relativistic matter.

Any metric describing the Universe as a whole has to obey the cosmological principle. As no privileged point exists, the synchronization of the clock of any observer throughout the entire Universe

¹A short overview of the main aspects of Riemannian geometry, in particular the Riemann curvature tensor, is provided in Appendix A.1.

has to be possible, and therefore $g_{0i} = g_{i0} = 0$. The identification of coordinate time with proper time yields $g_{00} = -c^2$. Another consequence of the cosmological principle is that space-like hypersurfaces at constant time need to be homogeneous and isotropic and are therefore *maximally symmetric spaces*, i.e. spaces with the maximum number of Killing vectors or equivalently the largest symmetry group possible (see Appendix A.1.3). In three dimensions there are six Killing vectors at most, which correspond to three independent translations and rotations. Maximally symmetric spaces are spaces of constant curvature K and one can distinguish three different cases

- (1) $K < 0$: *open universe*,
- (2) $K = 0$: *spatially flat universe*,
- (3) $K > 0$: *close universe*.

In hyperspherical coordinates (χ, θ, ϕ) these symmetries are most evident and the spatial part of the line element takes a particularly simple form

$$d\sigma^2 = d\chi^2 + f_K^2(\chi) (d\theta^2 + \sin^2 \theta d\phi^2) \quad \text{with} \quad f_K(\chi) = \begin{cases} \frac{\sinh(\sqrt{|K|}\chi)}{\sqrt{|K|}} & \text{if } K < 0, \\ \chi & \text{if } K = 0, \\ \frac{\sin(\sqrt{K}\chi)}{\sqrt{K}} & \text{if } K > 0. \end{cases} \quad (2.4)$$

Scaling of this line element by a time-dependent function is permissible since it preserves homogeneity and isotropy. Introducing the *scale factor* $a(t)$ (normalized to unity today, i.e. $a_0 \equiv a(t_0) = 1$) one obtains

$$ds^2 = -c^2 dt^2 + a^2(t) [d\chi^2 + f_K^2(\chi) (d\theta^2 + \sin^2 \theta d\phi^2)]. \quad (2.5)$$

The corresponding metric is called Robertson-Walker metric (Robertson, 1935; Walker, 1935).

The time evolution of the scale factor is found from Einstein's field equations (2.3). On large scales the Universe's energy momentum tensor may be modelled as that of a perfect fluid. A perfect fluid has neither anisotropic stress nor heat conduction, the presence of which would necessarily violate isotropy. Furthermore, being collisionless cold dark matter does not exhibit viscosity. Thus, the cosmic fluid is completely characterized by its (rest frame) energy density ρ and (isotropic) pressure p

$$T_{\mu\nu} = \left(\rho + \frac{p}{c^2}\right) u_\mu u_\nu + p g_{\mu\nu}. \quad (2.6)$$

Since for a comoving observer the cosmic fluid is at rest, i.e. its four-velocity reads $u^\mu = (c, 0, 0, 0)$, Einstein's field equations lead to the *Friedmann equations* (Friedmann, 1922, 1924; Lemaître, 1927)

$$H^2 = \frac{8\pi G}{3} \rho - \frac{Kc^2}{a^2} + \frac{\Lambda}{3}, \quad (2.7a)$$

$$\frac{\ddot{a}}{a} = -\frac{4\pi G}{3} \left(\rho + \frac{3p}{c^2}\right) + \frac{\Lambda}{3}. \quad (2.7b)$$

In equation (2.7a) the Hubble function

$$H(t) \equiv \frac{\dot{a}}{a} \quad (2.8)$$

measuring the expansion rate of the Universe has been introduced. Derivatives with respect to time are indicated by a dot. The Robertson-Walker metric along with the Friedmann equations for the scale factor constitutes the class of Friedmann-Lemaître-Robertson-Walker (FLRW) world models.

The Friedmann equations encode energy conservation as they can be combined to

$$d\rho = -3 \left(\rho + \frac{p}{c^2}\right) d \log a. \quad (2.9)$$

This equation is readily integrated for a given, possibly time-dependent, equation of state parameter $w(a)$ relating the pressure to the energy density, i.e. $p = w\rho c^2$,

$$\rho(a) = \rho_0 \exp\left(\int_a^1 \frac{da'}{a'} 3[1 + w(a')]\right). \quad (2.10)$$

For example, in case of pressureless matter $w = 0$ while for radiation $w = 1/3$ yielding $\rho_m(a) = \rho_{m,0}a^{-3}$ and $\rho_r(a) = \rho_{r,0}a^{-4}$, respectively. Obviously, the scaling of the matter density ensures mass conservation while that of the radiation density accounts for the conservation of particle number and for the fact that radiation is redshifted in proportion to the inverse scale factor due to the cosmic expansion (see Section 2.3.1).

The first Friedmann equation (2.7a) introduces a characteristic (energy) density, the so-called critical density

$$\rho_{\text{crit}}(t) = \frac{3H^2(t)}{8\pi G}. \quad (2.11)$$

The contributions of the different matter species to the total energy density can then be conveniently expressed by dimensionless density parameters Ω_i

$$\rho(a) = [\Omega_m(a) + \Omega_r(a)]\rho_{\text{crit}}(a) = [\Omega_{\text{CDM}}(a) + \Omega_b(a) + \Omega_r(a)]\rho_{\text{crit}}(a). \quad (2.12)$$

The last equality accounts for the fact that the matter density is made up of cold dark matter (CDM) and baryonic matter. If the time dependence of the density parameter is not explicitly stated its value observed today is assumed, e.g. $\Omega_m \equiv \Omega_m(a_0)$. Additionally, by introducing density parameters for both the curvature and the cosmological constant by setting

$$\Omega_K(a) = -\frac{Kc^2}{H^2(a)} \quad \text{and} \quad \Omega_\Lambda(a) = \frac{\Lambda}{3H^2(a)} \quad (2.13)$$

the first Friedmann equation (2.7a) can be rewritten as

$$H^2(a) = H_0^2 \left(\Omega_m a^{-3} + \Omega_r a^{-4} + \Omega_K a^{-2} + \Omega_\Lambda \right). \quad (2.14)$$

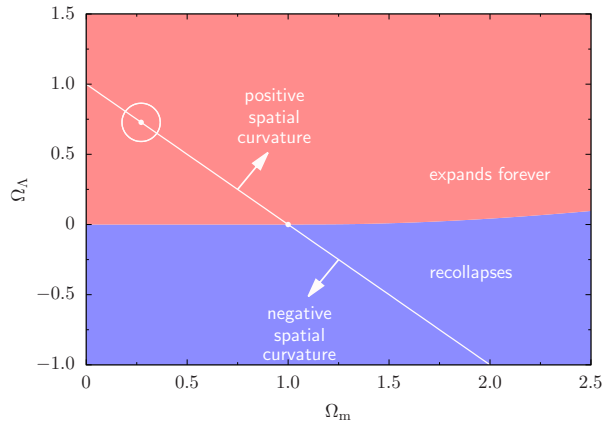


Figure 2.1.: Behaviour of a universe dominated by matter and dark energy. The encircled dot indicates the *WMAP7* best-fitting values.

Not all four density parameters are independent because they necessarily have to add up to unity. In particular, a universe where $\Omega_m(a) + \Omega_r(a) + \Omega_\Lambda(a) = 1$ is spatially flat. Since today the radiation density is negligible, the possible ongoing expansion or future collapse of the Universe can be conveniently analysed in the Ω_m - Ω_Λ -plane as shown in Figure 2.1.

In Table 2.1 the values of the density parameters recommended by the *WMAP* team after the seven-year-data release are given. These constraints are derived from CMB observations in combination with measurements of baryon acoustic oscillations² (BAO) as well as a local measurement of the Hubble constant (Komatsu, E. et al., 2011). Most recently, the *WMAP* results have been largely confirmed by the first *Planck* data release (Planck Collaboration, 2013a).

²Before recombination baryons were tightly coupled to the CMB photons. The oscillations of sound waves, resulting from the radiation pressure counteracting gravitational collapse, are therefore expected to be imprinted in the baryon perturbations as well as the CMB temperature anisotropies (cf. Section 7.1.1).

Table 2.1.: Cosmological parameters.

Parameter	<i>WMAP</i>	<i>Planck</i>	Description
Ω_m	$0.272^{+0.015}_{-0.016}$	0.314 ± 0.020	total matter density
Ω_b	0.0456 ± 0.0016	0.0486 ± 0.0021	baryonic matter density
Ω_{CDM}	0.227 ± 0.014	0.263 ± 0.013	cold dark matter density
Ω_r	$(8.421^{+0.311}_{-0.335}) \times 10^{-5}$	$(9.187 \pm 0.382) \times 10^{-5}$	radiation density
Ω_Λ	$0.728^{+0.015}_{-0.016}$	0.686 ± 0.020	cosmological constant
h	$0.704^{+0.013}_{-0.014}$	0.674 ± 0.014	Hubble parameter ($H_0 = 100 h \text{ km s}^{-1} \text{ Mpc}^{-1}$)
n_s	0.963 ± 0.012	0.962 ± 0.009	spectral index of primordial power spectrum
$\Delta_{\mathcal{R}}^2$	$(2.441^{+0.088}_{-0.092}) \times 10^{-9}$	$(2.23 \pm 0.16) \times 10^{-9}$	amplitude of primordial power spectrum
σ_8	0.809 ± 0.024	0.834 ± 0.027	normalization of the linear matter power spectrum smoothed on a scale of 8 Mpc

The second column gives the seven-year Λ CDM *WMAP*+BAO+ H_0 best-fitting cosmological parameters (Komatsu, E. et al., 2011), while the third column contains the results for the *Planck* CMB temperature power spectrum alone (Planck Collaboration, 2013a). The radiation density parameter is obtained via the relation $\Omega_r = 2.469 \times 10^{-5} h^{-2} (1 + 0.2271 N_{\text{eff}})$. It includes the contributions from neutrinos with an effective number of species $N_{\text{eff}} = 3.04$.

2.2.1. Dark energy

Since the Hubble expansion of the Universe has to counteract the gravitational attraction of its matter content, it is expected to gradually slow down. Observations of Supernovae Type Ia (SN Ia),³ however, show that the Universe currently undergoes a stage of *accelerated* expansion (Riess, A. G. et al., 1998; Perlmutter, S. et al., 1999). In terms of the scale factor accelerated expansion means $\ddot{a} > 0$. According to the second Friedmann equation (2.7b) this requires matter violating the strong energy condition $\rho c^2 + 3p > 0$ or equivalently in terms of the equation of state $w < -1/3$. The exceptional property of negative pressure not present for any known form of matter gave rise to the name *dark energy*. One possible candidate for dark energy is the cosmological constant. Interpreting it as a contribution to the Universe's energy content instead of being a geometrical quantity it can be described by a fluid with negative pressure equal to its energy density, i.e. $w = -1$. It is then plausible to relate the cosmological constant to the Universe's vacuum energy density. But a rough estimate of the latter, for example obtained by adding all zero-point energies up to the Planck mass, yields $\rho_{\text{vac}} \approx 10^{74} \text{ GeV}^4$ which is in tremendous contrast to $\rho_\Lambda \approx 10^{-47} \text{ GeV}^4$. This discrepancy with all possible fundamental energy scales is sometimes referred to as *fine-tuning problem*. Yet another troublesome issue with a cosmological constant is the so-called *coincidence problem*: the cosmological constant only recently started to dominate the Universe's energy budget, leaving today's observer in the rather privileged position to measure an accelerated expansion.

These difficulties motivate the invention of dynamical dark energy models. The huge variety of models proposed so far can be divided into two main categories modifying the left- or the right-hand side of Einstein's equations (2.3), respectively. The first class of models covers modified theories of gravity, while the second class contains specific forms of the energy momentum tensor with a

³Supernovae of Type Ia can be observed when a white dwarf accretes gas from a companion star in a binary system thereby exceeding the Chandrasekhar mass limit (Chandrasekhar, 1931). The absolute luminosity of the explosion is nearly constant at the peak of brightness. Therefore the distance to the nova can be inferred from measurements of the apparent luminosity. Hence, SN Ia serve as standard candles by which the luminosity distance (2.24) can be measured observationally.

negative pressure. For a comprehensive presentation of the different approaches I refer to [Amendola & Tsujikawa \(2010\)](#).

Present observational data of SN Ia, the CMB and BAO are consistent with a cosmological constant, $w = -0.980 \pm 0.053$ at the 68 per cent confidence level ([Komatsu, E. et al., 2011](#)). Although some dark energy models could have already been ruled out by observations the quality of data does not allow to discriminate between different models in general. The main objective of forthcoming dark energy studies is therefore to search for deviations from a constant equation of state of the dark energy component. For this purpose the phenomenological parametrization proposed by [Chevallier & Polarski \(2001\)](#) and [Linder \(2003\)](#)

$$w(a) = w_0 + (1 - a)w_a \quad (2.15)$$

proves most convenient, covering a wide range of different dark energy models. The cosmological constant is recovered for $w_0 = -1$ and $w_a = 0$.

2.3. Cosmological redshift and distances

2.3.1. Cosmological redshift

Almost all information that constitutes the contemporary picture of the Universe is provided by light in its different wavebands. Therefore, understanding light propagation in an expanding universe is of major importance. In the following, I will assume that an observer located at the origin of the coordinate system receives light propagating in radial direction. The analysis can be further simplified by introducing conformal time

$$\eta \equiv \int_0^t \frac{dt'}{a(t')}, \quad (2.16)$$

which allows to bring the Robertson-Walker line element (2.5) into the following form

$$ds^2 = -a^2(t) \left(c^2 d\eta^2 - \left[d\chi^2 + f_K^2(\chi) \left(d\theta^2 + \sin^2 \theta d\phi^2 \right) \right] \right). \quad (2.17)$$

Radial trajectories along constant angles θ and ϕ are geodesics and since photons follow null or light-like geodesics, i.e. $ds^2 = 0$, light rays are characterized by a linear η - χ -relation

$$d\chi^2 = c^2 d\eta^2 \quad \iff \quad \chi(\eta) = \pm c\eta + \text{const.} \quad (2.18)$$

Consequently, the conformal time interval $\Delta\eta$ of a light signal is the same for the emitter at $(\eta_{\text{em}}, \chi_{\text{em}})$ and the observer at $(\eta_{\text{obs}}, 0)$. The physical time interval, however, does change according to

$$\Delta t_{\text{em}} = a(\eta_{\text{em}})\Delta\eta \quad \text{and} \quad \Delta t_{\text{obs}} = a(\eta_{\text{obs}})\Delta\eta. \quad (2.19)$$

Since the measured wavelength of the signal is proportional to the physical time interval and the scale factor is increasing with (conformal) time (in case of an expanding universe), the observed wavelength is enlarged. The light is shifted towards smaller frequencies, it is *redshifted*. Because the scale factor today is unity, there is a one-to-one correspondence between the cosmological redshift z , defined as the fractional change in wavelength, and the scale factor at emission

$$1 + z \equiv 1 + \frac{\lambda_{\text{obs}} - \lambda_{\text{em}}}{\lambda_{\text{em}}} = \frac{a(\eta_{\text{obs}})}{a(\eta_{\text{em}})} = \frac{1}{a}. \quad (2.20)$$

2.3.2. Distances

Cosmological observations are that far extended in redshift that spacetime effects become appreciable and Euclidean geometry breaks down. In order to restore the Euclidean notion of distance in an arbitrarily curved spacetime, distance measures have to be chosen carefully according to the physical

process under consideration. Relating the apparent brightness of an object to its luminosity requires a different distance definition (*luminosity distance* d_L) than a relation between the object's apparent angular velocity and its intrinsic transverse speed (*proper motion distance* d_M).

For this work the *angular diameter distance* d_A is most important. It mediates between the proper (transverse) size Δl of an object and its observed angular diameter $\Delta\theta$ (which is supposed to be sufficiently small such that $\sin \Delta\theta \sim \Delta\theta$)

$$d_A = \frac{\Delta l}{\Delta\theta} \quad (2.21)$$

as shown in Figure 2.2. The proper size can be inferred from the Robertson-Walker line element (2.5) by noting that a relativistically correct measurement of length needs to be carried out simultaneously, i.e. $\Delta t = 0$, and that in case of the transverse size $\Delta\chi$ and $\Delta\phi$ may be set to zero

$$\Delta l = \sqrt{\Delta s^2} = a(t_{\text{em}}) f_K(\chi_{\text{em}}) \Delta\theta. \quad (2.22)$$

Accordingly, the angular diameter distance is given by

$$d_A = a(t_{\text{em}}) f_K(\chi_{\text{em}}). \quad (2.23)$$

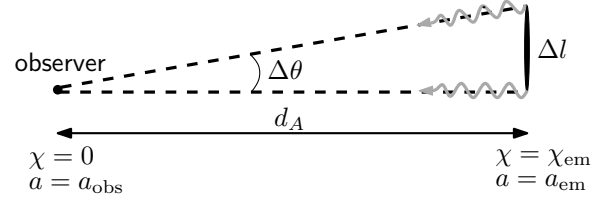


Figure 2.2.: Visualization of the angular diameter distance.

It is interesting to note that all three distances can readily be converted into each other (Weinberg, 1976)

$$d_L = (1+z)d_M = (1+z)^2 d_A \quad (2.24)$$

providing a valuable tool for testing independently the consistency of different cosmological models.

The radial *comoving distance* χ can be related to the scale factor by means of the Hubble function

$$\chi(a_{\text{obs}}, a_{\text{em}}) = c [\eta(a_{\text{obs}}) - \eta(a_{\text{em}})] = c \int_{a_{\text{em}}}^{a_{\text{obs}}} \frac{da'}{a'^2 H(a')}. \quad (2.25)$$

Evaluating this formula for the initial scale factor, i.e. setting $a_{\text{em}} = a_{\text{ini}}$, one obtains the (comoving) *particle horizon* χ_p , the maximum comoving distance light can propagate. It describes the radial extent of regions which can be causally connected. The particle horizon is a scale set by the finite speed of light. It is therefore a kinematical horizon which should be distinguished from the *Hubble* or *curvature scale* c/H which, in contrast, is a dynamical scale. Characterizing the expansion of the universe, the latter is crucial in the description of structure formation (cf. Section 2.4). Furthermore, it is comparable to the four-curvature scale of the entire spacetime and can consequently be used to estimate the size of the local inertial frame in which a Newtonian treatment of non-relativistic matter is applicable.

2.4. Structure formation

Both, the tiny fluctuations of the CMB and the plethora of structures of today's Universe, emerge from the very same initial fluctuations in the cosmic density field. Since non-relativistic matter clusters and is unstable to gravitational collapse, the initially tiny inhomogeneities could have been substantially amplified in the course of time, resulting in a structure-rich universe.

2.4.1. Homogeneous structure growth

Although General Relativity needs to be invoked for a consistent description of the Universe as a whole many aspects of structure formation can be treated in Newtonian theory. Such an analysis is necessarily restricted to non-relativistic matter and must not exceed the Hubble scale (cf. Section 2.3.2). On

sufficiently large scales the Universe's matter content can be described as a perfect fluid. The evolution of its energy density ρ , velocity \mathbf{V} and pressure P is then governed by a set of hydrodynamical equations along with a field equation for the gravitational potential Ψ

$$\frac{\partial \rho}{\partial t} + \nabla \cdot (\rho \mathbf{V}) = 0 \quad (\text{continuity equation}), \quad (2.26a)$$

$$\frac{\partial \mathbf{V}}{\partial t} + (\mathbf{V} \cdot \nabla) \mathbf{V} = -\nabla \Psi - \frac{\nabla P}{\rho} \quad (\text{Euler equation}), \quad (2.26b)$$

$$\Delta \Psi = 4\pi G \rho \quad (\text{Poisson equation}). \quad (2.26c)$$

For a long phase of cosmic evolution the deviations of the density from the homogeneous and isotropic background ρ_{bg} which are characterized by the *density contrast*

$$\delta(\mathbf{x}, t) \equiv \frac{\rho(\mathbf{x}, t) - \rho_{\text{bg}}(t)}{\rho_{\text{bg}}(t)} \quad (2.27)$$

are so small that a linearization of the hydrodynamical equations is well applicable. Decomposing the fields into a background solution and small perturbations yields

$$\rho(\mathbf{x}, t) = \rho_{\text{bg}}(t) [1 + \delta(\mathbf{x}, t)], \quad (2.28)$$

$$\mathbf{V}(\mathbf{x}, t) = \mathbf{V}_{\text{bg}}(\mathbf{x}, t) + \mathbf{v}(\mathbf{x}, t) = H(t)\mathbf{x} + \mathbf{v}(\mathbf{x}, t), \quad (2.29)$$

$$\Psi(\mathbf{x}, t) = \Psi_{\text{bg}}(\mathbf{x}, t) + \Phi(\mathbf{x}, t). \quad (2.30)$$

The pressure is assumed to be only a function of the energy density ρ , i.e.

$$P(\mathbf{x}, t) = P(\rho_{\text{bg}}(t) [1 + \delta(\mathbf{x}, t)]) = P_{\text{bg}}(\mathbf{x}, t) + p(\mathbf{x}, t). \quad (2.31)$$

Thus, to first order its perturbation may be expressed in terms of the energy density

$$p(\mathbf{x}, t) = \left(\frac{\partial P}{\partial \rho} \right) \rho_{\text{bg}}(t) \delta(\mathbf{x}, t) \equiv c_S^2 \rho_{\text{bg}}(t) \delta(\mathbf{x}, t). \quad (2.32)$$

In the last step I identified the square of the adiabatic sound speed c_S^2 . This relation between pressure and density perturbations allows to derive a closed set of linearized equations

$$\frac{\partial \delta}{\partial t} + \frac{1}{a} \nabla_{\mathbf{q}} \cdot \mathbf{v} = 0 \quad (\text{linearized continuity equation}), \quad (2.33a)$$

$$\frac{\partial \mathbf{v}}{\partial t} + H\mathbf{v} = -\frac{1}{a} \nabla_{\mathbf{q}} \Phi - \frac{c_S^2}{a} \nabla_{\mathbf{q}} \delta \quad (\text{linearized Euler equation}), \quad (2.33b)$$

$$\Delta_{\mathbf{q}} \Phi = 4\pi G a^2 \rho_{\text{bg}} \delta \quad (\text{Poisson equation}). \quad (2.33c)$$

Here Lagrangian coordinates \mathbf{q} have been introduced. They are related to Eulerian coordinates by $\mathbf{x} = a(t)\mathbf{q}$. The operators $\nabla_{\mathbf{q}}$ and $\Delta_{\mathbf{q}}$ act on comoving coordinates and time derivatives now have to be carried out at constant \mathbf{q} . From an appropriate combination of these equations an equation for the time evolution of the density contrast can be derived

$$\ddot{\delta} + 2H\dot{\delta} - \frac{c_S^2}{a^2} \Delta_{\mathbf{q}} \delta - 4\pi G \rho_{\text{bg}} \delta = 0. \quad (2.34)$$

On large and intermediate scales, more precisely on scales larger than the Jeans length $\lambda_J = c_S \sqrt{\frac{\pi}{G\rho_{\text{bg}}}}$, where gravity dominates, the pressure can be safely neglected and the spatial derivatives drop out in equation (2.34). In this regime the density contrast evolves homogeneously and the growth of structure is fully described by the *growth function* $D_+(a)$ in terms of which the density contrast takes the form

$$\delta(\mathbf{q}, a) = D_+(a) \delta_0(\mathbf{q}) \quad \text{with} \quad \delta_0(\mathbf{q}) \equiv \delta(\mathbf{q}, a_0). \quad (2.35)$$

Accordingly, the growth function is obtained from the *growth equation* (Turner & White, 1997; Wang & Steinhardt, 1998; Linder & Jenkins, 2003)

$$\frac{d^2}{da^2}D_+(a) + \frac{1}{a} \left(3 + \frac{d \log H(a)}{d \log a} \right) \frac{d}{da}D_+(a) = \frac{3}{2a^2} \Omega_m(a) D_+(a). \quad (2.36)$$

which is equivalent to equation (2.34) (neglecting the pressure term).

In an Einstein-de Sitter universe, where $\Omega_m(a) \equiv 1$, the density contrast grows in proportion to the scale factor, i.e. $D_+(a) = a$. Comparing this to the results from Jeans theory of a static universe where inhomogeneities are exponentially amplified shows that gravitational instability is much less efficient in an expanding universe. While the growth of structures is driven by the matter density, because it sources the gravitational potential whose strength in turn determines the rate of structure formation, the Hubble expansion prevents structures from collapse. This is formally expressed in the friction-like term of equation (2.34) involving the Hubble function.

Finally, I would like to briefly address the influence of a relativistic component, i.e. radiation on the formation of structures. So far the analysis has been restricted to scales sufficiently smaller than the Hubble scale which is comparable to the particle horizon (cf. Section 2.3.2). The latter, however, is of the order of the Jeans length for relativistic matter. Consequently, only scales smaller than the Jeans length are involved and the relativistic component may be treated as homogeneous. It therefore solely changes the expansion rate of the Universe.

Introducing the normalized scale factor $y \equiv a/a_{\text{eq}}$, where a_{eq} denotes the scale factor of radiation matter equality, the growth equation (2.36) can be brought into a form which is known as Mészáros equation (Mészáros, 1974)

$$\frac{d^2}{dy^2}D_+(y) + \frac{(2+3y)}{2y(1+y)} \frac{d}{dy}D_+(y) - \frac{3}{2y(1+y)} D_+(y) = 0. \quad (2.37)$$

Its (growing) solution is given by

$$D_+(y) \propto 1 + \frac{3}{2}y. \quad (2.38)$$

During radiation domination $y \ll 1$ and consequently, the growth of structures is strongly suppressed even in the dark matter component. Acting only gravitationally dark matter is not directly affected by the strong radiation pressure itself but it is sensitive to the expansion rate which is influenced by the radiation component.

2.4.2. Beyond linear approximation

The linearization of the hydrodynamical equations becomes inappropriate when the density contrast approaches unity. An analytical description of nonlinear structure growth is only possible for a few idealized situations which possess special symmetry properties. From these particular solutions, however, one can extract useful *approximations* of inhomogeneous structure growth which hold at least in the translinear regime. Starting point is the strain tensor

$$\mathbf{J}_{ij}(\mathbf{q}, t) \equiv \frac{\partial x^i(\mathbf{q}, t)}{\partial q^j}, \quad (2.39)$$

i.e. the Jacobian matrix of the transformation from Eulerian to Lagrangian coordinates. Using the *unperturbed* hydrodynamical equations (2.26) an expression for the evolution of its determinant $J \equiv \det \mathbf{J}$ can be derived (Mukhanov, 2005)

$$(\log J)^\cdot + \text{tr} \left[\left(\mathbf{J} \mathbf{J}^{-1} \right)^2 \right] + 4\pi G \rho_{\text{bg},0} J^{-1} = 0. \quad (2.40)$$

For scalar perturbations the peculiar velocity field is irrotational and can be derived from a potential Ψ , thus

$$\mathbf{x}(\mathbf{q}, t) = a(t) \left(\mathbf{q} - \nabla_{\mathbf{q}} \Psi(\mathbf{q}, t) \right). \quad (2.41)$$

If the perturbation is one-dimensional, equation (2.40) reduces to

$$\ddot{\alpha} + 2H\dot{\alpha} - 4\pi G\rho_{\text{bg}}\alpha = 0 \quad \text{with} \quad \alpha \equiv \frac{\partial^2 \Psi}{\partial q^2}, \quad (2.42)$$

which has the same form as equation (2.34) without the pressure term. But in this case it is *exact* regardless of the size of the perturbation. Consequently, the (growing) solution is given by

$$\alpha(q, a) = D_+(a)\alpha_0(q) \quad (2.43)$$

and the energy density evolves according to

$$\rho(q, a) = \frac{\rho_{\text{bg},0}}{J(q, a)} = \frac{\rho_{\text{bg}}(a)}{1 - \alpha(q, a)}. \quad (2.44)$$

The approximation proposed by Zel'dovich (1970) extends the exact one-dimensional solution to three dimensions setting

$$\rho(\mathbf{q}, a) = \frac{\rho_{\text{bg}}(a)}{[1 - \alpha_1(\mathbf{q}, a)][1 - \alpha_2(\mathbf{q}, a)][1 - \alpha_3(\mathbf{q}, a)]} \quad \text{with} \quad \alpha_i(\mathbf{q}, a) \equiv D_+(a) \frac{\partial^2 \Psi_0}{\partial q_i^2}. \quad (2.45)$$

This expression corresponds to the leading order solution of equation (2.40) and its applicability is therefore limited to the translinear regime. In this regime one might approximate even further

$$\rho(\mathbf{q}, a) \approx \rho_{\text{bg}}(a) [1 + \alpha_1(\mathbf{q}, a) + \alpha_2(\mathbf{q}, a) + \alpha_3(\mathbf{q}, a)] = \rho_{\text{bg}}(a) \left[1 + D_+(a) \Delta_{\mathbf{q}} \Psi_0(\mathbf{q}) \right], \quad (2.46)$$

revealing that the displacement potential Ψ_0 is proportional to the gravitational potential Φ_0 (which can be immediately inferred from equation 2.28 and 2.33c). The Zel'dovich approximation ultimately breaks down when the trajectories of particles start crossing.

To follow the evolution of structures into the highly nonlinear regime one has to resort to cosmological N -body simulations. Very large high-resolution simulations reach a spatial resolution of about $100 \text{ kpc } h^{-1}$ predicting the mass distribution in the Universe on both the largest and the smallest scales (Springel, V. et al., 2005; Boylan-Kolchin et al., 2009). These simulations, however, require the use of today's most powerful supercomputers and have to be run for each particular choice of cosmological parameters separately, making them very costly and inflexible. Therefore, the development of improved semi-analytical perturbation theory methods is of great interest. Currently, renormalization group inspired approaches seem to be most promising (Croce & Scoccimarro, 2006; Pietroni, 2008; Anselmi et al., 2011; Anselmi & Pietroni, 2012).

2.4.3. Statistical description

Inflationary cosmology

In the previous section I have shown how fluctuations in the matter density evolve to build the cosmic structures observed today. In modern cosmology, the origin of the primordial inhomogeneities is explained by the theory of *inflation* (see Liddle, 1999; Langlois, 2010, for detailed introductions). Originally invented to explain the absence of magnetic monopoles, it was soon realized that an inflationary epoch, i.e. an epoch of *accelerated expansion*, could naturally explain why the Universe is spatially flat (the so-called *flatness problem*), as well as why the CMB temperature is uniform even on scales which exceed the particle horizon at recombination (the so-called *horizon problem*) (Guth,

1981). Today, the most important aspect of inflationary cosmology is its predictive power concerning the *statistical properties* of the primordial inhomogeneities.

As seen in Section 2.2.1 an inflationary phase requires a form of matter with negative pressure or, more precisely, with an equation of state $w < -1/3$. Due to its small energy density (cf. Table 2.1) the cosmological constant, or more generally the dark energy component, has been unable to dominate the cosmic evolution at early times and could therefore not drive inflation. Instead a possible and particularly instructive scenario is given by a homogeneous scalar field (scalar condensate), the so-called *inflaton* φ which follows slowly its potential $V(\varphi)$. Its energy density and pressure can be calculated to be

$$\rho_\varphi c^2 = \frac{1}{2}\dot{\varphi}^2 + V(\varphi) \quad \text{and} \quad p_\varphi = \frac{1}{2}\dot{\varphi}^2 - V(\varphi). \quad (2.47)$$

The slow-roll condition requires $\dot{\varphi}^2 \ll V(\varphi)$ and therefore $w_\varphi = p_\varphi/(\rho_\varphi c^2) \approx -1$. Whether the slow-roll condition is fulfilled for a given potential may be inferred from its (relative) slope and curvature, which constitute the so-called slow-roll parameters (Liddle & Lyth, 1992)

$$\epsilon \equiv \frac{1}{16\pi G} \left(\frac{V'}{V} \right)^2 \quad \text{and} \quad \eta \equiv \frac{1}{8\pi G} \left(\frac{V''}{V} \right), \quad (2.48)$$

where $V' \equiv \frac{dV}{d\varphi}$. Successful inflation demands that both parameters are much smaller than unity. The smallness of the first parameter ensures that the equation of state becomes sufficiently negative, i.e. $w_\varphi < -1/3$, while that of the second one makes the inflationary epoch last long enough. The very same conditions apply to scalar field realizations of dark energy, i.e. quintessence models (Wetterich, 1988; Ratra & Peebles, 1988; Caldwell et al., 1998) previously mentioned in Section 2.2.1.

During the inflationary phase the Universe's energy density is expected to be dominated by the inflaton, which is independent of the scale factor. Thus, the Hubble function is constant and the scale factor grows exponentially with time (an immediate consequence of the first Friedmann equation 2.7a). It is interesting to note that this implies that the curvature scale, i.e. c/H , is constant, while the physical size of the causally connected region set by the particle horizon grows exponentially fast, too. That is exactly the reason why inflation solves the flatness as well as the horizon problem.

As any quantum field, the inflaton exhibits vacuum fluctuations due to Heisenberg's uncertainty principle. The amplitudes of these fluctuations are only substantial on scales which are of the order of the Planck length. In the course of inflationary expansion, however, they are stretched to galactic scales, whereas their amplitudes are almost unchanged. The quantum fluctuations necessarily introduce (primordial) perturbations in the gravitational potential which in turn are manifest in the (initial) inhomogeneities of the matter density. The spectrum of these inhomogeneities has a nearly universal shape and depends only weakly on the concrete inflationary model. This is due to the fact that generically the fluctuations on a given physical scale cease evolving when the scale crosses the curvature scale. As noticed earlier, during inflation, physical sizes grow exponentially, whereas the curvature scale is almost constant. Consequently, the fluctuation amplitude is approximately the same for all scales, i.e. the resulting spectrum is nearly flat. Actually, perturbations on larger scales are slightly enhanced, allowing for a graceful exit of inflation, i.e. a smooth transition to a decelerating Friedmann-Lemaître-Robertson-Walker universe. Reheating sets in, and the potential energy of the inflaton is converted into a thermalized gas of matter and radiation.

Basic definitions

As described before, inflationary cosmology predicts the spectrum of the gravitational potential fluctuations or likewise the density contrast. This suggests to treat them as *random fields* the statistical properties of which have to reflect the cosmological principle (see Section 2.1). Thus, they have to be statistically homogeneous and isotropic. All quantities, for example the mean or the variance, should neither depend on position nor direction. From the statistical perspective, the observable Universe

is just one particular realization of the initial conditions, whereas in principle any average needs to be performed over a *statistical ensemble* of universes. The ensemble average, however, is equivalent to the sample average, i.e. averaging over the volume of the whole observable Universe, as long as ergodicity can be assumed (Adler, 1981; Marinucci & Peccati, 2010).

In the following I denote a statistically homogeneous and isotropic random field by $Q(\mathbf{x})$. Furthermore, I assume that its expectation value vanishes, i.e. $\langle Q(\mathbf{x}) \rangle = 0$. Its spatial *two-point correlation function* is then given by

$$\xi_Q(|\mathbf{x} - \mathbf{y}|) \equiv \langle Q(\mathbf{x})Q(\mathbf{y}) \rangle. \quad (2.49)$$

Its dependence on the modulus of the separation ensures that neither any point nor any direction is privileged. In case that $Q(\mathbf{x})$ is a Gaussian random field all higher order correlators can be expressed in terms of the correlation function by virtue of Wick's theorem (see Section A.2.1). This allows to capture deviations from Gaussianity by the *connected part* $\langle \dots \rangle_c$ of the n -point correlator. I give here the explicit expression for $n = 4$ only:

$$\begin{aligned} \langle Q(\mathbf{x}_1)Q(\mathbf{x}_2)Q(\mathbf{x}_3)Q(\mathbf{x}_4) \rangle_c &= \langle Q(\mathbf{x}_1)Q(\mathbf{x}_2)Q(\mathbf{x}_3)Q(\mathbf{x}_4) \rangle - [\langle Q(\mathbf{x}_1)Q(\mathbf{x}_2) \rangle \langle Q(\mathbf{x}_3)Q(\mathbf{x}_4) \rangle \\ &+ \langle Q(\mathbf{x}_1)Q(\mathbf{x}_3) \rangle \langle Q(\mathbf{x}_2)Q(\mathbf{x}_4) \rangle + \langle Q(\mathbf{x}_1)Q(\mathbf{x}_4) \rangle \langle Q(\mathbf{x}_2)Q(\mathbf{x}_3) \rangle]. \end{aligned} \quad (2.50)$$

If the underlying probability distribution is skewed odd correlators may be non-vanishing.

While in observations the correlation function is direct accessible its Fourier representation proves more convenient for theoretical considerations. The Fourier transform of the field $Q(\mathbf{x})$ is defined by

$$Q(\mathbf{k}) = \int d^3x Q(\mathbf{x})e^{-i\mathbf{x}\cdot\mathbf{k}} \quad \longleftrightarrow \quad Q(\mathbf{x}) = \int \frac{d^3k}{(2\pi)^3} Q(\mathbf{k})e^{i\mathbf{x}\cdot\mathbf{k}}. \quad (2.51)$$

The two-point statistics of the (complex) modes is described by the *power spectrum* $P_{QQ}(k)$

$$\langle Q(\mathbf{k})Q^*(\mathbf{k}') \rangle = (2\pi)^3 \delta_{\mathbb{D}}(\mathbf{k} - \mathbf{k}') P_{QQ}(k). \quad (2.52)$$

The Dirac δ -function guarantees that different modes are statistically independent reflecting homogeneity, while isotropy is manifest in the directional independence of the power spectrum. The next higher order statistics is given by the *bispectrum* $B_{QQQ}(\mathbf{k}_1, \mathbf{k}_2, \mathbf{k}_3)$

$$\langle Q(\mathbf{k}_1)Q(\mathbf{k}_2)Q(\mathbf{k}_3) \rangle = (2\pi)^3 \delta_{\mathbb{D}}(\mathbf{k}_1 + \mathbf{k}_2 + \mathbf{k}_3) B_{QQQ}(\mathbf{k}_1, \mathbf{k}_2, \mathbf{k}_3), \quad (2.53)$$

which vanishes identically for any symmetric probability distribution function and is therefore a primary diagnostic in the search for deviations from Gaussianity.

Matter power spectrum and transfer function

Most inflationary models predict that the initial fluctuations follow a Gaussian distribution and current observations confirm that the amount of primordial non-Gaussianity, if present at all, is rather small (Komatsu, E. et al., 2011). A Gaussian random process is completely characterized by its variance. Thus, in order to describe the statistics of the metric perturbations or equivalently of the density contrast, knowledge of the power spectrum is sufficient. According to inflationary cosmology the dimensionless spectrum of primordial fluctuations is almost flat with a small tilt towards larger scales

$$k^3 \mathcal{P}_{\Phi\Phi}(k) = 2\pi^2 \Delta_{\mathcal{R}}^2 k^{n_s - 1}, \quad (2.54)$$

where $\Delta_{\mathcal{R}}^2$ is the scalar fluctuations amplitude and n_s is the spectral index which is slightly smaller than one (cf. Table 2.1). Its deviation from unity may be expressed in terms of the two slow-roll parameters of equation (2.48) (Liddle & Lyth, 1992): $n_s - 1 = -6\epsilon + 2\eta$.

While during the subsequent evolution of the universe the statistical properties are preserved, the shape of the spectrum does change. The transition from the radiation dominated epoch to matter domination is captured by the *transfer function* $T(k)$, whereas the time evolution during matter domination is governed by the (linear) growth function, thus

$$P_{\delta\delta}(k, a) = D_+^2(a) T^2(k) k^4 \mathcal{P}_{\Phi\Phi}(k) \propto D_+^2(a) T^2(k) k^{n_s}. \quad (2.55)$$

It is important to note that the transfer function is a function of wavenumber only, avoiding mode coupling which would inevitably change the underlying probability distribution. The relation between the primordial power spectrum of the gravitational potential and that of the density contrast has been established via the Poisson equation (2.33c), i.e. via $\mathcal{P}_{\delta\delta}(k) \propto k^4 \mathcal{P}_{\Phi\Phi}(k)$. Perturbations which reenter the curvature scale before matter radiation equality are suppressed according to the Mészáros-mechanism presented at the end of Section 2.4.1. Realizing that on smallest scales the growth of structures almost completely stops, thus $k^3 P_{\delta\delta}(k) \sim \text{const.}$, one finds $T(k) \sim k^{-2}$ for $k \gg k_{\text{eq}}$. In contrast to this, supercurvature modes evolve freely hence $T(k) \sim 1$ for $k \ll k_{\text{eq}}$.

The transfer function is very well described by the fitting formula of Bardeen et al. (1986)

$$T(q) = \frac{\log(1 + 2.34q)}{2.34q} \left[1 + 3.89q + (16.2q)^2 + (5.47q)^3 + (6.71q)^4 \right]^{-\frac{1}{4}}. \quad (2.56)$$

The rescaling of the wavenumber $q = k/\Gamma$ by the shape parameter

$$\Gamma = \Omega_m h \exp \left[-\Omega_b \left(1 + \frac{\sqrt{2h}}{\Omega_m} \right) \right] \quad (2.57)$$

accounts for the influence of the baryon density on the peak shape of the spectrum (Sugiyama, 1995). Improved fitting formulae take additionally baryonic acoustic oscillations into account (Eisenstein & Hu, 1998, 1999).

Inflationary cosmology predicts the shape of the spectrum but not its amplitude. This has to be determined by observations. Commonly, the power spectrum is normalized to the variance of the linearly evolved density field at redshift zero smoothed by a top hat filter on the scale $R = 8 \text{ Mpc } h^{-1}$

$$\sigma_R^2 = \frac{1}{2\pi^2} \int k^2 dk W^2(kR) P_{\delta\delta}(k). \quad (2.58)$$

The Fourier transform of the top hat filter can be expressed by the first order spherical Bessel function $j_1(x)$ (Abramowitz & Stegun, 1972): $W(x) = 3j_1(x)/x$.

Nonlinear evolution

As the growth equation (2.36) is scale-independent, each mode of the density field evolves in the same way. The statistical properties of the density field are unchanged. The validity of the growth equation, however, is restricted to the linear regime. With the onset of nonlinear structure growth, density modes cannot longer evolve independently. Mode coupling sets in and the statistics of the fluctuation field is necessarily altered. It becomes inevitably non-Gaussian, even in case of purely Gaussian initial metric perturbations. For a complete statistical description the power spectrum is no longer sufficient and higher-order statistics (in principle all, i.e. infinitely many, *moments* [see Section A.2.2]) of the density contrast needs to be taken into account. In particular, the probability distribution function becomes more and more skewed due to the fact that a lower bound, namely $\delta \geq -1$ by definition, but no upper bound exists.

Nonlinear evolution transfers power from large to small scales as structures collapse. Consequently, the amplitude of the power spectrum increases on small scales at the expense of intermediate scales, while the largest scales still follow linear evolution. Since inhomogeneous structure growth cannot be

followed analytically (cf. Section 2.4.2) the fully nonlinear matter power spectrum has to be inferred from numerical simulations. For most practical purposes, however, an approximation by the semi-analytical fitting formula of [Smith, R. E. et al. \(2003\)](#) is sufficient. Figure 2.3 shows the linear and the approximative nonlinear matter power spectrum for different redshifts. The cosmological parameters are chosen according to Table 2.1. As expected, the smaller the redshift, the larger the scale being affected by inhomogeneous structure growth.

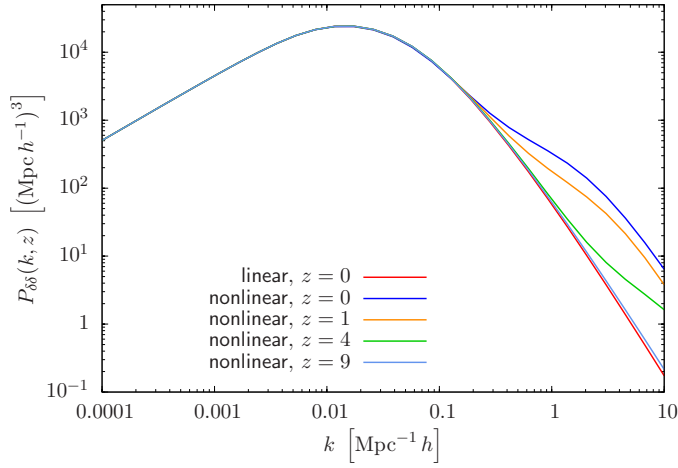


Figure 2.3: Linear and nonlinear matter power spectrum for different redshifts.

3

Chapter 3

Weak gravitational lensing

In this chapter the basic principles of weak gravitational lensing are presented. The meaning of the term *weak* is twofold in this context. First, it is used in order to distinguish the effects investigated in this work from other gravitational light deflection phenomena such as strong or micro lensing. These phenomena are discussed in detail by [Schneider et al. \(2006\)](#). Second, it emphasizes that the individual deflections, which light rays experience passing gravitational lenses on their way from the source to the observer, are small. The sources are distant background galaxies, i.e. light emitted by *baryonic* matter, while the inhomogeneities in *any* matter or likewise energy component of the Universe serve as gravitational lenses. These lenses are characterized by their Newtonian gravitational potential which is assumed to be weak in the sense that $\Phi \ll c^2$. Furthermore, the peculiar velocities of the lenses are supposed to be small in comparison to the speed of light, i.e. they move slowly with respect to the mean cosmic flow. Finally, all considerations are made under the assumption that the deflection of light by local inhomogeneities and the effect of the homogeneous and isotropic background completely separate. These assumptions are valid in all astrophysical applications apart from light propagation near compact objects.

The presentation given here follows to some extent [Bartelmann \(2010b\)](#) and [Amendola & Tsujikawa \(2010\)](#). A more detailed review of weak gravitational lensing provide [Bartelmann & Schneider \(2001\)](#).

3.1. Jacobi equation

In Section 2.3.2 several distance measures have been introduced to accommodate for the effects of a curved spacetime on the propagation of light. So far only a single light ray has been considered. Now, I would like to extend the discussion to a thin bundle of light rays. The propagation of any of these light rays is determined by the *geodesic equation*

$$\nabla_k k = 0, \quad (3.1)$$

i.e. the parallel transport along the light ray preserves the tangent vector

$$k^\mu = \frac{dx^\mu}{d\lambda} \quad (3.2)$$

to the light ray⁴. Since the affine parameter λ is arbitrary, it can be chosen such that $d\lambda = a^2 d\eta$. With this choice its projection on the four-velocity of a freely falling observer is unity, i.e. $\langle k, u \rangle = 1$.

⁴Although using the same symbol, confusion with the usual gradient in three dimensions can be avoided by realizing that the covariant derivative along a vector field X always carries that vector field as subscript, thus is indicated by ∇_X , whereas the gradient, if at all, is labelled by a three-dimensional vector, e.g. ∇_q .

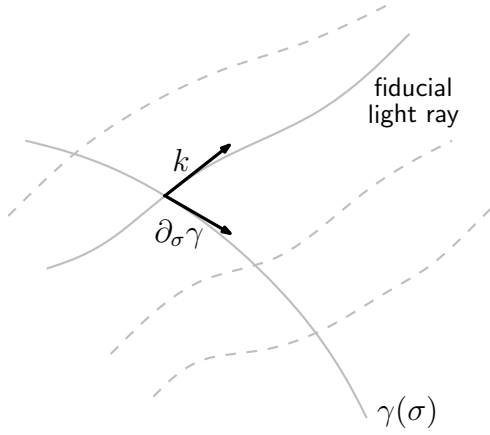


Figure 3.1.: Geodesic deviation.

Selecting a fiducial light ray of the bundle and connecting it to a neighbouring ray via a curve $\gamma(\sigma)$, the change of the connecting vector $v = \partial_\sigma \gamma$ along the fiducial light ray is quantified by the equation of *geodesic deviation* or *Jacobi equation*

$$\nabla_k^2 v = R(k, v)k. \quad (3.3)$$

The situation is illustrated in Figure 3.1. It is important to note that it is the curvature of spacetime which makes adjacent light rays approach to or recede from another. Initially parallel light rays remain parallel only in a flat spacetime where the Riemann tensor $R(X, Y)Z$ vanishes. The Jacobi equation (3.3) is the generalization of the tidal force equation in Newtonian mechanics.

The bending of the light rays towards, or away from, each other will be observed on a screen in the three-space of the observer perpendicular to the light ray, i.e. the connecting vector is two-dimensional. Introducing the optical tidal matrix \mathbf{T} the Jacobi equation (3.3) can be recast into

$$\nabla_k^2 \begin{pmatrix} v^1 \\ v^2 \end{pmatrix} = \mathbf{T} \begin{pmatrix} v^1 \\ v^2 \end{pmatrix}. \quad (3.4)$$

For the homogeneous and isotropic background described by the Friedmann-Lemaître-Robertson-Walker models this equation takes a particularly simple form. If one uses the comoving radial coordinate χ as the affine parameter along the fiducial ray equation (3.4) reduces to

$$\left(\frac{d^2}{d\chi^2} + K \right) \frac{v^i}{a} = 0, \quad (3.5)$$

where K is the curvature parameter introduced in Section 2.2.

3.2. Perturbed photon propagation

Given an expression for the background contribution to the optical tidal matrix it now needs to be extended by the contributions of matter and energy inhomogeneities. In Section 2.4 perturbations of the homogeneous and isotropic background have been treated in Newtonian theory. This approach is naturally limited to subcurvature scales and non-relativistic matter. Accordingly, light propagation necessarily has to be considered in the framework of General Relativity. In General Relativity, however, there is no preferred coordinate system and the freedom of coordinate transformations, or more precisely *gauge freedom*, may lead to fictitious, i.e. unphysical, perturbations resulting from the particular choice of coordinate system. Therefore, any observable needs to be expressed by gauge-invariant quantities.

I only consider scalar perturbations and invoke *longitudinal* or *conformal Newtonian gauge* in terms of which the perturbed metric can be written as

$$ds^2 = -a^2(\eta) \left[c^2 \left(1 - \frac{2\Phi_N}{c^2} \right) d\eta^2 - \left(1 - \frac{2\Psi_N}{c^2} \right) \hat{\gamma}_{ij} dx^i dx^j \right] \quad (3.6)$$

with

$$\hat{\gamma}_{ij} dx^i dx^j = d\chi^2 + \chi^2 (d\theta^2 + \sin^2 \theta d\phi^2). \quad (3.7)$$

The two Bardeen potentials Φ_N and Ψ_N are a generalization of the Newtonian gravitational potential. In the following I assume that there are no anisotropic stresses present, hence $\Phi_N = -\Psi_N$, and identify $\Phi \equiv \Phi_N$. The restriction to a spatially flat metric is appropriate since the spatial extent of the perturbation deflecting the light ray is much smaller than the curvature scale.

One common approach to analyse the propagation of light in the perturbed metric given by the line element of equation (3.6) is to split all quantities involved in an unperturbed background part, plus a perturbation. The latter is assumed to be small due to the assumptions made at the beginning of this chapter. Thus, only terms which are first order in the Newtonian gravitational potential will be kept. The light ray is then characterized by $k^\mu = \hat{k}^\mu + \delta k^\mu$ and the coordinate representation of the geodesic equation (3.1) reads

$$\frac{d}{d\lambda} k^\mu + \left(\hat{\Gamma}_{\alpha\beta}^\mu + \delta\Gamma_{\alpha\beta}^\mu \right) k^\alpha k^\beta = 0. \quad (3.8)$$

The explicit form of the Christoffel symbols $\hat{\Gamma}_{\alpha\beta}^\mu, \delta\Gamma_{\alpha\beta}^\mu$ is given in Appendix A.1.1. The deflection of the light ray in the two directions $x^{1,2}$ perpendicular to the propagation direction $x^3 = \chi$ is given by the spatial part of the perturbed geodesic equation (3.8)

$$\frac{d^2 x^i}{d\lambda^2} + 2aH(a) \frac{d\eta}{d\lambda} \frac{dx^i}{d\lambda} = -2 \left(\frac{d\eta}{d\lambda} \right)^2 \frac{\partial\Phi}{\partial x^i}. \quad (3.9)$$

Using that

$$\frac{d^2 x^i}{d\lambda^2} = \frac{c^2}{a^4} \frac{d^2 x^i}{d\chi^2} - 2aH(a) \frac{d\eta}{d\lambda} \frac{dx^i}{d\lambda} \quad (3.10)$$

and keeping in mind that $a^2 d\eta = d\lambda$ equation (3.9) can be brought into a form similar to that of equation (3.5)

$$\frac{d^2 x^i}{d\chi^2} = -\frac{2}{c^2} \frac{\partial\Phi}{\partial x^i}. \quad (3.11)$$

This equation describes the transverse displacement of a light ray in the vicinity of a local inhomogeneity. Cosmic lensing is then the combination of both, the distortions by localized lenses and the bending of light due to the curvature of the homogeneous and isotropic background (described by equation 3.5)

$$\left(\frac{d^2}{d\chi^2} + K \right) x^i = -\frac{2}{c^2} \frac{\partial\Phi}{\partial x^i}. \quad (3.12)$$

Specifying appropriate boundary conditions the differential equation for the (comoving) bundle dimension (3.12) can be solved by the method of Green's functions. Since the observer located at the origin of the coordinate frame receives adjacent light rays enclosing an angle $\theta = (\theta^1, \theta^2)$ the boundary conditions read

$$x^i \Big|_{\chi=0} = 0 \quad \text{and} \quad \frac{dx^i}{d\chi} \Big|_{\chi=0} = \theta^i. \quad (3.13)$$

By coincidence the Green's function of the operator $\frac{d^2}{d\chi^2} + K$ is identical to the comoving angular diameter distance $f_K(\chi)$ defined in equation (2.4)

$$G(\chi, \chi') = f_K(\chi) \Theta_H(\chi - \chi') \quad \text{with} \quad \Theta_H(\chi - \chi') = \begin{cases} 1 & \text{if } \chi > \chi', \\ 0 & \text{else.} \end{cases} \quad (3.14)$$

Thus, the solution of equation (3.12) is given by

$$x^i(\chi) = f_K(\chi) \theta^i - \frac{2}{c^2} \int_0^\chi d\chi' f_K(\chi - \chi') \frac{\partial}{\partial x^i} \Phi(x^j(\chi'), \chi'). \quad (3.15)$$

In principle, this integral needs to be evaluated along the actual trajectory of the photon. But since the deflections are supposed to be small in accordance with the assumption that the Newtonian potential is

weak, i.e. $\Phi \ll c^2$, it is justified to invoke the *Born approximation*: the actual transverse separation of neighbouring light rays may be well approximated by their intrinsic separation, i.e. $x^j(\chi') \rightarrow f_K(\chi') \theta^j$. The validity of the Born approximation has been confirmed by numerical simulations (Dodelson et al., 2005; Hilbert et al., 2009) and perturbative calculations (Cooray & Hu, 2002; Krause & Hirata, 2010; Schäfer et al., 2012).

In order to describe the typical situation in observations it is more convenient to work in terms of (separation) angles. As long as the curvature of the celestial sphere does not explicitly have to be taken into account, these angular coordinates can be described by two-dimensional Cartesian vectors and the corresponding derivatives are usual partial derivatives. Later on, in Chapter 5, more elaborate techniques will be presented which go beyond the flat-sky approximation. There the partial derivatives have to be replaced by covariant derivatives on the unit sphere. Introducing the angle β via $x^i = f_K(\chi_s) \beta^i$, where χ_s denotes the radial position of a source, equation (3.15) can be brought into the form of the *lens equation*

$$\beta = \theta - \alpha(\theta). \quad (3.16)$$

The (reduced) deflection angle α is obtained as angular gradient of the *lensing potential* $\phi(\theta)$, which emerges as the line-of-sight projection of the Newtonian gravitational potential

$$\alpha^i(\theta) = \frac{\partial}{\partial \theta^i} \phi(\theta) \equiv \frac{\partial}{\partial \theta^i} \frac{2}{c^2} \int_0^{\chi_s} d\chi' \frac{f_K(\chi_s - \chi')}{f_K(\chi_s) f_K(\chi')} \Phi(f_K(\chi') \theta^j, \chi'). \quad (3.17)$$

Light rays originally emitted at β are detected at the lensed position θ . Consequently, gravitational lensing alters the observed shape of galaxies. In a locally linearized form, which is permissible due to the smallness of the individual deflection, this effect is captured by the Jacobian of the lens mapping (3.16)

$$\mathbf{A} = \frac{\partial \beta}{\partial \theta} = \begin{pmatrix} 1 - \kappa - \gamma_+ & -\gamma_\times \\ -\gamma_\times & 1 - \kappa + \gamma_+ \end{pmatrix} = (1 - \kappa) \begin{pmatrix} 1 - g_+ & -g_\times \\ -g_\times & 1 + g_+ \end{pmatrix}. \quad (3.18)$$

In terms of the lensing potential the individual contributions read

$$\kappa = \frac{1}{2} \left(\frac{\partial^2 \phi}{\partial (\theta^1)^2} + \frac{\partial^2 \phi}{\partial (\theta^2)^2} \right), \quad \gamma_+ = \frac{1}{2} \left(\frac{\partial^2 \phi}{\partial (\theta^1)^2} - \frac{\partial^2 \phi}{\partial (\theta^2)^2} \right) \quad \text{and} \quad \gamma_\times = \frac{\partial^2 \phi}{\partial \theta^1 \partial \theta^2}. \quad (3.19)$$

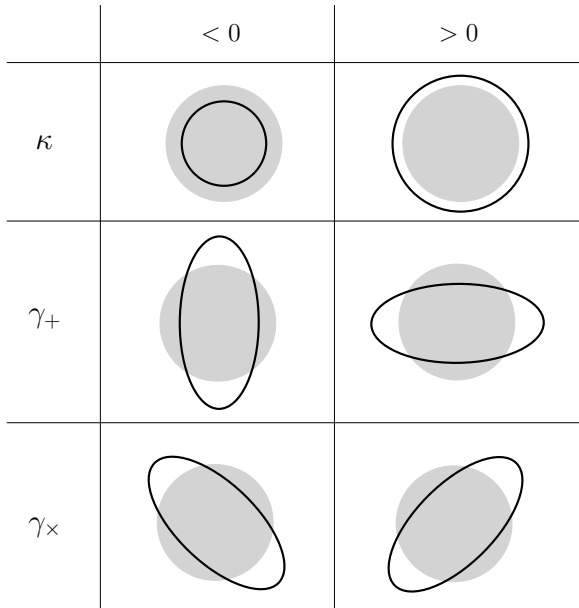


Figure 3.2.: Illustration of the distortion caused by the convergence and the two shear components, respectively. The source is indicated by the shaded circle.

The convergence κ describes the isotropic change in size of the image, while the two shear components γ_+ and γ_\times encode the deformation of the source galaxy. The γ_+ component describes the stretching in the x^1 - x^2 directions. The stretching along axes rotated by 45° is given by γ_\times . This is illustrated in Figure 3.2. Rotations of the image may not be generated in this linearized treatment.

The last equality in equation (3.18) shows that the convergence and the two shear components are not observable independently. The prefactor $1 - \kappa$ causes a homogeneous distortion of the source which is unobservable because the intrinsic size of the source is unknown. Thus, the components of the *reduced shear* $g_{+,\times} = \gamma_{+,\times} / (1 - \kappa)$ are the primary observable in weak lensing analyses. This will be discussed in more detail in Chapter 5.

It should be emphasized that all observable quantities are *second* derivatives of the lensing

potential. The choice of reference light ray with respect to which the transverse distortion within a light bundle is computed is ambiguous, leaving *absolute* deflection angles unobservable. Only their differences or derivatives are measurable. This gives rise to extend the analysis to third order derivatives of the lensing potential, which are combined to the first and second flexion, respectively (Goldberg & Bacon, 2005; Bacon et al., 2006). Gravitational flexion will not be considered in this work.

3.3. Weak lensing power spectra

In contrast to strong lensing phenomena, where, for example, a single galaxy is multiply imaged, the effect of weak gravitational lensing is only *statistically* observable. It is a reasonable assumption that the convergence, as well as the two shear components, vanish on average because, according to the cosmological principle (see Section 2.1), there must not be any preferred deflection angle. But due to the fact that light rays are deflected by the coherent large-scale structure of the Universe the two-point statistics of these fields are expected to reflect the statistical properties of the underlying cosmic density field described in Section 2.4.3.

In equation (3.17) the deflection angle is given for one particular source located at a certain (co-moving) radial distance χ_s . For a realistic survey the whole population of lensed sources along the line-of-sight needs to be taken into account. Since the deflection angle or likewise the lensing potential has been derived in linear theory all individual contributions can be simply summed up using the number density of sources $n(\chi_s) d\chi_s$. Introducing the weight function $G(\chi)$

$$G(\chi) = \int_{\chi}^{\infty} d\chi_s \frac{f_K(\chi_s - \chi)}{f_K(\chi_s)} f_K(\chi) n(\chi_s) \quad (3.20)$$

the expressions for the convergence and the two shear components read

$$\left. \begin{array}{l} \kappa \\ \gamma_+ \\ \gamma_{\times} \end{array} \right\} = \frac{2}{c^2} \int_0^{\infty} d\chi G(\chi) D_{\circ,+,\times} \Phi(x^j(\chi), \chi) \quad \text{with} \quad D_{\circ,+,\times} = \begin{cases} \frac{1}{2} \left(\frac{\partial^2}{\partial(x^1)^2} + \frac{\partial^2}{\partial(x^2)^2} \right), & \circ \\ \frac{1}{2} \left(\frac{\partial^2}{\partial(x^1)^2} - \frac{\partial^2}{\partial(x^2)^2} \right), & + \\ \frac{\partial^2}{\partial x^1 \partial x^2}, & \times. \end{cases} \quad (3.21)$$

Here the angular derivatives have been reformulated in terms of (comoving) Cartesian coordinates to facilitate the use of the Fourier representation of the gravitational potential in the following. In particular, the power spectra of the various lensing observables should be related to that of the Newtonian potential. While the convergence is a true scalar the two shear fields are not. They are the components of a symmetric trace-free rank-2 tensor defined on the unit sphere instead. This will be discussed in Chapter 5. Therefore, it is more convenient to express these two degrees of freedom by scalar quantities, the so-called *E*- and *B*-mode (Stebbins, 1996; Kamionkowski et al., 1997). The latter is actually a pseudo scalar, i.e. it changes sign under parity transformations. They are obtained from the shear components via differentiation

$$D_{\circ} \begin{pmatrix} E \\ B \end{pmatrix} = \begin{pmatrix} D_+ & D_{\times} \\ D_{\times} & -D_+ \end{pmatrix} \begin{pmatrix} \gamma_+ \\ \gamma_{\times} \end{pmatrix}. \quad (3.22)$$

A detailed discussion of the complex shear $\gamma = \gamma_+ + i\gamma_{\times}$ and the corresponding *E/B*-mode decomposition is also provided in Chapter 5.

In order to compute the (angular) power spectra of the four lensing quantities, κ , $|\gamma|$ and *E/B*-mode, the Fourier space version of Limber projection is invoked (Limber, 1953). Starting with the line-of-sight projection q of a three-dimensional fluctuation field Q weighted by an appropriate function w

$$q(\boldsymbol{\theta}) = \int_0^{\infty} d\chi w(\chi) Q(f_K(\chi)\boldsymbol{\theta}, \chi) \quad (3.23)$$

the (angular) power spectrum of q is given by

$$C_\ell^{qq} = \int_0^\infty \frac{d\chi}{\chi^2} w^2(\chi) P_{QQ}(\ell/\chi). \quad (3.24)$$

It turns out that in case of lensing $P_{\kappa\kappa} = P_{EE} = P_{|\gamma||\gamma|}$, whereas the B -mode vanishes identically. This can be seen most easily by reformulating equation (3.22) in Fourier space, where

$$D_{\circ,+,\times} = \begin{cases} -\frac{1}{2}(k_1^2 + k_2^2), & \circ \\ -\frac{1}{2}(k_1^2 - k_2^2), & + \\ -k_1 k_2, & \times \end{cases} \quad (3.25)$$

thus

$$D_\circ \begin{pmatrix} E \\ B \end{pmatrix} = \begin{pmatrix} D_+ & D_\times \\ D_\times & -D_+ \end{pmatrix} \begin{pmatrix} \gamma_+ \\ \gamma_\times \end{pmatrix} = \frac{2}{c^2} \int_0^\infty d\chi G(\chi) \begin{pmatrix} D_+ & D_\times \\ D_\times & -D_+ \end{pmatrix} \begin{pmatrix} D_+ \\ D_\times \end{pmatrix} \Phi = D_\circ \begin{pmatrix} \kappa \\ 0 \end{pmatrix}. \quad (3.26)$$

For the last equality I used the fact that $D_+^2 + D_\times^2 = D_\circ^2$, which at the same time shows that indeed $P_{\kappa\kappa} = P_{|\gamma||\gamma|}$. For completeness it should be mentioned that there are small corrections to the relation between the shear and the convergence due to the peculiar motion of galaxies (Bonvin, 2008), but these corrections are unimportant in the context of this work. Finally, the angular power spectrum of the convergence is found by noting that the two-dimensional Laplacian $2D_\circ$ can be safely replaced by the three-dimensional one because derivatives of the potential along the light path average to zero (White & Hu, 2000). The three-dimensional Laplacian of the potential may then be substituted by the density contrast according to the Poisson equation (2.33c), i.e. $P_{\kappa\kappa} \sim k^4 P_{\Phi\Phi} \sim P_{\delta\delta}$. This allows to bring the convergence angular power spectrum into its final form

$$C_\ell^{\kappa\kappa} = \int_0^\infty \frac{d\chi}{\chi^2} W_\kappa^2(\chi) P_{\delta\delta}(\ell/\chi, \chi), \quad (3.27)$$

with the *lensing efficiency function*

$$W_\kappa(\chi) = \frac{3H_0^2 \Omega_m}{2c^2} \frac{G(\chi)}{a}. \quad (3.28)$$

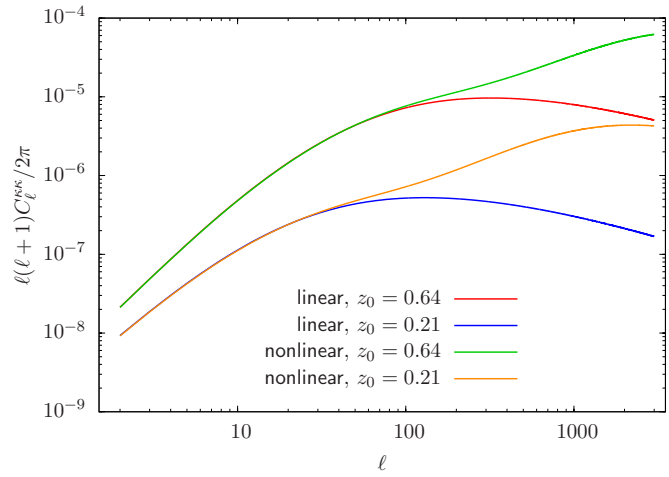
The distribution of lensed background galaxies entering the lensing efficiency function via the weight function G defined in equation (3.20) is usually parametrized in redshift space. A commonly adapted parametrization is given by

$$p(z)dz = p_0 \left(\frac{z}{z_0}\right)^2 \exp\left[-\left(\frac{z}{z_0}\right)^\beta\right] dz \quad \text{with} \quad \frac{1}{p_0} = \frac{z_0}{\beta} \Gamma\left(\frac{3}{\beta}\right). \quad (3.29)$$

The conversion to the distribution in terms of the comoving radial distribution is established via $p(z)dz = n(\chi)d\chi$, i.e. $n(\chi) = p(z)\frac{dz}{d\chi} = \frac{p(z)}{H(z)}$.

In Figure 3.3 the convergence power spectrum for a shallow ($\beta = 3/2$, $z_0 = 0.21$) and a deep ($\beta = 3/2$, $z_0 = 0.64$) redshift survey, respectively, is plotted. The underlying cosmology is that of Table 2.1. In addition, the power enhancement on small scales resulting from the usage of the nonlinear matter power spectrum in equation (3.27) is shown.

Figure 3.3: Convergence angular power spectrum for a shallow and a deep redshift survey, respectively. The contributions from nonlinear structure growth are also shown.



4

Chapter 4

Galactic angular momenta and angular momentum couplings in the large-scale structure

This chapter reconsiders the one- and two-point distribution functions of angular momenta in the large-scale structure. The angular momentum acquisition is described in the framework of linear tidal torque theory. This allows to model the galactic angular momentum vector by a set of 12 Gaussian random variates, the covariance of which is expressed in terms of the spectral moments of the linearly evolved matter power spectrum. The two-point correlation function is then obtained from the 24-dimensional joint probability distribution function. The one- and two-point distribution functions are subjected to appropriate peak constraints, accounting for the fact that haloes form at maxima in the cosmic density field. The numerical evaluation of the resulting discrete random process is accomplished by a suitable sampling scheme especially adapted to the very high dimensionality of this problem. With this the anticipated scaling of the specific angular momentum with halo mass, namely $\mathcal{L} \propto M^{2/3}$, is confirmed. Furthermore, I find that the correlation length between the angular momenta of two Milky Way-sized haloes is approximately $r_0 \sim 1 \text{ Mpc } h^{-1}$, whereas their correlation function is well described by the empirically fitting formula $C_{\mathcal{L}}(r) \propto \exp[-(r/r_0)^{3/2}]$.

The contents of this chapter have been published in Schäfer & Merkel (2012).

4.1. Introduction

More than 50 years ago Hoyle (1949) and Sciama (1955) proposed that galactic angular momenta emerge from tidal interactions between the host halo and the ambient cosmic matter field. This has stimulated the development of tidal torque theory (Doroshkevich, 1970; Heavens & Peacock, 1988; Catelan & Theuns, 1996a,b; Lee & Pen, 2000; Lee, 2006; Lee & Park, 2006, see Schäfer, 2009 for a recent review), the basic mechanism of which has nowadays been confirmed by a number of N -body simulations (White, 1984; Sugerman et al., 2000; Catelan et al., 2001; Porciani et al., 2002b,a; Hahn et al., 2007, 2010). As a result of the shearing process the spin vectors are orientated along the tidal field, which has important observational consequences. Specifically, the alignment of galactic angular momenta introduces alignments in the intrinsic ellipticities of adjacent galaxies (Catelan & Porciani, 2001; Jing, 2002). These intrinsic ellipticity alignments are one of the most important systematics in weak lensing measurements which will be discussed in Chapters 5 and 6. Moreover, aligned angular momenta even affect galaxy surveys as they provoke correlated inclination angles of galactic discs which give rise to selection effects (Krause & Hirata, 2011).

This chapter aims at a statistical description of galactic angular momenta derived in the framework

of tidal torque theory. I am particularly interested in their two-point correlation function. The following analysis contents itself with linear theory, where the statistics of the cosmic density (contrast) is Gaussian. This is one of the key assumptions which makes a completely analytical treatment feasible. Relating the statistics of the angular momentum field to the initial conditions of the large-scale structure renders my approach insensitive to the protohalo's peculiar motion. It typically shifts the object by about one correlation length of the density field, distorting the angular momentum distribution as well as its correlation properties. [Porciani et al. \(2002a\)](#) and [Lee & Pen \(2008\)](#) show that nonlinear clustering is able to enhance the correlation length in the angular momentum field considerably in comparison to the linear evolution of stationary haloes. In addition, [Catelan & Theuns \(1996b, 1997\)](#) find that higher-order corrections to Lagrangian perturbation theory increase the angular momentum variance by approximately 30 per cent. All these nonlinear effects do not enter my approach.

Furthermore, there are a number of effects concerning the formation history of a halo which are not accessible to an analytical treatment but need to be addressed by numerical simulations. These are, for instance, dissipative processes and tidal interactions between neighbouring haloes ([Sugerman et al., 2000](#); [Song & Lee, 2012](#)) on the one hand and halo mergers and matter accretion on the other hand ([Peirani et al., 2004](#)). I neglect these effects in favour of a purely analytical description.

There are two more simplifications which have to be made concerning the protohalo's shape and the tidal field acting on it. Although it is known that the collapse dynamics is determined by the protohalo's gravity in combination with the tidal forces of the ambient matter ([Desjacques, 2008](#)), I follow standard tidal torque theory where the triaxial shape of the protohalo is kept fixed as tidal shearing is neglected in its eigenframe ([Bond & Myers, 1996a,b,c](#)). According to [Ludlow & Porciani \(2011a\)](#), however, the halo triaxiality is largely attributed to the deformation by tidal forces and it may be inadequate to describe the boundary of the object by an isocontour in the initial density field. Another aspect which points at a certain inflexibility inherent to the model for angular momentum acquisition used in this work is that it keeps the shear field constant within the entire protohalo. It is approximated by its value at the protohalo's centre, i.e. at the location of the corresponding peak in the density field. This simplification mainly affects the magnitude of the angular momentum (being underestimated), but not its orientation.

Despite these limiting assumptions I am convinced that my approach helps to improve previous studies. In particular, I aim at an improvement of the following aspects.

- (i) The angular momentum distribution functions employed in this work explicitly account for the fact that galaxies form at peaks in the cosmic density field. They are consistently derived from a discrete (Gaussian) random process, abandoning a continuous formulation. This ensures the correct statistical weighting of specific peak shapes. There are some objections concerning the one-to-one correspondence between the maxima of a suitably smoothed density field and the actual halo forming regions. [Porciani et al. \(2002b\)](#) point out that only about 40 per cent of the protohaloes in numerical simulations emerge from primordial peaks. This is contrasted by the findings of [Ludlow & Porciani \(2011b\)](#) who report that nearly 70 per cent of all haloes in their simulations arise in the vicinity of density peaks. Nonetheless, there remains a considerable fraction of haloes which do not belong to a peak region and the statistical properties of which may differ substantially. By construction, my ansatz for the angular momentum correlation function cannot accommodate for this fraction.
- (ii) I treat the protohalo's inertia on an equal footing with the tidal shear field, which makes a discrimination with respect to differences in the correlation lengths of these two quantities unnecessary. Thus, my ansatz for the two-point correlation function is not confined to regions beyond the short-ranged correlations in the peak shapes but is valid for all, even smallest, separations.
- (iii) In order to be able to distinguish between the parallel and antiparallel orientation of the spin axes, the correlation function must be more flexible than being purely quadratic in the angu-

lar momenta. I accomplish this via a suitable antisymmetrization of the correlation function yielding negative values in case of antiparallel orientated, i.e. anti-correlated, spins.

- (iv) Another important improvement is that this antisymmetrization avoids any phenomenological parametrization of the average misalignment between the eigenframe of the inertia tensor and that of the tidal field (Lee & Pen, 2000; Crittenden et al., 2001). Configurations in which both eigenframes coincide give no rise to angular momentum acquisition in the framework of tidal torque theory. The antisymmetric form of the two-point correlation function automatically rejects such (unphysical) configurations right from the start and associates the appropriate statistical weight to each physical configuration individually.

This chapter has the following structure: Section 4.2 lays down the formalism. After a short review of tidal torque theory the peak-restricted Gaussian model used for describing the one- and two-point statistics of galactic angular momenta is introduced. In addition, the influence of dark energy on their time evolution is addressed. Section 4.3 is then devoted to the numerical evaluation of the expressions for the angular momentum variance and the two-point correlation function. The integration scheme employed is explained in detail and several tests of its accuracy and reliability are presented. The main results of this chapter are finally summarized in Section 4.4.

Throughout this chapter I choose a spatially flat Λ CDM cosmology as reference model. The relevant parameters describing its matter content are $\Omega_m = 0.25$, including the baryon fraction $\Omega_b = 0.04$, and $\Omega_\Lambda = 0.75$. The adiabatic initial perturbations in the cold dark matter distribution are assumed to be Gaussian and are characterized by $n_s = 1$ and $\sigma_8 = 0.9$. For today's value of the Hubble rate I set $H_0 = 100 h \text{ km s}^{-1} \text{ Mpc}^{-1}$ with $h = 0.72$. The influence of dark energy on the spin-up of haloes will be discussed in Section 4.2 in comparison to the time evolution in an Einstein-de Sitter universe (SCDM), where $\Omega_m = 1$ and the dark energy density vanishes.

4.2. Formalism

In this section the two-point correlation function of angular momenta in the cosmic large-scale structure is derived. This involves several rather technical steps which are now briefly outlined in order to make the line of argument more readily accessible to the reader. Section 4.2.1 starts with the description of angular momentum acquisition in the framework of tidal torque theory. Having derived an expression for the angular momentum vector in terms of the inertia tensor and the tidal field, its (Gaussian) statistics is addressed next (Section 4.2.2). In the subsequent section the covariance matrices entering the one- and two-point distribution functions are computed in an appropriately chosen coordinate frame. The entries of these covariance matrices are then illustrated in Section 4.2.4. In a last step the constraints accounting for the confinement of angular momentum build-up to peak regions are specified and imposed (Section 4.2.5). I conclude with some comments on the functional form of the angular momentum correlation function in Section 4.2.6.

4.2.1. Acquisition of angular momentum by tidal shearing

In the framework of tidal torque theory the angular momentum of galaxies results from tidal interactions between the protogalactic region and the ambient matter distribution prior to collapse (Doroshkevich, 1970; White, 1984). Generally, the mechanical angular momentum of an object with continuous mass distribution $\rho(\mathbf{r}, t)$ is given by

$$\mathbf{L}(t) = \int_V d^3r (\mathbf{r} - \bar{\mathbf{r}}) \times \mathbf{v}(\mathbf{r}, t) \rho(\mathbf{r}, t), \quad (4.1)$$

where $\mathbf{v}(\mathbf{r}, t)$ denotes the (rotational) velocity of the corresponding mass element. The integration ranges over the physical extent V of the rotating object. In this description the body's centre of

gravity $\bar{\mathbf{r}}$ serves as reference point. The shape of the rotating object is crucial for the actual angular momentum acquisition rate. Assuming a matter dominated universe, spherical objects acquire their angular momentum from convective matter streams onto the boundary surface (Peebles, 1969). This is only a second order effect, whereas the angular momentum of less regularly shaped objects, e.g. ellipsoids, grows at first order and linearly with time.

So far, there are two dynamical fields involved the density ρ and the (rotational) velocity \mathbf{v} . For further progress I approximate the density inside the protogalactic region by the (spatially constant) average density $\bar{\rho} \equiv \Omega_m \rho_{\text{crit}}$ and invoke a description in Lagrangian perturbation theory in accordance with White (1984), Catelan & Theuns (1996a) and Crittenden et al. (2001). The (leading order) expression of the angular momentum vector then reads

$$\mathbf{L} = \bar{\rho} a^5 \int_{V_L} d^3 q (\mathbf{x} - \bar{\mathbf{x}}) \times \dot{\mathbf{x}} \simeq \bar{\rho} a^5 \int_{V_L} d^3 q (\mathbf{q} - \bar{\mathbf{q}}) \times \dot{\mathbf{x}}. \quad (4.2)$$

The rotating object is confined to the comoving, i.e. Lagrangian, volume V_L . The comoving particle velocity $\dot{\mathbf{x}}$ may be derived from the Zel'dovich relation (2.41) via differentiation with respect to the time variable

$$\mathbf{x}(\mathbf{q}, t) = \mathbf{q} - D_+(t) \nabla \Psi_0(\mathbf{q}) \quad \longrightarrow \quad \dot{\mathbf{x}} \equiv \frac{\partial \mathbf{x}}{\partial t} = -\frac{\partial D_+}{\partial t} \nabla \Psi_0. \quad (4.3)$$

Since the time evolution of the Zel'dovich potential is independent of its spatial dependence I set $\Psi \equiv \Psi_0$ for the remainder of this chapter.

In order to separate the translation of the protogalactic object as a whole from the differential advection velocities responsible for rotation I perform a second order Taylor expansion of the velocity term, i.e. I set

$$\partial_i \Psi(\mathbf{q}) \simeq \partial_i \Psi|_{\bar{\mathbf{q}}} + \sum_j (\mathbf{q} - \bar{\mathbf{q}})_j \Psi_{ij}, \quad (4.4)$$

where I abbreviate $\partial_i \equiv \frac{\partial}{\partial x^i}$ from now on. In the following the constant shift in position $\partial_i \Psi|_{\bar{\mathbf{q}}}$ will be neglected. Terms higher than second order are not expected to significantly contribute because the gradient of the Zel'dovich potential is only slowly varying across the region of interest. The expansion coefficients $\Psi_{ij} \equiv \partial_i \partial_j \Psi$ may be identified with the tidal shear field (evaluated at the centre of gravity $\bar{\mathbf{q}}$) due to the fact that the Zel'dovich potential follows from the density contrast in the very same way as the gravitational potential; in both cases the relation is established by a Poisson-like equation (cf. equation 2.33c and Section 2.4.2).

As an important intermediate result the angular momentum vector can now be reformulated in terms of the shear field Ψ_{ij} and the protogalactic object's inertia I_{ij}

$$L_i = a^2 \dot{D}_+ \epsilon_{ijk} I_{jl} \Psi_{lk} = a^3 H(a) \frac{dD_+}{da} \epsilon_{ijk} I_{jl} \Psi_{lk}. \quad (4.5)$$

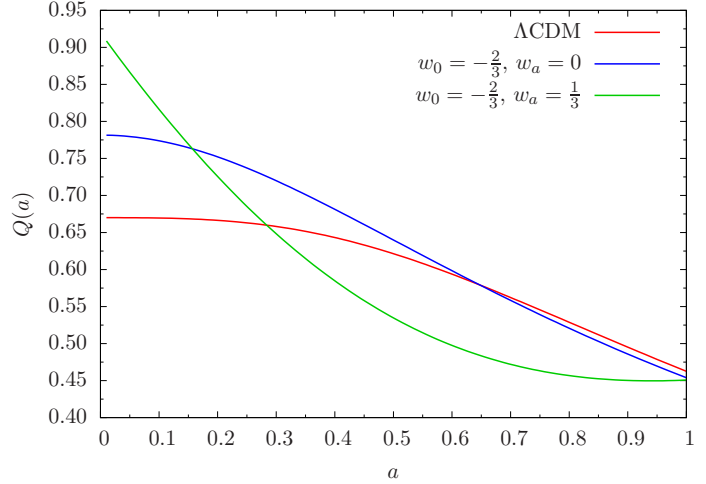
To get the second equality the entire time dependence was expressed in terms of the scale factor. The inertia tensor is computed from the second moments of the mass distribution

$$I_{ij} = \bar{\rho} a^3 \int_{V_L} d^3 q (\mathbf{q} - \bar{\mathbf{q}})_i (\mathbf{q} - \bar{\mathbf{q}})_j. \quad (4.6)$$

The time evolution of the angular momentum is captured by $q(a) = a^3 H(a) dD_+/da$. In an Einstein-de Sitter universe the Hubble function is given by $H(a) = H_0 a^{-3/2}$ (cf. equation 2.14), while the growth function coincides with the scale factor, i.e. $D_+(a) = a$ (see Section 2.4.1). Putting things together one obtains $q_{\text{SCDM}}(a) = H_0 a^{3/2}$. This can be compared to the time evolution in dark energy cosmologies. The function $q_{\text{DE}}(a)$ can be computed by numerically solving the growth equation (2.36) for the derivative of the growth function. For the dark energy equation of state the parametrization (2.15) is used.

Figure 4.1 shows the ratio $Q(a) \equiv q_{\text{DE}}(a)/q_{\text{SCDM}}(a)$. One immediately recognizes that the spin-up of haloes is considerably slower in the presence of dark energy. Furthermore, it turns out that the time evolution is quite sensitive to its particular realization. The influence of a cosmological constant and of classical quintessence, $w_0 = -\frac{2}{3}$, is rather similar, while the behaviour for a time varying equation of state is qualitatively different.

Figure 4.1: The influence of the dark energy model on the time evolution of galactic angular momenta.



4.2.2. Gaussian model of the angular momentum correlations

Having expressed the galactic angular momentum vector in terms of the tidal shear field and the tensor of inertia the next aim is its statistical description. It proves most convenient that both constituents can directly be related to the cosmic density field. The statistics of the latter is well understood in linear theory where it follows a Gaussian distribution. For this reason I restrict my analysis entirely to the linear regime although several extensions to tidal torque theory exist. They comprise contributions from second order perturbation theory (Catelan & Theuns, 1996b), as well as effects of non-Gaussian initial conditions (Catelan & Theuns, 1997).

The relation between the tidal shear tensor and the density contrast is straightforward due to the aforementioned Poissonian relation. In case of the tensor of inertia one has to make some further assumptions regarding the shape of the protogalactic region. In favour of an analytical treatment the highly idealized form of an ellipsoid is chosen. The expression for the corresponding density profile becomes particularly simple in the eigenframe of the so-called mass tensor. It is constituted by the *negative* second derivatives of the density contrast, i.e. $\delta_{ij} \equiv -\partial_i \partial_j \delta$. Since the protogalactic object Γ under consideration forms at a peak in the density field, the first derivatives of the latter vanish and it may be well approximated by

$$\delta(\mathbf{x}) = \delta(\mathbf{x}_p) - \frac{1}{2} \sum_{i=1}^3 \tilde{\delta}_i (\mathbf{x} - \mathbf{x}_p)_i^2, \quad (4.7)$$

where the $\tilde{\delta}_i$ denote the eigenvalues of the mass tensor evaluated at the peak location \mathbf{x}_p (Catelan & Theuns, 1996a). The boundary $\partial\Gamma$ of the peak region is defined by the condition that the surrounding matter distribution drops to zero, hence $\delta|_{\partial\Gamma} = 0$. This yields an ellipsoid equation

$$\partial\Gamma : \sum_{i=1}^3 \tilde{\delta}_i (\mathbf{x} - \mathbf{x}_p)_i^2 = 2\delta(\mathbf{x}_p), \quad (4.8)$$

from which one readily infers its semi-axes

$$A_i = \sqrt{2\nu\sigma_0 \tilde{\delta}_i^{-1}}. \quad (4.9)$$

Here, the peak height has been expressed in units of the variance of the density field σ_0 (see equation 4.19), i.e. $\delta(x_p) = \nu\sigma_0$. In terms of the semi-axes the volume of the protohalo is given by

$$V_\Gamma = \frac{4\pi}{3}A_1A_2A_3, \quad (4.10)$$

which allows to estimate its mass to be $M_\Gamma = \rho_m V_\Gamma$. Finally, the integration of equation (4.6) can be carried out in order to obtain the inertia tensor. It is obviously diagonal in the mass tensor eigenframe and reads

$$I_{ij} = \frac{M_\Gamma}{5} \text{diag} (A_2^2 + A_3^2, A_1^2 + A_3^2, A_1^2 + A_2^2). \quad (4.11)$$

This constitutes the desired relation between the protogalactic object's tensor of inertia and the cosmic density field and derivatives thereof, respectively. Before I go on I would like to emphasize the involved structure of this relation: the tensor of inertia is linked to the second derivatives of the density contrast via the (inverse) eigenvalues of the mass tensor. This contrasts with the simple Poissonian relation for the shear field.

Now the statistical description of galactic angular momenta can be further developed. In total, there are 15 random variates that need to be considered: the first and second derivatives of the density field as well as the shear tensor. Since second derivatives are interchangeable both the mass and the shear tensor contribute six instead of nine degrees of freedom. All 15 variates are linked to the density contrast which becomes most evident in Fourier space

$$\delta(\mathbf{x}) = \int \frac{d^3k}{(2\pi)^3} \delta(\mathbf{k}) e^{i\mathbf{k}\cdot\mathbf{x}}, \quad (4.12)$$

$$\delta_i(\mathbf{x}) \equiv \partial_i \delta(\mathbf{x}) = i \int \frac{d^3k}{(2\pi)^3} k_i \delta(\mathbf{k}) e^{i\mathbf{k}\cdot\mathbf{x}}, \quad (4.13)$$

$$\delta_{ij}(\mathbf{x}) \equiv -\partial_i \partial_j \delta(\mathbf{x}) = \int \frac{d^3k}{(2\pi)^3} k_i k_j \delta(\mathbf{k}) e^{i\mathbf{k}\cdot\mathbf{x}}, \quad (4.14)$$

$$\Psi_{ij}(\mathbf{x}) \equiv \partial_i \partial_j \Psi(\mathbf{x}) = \int \frac{d^3k}{(2\pi)^3} \frac{k_i k_j}{k^2} \delta(\mathbf{k}) e^{i\mathbf{k}\cdot\mathbf{x}}. \quad (4.15)$$

It is important to note that despite the fact that all dynamical quantities are related to the cosmic density field the density field itself does not enter because it is fully degenerate with the trace of the shear field, i.e. $\text{tr}(\Psi_{ij}) = \Delta\Psi = \delta$. This is an immediate consequence of applying the Zel'dovich approximation (cf. Section 2.4.2) and is nicely demonstrated by equations (4.12) and (4.15). The density contrast is thus treated as a derived quantity in my analysis. In contrast to the entries of the tidal shear matrix it represents no degree of freedom. They all need to be considered because the tidal shear matrix enters the expression for the angular momentum (4.5) as a whole. Once the components of the shear field are given, the density contrast follows from its trace unambiguously. Comparing equation (4.14) to equation (4.15) one immediately realizes that correlations in the peak shapes, and therefore in the inertia, are short-ranged with respect to those in the tidal field.

Since I am working in linear theory the statistics of the density contrast and its derivatives is Gaussian. Accordingly, the angular momentum distribution follows a 15-dimensional multivariate Gaussian probability density function (Bardeen et al., 1986)

$$p(\mathbf{v})d\mathbf{v} = \frac{1}{(2\pi)^{15/2} \sqrt{\det \mathbf{V}}} \exp\left(-\frac{1}{2} \mathbf{v}^\top \mathbf{V}^{-1} \mathbf{v}\right) d\mathbf{v}, \quad (4.16)$$

where the vector \mathbf{v} comprises the 15 individual random variates collected in equations (4.13)-(4.15). Their covariance matrix $V_{ij} = \langle v_i v_j^* \rangle$, ($i, j = 1, \dots, 15$) will be expressed in terms of the linear matter power spectrum in the subsequent section. Aiming at the two-point correlation function of galactic angular momenta the probability density function (4.16) is extended by the corresponding set of

variables \mathbf{v}' , which describe a second peak in the large-scale structure. The joint set of random variables containing both peaks under consideration is denoted by $\mathbf{w} = (\mathbf{v}, \mathbf{v}')$ and the 30-dimensional probability density function takes on the familiar form

$$p(\mathbf{w})d\mathbf{w} = \frac{1}{(2\pi)^{15} \sqrt{\det \mathbf{W}}} \exp\left(-\frac{1}{2}\mathbf{w}^\top \mathbf{W}^{-1} \mathbf{w}\right) d\mathbf{w}. \quad (4.17)$$

As before, the covariance matrix is given in terms of the outer product $W_{ij} = \langle w_i w_j^* \rangle$, ($i, j = 1, \dots, 30$).

4.2.3. Computation of the covariance matrices

In this section I compute the covariance matrices entering the angular momentum probability density functions (4.16) and (4.17), respectively. Regos & Szalay (1995) and Heavens & Sheth (1999) pointed out that the computation is most readily carried out in spherical coordinates assuming that the two peaks under consideration are located symmetrically along the z -axis. Hence, their positions, separated by a distance r , read $\mathbf{x} = (0, 0, r/2)$ and $\mathbf{x}' = (0, 0, -r/2)$, respectively. In order to take full advantage of this special choice of coordinate system one additionally introduces the following set of dimensionless complex variables

$$y_{\ell m}^n(\mathbf{x}) = \sqrt{4\pi} \frac{i^{\ell+2n}}{\sigma_{\ell+2n}} \int \frac{d^3 k}{(2\pi)^3} k^{\ell+2n} \delta(\mathbf{k}) Y_{\ell m}(\hat{\mathbf{n}}_k) e^{i\mathbf{k}\cdot\mathbf{x}}. \quad (4.18)$$

Appropriate combinations of these variables then reveal the desired correlations between the various derivatives of the density field as demonstrated below. The weighted moments of the linear matter power spectrum $P_{\delta\delta}(k)$ entering equation (4.18) are defined by

$$\sigma_j^2 = \frac{1}{2\pi^2} \int dk k^{2j+2} P_{\delta\delta}(k). \quad (4.19)$$

An adequate smoothing of equation (4.19) on large wavenumbers allows to select objects of a certain mass scale. The diameter R of the isotropic filter function $S_R(k)$ corresponds to the size of the objects at the onset of collapse which in turn is related to their mass via $M = 4\pi/3\rho_m R^3$. In this work a Gaussian filter function is applied, thus

$$P_{\delta\delta}(k) \longrightarrow P_{\delta\delta}(k) S_R^2(k) \quad \text{with} \quad S_R(k) = \exp(-k^2 R^2/2). \quad (4.20)$$

In the following the correspondence between the physical quantities and the $y_{\ell m}^n$ -moments is gathered, starting with the scalar density field $\delta(\mathbf{x})$:

$$\sigma_0 y_{00}^0(\mathbf{x}) = \delta(\mathbf{x}). \quad (4.21)$$

For the density gradient $\delta_i(\mathbf{x})$ one has

$$\sigma_1 y_{10}^0(\mathbf{x}) = \sqrt{3} \delta_3(\mathbf{x}), \quad (4.22a)$$

$$\sigma_1 y_{11}^0(\mathbf{x}) = -\sqrt{\frac{3}{2}} [\delta_1(\mathbf{x}) + i\delta_2(\mathbf{x})], \quad (4.22b)$$

while for the mass tensor $\delta_{ij}(\mathbf{x})$ one finds

$$\sigma_2 y_{20}^0(\mathbf{x}) = -\sqrt{\frac{5}{4}} [\delta_{11}(\mathbf{x}) + \delta_{22}(\mathbf{x}) - 2\delta_{33}(\mathbf{x})], \quad (4.23a)$$

$$\sigma_2 y_{21}^0(\mathbf{x}) = -\sqrt{\frac{15}{2}} [\delta_{13}(\mathbf{x}) + i\delta_{23}(\mathbf{x})], \quad (4.23b)$$

$$\sigma_2 y_{22}^0(\mathbf{x}) = \sqrt{\frac{15}{8}} [\delta_{11}(\mathbf{x}) - \delta_{22}(\mathbf{x}) + 2i\delta_{12}(\mathbf{x})], \quad (4.23c)$$

$$\sigma_2 y_{00}^1(\mathbf{x}) = \delta_{11}(\mathbf{x}) + \delta_{22}(\mathbf{x}) + \delta_{33}(\mathbf{x}). \quad (4.23d)$$

In case of the components of the tidal shear tensor one proceeds in complete analogy. It turns out that they merely differ by a factor of σ_2/σ_0 and that the n -index of the corresponding $y_{\ell m}^n$ -coefficients is lowered by one, underlining the enhanced correlation length of the tidal field with respect to the mass tensor. The explicit form of the coefficients reads

$$\sigma_0 y_{20}^{-1}(\mathbf{x}) = -\sqrt{\frac{5}{4}} [\Psi_{11}(\mathbf{x}) + \Psi_{22}(\mathbf{x}) - 2\Psi_{33}(\mathbf{x})], \quad (4.24a)$$

$$\sigma_0 y_{21}^{-1}(\mathbf{x}) = -\sqrt{\frac{15}{2}} [\Psi_{13}(\mathbf{x}) + i\Psi_{23}(\mathbf{x})], \quad (4.24b)$$

$$\sigma_0 y_{22}^{-1}(\mathbf{x}) = \sqrt{\frac{15}{8}} [\Psi_{11}(\mathbf{x}) - \Psi_{22}(\mathbf{x}) + 2i\Psi_{12}(\mathbf{x})], \quad (4.24c)$$

$$\sigma_0 y_{00}^0(\mathbf{x}) = \Psi_{11}(\mathbf{x}) + \Psi_{22}(\mathbf{x}) + \Psi_{33}(\mathbf{x}). \quad (4.24d)$$

Equations (4.21) and (4.24d) once more demonstrate the complete degeneracy between the density contrast and the trace of the shear field. The entire set of $y_{\ell m}^n(\mathbf{x})$ -coefficients may be grouped to a vector $\mathbf{y}(\mathbf{x})$. The transition from the physical quantities compiled in the vector \mathbf{v} to the vector \mathbf{y} is accomplished by a linear unitary transformation \mathbf{R} . The explicit expression for this matrix can readily be inferred from the relations given above. Having the transformation \mathbf{R} at hand, including a second peak characterized by the vector $\mathbf{y}' \equiv \mathbf{y}(\mathbf{x}')$ is then straightforward. The corresponding transformation matrix \mathbf{S} , mediating between the two vectors (\mathbf{y}, \mathbf{y}') and \mathbf{w} , simply reads

$$\mathbf{S} = \begin{pmatrix} \mathbf{R} & \mathbf{0} \\ \mathbf{0} & \mathbf{R} \end{pmatrix}. \quad (4.25)$$

Having once computed the covariance matrix in the $y_{\ell m}^n$ -basis inversion of this matrix allows to transform the result back to the physical frame. The explicit computation of the covariance matrix will be addressed in the following section. Formally, it is defined as the expectation value

$$Y_{ij} \equiv \langle (y, y')_i (y, y')_j^* \rangle. \quad (4.26)$$

By construction it can be decomposed into two 15×15 submatrices: the auto-correlation matrix \mathbf{A} and the cross-correlation matrix $\mathbf{C} = \mathbf{C}(r)$. In terms of these two matrices the full covariance matrix takes the following form

$$\mathbf{Y} = \begin{pmatrix} \mathbf{A} & \mathbf{C} \\ \mathbf{C}^+ & \mathbf{A} \end{pmatrix}, \quad (4.27)$$

where \mathbf{C}^+ denotes the Hermitian conjugate of the cross-correlation. In the following it is sufficient to focus on the matrix \mathbf{C} because the auto-correlation matrix is then obtained from evaluating the cross-correlation at zero lag.

4.2.4. Shape of the covariance matrices

Employing the $y_{\ell m}^n$ -basis, the entries of the covariance matrix of two spinning objects separated by a distance \mathbf{r} are obtained from the expectation value

$$\mathbf{C}(r) = C_{\ell\ell'mm'}^{nn'}(r) = \langle y_{\ell m}^n(\mathbf{x}) y_{\ell' m'}^{n'*}(\mathbf{x} + \mathbf{r}) \rangle. \quad (4.28)$$

Since the underlying fluctuation field, i.e. the matter density contrast, is (statistically) homogeneous and isotropic, the covariance matrix is only a function of the modulus r of the separation vector. Inserting the explicit expressions from equation (4.18) and carrying out the average one k -integration trivializes and one gets

$$C_{\ell\ell'mm'}^{nn'}(r) = \frac{(-1)^{n-n'}}{\sigma_{\ell+2n}\sigma_{\ell'+2n'}} i^{\ell-\ell'} \int \frac{d^3k}{2\pi^2} P_{\delta\delta}(k) k^{\ell+\ell'+2(n+n')} Y_{\ell m}(\hat{\mathbf{n}}_k) Y_{\ell' m'}^*(\hat{\mathbf{n}}_k) e^{i\mathbf{k}\cdot\mathbf{r}}. \quad (4.29)$$

Further progress is then achieved by making use of the plane wave expansion (Arfken & Weber, 2005)

$$e^{i\mathbf{k}\cdot\mathbf{r}} = 4\pi \sum_{\ell=0}^{\infty} i^{\ell} j_{\ell}(kr) \sum_{m=-\ell}^{+\ell} Y_{\ell m}^*(\hat{\mathbf{n}}_r) Y_{\ell m}(\hat{\mathbf{n}}_k), \quad (4.30)$$

which takes a particularly simple shape because the peaks are located along the z -axis, namely

$$e^{i\mathbf{k}\cdot\mathbf{r}} \Big|_{\mathbf{r}\sim\hat{\mathbf{e}}_z} = 4\pi \sum_{\ell=0}^{\infty} i^{\ell} \sqrt{2\ell+1} j_{\ell}(kr) Y_{\ell 0}(\hat{\mathbf{n}}_k). \quad (4.31)$$

The remaining product of three spherical harmonics can then be expressed in terms of Wigner 3j-symbols (e.g. Messiah, 1962; Abramowitz et al., 1988) according to

$$\int d\Omega Y_{\ell_1 m_1}(\hat{\mathbf{n}}) Y_{\ell_2 m_2}(\hat{\mathbf{n}}) Y_{\ell_3 m_3}(\hat{\mathbf{n}}) = \sqrt{\frac{(2\ell_1+1)(2\ell_2+1)(2\ell_3+1)}{4\pi}} \begin{pmatrix} \ell_1 & \ell_2 & \ell_3 \\ 0 & 0 & 0 \end{pmatrix} \begin{pmatrix} \ell_1 & \ell_2 & \ell_3 \\ m_1 & m_2 & m_3 \end{pmatrix}. \quad (4.32)$$

After reordering and further simplifications, the final expression for the cross-correlation reads

$$C_{\ell\ell'mm'}^{nn'}(r) = \frac{(-1)^{m'+n-n'}}{\sigma_{\ell+2n}\sigma_{\ell'+2n'}} \sum_{L=|\ell-\ell'|}^{\ell+\ell'} (2L+1) \sqrt{(2\ell+1)(2\ell'+1)} i^{L+\ell-\ell'} K_{\frac{1}{2}(\ell+\ell'+n+n')}^L(r) \times \begin{pmatrix} \ell & \ell' & L \\ 0 & 0 & 0 \end{pmatrix} \begin{pmatrix} \ell & \ell' & L \\ m & -m' & 0 \end{pmatrix}, \quad (4.33)$$

where the k -integration has been absorbed into the generalized spectral moment

$$K_m^{\ell}(r) \equiv \frac{1}{2\pi^2} \int dk k^{2m+2} j_{\ell}(kr) P_{\delta\delta}(k). \quad (4.34)$$

The entries of the cross-correlation matrix $C_{\ell\ell'mm'}^{nn'}$ are real because the first Wigner 3j-symbol ensures that the sum $L + \ell - \ell'$ is even. The second Wigner 3j-symbol vanishes if $m \neq m'$, leaving the cross-correlation diagonal in m . It is interesting to note that the matrix \mathbf{C} adopts block diagonal shape provided that the $y_{\ell m}^n$ -coefficients are suitably grouped in the vector \mathbf{y} . Specifically, it is advantageous to combine coefficients with the same value of m and to sort them by increasing modulus of m . From the derivation given above it becomes clear that the effect of interchanging the peaks is captured by

$$\langle y_{\ell m}^n(\mathbf{x}) y_{\ell' m'}^{n'*}(\mathbf{x}') \rangle = (-1)^L \langle y_{\ell m}^{n*}(\mathbf{x}') y_{\ell' m'}^{n'}(\mathbf{x}) \rangle. \quad (4.35)$$

Setting the separation in equation (4.33) to zero immediately yields the auto-correlation matrix. For $r \rightarrow 0$ the generalized spectral moment (4.34) approaches $K_m^{\ell}(r) \rightarrow \sigma_m^2 \delta_{\ell 0}$, which makes the sum in equation (4.33) collapse. Furthermore, the Wigner 3j-symbols reduce to the orthonormality relation of spherical harmonics as can be easily seen from equation (4.32)

$$(-1)^{m'} \sqrt{(2\ell+1)(2\ell'+1)} \begin{pmatrix} \ell & \ell' & 0 \\ 0 & 0 & 0 \end{pmatrix} \begin{pmatrix} \ell & \ell' & 0 \\ m & -m' & 0 \end{pmatrix} = \int d\Omega Y_{\ell m}(\hat{\mathbf{n}}) Y_{\ell' m'}^*(\hat{\mathbf{n}}) = \delta_{\ell\ell'} \delta_{mm'}. \quad (4.36)$$

Thus, the auto-correlation matrix has the remarkably simple form

$$\mathbf{A} = A_{\ell\ell'mm'}^{nn'} = (-1)^{n-n'} \frac{\sigma_{\ell+n+n'}^2}{\sigma_{\ell+2n}\sigma_{\ell+2n'}} \delta_{\ell\ell'} \delta_{mm'}, \quad (4.37)$$

which is diagonal in both angular indices ℓ and m .

Figure 4.2 shows typical entries of the correlation matrix (4.33) as a function of the peak separation r . In order to represent galaxies a smoothing scale (cf. equation 4.20) of $R = 1 \text{ Mpc } h^{-1}$ is chosen

and the density threshold ν is set to unity. The associated mass scale is then $M \simeq 3.1 \times 10^{11} M_{\odot} h^{-1}$. There is one residual freedom concerning the frame of reference. For the purpose of illustration I use two different frames. In the first frame the auto-correlation matrix is given by the unit matrix (left panel), while in the second frame it adopts a diagonal shape instead (right panel). Comparing the matrix elements $C_{\ell\ell'mm'}^{mm'}(r)$ in the two different frames one recognizes the elongation of the isoprobability contours in the second frame. Additionally, the semi-axis ratios are approximately five and the overall behaviour becomes less oscillatory in this frame.

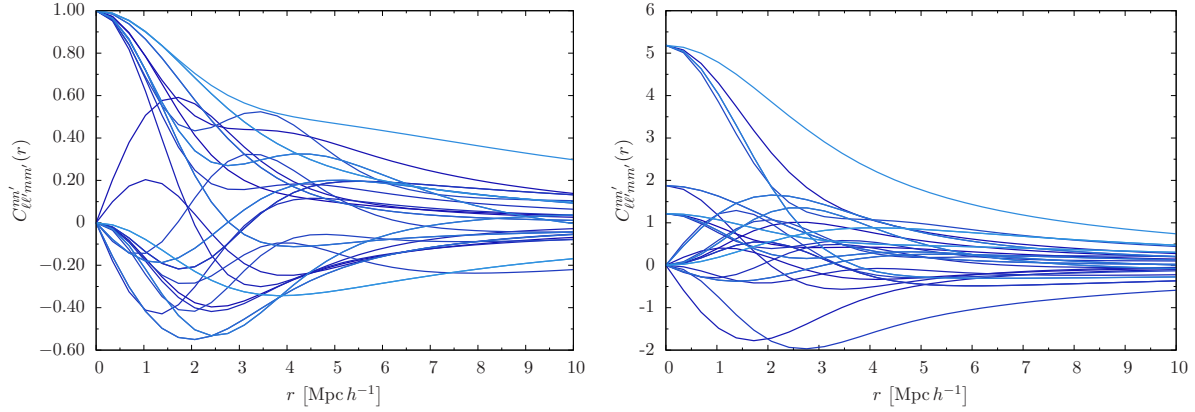


Figure 4.2.: Covariance matrix of the angular momentum distribution function transformed into a frame, where the auto-correlation matrix is equal to the unit matrix (left panel) and into a frame, where the auto-correlation matrix is diagonal (right panel).

4.2.5. Ansatz for the angular momentum correlations

The analysis presented so far emphasized that the acquisition of angular momentum takes place at peaks in the cosmic density field. But the fact that the distribution of density maxima is discrete has not yet been accounted for. This requires to impose several additional constraints on the Gaussian probability density functions introduced in equations (4.16) and (4.17) (Schäfer, 2009).

In order to make the discrete number of density maxima accessible to a continuous formulation one reverts to its number density constituted by a set of Dirac δ -functions (Bardeen et al., 1986; Regos & Szalay, 1995; Heavens & Sheth, 1999)

$$n_{\text{peak}} = \sum_p \delta_{\text{D}}(\mathbf{x} - \mathbf{x}_p). \quad (4.38)$$

In a second step one can get rid of the peak locations \mathbf{x}_p by reformulating the argument of the δ -function. In the vicinity of a maximum the gradient is safely approximated by its first order Taylor expansion, i.e.

$$\delta_i(\mathbf{x}) = \sum_j \delta_{ij}(\mathbf{x}_p)(\mathbf{x} - \mathbf{x}_p)_j. \quad (4.39)$$

Solving this equation for the spatial components and inserting the result in equation (4.38) one obtains

$$n_{\text{peak}} = \sum_p \delta_{\text{D}} \left[\delta_{ij}^{-1}(\mathbf{x}_p) \delta_i \right] = |\det \delta_{ij}| \delta_{\text{D}}(\delta_i). \quad (4.40)$$

As it is independent of the particular choice of the coordinate system, the determinant is most conveniently expressed in terms of the eigenvalues of the mass tensor, thus $\det \delta_{ij} = \tilde{\delta}_1 \tilde{\delta}_2 \tilde{\delta}_3$.

For the purpose of this work the number density of extrema needs to be further constrained to only contain maxima. This is assured by restricting the peak density to points \mathbf{x}_p where the density contrast exceeds a certain threshold, i.e. $\delta(\mathbf{x}_p) \geq \nu \sigma_0$, and where its curvature is negative definite as well. The

expectation value for the number density of peaks in the fluctuating density field is then described by the masked multivariate Gaussian random process

$$\bar{n}_{\text{peak}} = \int d\mathbf{v} C(\mathbf{v}) p(\mathbf{v}) \quad (4.41)$$

with

$$C(\mathbf{v}) = \delta_D [\delta_i(\mathbf{x})] (\tilde{\delta}_1 \tilde{\delta}_2 \tilde{\delta}_3) \prod_r \Theta_H(\tilde{\delta}_r) \Theta_H[\delta(\mathbf{x}) - \sigma_0 \nu]. \quad (4.42)$$

Note that the curvature of the peak is given by the negative mass tensor. Thus, the peak is negatively curved if all eigenvalues of the mass tensor are positive, which is manifest in the first Heaviside step function Θ_H on the right-hand side. The expression for the mean number density of peaks (4.41) corresponds to the integral of the differential peak density $n_{\text{peak}}(\nu)d\nu$ derived by [Bardeen et al. \(1986\)](#).

Now one can formulate the expectation value of the angular momentum vector of a protogalactic object corresponding to a peak region in the Universe's large-scale structure

$$\langle \mathbf{L} \rangle = \frac{1}{\bar{n}_{\text{peak}}(> \nu)} \int d\mathbf{v} C(\mathbf{v}) p(\mathbf{v}) \mathbf{L}(\mathbf{v}). \quad (4.43)$$

Obviously, its variance is given by

$$\langle \mathbf{L}^2 \rangle = \frac{1}{\bar{n}_{\text{peak}}(> \nu)} \int d\mathbf{v} C(\mathbf{v}) p(\mathbf{v}) \mathbf{L}^2(\mathbf{v}). \quad (4.44)$$

In each case the normalization $\bar{n}_{\text{peak}}^{-1}$ explicitly accounts for the discreteness of the underlying random process.

The angular momentum two-point correlation function also becomes readily accessible in this formalism. Extending the joint Gaussian probability density for both peaks (4.17) by the corresponding mask for each individual peak, one is left with

$$\langle L_i(\mathbf{x}) L_j(\mathbf{x}') \rangle = \frac{1}{\bar{n}_{\text{peak}}^2(> \nu)} \int d\mathbf{v} C(\mathbf{v}) \int d\mathbf{v}' C(\mathbf{v}') p(\mathbf{v}, \mathbf{v}') L_i(\mathbf{v}) L_j(\mathbf{v}'). \quad (4.45)$$

Since generally the thresholds imposed on the peaks are equal, the normalization is given by $\bar{n}_{\text{peak}}^{-2}$. The individual components of the angular momentum vector are given in terms of the inertia tensor I_{ij} and the tidal shear field Ψ_{ij} (cf. Section 4.2.1). They can be put together to form a matrix

$$X_{ij}(\mathbf{x}) \equiv \sum_k I_{ik}(\mathbf{x}) \Psi_{kj}(\mathbf{x}) \quad (4.46)$$

with which the angular momentum components are expressed in a more compact way

$$L_i = a^2 \dot{D}_+ \epsilon_{ijk} I_{jl} \Psi_{lk} = a^2 \dot{D}_+ \epsilon_{ijk} X_{jk}. \quad (4.47)$$

Accordingly, one finds

$$\langle L_i(\mathbf{x}) L_{i'}(\mathbf{x}') \rangle = a^4 \dot{D}_+^2 \epsilon_{ijk} \epsilon_{i'j'k'} \langle X_{jk}(\mathbf{x}) X_{j'k'}(\mathbf{x}') \rangle. \quad (4.48)$$

This expression for the one-dimensional covariance between different angular momentum components, however, is not independent of the coordinate system chosen. This disadvantage can be compensated for by taking the trace of equation (4.48), resulting in a coordinate-frame independent expression for the covariance of the full three-dimensional angular momentum vector

$$C_L(r) \equiv \text{tr} \langle L_i(\mathbf{x}) L_{i'}(\mathbf{x}') \rangle = \langle L_i(\mathbf{x}) L_i(\mathbf{x}') \rangle = 3a^4 \dot{D}_+^2 \left[\langle X_{jk}(\mathbf{x}') X_{jk}(\mathbf{x}) \rangle - \langle X_{ik}(\mathbf{x}) X_{ki}(\mathbf{x}') \rangle \right]. \quad (4.49)$$

For the last equality I exploited the identity $\epsilon_{ijk}\epsilon_{ij'k'} = \delta_{jj'}\delta_{kk'} - \delta_{jk'}\delta_{j'k}$. It is crucial that the indices are interchanged in the right most term. Otherwise, the correlation function would identically vanish, as it is the case for symmetric matrices. This becomes even more apparent in the matrix formulation of the correlation function

$$\begin{aligned} C_L(r) &= \text{tr} \langle \mathbf{L}(\mathbf{x})\mathbf{L}^\top(\mathbf{x}') \rangle = 3a^4 \dot{D}_+^2 \text{tr} \left[\langle \mathbf{X}(\mathbf{x})\mathbf{X}^\top(\mathbf{x}') \rangle - \langle \mathbf{X}(\mathbf{x}')\mathbf{X}(\mathbf{x}) \rangle \right] \\ &= 3 \frac{a^4 \dot{D}_+^2}{\bar{n}_{\text{peak}}^2(> \nu)} \int d\mathbf{v} C(\mathbf{v}) \int d\mathbf{v}' C(\mathbf{v}') p(\mathbf{v}, \mathbf{v}') \text{tr} \left[\mathbf{X}(\mathbf{v})\mathbf{X}^\top(\mathbf{v}') - \mathbf{X}(\mathbf{v}')\mathbf{X}(\mathbf{v}) \right]. \end{aligned} \quad (4.50)$$

The possible emergence of symmetric matrices and its interpretation will be discussed in the next section.

Finally, I would like to emphasize that the correlation function (4.50) treats the correlations in both the tidal shear field and the inertia tensor on the same footing. It intentionally avoids any decomposition of the two quantities according to their differences in correlation length. Schematically, one could think of the following ansatz

$$\langle \mathbf{I}(\mathbf{x})\mathbf{\Psi}(\mathbf{x}) \mathbf{I}(\mathbf{x}')\mathbf{\Psi}(\mathbf{x}') \rangle = P(\mathbf{I}|\mathbf{\Psi}) P(\mathbf{I}'|\mathbf{\Psi}') \langle \mathbf{\Psi}(\mathbf{x}) \mathbf{\Psi}(\mathbf{x}') \rangle, \quad (4.51)$$

where $P(\mathbf{I}|\mathbf{\Psi})$ indicates the probability distribution function of the inertia tensor \mathbf{I} given the tidal field $\mathbf{\Psi}$. This ansatz, however, is necessarily restricted to scales where the inertia tensors are uncorrelated.

4.2.6. Misalignment of the shear and inertia eigensystems

The matrix $\mathbf{X} = \mathbf{I}\mathbf{\Psi}$ may be decomposed into its symmetric (\mathbf{X}^+) and its antisymmetric part (\mathbf{X}^-) respectively, such that $\mathbf{X} = \mathbf{X}^+ + \mathbf{X}^-$. The former is obtained from the *anticommutator*

$$\mathbf{X}^+ \equiv \frac{1}{2} \{\mathbf{I}, \mathbf{\Psi}\}, \quad X_{ij}^+ = \frac{1}{2} \sum_k (I_{ik}\Psi_{kj} + \Psi_{ik}I_{kj}), \quad (4.52)$$

whereas the latter is given by the *commutator*

$$\mathbf{X}^- \equiv \frac{1}{2} [\mathbf{I}, \mathbf{\Psi}], \quad X_{ij}^- = \frac{1}{2} \sum_k (I_{ik}\Psi_{kj} - \Psi_{ik}I_{kj}). \quad (4.53)$$

Since the inertia tensor and the shear field are both symmetric it is easy to verify that $(\mathbf{X}^+)^\top = +\mathbf{X}^+$ and $(\mathbf{X}^-)^\top = -\mathbf{X}^-$. Inserting this decomposition in equation (4.47) one immediately finds

$$L_i = a^2 \dot{D}_+ \epsilon_{ijk} X_{jk} = a^2 \dot{D}_+ \epsilon_{ijk} (X_{jk}^+ + X_{jk}^-) = a^2 \dot{D}_+ \epsilon_{ijk} X_{jk}^-, \quad (4.54)$$

due to the fact that the contraction of an antisymmetric and a symmetric tensor vanishes.

Thus, the acquisition of angular momentum requires that the commutator \mathbf{X}^- between the inertia tensor and the tidal shear field does not vanish. In other words, they must not share a common eigensystem where both simultaneously adopt diagonal shape. The need for a net misalignment between the inertia tensor and the shear field motivated [Lee & Pen \(2000\)](#) and [Crittenden et al. \(2001\)](#) to introduce an effective parametrized description of the average misalignment. Its single free parameter then needs to be inferred from numerical simulations. In my approach, however, the misalignment is directly accounted for by the ansatz for the correlation function (4.50), providing a self-consistent description which intentionally avoids any additional parameter. A common eigensystem of the inertia tensor and the shear field is excluded by the fact that the correlation function is identically zero for any symmetric matrix \mathbf{X} . But the matrix \mathbf{X} necessarily assumes a symmetric shape in the particular coordinate frame in which both the shear field and the inertia tensor are diagonal. Since the trace is independent of the specific choice of coordinate basis, this argument holds true in general. Thus, field

configurations which do not give rise to angular momentum acquisition, because they are perfectly aligned, do not contribute to the correlation function at all.

In the extreme case of completely unaligned eigensystems of the shear and the inertia field, i.e. if $\mathbf{X} = \mathbf{X}^-$ and $\mathbf{X}^+ = 0$, the angular momentum correlation function becomes purely quadratic in \mathbf{X} and its amplitude is maximized due to the fact that $\mathbf{X}^\top = (\mathbf{X}^-)^\top = -\mathbf{X}^- = -\mathbf{X}$. Hence, one obtains

$$C_L^{\max}(r) = -6 \frac{a^4 \dot{D}_+^2}{\bar{n}_{\text{peak}}^2(> \nu)} \int d\mathbf{v} C(\mathbf{v}) \int d\mathbf{v}' C(\mathbf{v}') p(\mathbf{v}, \mathbf{v}') \text{tr}[\mathbf{X}(\mathbf{v})\mathbf{X}(\mathbf{v}')], \quad (4.55)$$

while the corresponding one-point variance is given by

$$\langle L_{\max}^2 \rangle = \frac{1}{\bar{n}_{\text{peak}}(> \nu)} \int d\mathbf{v} C(\mathbf{v}) p(\mathbf{v}) L_{\max}^2(\mathbf{v}). \quad (4.56)$$

The last two expressions underline the fact that any alignment of the eigensystems of the shear field and the inertia tensor effectively reduces the fluctuation amplitude in the galactic angular momentum field with respect to the case in which both fields are fully unaligned.

Finally, I would like to briefly comment on the physical interpretation of the anticommutator \mathbf{X}^+ . While the commutator \mathbf{X}^- is responsible for the protohalo's angular momentum acquisition, the anticommutator \mathbf{X}^+ leads to an anisotropic deformation of the protogalactic region in the course of linear structure formation prior to gravitational collapse. This could be interesting in the context of triaxiality predictions derived in the framework of Gaussian random fields (Bardeen et al., 1986) because the deformations due to \mathbf{X}^+ are likely to already alter the ellipticity distribution during the epoch of linearly evolving structures.

4.3. Numerical results

4.3.1. Outline of the integration scheme

The main difficulty encountered by the numerical evaluation of the angular momentum distribution (4.44) and correlation function (4.50) is the high dimensionality; 15 dimensions for the distribution function and twice as many in case of the two-point correlation function. This high dimensionality calls for the use of Monte Carlo integration methods. These methods can be refined and accelerated if one includes all prior knowledge about the underlying distribution function. In the present work the probability density function has the particularly simple form of a Gaussian. However, the sampling process is complicated by the peak restriction, i.e. by applying the mask (4.42), because it results in the rejection of a large fraction of the drawn samples. Thus, a reliable evaluation of the integrals requires to generate an extremely large set of random variates following the distribution functions (4.16) and (4.17), respectively.

Major simplification of this task can be achieved by noting that Gaussian random variables, obeying a given covariance structure, can be obtained from a set of unit Gaussian variates which are subsequently multiplied by the Cholesky decomposition of the covariance matrix. The Cholesky decomposition has to be carried out only once, whereas unit Gaussian variates can be very efficiently generated by a number of methods, for instance by the ziggurat algorithm (Marsaglia & Tsang, 2000). While the computation of the covariance matrices is most easily carried out in the $y_{\ell m}^n$ -basis introduced in Section 4.2.3 the peak constraints are more readily evaluated in the physical frame. Therefore, I start with the covariance matrices in the $y_{\ell m}^n$ -basis and transform them into the physical frame afterwards via the matrices \mathbf{R} and \mathbf{S} , respectively (cf. equation 4.25). The construction of the inertia ellipsoid, which approximates the protogalactic object, demands the diagonalization of the mass tensor. Regarding the computational efforts, it turns out that this procedure is rather time consuming, hence it is desirable to perform the least number of diagonalizations possible, i.e. exclusively for accepted samples. This can be achieved by finding an alternative criterion for the positive definiteness of the mass tensor which is

independent of its eigenvalues. Such a criterion can be formulated in terms of the basis-independent quantities $\text{tr}(\delta_{ij}^n)$, $n = 1, 2$ and $\det \delta_{ij}$. Its application reduces the computational efforts considerably.

Another simplification of the sampling process results from the fact that the peak constraint enforces the gradient of the density field to vanish. Thus, its components are no degree of freedom reducing the *effective* number of dimensions by three. It is important to note that the dimensionality of the underlying Gaussian distribution, however, remains the same. In other words, one has to retain the correct normalization of the 15- and 30-dimensional case, respectively. Finally, I would like to emphasize once more that the actual peak height does not enter the distribution function independently but is treated as a derived quantity exploiting its relation to the trace of the tidal shear field in the Zel'dovich approximation.

4.3.2. Test of the integration scheme

As a first test of the integration scheme explained before, the mean peak density (4.41) is computed and compared to the analytical solution provided by [Bardeen et al. \(1986\)](#). The agreement between the two is very good and can be arbitrarily refined by increasing the number of samples. Furthermore, it was assured that this method correctly reproduces the limiting extreme case of $\lim_{\nu \rightarrow -\infty} \bar{n}_{\text{peak}}(\nu)$. Finally, the peak correlation function presented by [Regos & Szalay \(1995\)](#) is addressed. I recover their results regarding the functional form, as well as the amplitude for different values of the density threshold ν and smoothing scale R of the matter power spectrum. The agreement is very good for both galaxies and clusters of galaxies up to distances of about $100 \text{ Mpc } h^{-1}$. Another viable test concerning performance and reliability of this integration method is provided by the scaling relation between the variance of the specific angular momentum and the corresponding halo mass to be discussed in Section 4.3.3.

In order to estimate the error of the integration procedure each sampling process is repeated several times for different random seeds. The results are consistent and exhibit only small scatter which is quantified in terms of the corresponding 1σ error. In addition, it is ensured that the number of accepted samples is at least of the order of 10^5 for all computations. Ultimately, the reliability of the integration method is tested by investigating the scaling behaviour with respect to changes in both the smoothing scale (4.20) and the relevant cosmological parameters. These are in particular all parameters which influence the shape of the linear power spectrum because changes in the matter spectrum propagate through the weighted moments (4.19) to the covariance matrices of the one- and two-point distribution function, respectively.

4.3.3. Angular momentum variance

For the visualization of my results it is convenient to introduce the specific angular momentum via

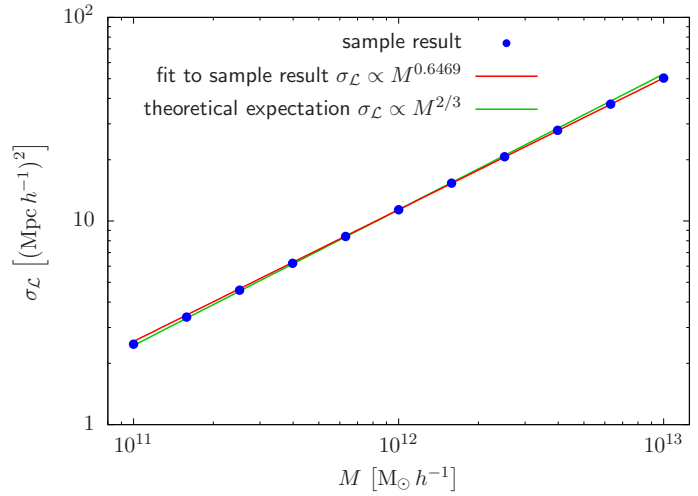
$$\mathcal{L} \equiv \frac{L}{H_0 M}. \quad (4.57)$$

As it is normalized with respect to the mass scale under consideration as well as the Hubble constant, the specific angular momentum is measured in units of $(\text{Mpc } h^{-1})^2$. Its standard deviation $\sigma_{\mathcal{L}}$ exhibits a clear dependence on mass ([Peebles, 1969](#); [Heavens & Peacock, 1988](#)). After dividing out a factor of σ_0 for convenience, it scales in proportion to $M^{2/3}$. This scaling relation serves as another valuable test of my numerical integration strategy. Figure 4.3 shows the sampling results for two orders of magnitude in halo mass. For the actual computation the halo mass is converted into an appropriate smoothing scale (cf. equation 4.20) and the threshold of the peak height is set to one. In order to compare my results to the theoretical expectation the data points are fitted by a power law. The fit accounts for the sampling error. For the best-fitting values one finds

$$\frac{\sigma_{\mathcal{L}}}{\sigma_{\mathcal{L},0}} = \left(\frac{M}{M_0} \right)^{0.6469 \pm 0.001}, \quad (4.58)$$

with $\sigma_{\mathcal{L},0} = 11\,362\sigma_0(\text{Mpc } h^{-1})^2$ and $M_0 = 10^{12}M_\odot h^{-1}$, within three per cent of the theoretical value. A physical situation one can think of in order to illustrate the specific angular momentum is provided by a homogeneous sphere with radius $1\text{ Mpc } h^{-1}$ and mass $10^{12}M_\odot h^{-1}$ that revolves once every $\sim 10^9$ years. The specific angular momentum of this object is exactly given by the $1\sigma_{\mathcal{L}}$ -value.

Figure 4.3: Standard deviation $\sigma_{\mathcal{L}}$ of the specific angular momentum as a function of halo mass. A power law fit (red line) demonstrates the excellent agreement with the theoretical expectation $\sigma_{\mathcal{L}} \propto M^{2/3}$ (green line).



4.3.4. Scaling with peak height and dependence on a high-mass cutoff

Figure 4.4 illustrates the scaling of the specific angular momentum standard deviation $\sigma_{\mathcal{L}}$ with the peak height ν together with its dependence on a high-mass cutoff. This cutoff rejects objects which exceed a certain mass limit given in units of the mass scale M_{scale} , associated with the smoothed fluctuation spectrum (cf. equation 4.20). The mass of the object is estimated from the protohalo's volume in ellipsoidal approximation (cf. equation 4.10). Hence, this procedure excludes very weakly curved density peaks.

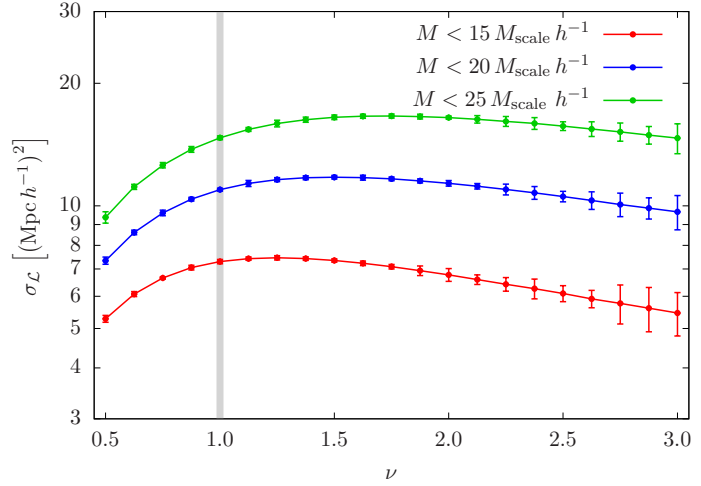
The high mass cutoff is necessary because the moments of the angular momentum distribution function are not finite. This might seem surprising at first glance since only Gaussian random fields are involved. However, there is an instructive analogy to the Cauchy distribution. All of the moments of the Cauchy distribution are undefined although it emerges as the Gaussian ratio distribution. Taking into account that the angular momentum vector is build up by, for example, the inverse of the eigenvalues of the mass tensor (cf. equation 4.9), the need for a high mass cutoff turns out to be rather natural. In general a cutoff of $20 M_{\text{scale}} h^{-1}$ is used as default.

Figure 4.4 reveals that the influence of variations in the (upper) mass bound is quite strong. It amounts to changes in the specific angular momentum by a factor of about two. Opposed to that the specific angular momentum is rather insensitive to changes in the peak height. The amplitude of its standard deviation varies by 30 per cent at most over the whole ν -interval under consideration. It is interesting to note that the standard deviation retains its maximum in the interval $\nu \in [1, 2]$ corresponding to galaxy-sized objects. This ν -range is therefore of primary interest for my analysis and I adopt a threshold of $\nu = 1$ for the computation of the angular momentum correlation function in the following section.

4.3.5. Angular momentum correlation function

In this section the most important result of this chapter is presented: the two-point angular momentum correlation function. It fully accounts for all correlations between the dynamical fields involved; on the one hand these are correlations between the inertia tensors of the two haloes under consideration and on the other hand the correlations in the tidal shear field exerting torquing moments on the very same haloes. As a matter of convenience the specific angular momentum is chosen for visualizing the

Figure 4.4: Standard deviation $\sigma_{\mathcal{L}}$ of the specific angular momentum as a function of peak height ν for three different mass cut-offs. The bars indicate the 1σ error of the numerical sampling scheme artificially enlarged by a factor of ten.



result. To be specific the correlation function for two Milky Way-sized haloes is shown, i.e. the mass scale is set to be $10^{12} M_{\odot} h^{-1}$, in Figure 4.5.

The correlation function decreases only slightly up to a separation of about $1 \text{ Mpc } h^{-1}$, where it starts to fall off exponentially. This transition indicates the typical correlation length of the angular momentum field of Milky Way-like density peaks in the large-scale structure. Furthermore, its dependence on separation motivates the following empirical fitting function

$$C_{\mathcal{L}}(r) = A \exp \left[- \left(\frac{r}{r_0} \right)^{\beta} \right] \quad (4.59)$$

with $A = (25010 \pm 165) \sigma_0^2 (\text{Mpc } h^{-1})^4$, $r_0 = (0.8628 \pm 0.008) \text{ Mpc } h^{-1}$ and $\beta = 3/2$. The error bounds indicate the 1σ error. The sharp exponential decrease for separations larger than approximately $1 \text{ Mpc } h^{-1}$ is the main difference with respect to the earlier work of Crittenden et al. (2001), who did not directly compute the angular momentum correlations but the closely related intrinsic ellipticity correlation function (for a detailed discussion of the relation between the two see Chapter 5). In the approach of Crittenden et al. (2001) the decline of the correlations is described by a power law, yielding a marginally enhanced correlation length. As a final remark I would like to point out that, according to my results, the angular momentum vectors are preferentially parallel aligned. Since the correlation function is not a quadratic form in the angular momenta (cf. equation 4.50), it is deliberately sensitive to the parallel or antiparallel spin alignment. The latter would result in an anticorrelation, i.e. a negative correlation function, which is not observed in my study.

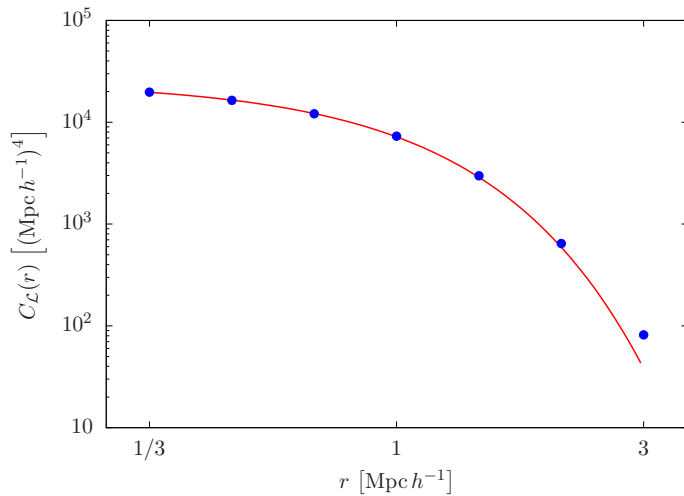


Figure 4.5: Angular momentum correlation function for two Milky Way-sized haloes. The red line indicates the empirical fitting formula (4.59).

4.4. Summary

In this chapter the one- and two-point angular momentum distribution functions were recomputed. Employing tidal torque theory in the Zel'dovich approximation allowed to model the statistics of the angular momentum field by a peak-restricted Gaussian random process.

- (i) In the framework of linear tidal torque theory the time evolution of the angular momentum is governed by the time derivative of the growth function, which is particularly sensitive to the presence of dark energy. In dark energy cosmologies the angular momentum growth is up to 30 per cent slower than in an Einstein-de Sitter universe. The results for a cosmological constant and classical quintessence with $w_0 = -\frac{2}{3}$ are quite similar, while there are qualitative differences for realizations with time-dependent equation of state.
- (ii) The angular momentum vector of a protogalactic object was built from two dynamical fields, its tensor of inertia and the shear field of the ambient matter distribution. I restricted my analysis entirely to the linear regime in order to allow for a Gaussian description of the angular momentum distribution function.
- (iii) The one-point statistics of the angular momentum vector is then captured by 15 Gaussian random variates: three for the gradient of the density field and six at a time for the inertia tensor and the tidal shear field, respectively. The density field itself is completely determined by the trace of the shear field and therefore does not explicitly enter the distribution function. Correlations between the angular momenta of neighbouring galaxies were modelled by the joint 30-dimensional Gaussian distribution. The entires of the corresponding covariance matrices could be exclusively expressed in terms of the spectral moments of the linear matter power spectrum.
- (iv) Since galaxy formation is assumed to take place at peaks in the cosmic density field the one- and two-point Gaussian distribution functions were subjected to an appropriate masking which enforced the peak constraints. Confined to density maxima exceeding a certain threshold the statistical description of galactic angular momenta did no longer obey a continuous formulation but became discrete instead.
- (v) Resulting in a large rejection rate of samples, this discrete nature further complicated the numerical evaluation of the high-dimensional angular momentum distribution. To overcome these difficulties I developed a specialized sampling routine, which even facilitated the integration of the effectively 24-dimensional angular correlation function. The effective dimension is rather 24 than 30 because focusing on density peaks necessarily requires that the density gradients both vanish, i.e. the corresponding six variates are set to zero throughout the entire analysis.
- (vi) Several tests of this integration method regarding its accuracy and reliability were carried out. Key among these was the recovery of the correct scaling relation of the specific angular momentum with halo mass. I could confirm the expected behaviour of $\mathcal{L} \propto M^{2/3}$ to a very high accuracy for a wide range in halo mass.
- (vii) The ansatz for the correlation function employed in my study improves on previous work because it treats both the inertia tensor and the tidal shear field on the same footing. It avoids their discrimination with respect to differences in the correlation length (the correlation length of the shear field is significantly enhanced in comparison to that of the peak shapes). By construction, the correlation function is only sensitive to field configurations in which the eigensystems of the inertia tensor and the shear field are not perfectly aligned. Thus, unphysical contributions are automatically excluded. Furthermore, it is exactly this construction principle which allows for the discrimination between the parallel and antiparallel orientation of the angular momentum vectors under consideration.

- (viii) The numerical evaluation of the two-point correlation function for the angular momenta of two Milky Way-sized haloes revealed that the spins are preferentially parallel aligned and that the correlation length r_0 is approximately $1 \text{ Mpc } h^{-1}$, in good agreement with the work of [Crittenden et al. \(2001\)](#). For larger separations the correlations in the angular momentum field decline exponentially. Their functional form is very well captured by the empirical fit $C_{\mathcal{L}}(r) \propto \exp[-(r/r_0)^{3/2}]$.

On the one hand the treatment in the framework of Gaussian random fields allows for a fully analytical description of the complex mechanism of galactic angular momentum acquisition, on the other hand it requires a number of rather far-reaching assumptions. In particular, modelling the peak shape by a simple parabolic density profile along with the resulting ellipsoidal shape of the inertia tensor are very coarse approximations. Furthermore, the motion of haloes and their nonlinear dynamics, which I completely neglected, are expected to influence the angular momentum amplitude, as well as its statistical properties like the correlation length ([Catelan & Theuns, 1996b, 1997](#); [Porciani et al., 2002a,b](#); [Lee & Pen, 2008](#)). It is important to keep these limitations in mind. However, they should not screen the numerous advantages of a purely analytical approach and the valuable insights it provides.

In the next chapter I will investigate the implications of galactic angular momentum correlations for gravitational lensing studies. A common assumption in weak lensing measurements is that galaxy shapes, i.e. their ellipticities, are intrinsically uncorrelated. Coupled angular momenta, however, give rise to the effect that the discs of neighbouring galaxies are viewed under similar angles of inclination so that their ellipticities do in fact become correlated. The angular scale of these intrinsic alignments may be estimated from the correlation length found above. For a deep redshift survey like *Euclid* one can approximate the distance to the lensed galaxies by 1 Gpc. Thus, the correlations subtend an angle of about 10^{-3} rad which corresponds to a multipole range of $\ell \sim 3000$. This highlights that intrinsic alignments are a small-scale phenomenon.

5

Chapter 5

Intrinsic alignments and $3d$ weak gravitational lensing

In this chapter it is shown how intrinsic alignments can be incorporated consistently in the formalism of $3d$ weak lensing. Two different descriptions of the intrinsic galaxy ellipticities are used, the so-called linear and quadratic model, respectively. For both models I derive the covariance matrix of the intrinsic alignment signal (II -alignments) and GI -alignments (the cross-correlation of intrinsic and lensing induced ellipticities). Evaluating the covariance matrices for the linear model numerically and comparing the results to the cosmic shear signal it is found that for a low redshift survey the total covariance matrix is dominated by the contributions of the II -alignments. For a *Euclid*-like survey II -alignments still dominate over GI -alignments but they are more than one order of magnitude smaller than the lensing signal. Most remarkably, the shape of the ellipticity covariance matrices is quite different in the k - k' -plane for cosmic shear on the one hand and intrinsic alignments on the other hand. In comparison to lensing both alignment types tend to be rather elongated along the diagonal $k = k'$. Moreover, for high multipoles ($\ell \sim 100$) intrinsic alignments are strongly concentrated along that diagonal.

The contents of this chapter have been published in [Merkel & Schäfer \(2013b\)](#).

5.1. Introduction

Forthcoming weak lensing surveys like the *Euclid* mission aim to constrain cosmological parameters to an accuracy of a few percent. Information from gravitational lensing ([Blandford et al., 1991](#); [Seitz et al., 1994](#); [Kamionkowski et al., 1998](#)) is eminently important because it is complementary to that obtained from the cosmic microwave background ([Hu, 2002b](#)). Being sensitive to all forms of matter, and particularly to its time evolution, gravitational lensing experiments are essential in the investigation of dark energy; the most significant parameters are its equation of state along with its time evolution, as well as the dark energy contribution to the Universe's matter content.

Conventionally, weak lensing or cosmic shear analyses are carried out in two dimensions. The main observables, angular correlation functions or equivalently angular power spectra, are obtained from a projection along the line-of-sight (see Chapter 3). Furthermore, one usually neglects the curvature of the sky considering only small patches which can be safely treated as flat. In order to overcome the line-of-sight projection and to make the valuable information contained in the time evolution of the lensing signal available, more advanced techniques have been developed in the past. These techniques take the photometric redshifts of the lensed galaxies into account. Simple stacking of usual (two-dimensional) lensing analysis carried out in several tomographic redshift slices already allows for tighter parameter constraints ([Hu, 1999](#); [Takada & White, 2004](#); [Hannestad et al., 2006](#)), especially in the case of the dark energy equation of state ([Hu, 2002a](#)). More elaborated than such tomographic

methods is the three-dimensional formalism developed by [Heavens \(2003\)](#) and [Castro et al. \(2005\)](#). They completely account for the three-dimensional character of weak gravitational lensing by maintaining the radial dependence of the lensing potential throughout the whole analysis, i.e. by abandoning the necessity of any projection. Additionally, they provide access to the full sky. The cost of this very general formalism is its enhanced numerical complexity, which is mainly due to the coupling of different density modes. This mode coupling underlines the fact that the lensing potential is not statistically homogeneous.

For both, tomography as well as three-dimensional weak lensing, good knowledge of the lensed galaxies' redshift is indispensable. The error in photometric redshift estimation is therefore considered as one of the most important systematics in cosmic shear studies ([Abdalla et al., 2008](#)). But the more the redshift accuracy improves, the more significant other systematical errors become. Thus, the systematical error budget might soon be dominated by intrinsic shape correlations. The correlations in the shapes of galaxies, more precisely their ellipticities, are only an unbiased estimator of the weak gravitational shear field if the intrinsic shapes are completely randomly orientated. Otherwise, intrinsic shape correlations will mimic the lensing signal, thereby corrupting cosmological parameters derived from lensing studies which are carried out under the null hypothesis of absent intrinsic alignments ([Bridle & King, 2007](#); [Joachimi & Bridle, 2010](#); [Kirk et al., 2010](#); [Capranico et al., 2013](#)). Employing shear tomography [Bridle & King \(2007\)](#) and [Kirk et al. \(2012\)](#) showed that in particular the equation of state parameter of dark energy is severely biased. [Kitching et al. \(2008\)](#) obtained similar results using 3d cosmic shear.

Intrinsic shape correlations have been observed in a number of Sloan Digital Sky Survey samples ([Mandelbaum et al., 2006](#); [Mandelbaum, R. et al., 2011](#); [Hirata et al., 2007](#); [Okumura et al., 2009](#)), as well as in numerical simulations ([Heavens et al., 2000](#); [Heymans et al., 2006](#); [Kuhlen et al., 2007](#)).

In order to remove, or at least reduce, the intrinsic alignment contamination of cosmic shear data a large variety of methods have been proposed and successfully applied. While [King & Schneider \(2002, 2003\)](#) and [Heymans & Heavens \(2003\)](#) exploit the locality of the intrinsic shape correlations to suppress the intrinsic alignment signal; the nulling techniques invented by [Joachimi & Schneider \(2008, 2009\)](#) modify the lensing efficiency function in such a way that the resulting cosmic shear measures are free from intrinsic alignment contributions. Both approaches provide unbiased estimates of cosmological parameters at the expense of precision due to the unavoidable loss of information inherent to these methods. Alternatively, one can circumvent data rejection by explicitly including intrinsic alignments in the analysis. The additional parameters used for modelling the intrinsic alignments then need to either be determined from the data or marginalized over, thereby weakening the constraints on the derived cosmological parameters ([King, 2005](#); [Bridle & King, 2007](#); [Bernstein, 2009](#); [Joachimi & Bridle, 2010](#); [Heymans, C. et al., 2013](#)).

All these methods, however, are tomographic methods. So far no comparable efforts have been made in case of 3d cosmic shear. This is particularly deplorable because 3d weak lensing improves upon tomographic analyses as it avoids the loss of information going along with any binning in redshift. Therefore, fully three-dimensional studies are extremely promising for measuring dark energy properties; very precise forecasts for the dark energy equation of state parameter and its time evolution can be achieved ([Heavens et al., 2006](#)). Furthermore, 3d weak lensing is less sensitive to errors in the photometric redshifts of galaxies than tomography. This makes intrinsic alignments very likely to dominate the systematical error budget in future 3d cosmic shear surveys. Thus, reliable control of this systematic error is increasingly important.

Nonetheless, the development of appropriate methods has received little attention in the past. This might be due to the fact that a consistent three-dimensional description of intrinsic alignments derived from physical alignment models is not yet available. Previous work analysing the impact of intrinsic alignments on 3d weak lensing measurements (e.g. [Kitching et al., 2008](#)) used the fitting formulae provided by [Heymans et al. \(2006\)](#). These intrinsic alignment parametrizations are derived from numerical simulations. This chapter aims at a more analytical description. I establish the constitutive

formalism necessary to incorporate intrinsic alignments into the framework of $3d$ weak lensing starting from physical alignment models. I concentrate on the two models proposed by [Catelan et al. \(2001\)](#) and [Hirata & Seljak \(2004\)](#) which have already been extensively used in the tomographic studies of intrinsic alignments mentioned above. Expressions for the resulting covariance matrices of the intrinsic alignment signal and for its cross-correlation with that of cosmic shear are presented. A comparison to the two-point statistics of weak cosmic shear then yields first insights into the strength of intrinsic alignment contamination, in particular its dependence on scale. Additionally, I investigate how this contamination varies with the depth of the lensing survey under consideration.

This chapter is structured as follows: Section 5.2 starts with a brief recapitulation of the key quantities in the description of galaxy ellipticities and their relation to (weak) gravitational lensing. Subsequently, the two intrinsic ellipticity models considered in this work are presented in detail. These models are then reformulated in the language of $3d$ cosmic shear in Section 5.3. Furthermore, I derive expressions for the resulting covariance matrices of the various intrinsic alignment types. Section 5.4 is devoted to the numerical evaluation of the covariance matrices derived before. Focusing on the linear alignment model, I illustrate my results for two different lensing survey specifications. Finally, the results are summarized in Section 5.5.

Throughout this chapter I assume a spatially flat Λ CDM universe characterized by the *WMAP7* best-fitting parameters detailed in Table 2.1

5.2. Intrinsic galaxy ellipticity and gravitational lensing

In projection, the shape of a galaxy on the sky can be characterized by its (complex) ellipticity

$$\epsilon = \epsilon_+ + i\epsilon_\times = |\epsilon|e^{2i\varphi}. \quad (5.1)$$

The real and imaginary part quantify the elongation and compression along two directions separated by 45° , respectively. The angle φ measures the misalignment between the local frame and the x -axis on the sky plane (assuming the line-of-sight along the z -axis). Obviously, the ellipticity is a spin-2 field. It is invariant under rotations of the coordinate frame by an angle of π . Accordingly, its complex conjugate carries spin weight -2 . Under idealized conditions, i.e. in the absence of pixelization, convolution and noise, the ellipticity components can be inferred from the second moments of the brightness distribution. The processing of real data, however, requires more involved methods and a variety of complementary shape measurement tools have been developed ([Kaiser et al., 1995](#); [Refregier, 2003](#); [Refregier & Bacon, 2003](#); [Miller et al., 2007](#); [Kitching et al., 2008](#); [Melchior et al., 2011](#)). A compilation of the different methods and their individual performance can be found in the handbooks of the GRavitational lEnsing Accuracy Testing Challenges 2008 and 2010 ([Bridle, S. et al., 2009](#); [Kitching, T. et al., 2010](#)).

Light rays reaching the observer from distant galaxies are deflected by gradients in the gravitational potential of the intervening large-scale structure as has been shown in Chapter 3. Consequently, the actually observed ellipticity of a galaxy $\epsilon^{(o)}$ is made up of two contributions

$$\epsilon^{(o)} = \epsilon + \gamma \quad (5.2)$$

with

$$\gamma = \gamma_+ + i\gamma_\times. \quad (5.3)$$

The shear γ encodes the deformation of the source due to gravitational lensing. By construction, it constitutes a spin-2 field, too. In addition to the deformation, lensing also changes the size of the source isotropically. This effect is captured by the convergence κ which is a real scalar quantity in contrast to the shear (see Figure 3.2 for an illustration of the different effects). The convergence is only directly observable in rare cases.

The simple superposition of intrinsic and lensing induced ellipticity in equation (5.2) only holds in the limit of *weak* gravitational lensing. Here the lensing effect on the individual galaxy is small, i.e. $|\gamma| \ll 1$ and $\kappa \ll 1$, and the reduced shear $g \equiv \gamma/(1 - \kappa)$ mediating between lensing and observed ellipticity

$$\epsilon^{(o)} = \frac{\epsilon + g}{1 + g^* \epsilon} \quad (5.4)$$

(Seitz & Schneider, 1997) can be well approximated by $\epsilon + \gamma$. Since the individual distortions are so small, the observable weak lensing signal is obtained as a statistical average over an ensemble of galaxies. Equation (5.2) underlines that the observed ellipticities are an unbiased estimator of the gravitational shear provided that the intrinsic shapes of the observed galaxies are randomly orientated and as long as lensing effects are weak, i.e. the approximation

$$\epsilon^{(o)} \sim \epsilon + g \sim \epsilon + \gamma \quad (5.5)$$

holds.

The intrinsic galaxy shapes emerge, at least partially, from the cosmic tidal field introducing correlations in the intrinsic shape of nearby galaxies, so-called *II-alignments* (Hirata & Seljak, 2004).

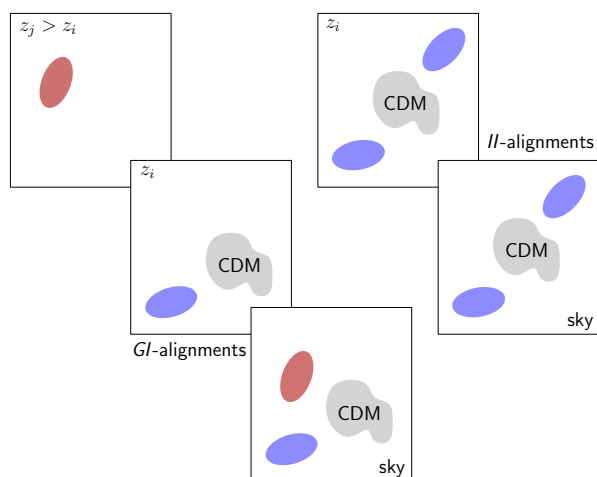


Figure 5.1: Illustration of the two types of intrinsic alignments. The red galaxy is lensed whereas the blue galaxies are intrinsically aligned. Both effects are due to the adjacent CDM structure. This figure has been adapted from Troxel & Ishak (2012).

Since both tidal field and gravitational lensing have the same origin, namely the gravitational potential, there may also be correlations between the intrinsic galaxy shapes and those being lensing induced. These correlations are commonly referred to as *GI-alignments*. It is interesting to note that the two different alignment types feature opposed redshift dependencies. *II-alignments* only arise from galaxy pairs which are physically close, i.e. their separation needs to be small both on the celestial sphere and in redshift, while the correlation length of *GI-alignments* in redshift is compatible with that of weak lensing. This complicates the removal of *GI-alignments* from cosmic shear data enormously. Another important difference between *II-* and *GI-alignments* arises from the fact that the latter can be negative, indicating an anti-correlation between intrinsic and lensing induced ellipticity. While a lensed background

galaxy appears preferentially tangentially aligned with the lens, the tidal field of the very same lens aims to radially align a close-by foreground galaxy. Both alignment types are illustrated in Figure 5.1.

Basically, there are two physical models used to describe the intrinsic alignment of galaxies. They are linear and quadratic in the tidal shear tensor, respectively. These models are rather simple and account neither for baryonic physics nor for the details of the formation process which are assumed to play a major role in building up the shape of an individual galaxy and for the orientation of its disc. Yet, they provide a very general and physically intuitive parametrization which is largely based on the symmetry or rather spin properties of the ellipticity. This is why they are a viable tool for an analytical treatment. Despite their simplicity, these models are expected to provide valuable information about the statistics of intrinsic alignments as for those the properties of a single galaxy should be of minor importance. For a more extensive discussion of the range of applicability of these models I refer to Mackey et al. (2002); Hirata & Seljak (2004).

5.2.1. Linear model

The simplest model for intrinsic alignments is linear in the shear field,

$$\epsilon_+ = -C_1 (\partial_x^2 - \partial_y^2) \Phi_S, \quad (5.6a)$$

$$\epsilon_\times = -2C_1 \partial_x \partial_y \Phi_S, \quad (5.6b)$$

assuming that the galaxy shape is at least partially determined by the shape of the dark matter halo the galaxy resides in. The host halo forms from gravitational collapse in a tidal field and is therefore expected to be triaxial and aligned with the principal axes of the tidal field. To physically motivate the ansatz in equation (5.6), one can consider the extremely simple case of an initially spherical arrangement of test particles moving in a spatially slowly varying potential Φ . A Taylor expansion of the potential about the origin then reveals that its gradient leads to a constant gravitational field shifting the test particles as a whole while the shape of the sphere is distorted by the quadratic term, i.e. the tidal field (Catelan et al., 2001).

This ansatz is usually used to describe the shape of elliptical galaxies, expecting that the baryonic matter, i.e. stars, fills up the gravitational well. The derivatives in equation (5.6) are comoving derivatives and the proportionality constant C_1 is a free parameter of the model which may be determined empirically by comparison with observations (cf. Catelan et al., 2001; Hirata & Seljak, 2004). Since I am interested in the intrinsic ellipticity of galaxies I have to apply an appropriate filter function to the Newtonian potential in equation (5.6), which is indicated by the subscripted S . The smoothing scale has to be chosen in such a way that it cuts off fluctuations corresponding to galaxy-sized objects. For instance, one could impose a Gaussian filter function, i.e. $\Phi_S(\mathbf{k}) = \Phi(\mathbf{k})e^{-(kR)^2/2}$, and adjust the filter scale R to the mass scale of galaxies via the mean cosmic matter density $\bar{\rho}_m$, i.e. by setting $M = 4/3\pi\bar{\rho}_m R^3$. Typical values for galaxies are $M \sim 10^{11} \dots 10^{12} M_\odot$. Moreover, I assume that galaxy formation takes place during matter domination so that the linear Newtonian potential becomes independent of the scale factor.

5.2.2. Quadratic model

In contrast to ellipticals the shape of spiral galaxies is believed to be determined by their angular momentum. Since the disc forms perpendicular to the spin axis the intrinsic ellipticity may be described by the following ansatz (Catelan et al., 2001)

$$\epsilon_+ = f(L, L_z)(L_x^2 - L_y^2) \quad \text{and} \quad \epsilon_\times = 2f(L, L_z)L_x L_y, \quad (5.7)$$

where L denotes the magnitude of the angular momentum. In the special case of an ideally thin disc, the function f is given by $f(L, L_z) = 1/(L^2 + L_z^2)$ so that

$$\epsilon_+ = \frac{\hat{L}_x^2 - \hat{L}_y^2}{1 + \hat{L}_z^2} \quad \text{and} \quad \epsilon_\times = \frac{2\hat{L}_x \hat{L}_y}{1 + \hat{L}_z^2} \quad (5.8)$$

with the angular momentum direction $\hat{\mathbf{L}} \equiv \mathbf{L}/L$. The finite thickness of a realistic disc can be accounted for by simply rescaling the expressions for the ellipticity by a constant factor, which weakens the dependence on the inclination angle, i.e. $f(L, L_z) = \alpha/(L^2 + L_z^2)$ with $\alpha \sim 0.75$, (Crittenden et al., 2001). It is interesting to note that the modulus of the ellipticity in equation (5.8) is constant. Hence, the ellipticity components just measure the galaxy's orientation. For actual computations it is more convenient to simplify equation (5.7) by assuming $f(L, L_z) = C_2 = \text{const}$. Since f determines how the ellipticity scales with the angular momentum, one expects $C_2 \sim \sqrt{\langle \epsilon^2 \rangle / \langle L^2 \rangle}$ (Mackey et al., 2002). This comprises the effect of the finite disc thickness as well, which weakens the correlation.

Under the assumption that the galaxy's angular momentum follows largely that of its host halo, one can compute the angular momentum in the framework of tidal torque theory, which was explained in

Chapter 4. There some of the limitations of this mechanism were also mentioned. In particular, recent results from cosmological simulations indicate that tidal torque theory breaks down at the turn around and virialization of the halo (Porciani et al., 2002b). Libeskind et al. (2013) suggest that from this point on the angular momentum may emerge from a vortical, rather than a shear flow. In this case, shape correlations could be related to correlations in the vorticity of the cosmic flow field and hence be described by a single dynamical field in a way similar to the linear model presented in Section 5.2.1.

Despite its limitations, the framework of tidal torque theory is very well suited for an analytical description of most of the fundamental properties of the spin of dark matter haloes (cf. Chapter 4). The statistical properties of both, the tensor of inertia and the shear field, are well understood in linear theory. In Section 4.3.1 it was explained that the actual computation of the resulting angular momentum correlation functions is quite involved due to the high dimensionality of the underlying probability distribution function. In the analysis of intrinsic alignments one therefore usually exploits the different correlation lengths of the tensor of inertia and the shear field, respectively. Recall that the correlations of the latter are typically long ranged, whereas correlations in the inertia tensor primarily arise from smaller scales. Thus, neglecting any correlations between tidal field and inertia tensor, one can first average over all possible orientations of the inertia tensor and subsequently over the realizations of the tidal field. Setting $f(L, L_z) = C_2$ in equation (5.7) as discussed above one finds

$$\epsilon_+ = C_2 \left[(\partial_x^2 \Phi_S)^2 - (\partial_y^2 \Phi_S)^2 \right], \quad (5.9a)$$

$$\epsilon_x = 2C_2 \left(\partial_x^2 \Phi_S + \partial_y^2 \Phi_S \right) \partial_x \partial_y \Phi_S. \quad (5.9b)$$

These relations were first derived by Catelan et al. (2001), while my presentation above follows more closely the argumentation of Mackey et al. (2002). As before, the derivatives are comoving derivatives and the constant of proportionality C_2 is a free parameter of the model which needs to be determined from observations.

5.3. 3d formalism

The lensing effect results from gradients in the Newtonian gravitational potential. It can therefore be related to the cosmic density field by means of the Poisson equation (2.33c). In the standard procedure of cosmic shear analysis the shear field enters as a projection along the line-of-sight $\gamma(\chi, \vartheta, \varphi) \rightarrow \gamma(\vartheta, \varphi)$ (cf. equation 3.21), thus providing an integrated measurement of the evolution of the cosmic density field. The projection, however, removes valuable information contained in its evolution as it inevitably mixes different spatial scales. This loss of information can be avoided, or at least reduced, by employing tomographic methods (Hu, 1999, 2002a; Takada & Jain, 2004; Kitching et al., 2011; Schäfer & Heisenberg, 2012). After dividing the population of lensed galaxies into redshift bins, the projection can be carried out piecewise over smaller redshift intervals thereby increasing the sensitivity of the lensing signal.

The focus of this work rests on another possibility to overcome the limitations of the line-of-sight projection: 3d weak lensing (Heavens, 2003; Castro et al., 2005). This formalism allows for a direct three-dimensional mapping of the cosmic density field.

As detailed in the preceding section, in the two simple models I am considering in this work intrinsic galaxy alignments may also be related to the Newtonian gravitational potential. The linear model is very similar to the description of weak cosmic shear. I shall therefore start with a short repetition of the formalism of 3d weak lensing in a very general way allowing for a convenient extension to intrinsic alignments later on.

5.3.1. Cosmic shear

3d weak lensing is formulated in harmonic space. Since all fields of interest carry spin weight two, the most natural choice of basis functions is given by a combination of spherical Bessel functions $j_\ell(z)$

(Abramowitz & Stegun, 1972) and spin-weighted spherical harmonics ${}_s Y_{\ell m}(\hat{\mathbf{n}})$ (Hu, 2000). Any spin- s quantity can then be expressed as

$$S(\mathbf{x}) = \sqrt{\frac{2}{\pi}} \sum_{\ell, m} \int k^2 dk S_{\ell m}(k) {}_s Y_{\ell m}(\hat{\mathbf{n}}) j_{\ell}(kx). \quad (5.10)$$

Inverting the last equation yields the expansion coefficients

$$S_{\ell m}(k) = \sqrt{\frac{2}{\pi}} \int d^3x S(\mathbf{x}) j_{\ell}(kx) {}_s Y_{\ell m}^*(\hat{\mathbf{n}}). \quad (5.11)$$

Here, and in the remainder of this work a spatially flat universe will be assumed. The generalization to a universe with arbitrary spatial curvature is straightforward. This spherical Fourier Bessel expansion has most recently been applied in the analysis of baryon acoustic oscillations (Pratten & Munshi, 2013).

The cosmic shear field, as well as the convergence, are derived from the lensing potential (cf. equation 3.17)

$$\phi(\mathbf{x}) = \phi(\chi, \vartheta, \varphi) = \frac{2}{c^2} \int_0^{\chi} d\chi' \frac{\chi - \chi'}{\chi\chi'} \Phi(\chi', \vartheta, \varphi) \quad (5.12)$$

by applying twice the eth operator \eth (Newman & Penrose, 1966; Goldberg et al., 1967) and its complex conjugate $\bar{\eth}$

$$\gamma(\mathbf{x}) = \frac{1}{2} \eth \bar{\eth} \phi(\mathbf{x}), \quad (5.13)$$

$$\kappa(\mathbf{x}) = \frac{1}{4} (\eth \bar{\eth} + \bar{\eth} \eth) \phi(\mathbf{x}) = \frac{1}{2} \Delta_{\vartheta\varphi} \phi(\mathbf{x}) \quad (5.14)$$

(Castro et al., 2005), respectively. Since a spatially flat universe is assumed, the distances χ in equation (5.12) are comoving distances.

Applied to a spin-weighted spherical harmonic the eth operator acts as a spin raising operator

$$\eth {}_s Y_{\ell m}(\hat{\mathbf{n}}) = \sqrt{(\ell - s)(\ell + s + 1)} {}_{s+1} Y_{\ell m}(\hat{\mathbf{n}}), \quad (5.15)$$

whereas its complex conjugate lowers the corresponding spin weight

$$\bar{\eth} {}_s Y_{\ell m}(\hat{\mathbf{n}}) = -\sqrt{(\ell + s)(\ell - s + 1)} {}_{s-1} Y_{\ell m}(\hat{\mathbf{n}}). \quad (5.16)$$

Noting that the lensing potential is a true scalar, i.e. spin-0 quantity, the following relations hold

$$\gamma_{\ell m}(k) = \frac{1}{2} \sqrt{\frac{(\ell + 2)!}{(\ell - 2)!}} \phi_{\ell m}(k), \quad (5.17)$$

$$\kappa_{\ell m}(k) = -\frac{\ell(\ell + 1)}{2} \phi_{\ell m}(k). \quad (5.18)$$

The coefficients of the lensing potential can be written in compact form as

$$\phi_{\ell m}(k) = \eta_{\ell}(k, k') \Phi_{\ell m}^0(k') \quad (5.19)$$

by introducing the matrix

$$\eta_{\ell}(k, k') \equiv \frac{4}{\pi} \int \chi^2 d\chi j_{\ell}(k\chi) \int_0^{\chi} d\chi' \frac{\chi - \chi'}{\chi\chi'} j_{\ell}(k'\chi') \frac{D_+(a')}{a'} \quad (5.20)$$

along with the following summation convention

$$\mathcal{A}(k, k') \mathcal{B}(k', k'') \equiv \int k'^2 dk' \mathcal{A}(k, k') \mathcal{B}(k', k''). \quad (5.21)$$

The inclusion of the linear growth function $D_+(a)$ allows for the use of today's gravitational potential $\Phi_{\ell m}^0(k)$, which in turn is related to the density contrast via the (comoving) Poisson equation (cf. equation 2.33c)

$$\Phi_{\ell m}(k) = -\frac{3\Omega_m}{2\chi_H^2} \frac{1}{a} \frac{\delta_{\ell m}(k)}{k^2}. \quad (5.22)$$

Here the Hubble distance $\chi_H \equiv c/H_0$ was introduced.

Having established a relation between the harmonic transform of the gravitational shear and that of the cosmic density field (cf. equations 5.17 and 5.19), a relation to the actually accessible observables in weak lensing measurements is still missing. Therefore, one considers the following discrete estimator

$$\hat{\gamma}_{\ell m}(k) = \sqrt{\frac{2}{\pi}} \sum_{\text{galaxies } g} \gamma_g(\mathbf{x}_g) j_\ell(k\chi_g) {}_2Y_{\ell m}^*(\hat{\mathbf{n}}_g) \quad (5.23)$$

(Heavens, 2003) constructed from the gravitational shears of individual galaxies. In order to calculate the expectation value of this estimator, one has to take observational uncertainties, as well as some specifications of the galaxy survey, into account.

In any realistic experiment the exact radial position of a galaxy is not known, however an estimate of its photometric redshift may be available. The conditional probability for the estimated redshift z , given the true redshift z_{true} , is typically modelled by a Gaussian

$$p(\chi|\chi_{\text{true}})d\chi = \frac{1}{\sqrt{2\pi}\sigma_z} \exp\left[-\frac{(z - z_{\text{true}})^2}{2\sigma_z^2}\right] dz. \quad (5.24)$$

For simplicity, I choose rather optimistically $\sigma_z = 0.02$ independent of redshift.

The survey itself is assumed to be a full-sky experiment, i.e. it is homogeneous and isotropic in its angular part. The radial galaxy number density is described by the distribution given in equation (3.29), i.e.

$$n(z)dz \propto z^2 \exp\left[-\left(\frac{z}{z_0}\right)^\beta\right] dz. \quad (5.25)$$

Having *Euclid* in mind one expects 100 galaxies per square arcminute and sets $z_0 = 0.64$ and $\beta = 3/2$ (Amendola, L. et al., 2012).

After the transition to a continuous formulation the expectation value of the estimator is given by

$$\bar{\gamma}_{\ell m}(k) = \mathcal{Z}_\ell(k, k') \mathcal{M}_\ell(k', k'') \gamma_{\ell m}(k''), \quad (5.26)$$

where I have defined the two new matrices by

$$\mathcal{Z}_\ell(k, k') \equiv \frac{2}{\pi} \int \chi'^2 d\chi' j_\ell(k\chi') \int d\chi p(\chi'|\chi) j_\ell(k'\chi) \quad (5.27)$$

and

$$\mathcal{M}_\ell(k, k') \equiv \frac{2}{\pi} \int \chi^2 d\chi j_\ell(k\chi) j_\ell(k'\chi) n(\chi). \quad (5.28)$$

As it is proportional to the linear density contrast, the expectation value itself is obviously zero. Valuable information, however, can be extracted from its covariance. It reads in terms of the linear matter power spectrum $P_{\delta\delta}(k)$

$$C_\ell^{\gamma\gamma}(k, k') = \langle \bar{\gamma}_{\ell m}(k) \bar{\gamma}_{\ell' m'}^*(k') \rangle = A^2 \frac{(\ell + 2)!}{(\ell - 2)!} \mathcal{B}_\ell(k, k'') \frac{P_{\delta\delta}(k'')}{k''^4} \mathcal{B}_\ell(k', k'') \quad (5.29)$$

with the constant $A \equiv 3\Omega_m/4\chi_H^2$ and the matrix $\mathcal{B}_\ell(k, k') \equiv \mathcal{Z}_\ell(k, k'') \mathcal{M}_\ell(k'', k''') \eta_\ell(k''', k')$.

In contrast to conventional cosmic shear studies, which are confined to the two-dimensional sky, the covariance matrix of the three-dimensional lensing field acquires off-diagonal elements in k -space.

Accordingly, the shear field has different statistical properties with respect to the underlying cosmic density field. The latter is statistically homogeneous and isotropic, characterized by a power spectrum which is diagonal in harmonic space, i.e.

$$\langle \delta_{\ell m}(k) \delta_{\ell' m'}^*(k') \rangle = \frac{P_{\delta\delta}(k)}{k^2} \delta_{\text{D}}(k - k') \delta_{\ell\ell'} \delta_{mm'}. \quad (5.30)$$

The lensing potential, as a projection along the line-of-sight, is no longer statistically homogeneous and isotropic in radial direction. Conversely, the covariance matrix is still diagonal in multipole space, highlighting that it does maintain statistical homogeneity and isotropy in angular direction at fixed radial position.

The structure of the covariance matrix becomes more involved if nonlinear structure growth is considered. Beyond linear theory the growth of cosmic structures becomes scale-dependent. Its time, or equivalently redshift, dependence cannot longer be expressed in terms of the growth function. Accordingly, equation (5.19) needs to be replaced by

$$\phi_{\ell m}(k) = \frac{4}{\pi} \int \chi^2 d\chi j_{\ell}(k\chi) \int_0^{\chi} d\chi' \frac{\chi - \chi'}{\chi\chi'} j_{\ell}(k'\chi') \Phi_{\ell m}(k', \chi'). \quad (5.31)$$

The computation of the cosmic shear covariance matrix then requires the evaluation of the matter power spectrum for modes located at different (comoving) distances (or instances of time), i.e. a term of the form $P_{\delta\delta}(k, \chi, \chi')$ enters equation (5.29) inside the χ -integrations. For further progress [Castro et al. \(2005\)](#) suggested, and justified, to set $P_{\delta\delta}(k, \chi, \chi') \simeq \sqrt{P_{\delta\delta}(k, \chi) P_{\delta\delta}(k, \chi')}$. From this it is easy to recover my expressions which are restricted to linear structure formation

$$P_{\delta\delta}(k, \chi, \chi') = \sqrt{P_{\delta\delta}(k, \chi) P_{\delta\delta}(k, \chi')} = \sqrt{D_+^2(a) P_{\delta\delta}(k) D_+^2(a') P_{\delta\delta}(k)} = D_+(a) D_+(a') P_{\delta\delta}(k). \quad (5.32)$$

Thus, the power spectrum does not enter the χ -integrations.

Large-scale modes of the estimator (5.26) can be safely treated as Gaussian random fields, hence the corresponding likelihood is completely determined by the covariance matrix (5.29). Extending the Gaussian likelihood to small-scale modes, however, is expected to introduce a significant bias in the derived cosmological parameters ([Takada & Jain, 2009](#); [Sato & Nishimichi, 2013](#)). While this is a consequence of nonlinear structure growth, a non-Gaussian likelihood may also arise from the finite volume of any realistic survey. Here, large-scale modes, which exceed the survey, couple adjacent large wavelength perturbations. This results in a (additional) non-Gaussian signature on scales which are much smaller than the survey ([Takada & Hu, 2013](#)).

5.3.2. Intrinsic alignments

For a realistic experiment the gravitational shear needs to be replaced by the observed ellipticity $\epsilon^{(0)}$ in the estimator given by equation (5.23). In the absence of intrinsic alignments the covariance matrix of the gravitational shear field is almost unaffected by this substitution. It just acquires an additional shot noise term given by

$$\mathcal{N}_{\ell}(k, k') = \frac{\sigma_{\epsilon}^2}{4} \mathcal{M}_{\ell}(k, k'), \quad (5.33)$$

where σ_{ϵ}^2 denotes the variance of the observed ellipticity, typically $\sigma_{\epsilon}^2 \lesssim 0.1$ ([Heavens, 2003](#)).

The situation, however, is completely different when the intrinsic galaxy shapes are correlated. There are then basically three distinct contributions to the total covariance (omitting the shape noise for simplicity in the following)

$$\langle \epsilon_{\ell m}^{(0)}(k) \epsilon_{\ell' m'}^{(0)*}(k') \rangle = C_{\ell}(k, k') = C_{\ell}^{\gamma\gamma}(k, k') + C_{\ell}^{\epsilon\epsilon}(k, k') + C_{\ell}^{\epsilon\gamma}(k, k'). \quad (5.34)$$

Assuming a completely covered sky guarantees that the covariance matrix is diagonal in ℓ and m . The second term describes *II*-alignments, whereas the third one captures *GI*-alignments. The last term

solely arises from the correlation between the intrinsic shape of a foreground galaxy and the lensing induced shear of a background galaxy. Lensed galaxies are typically located far enough from the lens in order to safely consider intrinsic shape and tidal field being uncorrelated, i.e. their distance exceeds several correlation lengths. Concentrating on linear theory, this term is only present in the linear model, because in case of the quadratic model the covariance involves the bispectrum of the gravitational potential which identically vanishes for a Gaussian random field. In order to compute the individual contributions to the covariance one has to find the corresponding 3d expressions for the intrinsic ellipticities first.

Linear model

I start with the linear model as given in equation (5.6). In a first step I convert the comoving derivatives into angular derivatives, i.e.

$$\epsilon_+ = -C_1 (\partial_x^2 - \partial_y^2) \Phi_S = -\frac{C_1}{\chi^2} (\partial_{\theta_1}^2 - \partial_{\theta_2}^2) \Phi_S(\chi\boldsymbol{\theta}, \chi), \quad (5.35a)$$

$$\epsilon_\times = -2C_1 \partial_x \partial_y \Phi_S = -2\frac{C_1}{\chi^2} \partial_{\theta_1} \partial_{\theta_2} \Phi_S(\chi\boldsymbol{\theta}, \chi), \quad (5.35b)$$

where $\boldsymbol{\theta} = (\theta_1, \theta_2)$ denotes a two-dimensional angular position on the sky. In order to facilitate the incorporation of the intrinsic ellipticity field in the 3d formalism the angular derivatives are then replaced by covariant derivatives (A.1) on the (unit) sphere. This step might seem worrisome because the tidal shearing responsible for the intrinsic ellipticity is not confined to the surface of the observed sky. However, in practice one is only interested in patches of the sky small enough to be considered as flat, so that then covariant derivatives reduce to partial derivatives again. The non-vanishing Christoffel symbols on the two-dimensional sphere are $\Gamma_{\varphi\varphi}^\vartheta = -\sin\vartheta \cos\vartheta$ and $\Gamma_{\vartheta\vartheta}^\varphi = \Gamma_{\vartheta\varphi}^\varphi = \cot\vartheta$. One then finds

$$\epsilon_+ = -\frac{C_1}{2\chi^2} (\nabla_\vartheta \nabla_\vartheta - \csc^2\vartheta \nabla_\varphi \nabla_\varphi) \Phi_S, \quad (5.36a)$$

$$\epsilon_\times = -\csc\vartheta \frac{C_1}{\chi^2} \nabla_\vartheta \nabla_\varphi \Phi_S. \quad (5.36b)$$

The additional $\csc\vartheta$ term in the last expression mirrors the fact that the two ellipticity modes form the components of a rank two tensor rather than those of a vector, i.e.

$$\epsilon_{\mu\nu} = \begin{pmatrix} \epsilon_+ & \sin\vartheta \epsilon_\times \\ \sin\vartheta \epsilon_\times & -\sin^2\vartheta \epsilon_+ \end{pmatrix}, \quad (5.37)$$

and that the basis vectors are orthogonal but not orthonormal.

The great advantage of reformulating the intrinsic ellipticity in terms of covariant derivatives is that one can now exploit its relation to the eth operator (Castro et al., 2005). The (complex) galaxy's ellipticity can be written in the most compact form, namely as second eth-derivative of a suitably constructed scalar potential

$$\epsilon(\mathbf{x}) = -\frac{C_1}{2} \eth\eth \Psi(\mathbf{x}) \quad (5.38)$$

with

$$\Psi(\chi, \vartheta, \varphi) \equiv \frac{\Phi_S(\chi, \vartheta, \varphi)}{\chi^2} \quad (5.39)$$

in complete analogy to the weak lensing case (cf. equation 5.13), replacing the lensing potential by the auxiliary potential Ψ . There is one important difference between the two potentials. In contrast to the lensing potential, the field Ψ does not evolve in time because it is assumed that galaxy formation takes

place during matter domination. Accordingly, the following relation for the harmonic coefficients is found

$$\epsilon_{\ell m}(k) = -\frac{C_1}{2} \sqrt{\frac{(\ell+2)!}{(\ell-2)!}} \Psi_{\ell m}(k). \quad (5.40)$$

They are connected to the smoothed Newtonian gravitational potential by

$$\Psi_{\ell m}(k) = \tilde{\eta}_{\ell}(k, k') \Phi_{\ell m}^{S,0}(k') \quad (5.41)$$

with

$$\tilde{\eta}_{\ell}(k, k') = \frac{2}{\pi} \int d\chi j_{\ell}(k\chi) j_{\ell}(k'\chi). \quad (5.42)$$

Due to the missing time dependence of the matrix $\tilde{\eta}_{\ell}(k, k')$ the matrix $\tilde{\mathcal{B}}_{\ell}(k, k')$, which is defined in complete analogy to the cosmic shear case, takes the particularly simple form

$$\tilde{\mathcal{B}}_{\ell}(k, k') = \frac{2}{\pi} \int d\chi j_{\ell}(k\chi) \int d\chi' p(\chi|\chi') j_{\ell}(k'\chi') \frac{n(\chi')}{\chi'^2}. \quad (5.43)$$

Finally, one arrives at the expressions for the covariance matrix of the II -alignments

$$C_{\ell}^{\epsilon\epsilon}(k, k') = \langle \bar{\epsilon}_{\ell m}(k) \bar{\epsilon}_{\ell' m'}^*(k') \rangle = A^2 \frac{(\ell+2)!}{(\ell-2)!} \tilde{\mathcal{B}}_{\ell}(k, k'') \frac{P_{\delta\delta}(k'')}{k''^4} \tilde{\mathcal{B}}_{\ell}(k', k'') \quad (5.44)$$

and of the GI -alignments

$$C_{\ell}^{\epsilon\gamma}(k, k') = \langle \bar{\epsilon}_{\ell m}(k) \bar{\gamma}_{\ell' m'}^*(k') \rangle = -A^2 \frac{(\ell+2)!}{(\ell-2)!} \tilde{\mathcal{B}}_{\ell}(k, k'') \frac{P_{\delta\delta}(k'')}{k''^4} \mathcal{B}_{\ell}(k', k''). \quad (5.45)$$

It is interesting to note that without the inverse χ^2 -weighting of the gravitational potential in equation (5.39), the matrix $\tilde{\eta}$ would reduce to the unit matrix because of the orthogonality relation of the spherical Bessel functions (cf. equation B.4). In this case, the intrinsic ellipticity field would be a statistically homogeneous field and the non-diagonal structure of its covariance matrix would solely result from the construction of the estimator $\bar{\epsilon}_{\ell m}(k)$.

Quadratic model

In order to find the 3d generalization of the quadratic alignment model the steps carried out for the linear model in the previous section could, in principle, be repeated. However, one can shorten the derivation by noting that

$$\epsilon = \frac{C_2}{\chi^4} \left(\partial_{\theta_1}^2 \Phi_S + \partial_{\theta_2}^2 \Phi_S \right) \left(\partial_{\theta_1}^2 \Phi_S - \partial_{\theta_2}^2 \Phi_S + 2i \partial_{\theta_1} \partial_{\theta_2} \Phi_S \right). \quad (5.46)$$

One then finds

$$\epsilon(\mathbf{x}) = \frac{C_2}{2} [\delta\bar{\delta} \Psi(\mathbf{x})] \left[(\delta\bar{\delta} + \bar{\delta}\delta) \Psi(\mathbf{x}) \right], \quad (5.47)$$

where the potential Ψ is defined as before (cf. equation 5.39). Obviously, the ellipticity in equation (5.47) has spin weight two. It is the most general quadratic function of the tidal shear tensor with spin-2.

Aiming at the statistics of the intrinsic alignments one needs to relate the harmonic coefficients of the ellipticity field to that of the gravitational potential next. This relation is much more involved than in case of the linear model. I start with the intermediate result

$$\begin{aligned} \epsilon_{\ell m}(k) &= (-1)^{m+1} \sqrt{\frac{2}{\pi^3}} C_2 \sum_{\ell_1, \ell_2, m_1, m_2} \ell_1(\ell_1+1) \sqrt{\frac{(\ell_2+2)!}{(\ell_2-2)!}} \mathcal{I}_{\ell_1 \ell_2 \ell}(k_1, k_2, k) {}_2\mathcal{W}_{m_1 m_2 m}^{\ell_1 \ell_2 \ell} \\ &\times \tilde{\eta}_{\ell_1}(k_1, k_3) \Phi_{\ell_1 m_1}^{S,0}(k_3) \tilde{\eta}_{\ell_2}(k_2, k_4) \Phi_{\ell_2 m_2}^{S,0}(k_4). \end{aligned} \quad (5.48)$$

Here several new quantities, which emerge from the quadratic structure in the potential, were introduced. The mode coupling is captured by

$$\mathcal{I}_{\ell_1 \ell_2 \ell}(k_1, k_2, k) \equiv \int \chi^2 d\chi j_{\ell_1}(k_1 \chi) j_{\ell_2}(k_2 \chi) j_{\ell}(k \chi), \quad (5.49)$$

while the angular mixing matrix is given by

$${}_2\mathcal{W}_{m_1 m_2 m}^{\ell_1 \ell_2 \ell} \equiv \Pi_{\ell_1 \ell_2 \ell} \begin{pmatrix} \ell_1 & \ell_2 & \ell \\ 0 & -2 & 2 \end{pmatrix} \begin{pmatrix} \ell_1 & \ell_2 & \ell \\ m_1 & m_2 & -m \end{pmatrix} \quad (5.50)$$

with

$$\Pi_{\ell_1 \ell_2 \ell} \equiv \sqrt{\frac{(2\ell_1 + 1)(2\ell_2 + 1)(2\ell + 1)}{4\pi}}. \quad (5.51)$$

The sixfold indexed quantities denote Wigner 3j-symbols which are related to spherical harmonics by

$$\int d\Omega s_1 Y_{\ell_1 m_1}(\hat{\mathbf{n}}) s_2 Y_{\ell_2 m_2}(\hat{\mathbf{n}}) s_3 Y_{\ell_3 m_3}(\hat{\mathbf{n}}) = \Pi_{\ell_1 \ell_2 \ell_3} \begin{pmatrix} \ell_1 & \ell_2 & \ell_3 \\ -s_1 & -s_2 & -s_3 \end{pmatrix} \begin{pmatrix} \ell_1 & \ell_2 & \ell_3 \\ m_1 & m_2 & m_3 \end{pmatrix} \quad (5.52)$$

(Hu, 2000). The corresponding expectation value of the estimator is then obtained from equation (5.26) replacing $\gamma_{\ell m}(k)$ by $\epsilon_{\ell m}(k)$.

For the calculation of its covariance one needs to evaluate the trispectrum of the Newtonian potential. Since I am focusing on linear theory, the trispectrum is completely characterized by its reducible part and I can therefore invoke Wick's theorem (see Appendix A.2.1). Here the final result is quoted, whereas a detailed derivation is relegated to Appendix B.1:

$$C_{\ell}^{\epsilon\epsilon}(k, k') = \frac{A^4 C_2^2}{2\ell + 1} \sum_{\ell_1, \ell_2} \mathcal{B}_{\ell \ell_1 \ell_2}^k(k_3, k_4) \frac{P_{\delta\delta}(k_3)}{k_3^4} \frac{P_{\delta\delta}(k_4)}{k_4^4} \left(\mathcal{B}_{\ell \ell_1 \ell_2}^{k'}(k_3, k_4) + (-1)^{\ell_1 + \ell_2 + \ell} \mathcal{B}_{\ell \ell_2 \ell_1}^{k'}(k_3, k_4) \right). \quad (5.53)$$

The definition of the matrix $\mathcal{B}_{\ell \ell_1 \ell_2}^k(k_3, k_4)$ is given in equation (B.11). Note that the covariance matrix is diagonal in multipole space reflecting the fact that full sky coverage was assumed. While it is independent of $m_{1,2}$, the quadratic form of the intrinsic ellipticities requires the evaluation of the double sum in $\ell_{1,2}$, leaving the numerical effort for its computation tremendous (cf. Section 5.4.2).

E/B-mode decomposition

Although I will not apply this formalism, I shall now briefly address the so-called *E/B-mode* (curl-gradient) decomposition, already mentioned in Section 3.3, of the intrinsic and lensing induced shear field for completeness. Since the gravitational shear tensor is symmetric and traceless (cf. equation 5.37 replacing ϵ by γ), it proves convenient to convert its two degrees of freedom into two *scalar* functions with a definite behaviour under parity transformations

$$E_{\gamma} \equiv \nabla^{-2} \left(\nabla^{\alpha} \nabla^{\beta} \gamma_{\alpha\beta} \right), \quad (5.54a)$$

$$B_{\gamma} \equiv \nabla^{-2} \left(\nabla^{\alpha} \nabla^{\tau} \gamma_{\alpha\beta} \epsilon_{\tau\beta} \right) \quad (5.54b)$$

(Stebbins, 1996; Kamionkowski et al., 1997; Crittenden et al., 2002), where

$$\epsilon_{\alpha\beta} \equiv \begin{pmatrix} 0 & \sin \vartheta \\ -\sin \vartheta & 0 \end{pmatrix} \quad (5.55)$$

and ∇^{-2} is the inverse Laplace operator on the sphere. The *gradient* part or *E-mode* is a true scalar, i.e. parity conserving, while the *curl* part or *B-mode* is a pseudo scalar, i.e. changing sign under reflections. Any statistical analysis of weak lensing data can then be performed in terms of the angular

power spectra of these two fields, which are invariant under rotations of the reference frame in contrast to the shear components.

The E - and B -mode of any spin-2 field η can be most readily accessed in harmonic space because there is a simple relation between the expansion coefficients of the two scalar functions and those of η and its complex conjugate η^* , which carries spin weight -2 , (Zaldarriaga & Seljak, 1999)

$$E_{\ell m}(k) = -\frac{1}{2} (2\eta_{\ell m}(k) + -2\eta_{\ell m}(k)), \quad (5.56a)$$

$$B_{\ell m}(k) = \frac{i}{2} (2\eta_{\ell m}(k) - -2\eta_{\ell m}(k)). \quad (5.56b)$$

Due to the fact that the expansion coefficients of the cosmic shear field and its complex conjugate are identical, i.e. $2\gamma_{\ell m} = -2\gamma_{\ell m}$, the shear field possesses no B -mode. Alternatively, this can be seen by recalling that any spin-2 quantity η may be expressed in terms of a complex potential

$$\eta(\mathbf{x}) = \frac{1}{2} \delta\delta (\phi_E(\mathbf{x}) + i\phi_B(\mathbf{x})) \quad (5.57)$$

(Newman & Penrose, 1966; Castro et al., 2005) and realizing that the lensing potential is purely real. It turns out that the statistics of the lensing E -mode are identical to that of the cosmic shear field, i.e. $C_\ell^{\gamma\gamma}(k, k') = C_\ell^{E_\gamma E_\gamma}(k, k')$, provided that the expansion coefficients of the potential ϕ_{E_γ} are appropriately normalized (Castro et al., 2005).

The detection of a B -mode in weak lensing data may then be used as a diagnostic for systematical errors in the experiment, assuming that any other potential B -mode source can be excluded. Possible B -mode contamination results from higher-order lensing effects, like source-lens clustering (Schneider et al., 2002), multiple lensing along the line-of-sight (Krause & Hirata, 2010) or violations of the Born approximation (Cooray & Hu, 2002; Shapiro & Cooray, 2006). Another possible source are intrinsic alignments. Obviously, the linear model cannot introduce any B -mode because in this model the intrinsic ellipticities are obtained from a real potential as well. Thus, the same reasoning as in the case of cosmic shear applies. The quadratic model, however, introduces inevitably a non-vanishing B -mode as can be seen as follows: Looking at equation (5.48) and realizing that

$$\delta\delta Y_{\ell m}(\hat{\mathbf{n}}) = \sqrt{\frac{(\ell+2)!}{(\ell-2)!}} {}_2Y_{\ell m}(\hat{\mathbf{n}}), \quad (5.58a)$$

$$\bar{\delta}\bar{\delta} Y_{\ell m}(\hat{\mathbf{n}}) = \sqrt{\frac{(\ell+2)!}{(\ell-2)!}} {}_{-2}Y_{\ell m}(\hat{\mathbf{n}}), \quad (5.58b)$$

one notes that the only potentially spin-dependent part is given by the angular mixing matrix defined in equation (5.50). Carrying out the decomposition of $\epsilon^*(\mathbf{x}) = \epsilon_+(\mathbf{x}) - i\epsilon_\times(\mathbf{x})$ one readily finds

$${}_{-2}\mathcal{W}_{m_1 m_2 m}^{\ell_1 \ell_2 \ell} = (-1)^{\ell_1 + \ell_2 + \ell} {}_2\mathcal{W}_{m_1 m_2 m}^{\ell_1 \ell_2 \ell} \quad (5.59)$$

and therefore ${}_2\epsilon_{\ell m}(k) \neq -{}_{-2}\epsilon_{\ell m}(k)$. Consequently, for the quadratic model the B -mode of the ellipticity field does not vanish.

Finally, I would like to mention that there are physical processes which transfer power from the E -mode of the intrinsic ellipticity field into its B -mode and vice versa. Recently, Giahi & Schäfer (2013a,b) investigated this E/B -mode conversion due to peculiar motion and gravitational lensing, respectively, in the flat-sky limit.

5.4. Numerical results

5.4.1. Linear model

After the derivation of the various covariance matrices in the last section, I would now like to illustrate my findings by presenting some numerical results. I focus on the linear alignment model, which in contrast to the quadratic model, exhibits both II - and GI -alignments. In general, the $3d$ weak shear formalism is numerically very demanding due to the large number of k -integrations required. A further complication arises from the fact that the functions which are to be integrated contain spherical Bessel functions which are highly oscillatory. [Ayaita et al. \(2012\)](#) showed how the numerical efforts can be minimized. I adapt their strategy in the numerical evaluation of the covariance matrices of the II - and GI -alignments predicted by the linear model.

In order to make the computation feasible I restrict my analysis to a (discrete) k -space interval from $k_{\min} = 10^{-3} \text{ Mpc}^{-1}$ to $k_{\max} = 10^{-1} \text{ Mpc}^{-1}$ covered by $N_k = 200$ equidistant steps. Therefore no additional filtering to the CDM power spectrum is applied. Likewise, the finite wavevector interval corresponds to a sharp cutoff filter in Fourier space which has been used by [Hirata & Seljak \(2004\)](#) in their two-dimensional analysis. Furthermore, $N_z = 1000$ steps in redshift space ranging from $z_{\min} = 10^{-4}$ to $z_{\max} = 10$ are considered.

In accordance with [Hirata & Seljak \(2004\)](#); [Bridle & King \(2007\)](#); [Joachimi et al. \(2011\)](#) the value for the constant of the linear alignment model, C_1 , is chosen in such a way that it matches the SuperCOSMOS observations at low redshift ([Brown et al., 2002](#)): $C_1 H_0^2 = 8.93 \times 10^{-3}$ (here natural units are used where the speed of light is set to unity).

First, I concentrate on the diagonal elements of the various covariance matrices. Figure 5.2 shows the results for four different multipoles, $\ell = 10, 20, 100$ and 200 , assuming a shallow survey with $z_{\text{median}} = 0.3$. Note the different k -range in each of the plots. Only the range where the amplitude of the covariance matrix is appreciable is depicted. The first observation is the expected trend that the larger the multipole order, the larger the k -value where the covariance matrix peaks. Interestingly, the peak position slightly differs for all three covariance matrices. The differences in the peak location increases with increasing multipole order. At low multipoles ($\ell = 10, 20$, corresponding to an angular scale of about ten degrees) the weak lensing signal dominates. It exceeds the signal of both intrinsic alignment types by more than one order of magnitude. For the smallest multipole the amplitude of the II -alignments is compatible to that of the GI -alignments but then starts to dominate the alignment signal and finally exceeds it by more than one order of magnitude for $\ell = 200$. On this angular scale the GI -contribution is almost as large as the cosmic shear signal. Consequently, for $\ell = 200$ the total covariance matrix is dominated by the II -alignment term.

The situation is different for a deeper survey. In Figure 5.3 I show the results for a survey with $z_{\text{median}} = 0.9$ corresponding to the *Euclid* mission. As before, the diagonal elements of all three covariance matrices for $\ell = 10, 20, 100$ and 200 are plotted. Again, only the k -range featuring substantial amplitude is shown for clarity. One finds that weak lensing contributes most to the diagonal elements of the covariance matrices for all four multipoles under consideration. The difference with respect to the II -contributions decreases with multipole order (from roughly three orders of magnitude for $\ell = 10$ to one order of magnitude for $\ell = 200$). While on large angular scales the GI -contributions are slightly enhanced in comparison to those from the II -alignments, the latter dominate vastly on smaller scales where the II -contributions exceed the GI -signal by more than one order of magnitude. Furthermore, one can see that the differences in the peak positions are much less pronounced than for the shallow survey.

Confronting the results obtained for the two different surveys one immediately recognizes that the maxima are shifted to larger scales in case of the higher redshift sample. It is interesting to note that for both survey specifications II -alignments on the one hand, and weak cosmic shear and GI -alignments on the other hand, exhibit a different dependence on the wavenumber k . The weak lensing as well as the GI -signal fall off much steeper than that of the II -alignments.

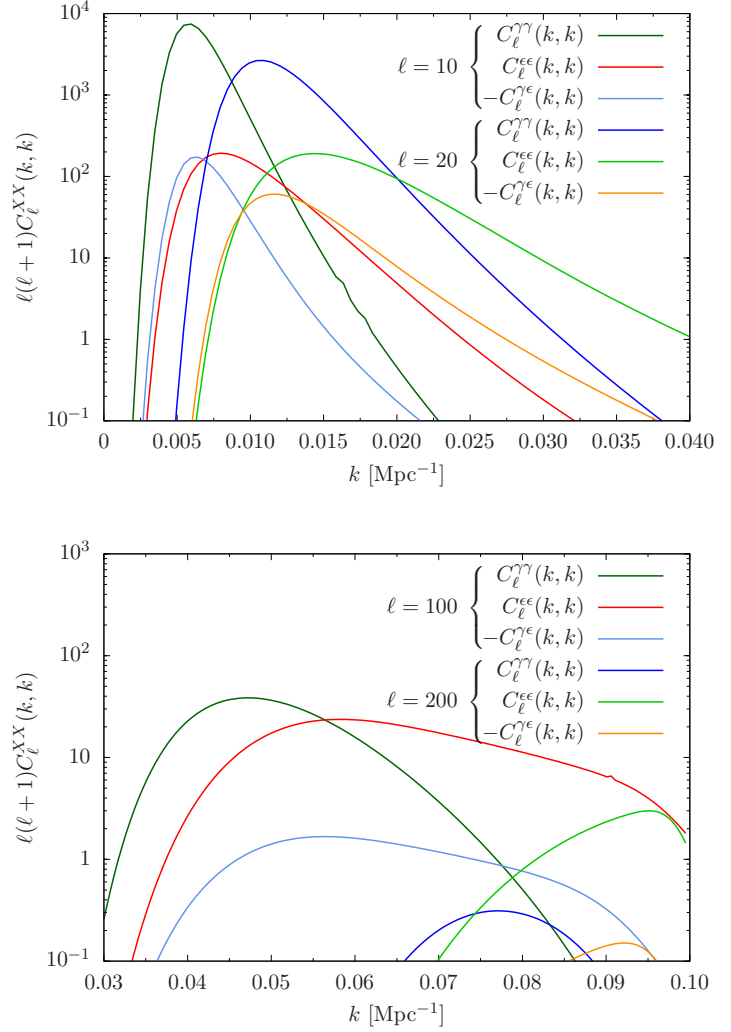


Figure 5.2: Diagonal elements of the covariance matrices of the cosmic shear field, *II*- and *GI*-alignments for the linear model. The results for multipoles $\ell = \{10, 20\}$ (top panel) and $\ell = \{100, 200\}$ (bottom panel) are shown. The median redshift has been set to $z_{\text{median}} = 0.3$.

A direct comparison of my results to the two-dimensional analysis carried out by [Hirata & Seljak \(2004\)](#) is of course not possible. However, one can draw some general, qualitative conclusions. As [Hirata & Seljak \(2004\)](#), I find that in case of a shallow survey the *II*-contributions dominate over the weak cosmic shear signal as well as the *GI*-signal. Increasing the depth of the survey the situation is reversed and lensing is the dominant contribution. This is also true for the two-dimensional power spectrum. However, as an important difference with respect to the work of [Hirata & Seljak \(2004\)](#) I find that for the deeper survey the major contamination of the weak lensing signal is not given by the *GI*-alignments but by the *II*-alignments.

Finally, I look at the shape of the full three-dimensional covariance matrices. Figure 5.4 shows from top to bottom the covariance matrices of the cosmic shear field, *II*-alignments and *GI*-alignments for multipoles $\ell = 10$ (left panel) and $\ell = 100$ (right panel), respectively. Here, only the *Euclid*-like high-redshift sample was considered. Note that not the entire k -range is shown but that the figure concentrates on the part from which the covariance matrices receive appreciable contributions. As already noted before, it is common to all three covariance matrices that the higher the multipole order the more the signal is shifted towards smaller scales. The individual shape of the matrices, however, is quite different. While the weak lensing signal is rather circular, the covariance of the *II*-alignments is elongated along the diagonal of the k -plane. This corresponds to the slow decline of the *II*-signal with increasing wavenumber, which has already been noticed during the discussion of the diagonal entries above. In contrast to this, the *GI*-contributions are much more compact. Their extent in the k -plane is several times smaller than that of the *II*-alignments. Interestingly, for $\ell = 100$ the contributions of

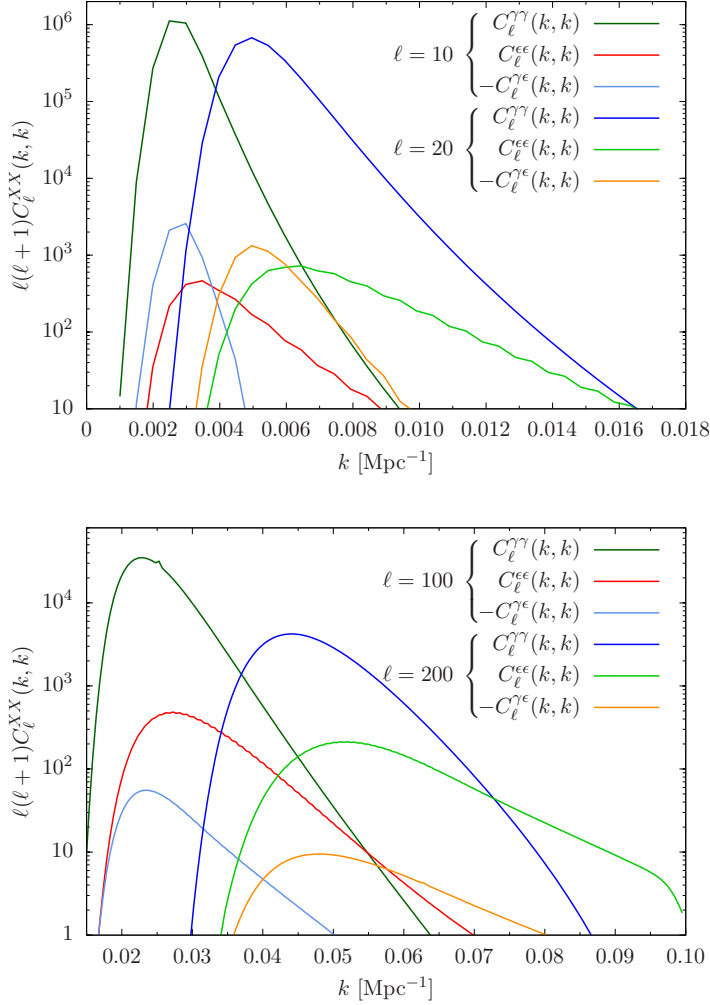


Figure 5.3: Diagonal elements of the covariance matrices of the cosmic shear field, II - and GI -alignments for the linear model. The results for the multipoles $\ell = \{10, 20\}$ (upper panel) and $\ell = \{100, 200\}$ (lower panel) are shown. In contrast to the shallow survey assumed in Figure 5.2 the median redshift has now been set to $z_{\text{median}} = 0.9$ as anticipated by the *Euclid* mission.

both alignment types are almost completely concentrated on the diagonal, whereas the shape of the cosmic shear covariance resembles that of an isosceles triangle. Especially the GI -alignments become extremely narrow in the k -plane.

These findings allow a first qualitative estimate of how intrinsic alignments may bias cosmological parameters inferred from 3d cosmic shear studies. With respect to the pure cosmic shear signal the total covariance matrix, i.e. the sum of all three matrices, would be tilted towards larger k -modes since the contributions from the II -alignments add power on smaller scales, whereas those of the GI -alignments reduce the amplitude at smaller wavenumbers. This tilt suggests that the normalization of the power spectrum σ_8 , the matter fraction Ω_m and the Hubble parameter h are particularly biased. The actual magnitude of this bias, however, is hard to predict because the effect of power enhancement and suppression is different for different multipoles.

5.4.2. Quadratic model

There are two main complications in evaluating the quadratic model numerically, the double sum in equation (5.53) and the mode coupling integral $\tilde{I}_{\ell_1 \ell_2 \ell}(k_1, k_2, k)$ defined by equation (B.5). The double sum results from the product of two gradient fields (cf. equation 5.47); the corresponding multipoles have to be considered as a kind of inner indices. Therefore, a truncation of the sum at relatively low multipoles, $\ell_{1,2} \sim \mathcal{O}(10^2)$, is not permissible. The very fact that this sum converges rather slowly casts a shadow of doubt on a numerical implementation.

The situation is further aggravated by the evaluation of the mode coupling integral $\tilde{I}_{\ell_1 \ell_2 \ell}(k_1, k_2, k)$.

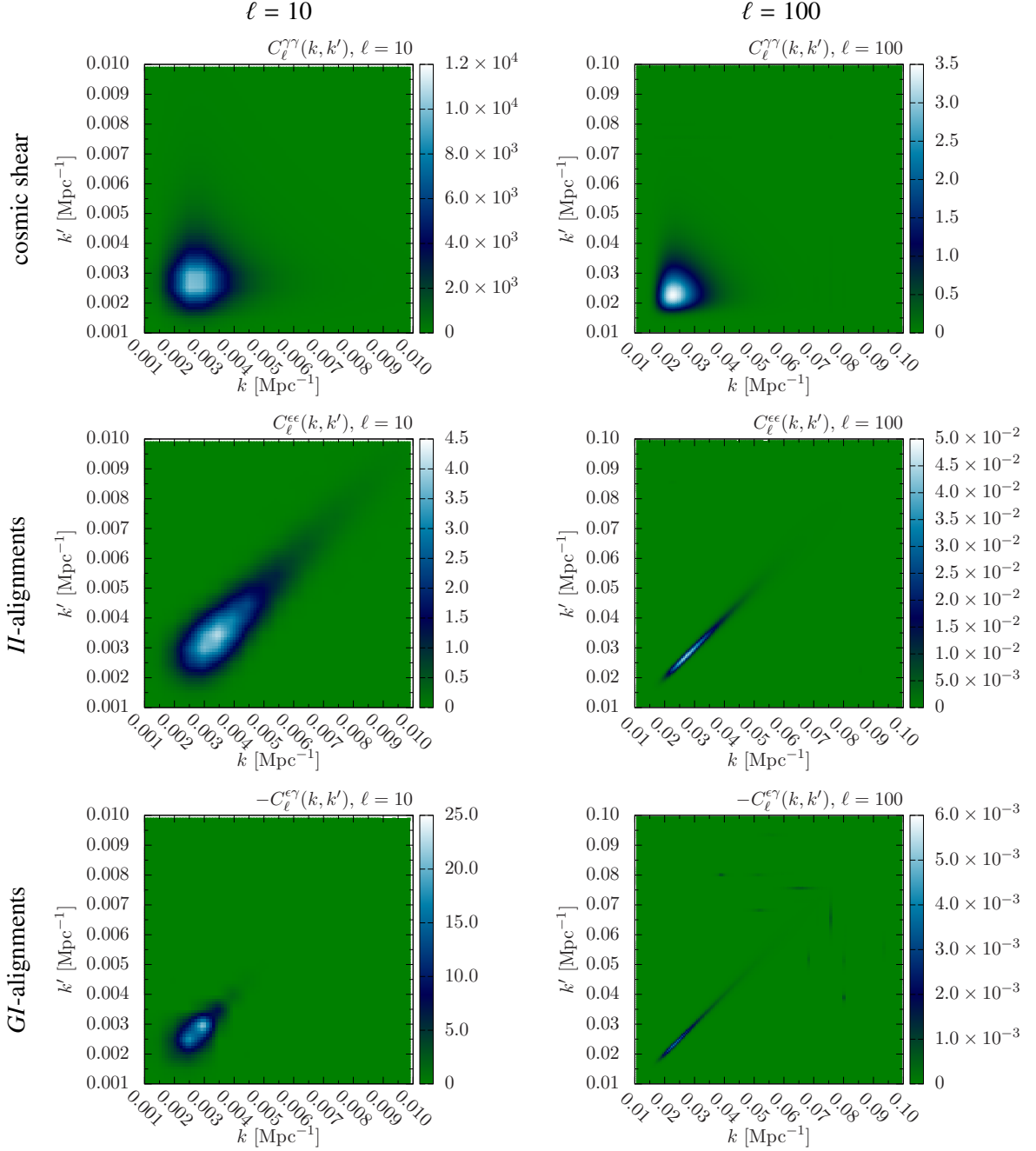


Figure 5.4.: Covariance matrices for the linear alignment model. From top to bottom: covariance of the lensing induced shear field (first row), II -alignments (second row) and GI -alignments (third row) for multipoles $\ell = 10$ (left column) and $\ell = 100$ (right column). The median redshift was chosen to be $z_{\text{median}} = 0.9$.

For large multipoles, as required by the double sum in order to converge, the computation is numerically problematic due to the oscillatory behaviour of higher-order spherical Bessel functions. This kind of integrals appears in nuclear scattering theory and analytical attempts to its evaluation exist (Mehrem et al., 1991; Mehrem & Hohenegger, 2010). These analytical expressions, however, contain multiple sums over Wigner $3j$ - and $6j$ -symbols, as well as associated Legendre functions, making the practical use for an efficient computation of a large number of these integrals quite limited. A more promising approach might be to resort to the asymptotic forms of spherical Bessel functions in the high ℓ -limit. But this obviously requires an elaborate distinction of cases since the multipoles enter

the sum of equation (5.53) in all possible combinations. Aiming at the constitutive formalism for a description of intrinsic alignments in the framework of 3d cosmic shear the explicit development of such a scheme is beyond the scope of this thesis and is reserved for future work.

5.5. Summary

I developed a formalism to incorporate the intrinsic alignment of galaxy shapes into the framework of 3d cosmic shear. For the description of the intrinsic galaxy ellipticities two different physical models were used, one linear and the other quadratic in the cosmic tidal field, respectively.

- (i) Introducing an appropriate auxiliary scalar potential, I was able to formulate the intrinsic ellipticity field for each of the two models in terms of second eth-derivatives emphasizing the spin-2 character of the ellipticity field.
- (ii) I then derived expressions for the covariance matrices of the intrinsic alignments. Both ellipticity models give rise to *II*-alignments but for Gaussian density fluctuations *GI*-alignments are only present in the linear model.
- (iii) In contrast to conventional two-dimensional weak lensing analyses, the covariance matrix of the three-dimensional shear field acquires off-diagonal elements in k -space reflecting the fact that the lensing potential is not a statistically homogeneous field. The same is true for the covariance matrices of the *II*- and *GI*-alignments. Statistical homogeneity, however, is maintained in the angular parts of the ellipticity and shear field, respectively, in case of an idealized observation with access to the full sky. As a consequence, the corresponding covariance matrices are diagonal with respect to the angular multipoles ℓ and m .
- (iv) In addition, I considered the *E/B*-mode decomposition of the ellipticity field and found that in case of the linear model the *B*-mode is identically zero. Thus, for the linear model the intrinsic ellipticities exhibit the same behaviour under parity transformations as those induced by lensing. Contrary to that, the quadratic model does possess a non-vanishing parity odd *B*-mode.
- (v) I numerically evaluated the covariance matrices of both *II*- and *GI*-alignments for the linear model and compared them to that of cosmic shear. In case of a shallow survey ($z_{\text{median}} = 0.3$) I found that for large multipoles the *II*-alignments dominate the signal underlining the fact that intrinsic alignments are a small-scale phenomenon. For a deep redshift survey like *Euclid* ($z_{\text{median}} = 0.9$), however, the lensing signal becomes dominant for all multipoles. In this case, the *II*-alignment contamination is more than one order of magnitude smaller with respect to the shear signal. Furthermore, I showed that in contrast to two-dimensional lensing studies the *GI*-contributions are only slightly enhanced, if at all, in comparison to the *II*-alignments which are the dominant contaminant on almost all scales for both survey specifications.
- (vi) Finally, I investigated the shape of the various covariance matrices in the k - k' -plane. Concentrating on a *Euclid*-like survey I found a fundamental difference between the covariance matrices of cosmic shear on the hand and of *II*- and *GI*-alignments, respectively, on the other hand. While the shape of the lensing covariance matrix is rather circular that of the intrinsic alignments is strongly elongated along the diagonal $k = k'$. For large multipoles ($\ell \sim 100$) the covariance matrices of both alignment types tend to almost completely concentrate along this diagonal.

Having established the basic formalism for a consistent treatment of the linear and quadratic alignment model in the framework of 3d weak lensing, future efforts should now be addressed to a detailed quantitative study of their impact on cosmological parameters derived from 3d cosmic shear measurements.

6

Chapter 6

The impact of intrinsic alignments for cosmic shear measurements

In this chapter the impact of intrinsic alignments for conventional two-dimensional cosmic shear measurements is considered. In particular I quantitatively investigate the bias which arises when weak lensing data are interpreted with a model which does not account for the intrinsic correlations present in the observed ellipticity field. In order to complement previous studies I concentrate on the quadratic alignment model. The parameters entering the alignment model may be inferred from observations other than galactic shape measurements avoiding marginalization over a large number of nuisance parameters. This allows for a clear distinction between statistical and systematic errors. It is found that the matter density and the normalization of the linear matter power spectrum are most severely biased, whereas the equation of state parameter of the dark energy component is almost totally unaffected. The latter result is in contrast to findings from investigations employing the linear alignment model.

The contents of this chapter have been published in [Capranico, Merkel & Schäfer \(2013\)](#).

6.1. Introduction

In the last chapter it was explained why the intrinsic alignment of galaxies is expected to bias cosmological parameters which are derived from weak lensing measurements under the null hypothesis of uncorrelated galaxy shapes. Due to the numerical complexity of 3d cosmic shear analyses the quantitative investigation of this bias is now carried out in the computationally much simpler framework of two-dimensional weak lensing. I do not employ tomographic methods but use the lensing potential in projection along the line-of-sight.

Similar studies have been carried out by [Bridle & King \(2007\)](#); [Joachimi & Bridle \(2010\)](#); [Kirk et al. \(2010, 2011, 2012\)](#), which found out that in particular the equation of state parameter of the dark energy component is severely biased. In all these studies the intrinsic shape correlations of galaxies are described by the linear alignment model. The impact of intrinsic alignments derived from the quadratic model, however, has not yet been considered and is therefore the main motivation for this part of my work.

An important aspect of angular momentum based alignment models is that their parameters may be constrained from information other than ellipticity data. The relation between the galactic angular momentum and the galaxy's shape is merely geometrically (cf. Section 5.2.2). Thus, knowledge of the statistical properties of galactic angular momenta in principle suffices to compute ellipticity correlations. For instance, the fact that galactic angular momentum can only build up if the shear tensor and the tensor of inertia are not simultaneously diagonalizable (cf. Section 4.2.6) gives rise to the angular momentum correlation model of [Lee & Pen \(2001\)](#). Here the only relevant parameter for

the angular momentum distribution is the so-called misalignment parameter. It describes the average orientation of the protohalo with respect to the tidal shear field. It may be inferred from structure formation simulations without any reference to the galactic ellipticity. In addition to that, geometrical effects like the finite thickness of any real galaxy can be captured by introducing another parameter that is then obtained from the average disc morphology of a given galaxy survey. Consequently, one is left with a two parameter model of intrinsic alignments. Both parameters have a distinct physical meaning and are complementary to ellipticity measurements. Such an ellipticity model was laid out by [Crittenden et al. \(2001\)](#).

In the following the actual computations will be carried out using the quadratic model in the form of equation (5.9). Albeit being less general than the ansatz (5.8) it is technically superior and the functional form of the resulting intrinsic ellipticity power spectra is quite similar for both approaches (cf. [Capranico et al., 2013](#)). In fact, the average misalignment of shear and inertia tensor and the disc thickness are used as physical parameters to determine the constant C_2 . It is chosen in such a way that the large-scale power of the intrinsic alignments is the same for both approaches. This is well justified by the reasonable assumption that large scales are least sensitive to the actual differences between the two approaches.

This chapter is structured as follows: In Section 6.2 several measures to describe the statistics of the intrinsic ellipticity field in comparison to the cosmic shear field are introduced. Section 6.3 is devoted to the quantitative analysis of how strong cosmological parameters are biased, when they are derived from weak lensing measurements without taking intrinsic alignments into account. Finally, the main findings of this chapter are summarized in Section 6.4.

As reference cosmology I choose a spatially flat w CDM model, which is characterized by the following set of parameters. The matter content is described by the matter density parameter $\Omega_m = 0.25$, including the small baryon fraction $\Omega_b = 0.04$. The equation of state parameter of the dark energy component is set to $w = -0.9$, while the dimensionless Hubble parameter takes the value $h = 0.72$. Finally, the primordial adiabatic density fluctuations are assumed to be scale invariant, i.e. $n_s = 1$ with a normalization given by $\sigma_8 = 0.8$.

6.2. Intrinsic ellipticity correlations

6.2.1. Angular power spectra

The starting point for the computation of the intrinsic ellipticity power spectra is the Fourier transform of equation (5.9). More precisely the Fourier transform of its E/B -mode decomposition (cf. equation 3.22) is used. As already mentioned in Section 5.3.2, II -alignments derived from the quadratic model exhibit a non-vanishing B -mode in contrast to the weak lensing field. Being quadratic in the gravitational potential, Fourier transformation of the gradient/curl-mode results in a convolution ([Mackey et al., 2002](#))

$$X(\mathbf{k}) = C_2 \int \frac{d^3 k'}{(2\pi)^3} \Phi_S(\mathbf{k}') \Phi_S(\mathbf{k} - \mathbf{k}') f_X(\mathbf{k}'_{\perp}, \mathbf{k}_{\perp} - \mathbf{k}'_{\perp}, k'_z), \quad X \in \{E, B\}. \quad (6.1)$$

Here I assume that the line-of-sight coincides with the z -axis. The entire dependence on the geometry of the wavevector configuration, which accounts for the differential structure in harmonic space, is contained in the functions f_E and f_B , respectively. As in case of the weak lensing shear field gradients along the line-of-sight are neglected (cf. Section 3.3). Thus, \mathbf{k}_{\perp} denotes a two-dimensional wavevector, i.e. $\mathbf{k}_{\perp} = (k_x, k_y)$. The explicit form of these functions is relegated to Appendix B.2. There I also discuss their symmetry properties, which can be used to simplify the (three-dimensional) power spectra. These will be computed next. The computation of the power spectra requires the evaluation of the four-point function of the Newtonian potential. This is accomplished by again invoking Wick's

theorem (A.6). The final expression reads

$$P_{XX}(k) = 2C_2^2 \int \frac{d^3k'}{(2\pi)^3} P_{\Phi\Phi}(k') P_{\Phi\Phi}(|\mathbf{k} - \mathbf{k}'|) f_X^2(\mathbf{k}'_{\perp}, \mathbf{k}_{\perp} - \mathbf{k}'_{\perp}, k'_z). \quad (6.2)$$

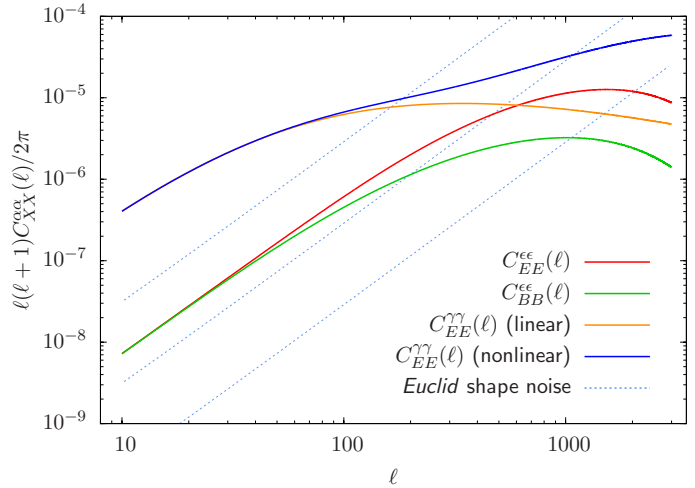
Applying Limber's equation (3.24) yields for the corresponding angular power spectra

$$C_{XX}^{\epsilon\epsilon}(\ell) = \int_0^{\chi_H} \frac{d\chi}{\chi^2} W_{\epsilon}^2(\chi) P_{XX}(\ell/\chi) \quad (6.3)$$

with the weighting function $W_{\epsilon}(\chi) = p(z) \frac{dz}{d\chi}$. The galaxy distribution is that of equation (3.29) with the parameters of a *Euclid*-like experiment: $z_0 = 0.64$, $\beta = 3/2$. Since I assume Gaussian fluctuations, *GI*-alignments are not present in the quadratic model (cf. Section 5.3.2).

The resulting power spectra are shown in Figure 6.1. I employed a Gaussian smoothing of the matter power spectrum (cf. equation 4.20) entering equation (6.2). The smoothing scale was set in such a way that galaxy size fluctuations corresponding to objects of $10^{11} M_{\odot} h^{-1}$ were filtered. The spectra of the *II*-alignments are accompanied by the cosmic shear power spectrum. The latter is shown with and without the small-scale power enhancement due to nonlinear structure growth. The functional form of gradient and curl mode of the intrinsic alignment signal is very similar. The power in the *E*-mode dominates the intrinsic alignment contributions but is about one order of magnitude smaller than the nonlinear cosmic shear signal. If nonlinear structure growth is not taken into account, the *E*-mode of the *II*-alignments even exceeds the amplitude of gravitational lensing on small scales ($\ell \sim 1000$). At even smaller scales both intrinsic alignment signals rapidly decrease due to the mass cutoff imposed. Albeit being well below the cosmic shear spectrum, the *B*-mode of the *II*-alignments may exceed the contributions of other *B*-mode sources which have been discussed in Section 5.3.2. For illustration the expected shape noise of the *Euclid* mission (cf. equation 6.11) is also plotted.

Figure 6.1: Angular power spectrum of the *E*- and *B*-mode of the intrinsic ellipticity field as obtained from the quadratic model. For comparison both, the linear and nonlinear cosmic shear power spectrum, as well as the anticipated shape noise of the *Euclid* mission (10 and 100 times amplified) are shown, too.



6.2.2. Aperture measures

In addition to the angular power spectra I compute two more measures of the intrinsic ellipticity field. Aperture measures are motivated by the fact that in an experiment correlation functions

$$\xi_{++}^{\epsilon\epsilon}(\theta) = \langle \epsilon_+(\boldsymbol{\theta}_1) \epsilon_+(\boldsymbol{\theta}_2) \rangle \quad (6.4a)$$

$$\xi_{\times\times}^{\epsilon\epsilon}(\theta) = \langle \epsilon_{\times}(\boldsymbol{\theta}_1) \epsilon_{\times}(\boldsymbol{\theta}_2) \rangle, \quad (6.4b)$$

with $\theta = |\boldsymbol{\theta}_1 - \boldsymbol{\theta}_2|$ are more readily accessible than the corresponding power spectra. Due to the different parity behaviour the cross-correlation $\xi_{\times+}^{\epsilon\epsilon}$ is identically zero. Correlation functions and power spectra

can be converted into each other according to

$$\xi_{++}^{\epsilon\epsilon}(\theta) + \xi_{\times\times}^{\epsilon\epsilon}(\theta) = \frac{1}{2\pi} \int \ell d\ell \left[C_{EE}^{\epsilon\epsilon}(\ell) + C_{BB}^{\epsilon\epsilon}(\ell) \right] J_0(\ell\theta), \quad (6.5a)$$

$$\xi_{++}^{\epsilon\epsilon}(\theta) - \xi_{\times\times}^{\epsilon\epsilon}(\theta) = \frac{1}{2\pi} \int \ell d\ell \left[C_{EE}^{\epsilon\epsilon}(\ell) - C_{BB}^{\epsilon\epsilon}(\ell) \right] J_4(\ell\theta) \quad (6.5b)$$

(e.g. Kamionkowski et al., 1998). Analogous expressions hold for the weak lensing shear field. Figure 6.2 shows the angular correlation functions of the intrinsic ellipticity field (6.4). Additionally, those of the cosmic shear field are shown, as well. For the calculation the power spectra depicted in Figure 6.1 were used. In particular, the gravitational lensing correlation functions include the small-scale power enhancement due to nonlinear structure growth. The plot suggests that the correlation length in the ellipticity field is about ten arcminutes. Noticeable differences between the two correlation functions arise on separations larger than three arcminutes.

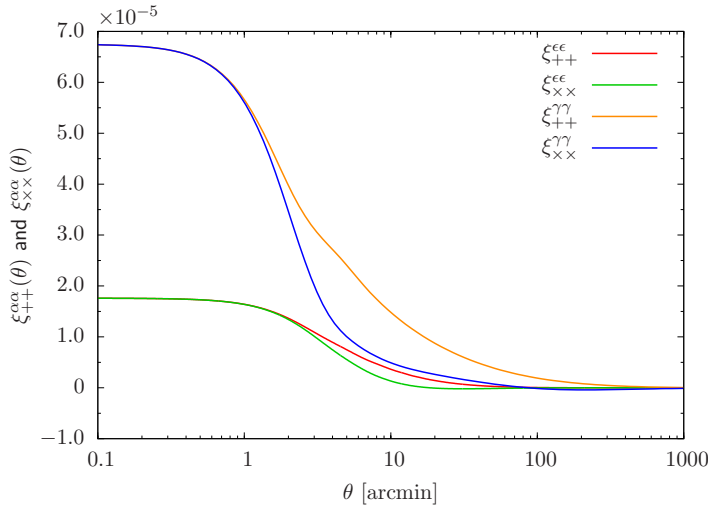


Figure 6.2: Angular correlation functions of the intrinsic ellipticity field. For comparison the corresponding quantities of the weak lensing field are shown, as well.

The Bessel functions $J_n(z)$ appearing in relation (6.5) are quite broad. Therefore, measures which filter the power spectra with a narrower function would be desirable. This motivates to introduce the variance of the shear/ellipticity field within a circular aperture of radius θ (Kaiser, 1992; Jain & Seljak, 1997)

$$\sigma_{\alpha\alpha}^2(\theta) = \frac{2}{\pi} \int \ell d\ell \left[C_{EE}^{\alpha\alpha}(\ell) + C_{BB}^{\alpha\alpha}(\ell) \right] \left[\frac{J_1(\ell\theta)}{\ell\theta} \right]^2, \quad \alpha \in \{\epsilon, \gamma\}. \quad (6.6)$$

In case of the weak lensing shear field the B -mode is zero (cf. equation 3.26) and measurements of the variance $\sigma_{\gamma\gamma}^2$ yield the filtered weak lensing angular power spectrum as desired. In contrast to this II -alignments derived from the quadratic model do exhibit a non-vanishing curl mode. Thus, a measure which allows for a separation of the signal in its E - and B -mode part would be more appropriate. One possibility is provided by the aperture mass statistics (Schneider et al., 1998, 2002; Crittenden et al., 2002)

$$M(\theta) = M_{\text{ap}}(\theta) + iM_{\perp}(\theta) = \int d^2\vartheta Q_{\theta}(\vartheta) [\epsilon_{\top}(\vartheta) + i\epsilon_{\perp}(\vartheta)], \quad (6.7)$$

with some weight function $Q_{\theta}(\vartheta)$. It is important to note that it is the *tangential* shear ϵ_{\top} , i.e. the component tangent to the centre of the aperture, which enters equation (6.7). Because of this the aperture mass $M_{\text{ap}}(\theta)$ is only sensitive to the gradient part of the signal, whereas $M_{\perp}(\theta)$ is exclusively

related to the curl part (cf. Schneider et al., 2005). Therefore I identify

$$\langle M_{\gamma\gamma}^2(\theta) \rangle = \frac{2}{\pi} \int \ell d\ell C_{EE}^{\gamma\gamma}(\ell) \left[\frac{12J_4(\ell\theta)}{(\ell\theta)^2} \right]^2, \quad (6.8a)$$

$$\langle M_{\text{ap}}^2(\theta) \rangle = \frac{2}{\pi} \int \ell d\ell C_{EE}^{\epsilon\epsilon}(\ell) \left[\frac{12J_4(\ell\theta)}{(\ell\theta)^2} \right]^2, \quad (6.8b)$$

$$\langle M_{\perp}^2(\theta) \rangle = \frac{2}{\pi} \int \ell d\ell C_{BB}^{\epsilon\epsilon}(\ell) \left[\frac{12J_4(\ell\theta)}{(\ell\theta)^2} \right]^2. \quad (6.8c)$$

Figure 6.3 gathers the aperture measures defined in equations (6.6) and (6.8). For the computation I again used the angular power spectra shown in Figure 6.1. In case of the weak lensing signal nonlinear power enhancement was taken into account. Cosmic shear therefore constitutes the dominant signal. Differences between the different intrinsic alignment contributions are less pronounced than in case of the angular power spectra (cf. Figure 6.1). This is expected since aperture measures are integrated measures which are extended over the whole multipole range. Generically, the functional form of the weighted variance (6.6) and the aperture mass (6.8) is quite different, irrespective of whether the intrinsic or lensing induced ellipticity field is considered. The weighted variance has a plateau-like structure starting to decline on an angular scale of about three arcminutes, whereas the aperture mass exhibits a rather broad peak at roughly ten arcminutes.

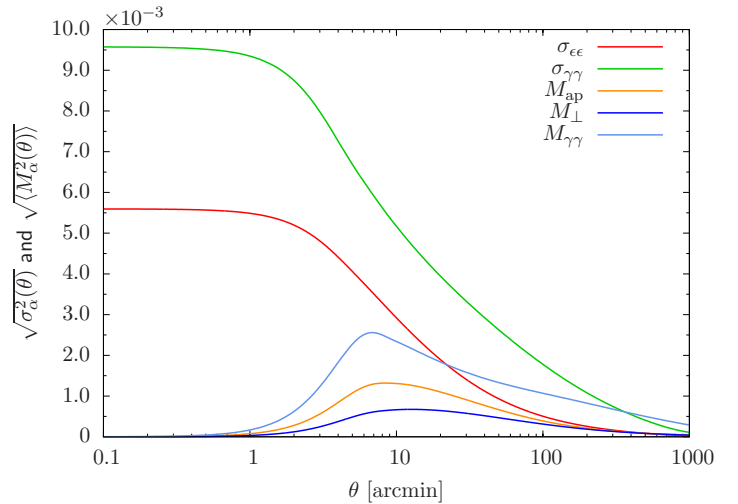


Figure 6.3: Aperture measures of the intrinsic ellipticity field. For comparison the corresponding quantities of the weak lensing field are also shown.

6.3. Interplay with cosmic shear

6.3.1. Fisher matrix

Since there are no *GI*-alignments present in the quadratic model for Gaussian density fluctuations, the angular power spectrum of the ellipticity field observed on the sky is the sum of both, the cosmic shear signal and the *II*-alignments. Interpreting this power spectrum while ignoring the contributions of the intrinsic alignments necessarily introduces a bias in the derived cosmological parameters. In the following I aim to quantify this bias. The key quantity in this analysis is the *Fisher information matrix* or just *Fisher matrix* (Tegmark et al., 1997).

Suppose the outcome of some experiment can be structured in the data vector $\mathbf{x} = (x_1, \dots, x_n)$, whereas the set of model parameters is given by the vector $\boldsymbol{\theta} = (\theta_1, \dots, \theta_m)$. The likelihood function $L(\boldsymbol{\theta}|\mathbf{x})$ then quantifies the probability of having the model (characterized by $\boldsymbol{\theta}$) given the results of the measurement (compiled in \mathbf{x}). The set of parameters which maximizes the likelihood, the *maximum likelihood (ML) estimator*, is denoted by $\hat{\boldsymbol{\theta}}$. Introducing the (negative) logarithmic likelihood

$\mathcal{L} \equiv -\log L$ for convenience, the Fisher matrix is defined as

$$F_{ij} \equiv \left\langle \frac{\partial^2 \mathcal{L}(\boldsymbol{\theta})}{\partial \theta_i \partial \theta_j} \right\rangle, \quad (6.9)$$

where the average has to be performed over the data distribution.

The power of the Fisher matrix is mainly attributed to the fact that it allows to forecast the minimal statistical error of the model parameters given their ML estimate. According to the *Cramér-Rao inequality*, the minimum standard deviation is given by $\Delta \theta_i \geq \sqrt{[\mathbf{F}^{-1}|_{\hat{\boldsymbol{\theta}}}]_{ii}}$; in the case that all parameters are estimated from the data simultaneously. If all parameters but θ_i are known, the lower error bound shrinks to $\Delta \theta_i \geq 1/\sqrt{F_{ii}|\hat{\boldsymbol{\theta}}}$ instead. Obviously, for a successful application of the Fisher matrix a functional form of the (logarithmic) likelihood, which can be treated analytically, is desirable. This is the case for Gaussian likelihoods. Gaussianity as a constraint is not too strong because one can expect that at least in the region close to its peak the likelihood is well approximated by a quadratic form. Of course, this has to be tested for every problem under consideration individually. Fortunately, in case of weak gravitational lensing, it turns out that the assumption of a Gaussian parameter likelihood is well justified (Wolz et al., 2012). The weak lensing Fisher matrix reads (see e.g. Carron et al., 2011)

$$F_{ij} = \sum_{\ell=\ell_{\min}}^{\ell_{\max}} \frac{\partial C_{EE}^{\gamma\gamma}(\ell)}{\partial \theta_i} \frac{1}{\text{cov}(\ell)} \frac{\partial C_{EE}^{\gamma\gamma}(\ell)}{\partial \theta_j}. \quad (6.10)$$

In the covariance matrix $\text{cov}(\ell)$ the small contributions from the *H*-alignments are not included. However, the shot noise as well as incomplete sky coverage are taken into account:

$$\text{cov}(\ell) = \frac{2}{2\ell + 1} \frac{1}{f_{\text{sky}}} \left(C_{EE}^{\gamma\gamma}(\ell) + \frac{\sigma_{\epsilon}^2}{n} \right)^2. \quad (6.11)$$

The *Euclid* mission is supposed to cover 50 per cent of the sky, i.e. $f_{\text{sky}} = 1/2$. The anticipated shot noise of this mission is characterized by the variance of the observed ellipticities $\sigma_{\epsilon} = 0.1$ and the galaxy number density $n = 30/\text{arcmin}^2$.

In this work I focus on the following subset of cosmological parameters $\{\Omega_m, \sigma_8, h, n_s, w\}$. The fiducial values are those given at the beginning of this chapter. It is instructive to reduce the full Fisher matrix to 2×2 matrices of parameter pairs by marginalizing over the remaining three parameters. Then the confidence regions are ellipses in the two-dimensional parameter plane. Figure 6.6 shows the 1, 2, 3 σ -ellipses for all possible parameter combinations obtained from a *Euclid*-like cosmic shear measurement, which has been carried out under the null hypothesis of absent intrinsic alignments.

6.3.2. Parameter sensitivities

In a next step I look at the sensitivity of the intrinsic ellipticity angular power spectra to the individual cosmological parameters. An appropriate measure of the sensitivity is provided by the differential change of the diagonal elements of the Fisher matrix with respect to the multipole order, i.e.

$$\frac{dF_{ii}}{d\ell} = \frac{1}{\text{cov}(\ell)} \left[\frac{\partial C_{XX}^{\epsilon\epsilon}(\ell)}{\partial \theta_i} \right]^2, \quad X \in \{E, B\}. \quad (6.12)$$

The Fisher matrix of the *H*-alignments is constructed in the very same way as the weak lensing one (6.10) replacing the corresponding power spectra in equations (6.10) and (6.11). Since I am interested in the parameter sensitivity of the intrinsic alignment signal I disregard the dominant correlations of the lensing induced ellipticities in this part of the analysis.

Figure 6.4 shows the resulting parameter sensitivities. Generically, the sensitivities increase with the multipole order until the shot noise starts dominating on small angular scales. The decline of the

sensitivities sets in later for the gradient mode signal than in the case of the curl mode, due to the smaller amplitude of the latter (cf. Figure 6.1). Conversely, the amplitude of the sensitivity is larger for the B -mode because of its smaller covariance. Both E - and B -mode angular power spectra are most sensitive to the matter density Ω_m . While the E -mode exhibits additionally a rather strong dependence on the normalization of the linear matter power spectrum σ_8 , the B -mode is much less sensitive to it. In particular, the curl mode depends more strongly on the dimensionless Hubble parameter h and the equation of state parameter of the dark energy component w , to which in turn the gradient mode is rather insensitive. This is contrary to previous studies (Bridle & King, 2007; Joachimi & Bridle, 2010; Kirk et al., 2010, 2011, 2012) which investigated the impact of intrinsic alignments derived from the linear model, in particular the influence of GI -alignments. A discussion of this discrepancy is postponed until the next section where I compute the actual biases in the cosmological parameters. There the discrepancy becomes even more apparent.

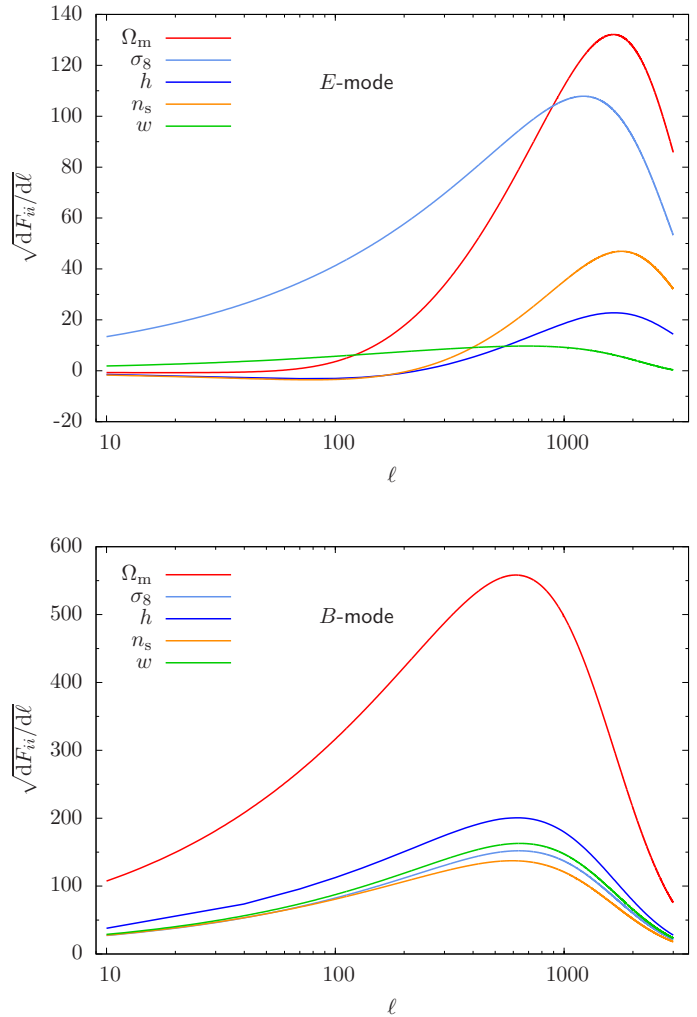


Figure 6.4: Parameter sensitivity of the intrinsic alignment angular power spectra. In the upper panel the gradient or E -mode is shown, while the lower panel contains the curl or B -mode.

6.3.3. Parameter estimation bias

Interpreting cosmic shear measurements with a model which takes intrinsic alignments into account necessarily alters the likelihood, even in the case that no additional model parameters are introduced. Accordingly, the resulting ML estimator, too, is different. In principle, this new estimator can be found from the direct evaluation of the likelihood employing for example Markov-Chain-Monte-Carlo (MCMC) methods. However in the case of Gaussian, or close to Gaussian, likelihoods an analytical approach exists which allows to compute the *bias vector*, i.e. the difference between the ML estimators

obtained for the two different models (Taburet et al., 2009). The agreement with results from MCMC methods is compelling (Taburet et al., 2010).

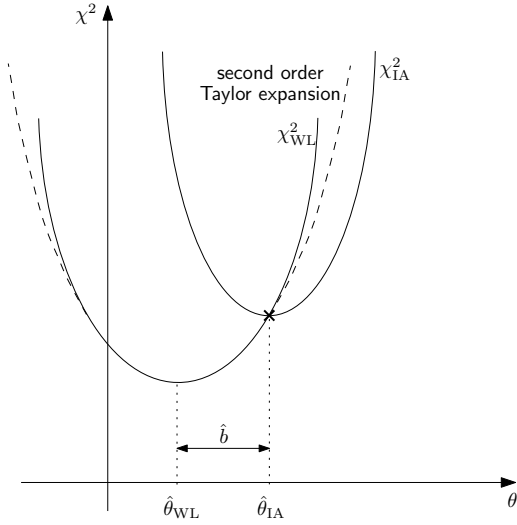


Figure 6.5.: Illustration of the analytical determination of the parameter estimation bias.

$C_{EE}^{\gamma\gamma}(\ell)|_{\hat{\theta}_{IA}} + C_{EE}^{\epsilon\epsilon}(\ell)|_{\hat{\theta}_{IA}}$. In order to establish a relation between the ML estimator for the pure weak lensing model, $\hat{\theta}_{WL}$, and that of the true model, $\hat{\theta}_{IA}$, one can Taylor expand the χ^2 -functional of the false model around the true ML estimator up to second order

$$\chi_{WL}^2(\theta) \approx \chi_{WL}^2(\hat{\theta}_{IA}) + \sum_i \left. \frac{\partial \chi_{WL}^2}{\partial \theta_i} \right|_{\hat{\theta}_{IA}} (\theta - \hat{\theta}_{IA})_i + \frac{1}{2} \sum_{i,j} \left. \frac{\partial^2 \chi_{WL}^2}{\partial \theta_i \partial \theta_j} \right|_{\hat{\theta}_{IA}} (\theta - \hat{\theta}_{IA})_i (\theta - \hat{\theta}_{IA})_j. \quad (6.14)$$

This is illustrated in Figure 6.5. The ML estimator is the set of model parameters for which the ensemble averaged χ^2 -functional becomes extremal, i.e. for which

$$\left. \frac{\partial \langle \chi_{WL}^2 \rangle}{\partial \theta_i} \right|_{\hat{\theta}_{WL}} = 0, \quad \forall \theta_i. \quad (6.15)$$

Inserting equation (6.14) then yields a system of linear equations

$$\underbrace{\left. \frac{\partial \langle \chi_{WL}^2 \rangle}{\partial \theta_i} \right|_{\hat{\theta}_{IA}}}_{\equiv a_i} = - \sum_j \underbrace{\left. \frac{\partial^2 \langle \chi_{WL}^2 \rangle}{\partial \theta_i \partial \theta_j} \right|_{\hat{\theta}_{IA}}}_{\equiv -G_{ij}} \hat{b}_j \quad (6.16)$$

which can be solved for the bias vector $\hat{\mathbf{b}} \equiv \hat{\theta}_{WL} - \hat{\theta}_{IA}$ by simple linear inversion, i.e. $\hat{\mathbf{b}} = \mathbf{G}^{-1} \mathbf{a}$. The vector \mathbf{a} and the matrix \mathbf{G} read

$$a_i = \sum_{\ell=\ell_{\min}}^{\ell_{\max}} \frac{1}{\text{cov}(\ell)} C_{EE}^{\epsilon\epsilon}(\ell) \frac{\partial C_{EE}^{\gamma\gamma}(\ell)}{\partial \theta_i}, \quad (6.17)$$

$$G_{ij} = \sum_{\ell=\ell_{\min}}^{\ell_{\max}} \frac{1}{\text{cov}(\ell)} \left[\frac{\partial C_{EE}^{\gamma\gamma}(\ell)}{\partial \theta_i} \frac{\partial C_{EE}^{\gamma\gamma}(\ell)}{\partial \theta_j} - C_{EE}^{\epsilon\epsilon}(\ell) \frac{\partial^2 C_{EE}^{\gamma\gamma}(\ell)}{\partial \theta_i \partial \theta_j} \right], \quad (6.18)$$

respectively. In case that intrinsic alignments are absent, i.e. the pure lensing model is the true model, the power spectrum of the H -alignments $C_{EE}^{\epsilon\epsilon}(\ell)$ is zero as is the vector \mathbf{a} in full agreement with the fact that then there is no parameter estimation bias.

In the following it is assumed that the likelihood is of the form $L \propto e^{-\chi^2/2}$ such that $\mathcal{L} \propto \chi^2$. Thus, the normalization is expected to be largely determined by the data and rather insensitive to the cosmological parameters. The χ^2 -functional generally reads

$$\chi^2 = \sum_{\ell=\ell_{\min}}^{\ell_{\max}} \frac{(C_{EE}^{\text{data}}(\ell) - C_{EE}^{\text{model}}(\ell))^2}{\text{cov}(\ell)}. \quad (6.13)$$

The parameter dependence only enters through the model power spectrum. The pure weak lensing model is given by $C_{EE}^{\text{model}}(\ell) = C_{EE}^{\gamma\gamma}(\ell)$, whereas the model which does take intrinsic alignments into account reads $C_{EE}^{\text{model}}(\ell) = C_{EE}^{\gamma\gamma}(\ell) + C_{EE}^{\epsilon\epsilon}(\ell)$. For the next step it is crucial to note that the angular power spectrum inferred from the data is on average $\langle C_{EE}^{\text{data}}(\ell) \rangle =$

The parameter estimation bias computed via the formalism outlined above is depicted in Figure 6.6. The bias vector is shown for all parameter pairs individually. For the computation all multipoles in the range from $\ell_{\min} = 10$ to $\ell_{\max} = 3000$ were used. The estimation bias is a systematical error. It becomes relevant if it exceeds the (minimal) statistical error, i.e. the corresponding confidence ellipses in Figure 6.6, which have been obtained from the Fisher analysis of Section 6.3.1. As already anticipated in Section 6.3.2, the biases are largest for the matter density Ω_m and the normalization of the power spectrum σ_8 . However, they exceed the 3σ -ellipses only in case of the latter. If not properly accounted for, the power of the II -alignments is erroneously attributed to the lensing signal. Since cosmic shear is directly sensitive to the universe's matter distribution projected along the line-of-sight, the additional small-scale power results in an overestimation of the matter density Ω_m . At the same time the large-scale part of the weak lensing spectrum is almost unchanged (intrinsic alignments are a small-scale phenomenon [cf. Figure 6.1]), thus a smaller fluctuation amplitude may compensate for the enhanced matter density. This explains why the sensitivity with respect to these two parameters, Ω_m and σ_8 , is strongest. However, these biases might be alleviated by including prior information from CMB experiments which provide tight constraints on both parameters, as will be discussed in Section 7.2. The spectral index n_s , the dimensionless Hubble parameter h and the dark energy equation

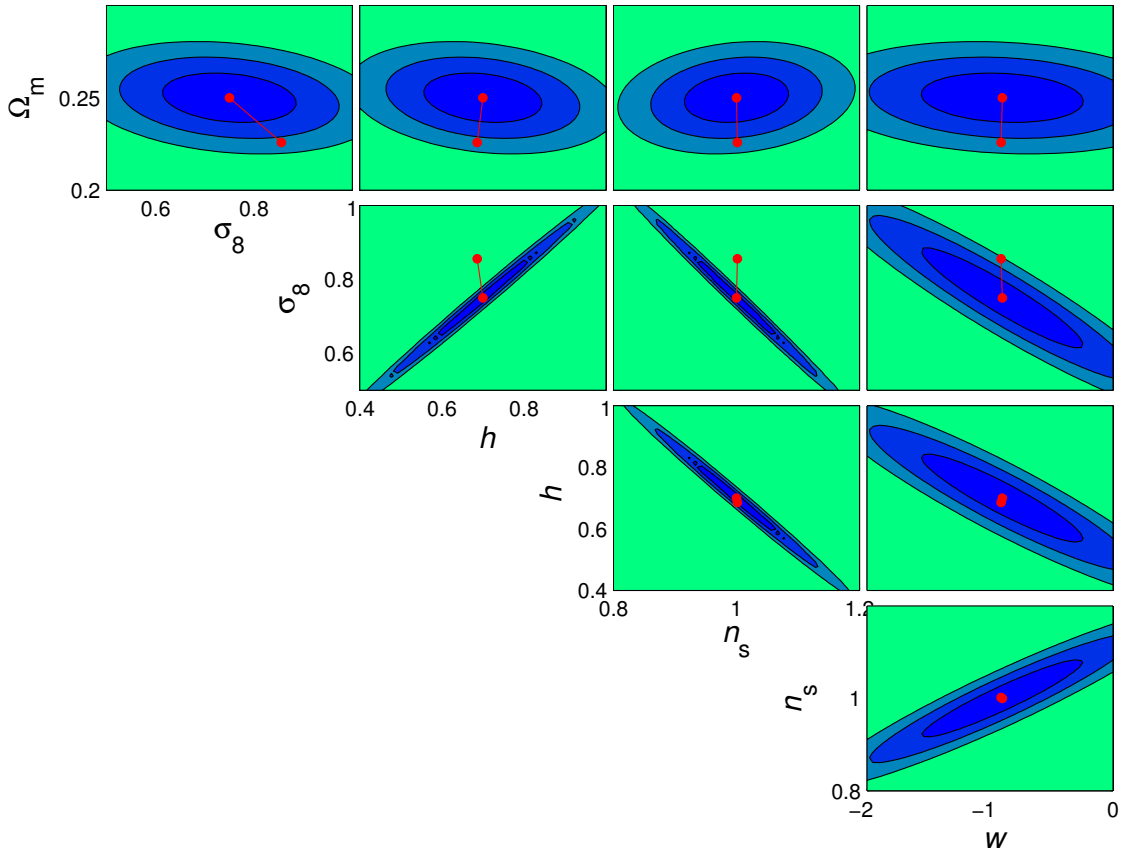


Figure 6.6.: Confidence regions for all pairs of the cosmological parameter set under consideration. The 1, 2, 3 σ -ellipses are obtained from a *Euclid*-like cosmic shear measurement which is carried out under the assumption of intrinsic alignments being absent. In addition the bias due to II -alignments, derived from the quadratic model, is shown.

of state parameter w are almost unaffected. The robustness of the latter is in some tension to previous studies (Bridle & King, 2007; Joachimi & Bridle, 2010; Kirk et al., 2010, 2011, 2012). They, however, have been carried out using exclusively the linear alignment model. Furthermore, Kirk et al. (2012) showed that the contaminating effect is crucially influenced by the concrete implementation chosen

within the class of linear alignment models (the different implementations are summarized in the appendix of Kirk et al., 2012). Therefore, most of the before mentioned studies intend to maintain the highest flexibility possible by introducing a set of nuisance parameters to account for the ignorance of the underlying intrinsic alignment signal. These additional parameters are allowed to vary in scale and redshift. Marginalizing over a sufficiently large number of nuisance parameters (more than 100), the bias can be removed at the cost of weaker constraints on the derived cosmological parameters.

The focus of my analysis was chosen differently. I concentrated on the quadratic, angular momentum based model characterized by a minimal set of physically motivated parameters, which may be inferred from observations complementary to galactic shape measurements (I converted the two physical parameters, the averaged misalignment of shear and inertia and the morphological disc thickness, into one single parameter, as explained at the beginning of this chapter). This approach is less flexible but it allows to reveal the influence of physical systematics in a much more direct way. It clearly distinguishes between statistics on the one hand and systematics on the other hand. This separation becomes more and more important in the future as the understanding of intrinsic alignments and models thereof will improve.

Another important aspect is that the quadratic alignment model is expected to be especially well suited for the description of spiral galaxies, whereas the linear model may rather be applied to ellipticals (cf. Section 5.2). Thus, any realistic morphological mix requires good knowledge and modelling of intrinsic alignments arising from both models. My analysis suggests that the investigation of the intrinsic ellipticity field derived from the quadratic model can be carried out almost independently of the dark energy equation of state parameter as opposed to the linear model. It is by no means unexpected that intrinsic alignments derived from differing alignment models predict different biases in the various cosmological parameters under consideration. Hence, my findings are not at all intended to question the results of previous works on intrinsic alignments, but rather aim to complete the description of the possible impacts of the various intrinsic alignment types on cosmic shear analyses.

6.4. Summary

The intrinsic alignment of galaxies is one of the most important systematics in cosmic shear studies. This chapter quantitatively investigated the contaminating effect of intrinsic shape correlations computed in the framework of the quadratic model (5.9). Since this model is rather geometrical and therefore closely related to the theory of galactic angular momenta, its parameters need not to be determined from the cosmic shear data set. This complementarity facilitates the separation of systematical and statistical error sources. The main findings can be summarized as follows.

- (i) I computed the angular power spectrum of the II -alignments. Working under the assumption that the cosmic density fluctuations are Gaussian, the quadratic model gives no rise to GI -alignments. However, it does exhibit a non-vanishing B -mode in contrast to weak lensing. Gradient and curl mode of the II -alignments have the same functional form, but the E -mode starts dominating on the sub-degree scale. For a *Euclid*-like survey the signal of the II -alignments stays below that of cosmic shear on all scales provided that the enhancement of small-scale power in the lensing field due to nonlinear structure growth is taken into account. In this case the difference between cosmic shear and II -alignment signal amounts to one order of magnitude.
- (ii) In addition to the angular power spectrum I computed several real space measures of the intrinsic ellipticity field statistics. As in case of the spectra aperture measures are dominated by the cosmic shear signal.
- (iii) Investigating the parameter sensitivity of the intrinsic alignment power spectra I found that both are particularly influenced by the total matter density Ω_m . The gradient mode is also appreciably sensitive to the normalization of the linear matter power spectrum σ_8 , while its dependence on

the spectral index n_s , the dimensionless Hubble parameter h and the dark energy equation of state parameter w is rather weak. The curl mode behaves differently. In comparison to the impact of the matter density Ω_m it is more or less insensitive to the other cosmological parameters under consideration.

- (iv) In accordance with the parameter sensitivity of the E -mode of the II -alignments the estimation of the matter density Ω_m and the power spectrum normalization σ_8 is most strongly biased if intrinsic alignments are not accounted for in cosmic shear measurements. The biases, however, hardly exceed the 3σ -confidence regions.
- (v) The indifference of the estimated dark energy equation of state parameter with respect to the presence of intrinsic alignments is a peculiarity of the quadratic model. The linear alignment model exhibits the very opposite behaviour.

The last point especially highlights the importance of a deeper understanding of the physical mechanisms of intrinsic alignments. Correct modelling of intrinsic shape correlations and reliable control of the resulting systematics are the decisive steps towards a successful exploitation of the full power of future cosmic shear measurements.

7

Chapter 7

The Cosmic Microwave Background

The contemporary picture of the Universe is largely based on results from observations of the cosmic microwave background (CMB). In this chapter I briefly compile the most important aspects of the CMB which alleviate the understanding of the two subsequent chapters. Special emphasis is put on two of its secondary anisotropies: *weak gravitational lensing* and the *integrated Sachs-Wolfe effect*, respectively. Beside the seminal work of [Seljak & Zaldarriaga \(1996\)](#) I would like to refer to the book of [Durrer \(2008\)](#) which covers all aspects of CMB physics in great detail.

7.1. The Cosmic Microwave Background

After Big Bang nucleosynthesis, when the first light elements had formed, the Universe was so hot and dense that all elements were ionized. Nuclei, electrons and photons formed a plasma which was kept in thermal equilibrium by photons Thomson scattering off free electrons. In the course of its expansion the Universe cooled and ionized helium and hydrogen nuclei were able to capture free electrons becoming electrically neutral. This process is called *recombination* and occurred when the Universe was approximately 400 000 years old. The Universe became transparent and baryons and photons decoupled. Since then CMB photons pervade the whole Universe with almost no further interaction, carrying detailed information about the physical conditions of the early Universe. Helium recombination alone, which naturally set in first, did not suffice to render the Universe transparent but it significantly changes the sound speed in the photon-baryon plasma. The contributions of the trace amounts of the other light elements, lithium and beryllium, can be safely neglected.

The spectrum of the photons at recombination is expected to be Planckian. The photons had been in thermal equilibrium with the, according to the cosmological principle (see Section 2.1), homogeneously and isotropically distributed baryons. Consequently, the spectrum had the form of a blackbody with temperature T

$$I(\nu, T) = \frac{2h}{c^2} \frac{\nu^3}{e^{h\nu/k_B T} - 1}, \quad (7.1)$$

where ν denotes the frequency of the emitted radiation, while h and k_B is the Planck and Boltzmann constant, respectively ([Rybicki & Lightman, 2004](#)). Although thermal equilibrium was not sustained after decoupling, the shape of the spectrum did not change. It remained Planckian with an effective temperature $T_0 = a_{\text{rec}} T_{\text{rec}}$. The temperature of recombination T_{rec} can be estimated using Saha's equation. It accounts for the huge photon-to-baryon ratio which delays recombination considerably. One finds $k_B T_{\text{rec}} \sim 0.3 \text{ eV}$, rather than $k_B T_{\text{rec}} \sim 13.6 \text{ eV}$, as suggested by the ionization potential of hydrogen. Since $a_{\text{rec}} \sim 10^{-3}$, the effective temperature observed today is expected to be $T_0 \sim 3 \text{ K}$. Hence, the corresponding spectrum should peak in the microwave band. It was first detected, though accidentally, by [Penzias & Wilson \(1965\)](#). More than 25 years latter the *FIRAS* instrument of the

COBE satellite measured the spectrum over a wide wavelength range finding it in perfect agreement with that of a blackbody with an effective temperature of

$$T_0 = (2.7260 \pm 0.0013) \text{ K} \quad (7.2)$$

(Fixsen, 2009). This level of agreement puts tight constraints on possible energy releases in the early Universe. The corresponding spectral distortions may be characterized by a non-vanishing chemical potential μ and the optical depth to free-free emission Y_{ff} . The current limits are $\mu < 9 \times 10^{-5}$ and $8 \times 10^{-8} < Y_{\text{ff}} < 1.9 \times 10^{-5}$ (Bersanelli et al., 1994; Fixsen et al., 1996; Haiman & Loeb, 1997). For a more recent discussion including the results of the *ARCADE 2* instrument I refer to Seiffert et al. (2011).

7.1.1. Primary CMB anisotropies

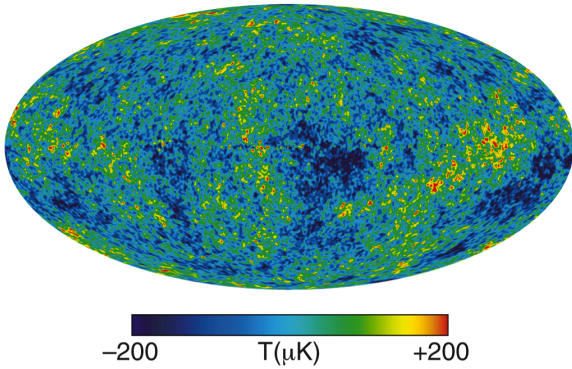


Figure 7.1.: All sky map of the CMB temperature fluctuations as measured by the *WMAP* satellite (Bennett, C. L. et al., 2012).

In Section 2.4 inhomogeneities in the cosmic density field have been discussed. They, or rather the corresponding perturbations in the gravitational potential, are necessarily imprinted on the CMB, too. Since decoupling happened that early, $z_{\text{rec}} \sim 1100$, perturbations in the gravitational potential have only grown slightly and fluctuations in the CMB temperature are tiny. They are at the level of one part in 100 000 as can be seen in Figure 7.1. Additionally, there do exist mK fluctuations resulting from the fact that the Earth is not perfectly comoving with the CMB. This dipole anisotropy, however, is of minor cosmological interest because it does not convey any information about the Universe at large. Measurements of it can be used to determine the Earth's velocity v_{\oplus} in the CMB rest frame. Fixsen & Mather (2002) found it to be

$$v_{\oplus} = (372 \pm 1) \text{ km s}^{-1}. \quad (7.3)$$

The quadrupole and all higher-order anisotropies do not depend on the observer's velocity.

The most important time scale in the discussion of these fluctuations is set by the mean free time of Thomson scattering τ_{T} , which is given in terms of the Thomson cross section σ_{T} , the number density of free electrons n_e and the speed of light c

$$\tau_{\text{T}} = \frac{1}{\sigma_{\text{T}} n_e c}. \quad (7.4)$$

In principle, the interaction between electrons and photons is described by Compton scattering. However, to good accuracy, the electrons can be taken to be non-relativistic and a description in the classical limit of Thomson scattering is appropriate. Due to the fact that Thomson scattering depends on the polarization of the incident radiation it results in a net *linear* polarization of CMB photons in the course of decoupling. Its degree of polarization accounts for about ten percent of the total intensity.

Well before recombination, the mean free time was much shorter than the expansion rate, i.e. $\tau_{\text{T}} \ll 1/H$. Consequently, Thomson scattering was sufficiently efficient to keep photons and electrons in thermal equilibrium. Photons were *tightly coupled* to the baryon fluid but not to the dark matter component. The tightly coupled baryon-photon fluid was compressed in the gravitational wells of the dark matter overdensities until gravity was balanced by the increasing pressure of the fluid, mainly the radiation pressure of the photons. Then the fluid began to expand again, thereby decreasing the

pressure and the process restarted. The result were sound waves or acoustic oscillations, respectively, in the baryon-photon fluid.

The coupling between the photons and baryons, however, was not perfect and therefore diffusion between the two components took place. *Silk damping* erased temperature fluctuations quite efficiently on scales smaller than the diffusion length. This effect was further enhanced by the finite duration of recombination which increased the damping length. In fact, recombination can only be considered to happen instantaneously on large angular scales. On small scales the finite thickness of the last scattering surface needs to be taken into account.

According to equation (7.4), the tremendous decrease in the number density of free electrons after recombination provoked a mean free time which by far exceeded the Hubble rate, $\tau_T \gg 1/H$. Thus, once decoupled from the baryons, the photons travelled without almost no further scattering. Most importantly, this *free streaming* of photons left the observable angular anisotropies in the temperature unchanged. Free streaming ended when the Universe started to reionize in the course of early structure formation at redshift $z_{\text{ion}} \sim 10 - 40$. Due to rescattering off free electrons photons originating from intrinsically uncorrelated temperature fluctuations intermingled and the statistical properties of the temperature fluctuations are tampered. While in case of the CMB temperature this is a small-scale effect, reionization affects the large-scale fluctuations of the polarization. This complementarity can be used to remove the reionization effect.

7.2. The CMB power spectrum

At the time of recombination the perturbations in the cosmic density field, imprinted in the tiny fluctuations of the CMB temperature, evolved linearly and thus preserved the statistical properties of the inflationary initial conditions. Accordingly, the fluctuation statistics of the CMB is identical to the primordial one. Observations of the CMB are therefore one of the most important tools in the investigation of inflationary models of the Universe. The autocorrelation function of the temperature fluctuations can be used to test the hypothesis of a scale invariant primordial power spectrum. Higher order statistics reveal possible deviations from Gaussianity helping to discriminate between different scenarios of inflation.

In analogy to perturbations in the matter content (2.27) one introduces the *temperature contrast*

$$\Theta(\hat{\mathbf{n}}) \equiv \frac{T(\hat{\mathbf{n}}) - T_0}{T_0}, \quad (7.5)$$

observed in the direction $\hat{\mathbf{n}}$. In contrast to the cosmic density the CMB is a field on the (unit) sphere rather than in three-dimensional space. Since it is extended over the whole sky, a precise description must take its curvature into account. The autocorrelation function of the density contrast then reads

$$\xi(\beta) = \langle \Theta(\hat{\mathbf{n}})\Theta(\hat{\mathbf{n}}') \rangle. \quad (7.6)$$

Here the cosmological principle (see Section 2.1), which enforces statistical homogeneity and isotropy, is manifest in the fact that the correlator only depends on the angle $\cos\beta = \hat{\mathbf{n}} \cdot \hat{\mathbf{n}}'$. In case of the density contrast the power spectrum has been introduced as the Fourier transform of the (spatial) correlation function (cf. equation 2.52). For the CMB temperature a decomposition in terms of Legendre polynomials $P_\ell(\mu)$ (Arfken & Weber, 2005) instead of plane waves proves more advantageous

$$\xi(\beta) = \frac{1}{4\pi} \sum_{\ell} (2\ell + 1) C_{\ell}^{\Theta\Theta} P_{\ell}(\cos\beta) \quad \longleftrightarrow \quad C_{\ell}^{\Theta\Theta} = 2\pi \int_{-1}^1 d\cos\beta \xi(\beta) P_{\ell}(\cos\beta). \quad (7.7)$$

The expansion coefficients $C_{\ell}^{\Theta\Theta}$ define the *angular power spectrum* of the CMB temperature fluctuations. The analogy with the three-dimensional power spectrum becomes more apparent if one

considers the harmonic space representation of the temperature contrast, i.e. its expansion in terms of spherical harmonics

$$\Theta(\hat{\mathbf{n}}) = \sum_{\ell,m} \Theta_{\ell m} Y_{\ell m}(\hat{\mathbf{n}}) \longleftrightarrow \Theta_{\ell m} = \int d\hat{\mathbf{n}} \Theta(\hat{\mathbf{n}}) Y_{\ell m}^*(\hat{\mathbf{n}}). \quad (7.8)$$

Reformulating the correlation function (7.6) in terms of this expansion one finds the following equality

$$\sum_{\ell,\ell',m,m'} \langle \Theta_{\ell m} \Theta_{\ell' m'}^* \rangle Y_{\ell m}(\hat{\mathbf{n}}) Y_{\ell' m'}^*(\hat{\mathbf{n}}') \stackrel{!}{=} \frac{1}{4\pi} \sum_{\ell} (2\ell + 1) C_{\ell}^{\Theta\Theta} P_{\ell}(\cos\beta) = \sum_{\ell,m} C_{\ell}^{\Theta\Theta} Y_{\ell m}(\hat{\mathbf{n}}) Y_{\ell m}^*(\hat{\mathbf{n}}'), \quad (7.9)$$

where in the last step the addition theorem of spherical harmonics (Arfken & Weber, 2005)

$$\sum_m Y_{\ell m}(\hat{\mathbf{n}}) Y_{\ell m}^*(\hat{\mathbf{n}}') = \frac{2\ell + 1}{4\pi} P_{\ell}(\cos\beta) \quad (7.10)$$

has been inserted. Exploiting the orthonormality relation of the spherical harmonics twice one finally gets the desired relation for the angular power spectrum in multipole space

$$\langle \Theta_{\ell m} \Theta_{\ell' m'}^* \rangle = C_{\ell}^{\Theta\Theta} \delta_{\ell\ell'} \delta_{mm'}. \quad (7.11)$$

Different multipoles of the temperature fluctuations are thus uncorrelated. This is one more manifestation of statistical homogeneity and isotropy. The power spectrum of the observed CMB, i.e. of one particular realization, is estimated by

$$\hat{C}_{\ell}^{\Theta\Theta} = \frac{1}{2\ell + 1} \sum_m |\Theta_{\ell m}|^2. \quad (7.12)$$

By the law of large numbers this estimator is limited by *cosmic variance* $\Delta C_{\ell}^{\Theta\Theta} \simeq (2\ell + 1)^{-1/2} C_{\ell}^{\Theta\Theta}$ even in the case of an ideal experiment due to the finite number of multipoles available.

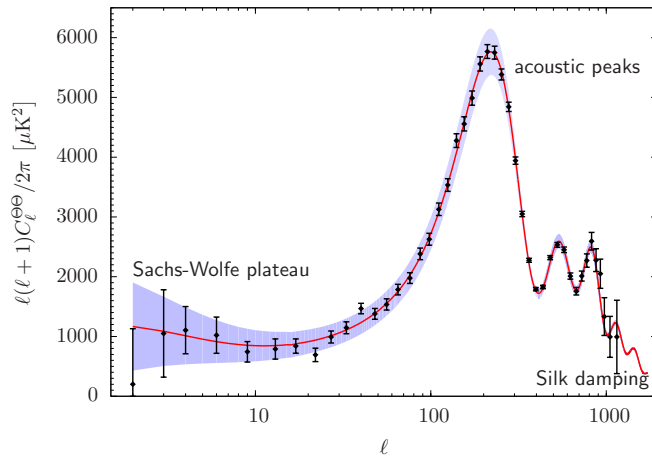


Figure 7.2.: CMB temperature power spectrum. The black data points represent the *WMAP* seven-year measurements along with an estimate of their uncertainty. The red curve is the best-fitting Λ CDM model, while the blue shaded band indicates cosmic variance (data taken from Larson, D. et al., 2011).

spectrum of large-scale potential fluctuations, however, is almost scale invariant (cf. Section 2.4.3) and so is the angular power spectrum of the CMB temperature. In the acoustic regime, $100 \lesssim \ell \lesssim 1000$, a harmonic series of peaks corresponds to the phases of sound waves in the photon-baryon plasma which were frozen in at decoupling. Finally, on small angular scales, $\ell \gtrsim 1000$, the fluctuations are almost completely wiped out by Silk damping.

In Figure 7.2 the CMB temperature power spectrum measured by *WMAP* along with the theoretical power spectrum obtained for the seven-year Λ CDM *WMAP*+BAO+ H_0 best-fitting parameters compiled in Table 2.1 is shown. Looking at Figure 7.2 one recognizes several characteristic features. They can be split in three distinct branches which reflect the physical processes, most of which have already been described in Section 7.1.1. The first part of the spectrum, $\ell \lesssim 100$, the Sachs-Wolfe plateau, is featureless. The corresponding angular scales exceeded the sound horizon at decoupling and the temperature fluctuations were solely determined by the perturbations in the gravitational potential as will be detailed in Section 7.4. The spectrum of large-scale potential fluctuations, however, is almost scale invariant (cf. Section 2.4.3) and so is the angular power spectrum of the CMB temperature. In the acoustic regime, $100 \lesssim \ell \lesssim 1000$, a harmonic series of peaks corresponds to the phases of sound waves in the photon-baryon plasma which were frozen in at decoupling. Finally, on small angular scales, $\ell \gtrsim 1000$, the fluctuations are almost completely wiped out by Silk damping.

The careful quantitative investigation of the CMB temperature power spectrum allows to derive powerful constraints on cosmological parameters. While the plateau carries information about the primordial fluctuation amplitude and the spectral index, the location of the first acoustic peak may serve as a standard ruler. Its location is strongly related to the sound horizon at recombination which is supposed to be known to high accuracy. Thus, the geometry of the Universe can be probed by means of the angular diameter distance (2.23). The height of the first two peaks is sensitive to the density of baryonic, as well as dark matter. Parameter degeneracies can be broken by exploiting the complementary information contained in the polarization power spectrum. A sufficiently accurate measurement of the latter will be provided by *Planck* for the first time.

7.3. CMB lensing

7.3.1. Secondary CMB anisotropies

In Chapter 3 I discussed how photon propagation is influenced by the intervening large-scale structure, as well as by the geometry of the homogeneous background. These effects also apply to CMB photons emanating from the last scattering surface. Gravitational lensing thus introduces *secondary anisotropies* in the CMB. An excellent review of CMB lensing is given by [Lewis & Challinor \(2006\)](#).

A good knowledge of secondary anisotropies is important in order to avoid confusion with the primordial ones present at recombination. The latter contain most valuable information on cosmological parameters (see the end of the previous section) which might be corrupted if secondary anisotropies are not properly accounted for. Conversely, a deep understanding and control of secondary anisotropies may allow to exploit them as an additional source of information. How this can be done in case of CMB lensing will be detailed in Chapter 8, whereas the importance of the *integrated Sachs-Wolfe (iSW) effect*, to be introduced in the next section, will become clear in Chapter 9. Apart from lensing and the iSW effect I would like to briefly mention the *Sunyaev-Zel'dovich (SZ) effect* ([Sunyaev & Zel'dovich, 1972](#)). On average, inverse Compton scattering off free electrons along the line-of-sight blueshifts CMB photons traversing the hot intracluster medium. The associated change in the photon spectrum is unique and therefore a viable tool in the detection of galaxy clusters. Additionally, there is the kinetic SZ effect which is due to the bulk motion of the cluster as a whole. In contrast to the thermal SZ effect, the kinetic SZ effect leaves the photon spectrum Planckian. Finally, the observation of both, primary and secondary anisotropies, is hindered by galactic foreground emissions which are superimposed on the CMB and need to be carefully removed from any observational CMB data. An overview of secondary CMB anisotropies is provided by [Aghanim et al. \(2008\)](#).

7.3.2. Power spectrum of the lensed CMB

Gravitational deflection of CMB photons is a *weak lensing* phenomenon as can be seen by the following estimate given in [Lewis & Challinor \(2006\)](#). The typical deflection of a single large-scale structure lens is of the order $\delta\alpha \sim 10^{-4}$ rad. The coherence length of the deflecting Newtonian gravitational potential is about 300 Mpc on average. Consequently, CMB photons encounter roughly 50 lenses on their way from the last scattering surface (located at a comoving distance of approximately 14 000 Mpc). Assuming that individual deflections are uncorrelated, the total deflection is $\delta\alpha_{\text{tot}} \sim \sqrt{50} \times \delta\alpha \sim 2$ arcmin. Thus, a treatment in the framework of weak lensing is well applicable.

Due to the fact that gravitational lensing conserves the surface brightness of the source, the lensing effect is captured by the simple remapping

$$\tilde{\Theta}(\hat{n}) = \Theta(\hat{n} + \alpha), \quad (7.13)$$

where the deflection angle α is defined in equation (3.17) with the upper integration bound set to be the comoving distance to the last scattering surface, i.e. $\chi_s = \chi_{\text{rec}}$. Lensed quantities will be denoted by a

tilde. Equation (7.13) is rather symbolic. It can be taken literally only in case of a flat sky. Neglecting the sky curvature, however, is inappropriate. The angular coherence length of a typical gravitational well is about 2° , which is much larger than the size of an individual deflection and comparable to the angular scale of the acoustic peaks. This indicates that for an accurate description the curvature of the celestial sphere has to be taken into account (Hu, 2000; Challinor & Lewis, 2005). The concepts of CMB lensing, however, are much more readily accessed in the flat-sky approximation. Therefore, the main part of the following presentation will content itself with a flat sky. Curvature effects become important for CMB experiments approaching the cosmic variance limit and are below the sensitivity of *Planck* (Challinor & Lewis, 2005).

Equation (7.13) suggests that the lensing effect might be accessed by a Taylor expansion in the deflection angle which has been shown to be small at the beginning of this section. But it turns out that a series expansion breaks down the latest at scales of a few arcminutes. Here the deflections start being of the same size as the structures in the unlensed CMB. Therefore, the non-perturbative approach of Seljak (1996a) is preferable. It starts with the correlation function of the lensed temperature contrast

$$\tilde{\xi}(r) = \langle \tilde{\Theta}(\mathbf{x}) \tilde{\Theta}(\mathbf{x}') \rangle = \langle \Theta[\mathbf{x} + \boldsymbol{\alpha}(\mathbf{x})] \Theta[\mathbf{x}' + \boldsymbol{\alpha}(\mathbf{x}')] \rangle, \quad (7.14)$$

with $r = |\mathbf{x} - \mathbf{x}'|$. Since sky-curvature is neglected, angular positions are represented by two-dimensional vectors and harmonic space is spanned by conventional Fourier modes:

$$\tilde{\xi}(r) = \int \frac{d^2\ell}{2\pi} \int \frac{d^2\ell'}{2\pi} \langle \Theta(\boldsymbol{\ell}) \Theta^*(\boldsymbol{\ell}') \rangle_{\Theta} \langle e^{i[\boldsymbol{\ell} \cdot (\mathbf{x} + \boldsymbol{\alpha}) - \boldsymbol{\ell}' \cdot (\mathbf{x}' + \boldsymbol{\alpha}')] } \rangle_{\alpha} = \int \frac{d^2\ell}{(2\pi)^2} C_{\ell}^{\Theta\Theta} e^{i\boldsymbol{\ell} \cdot \mathbf{r}} \langle e^{i\boldsymbol{\ell} \cdot (\boldsymbol{\alpha} - \boldsymbol{\alpha}') } \rangle_{\alpha}. \quad (7.15)$$

A separate evaluation of the average over CMB temperature fluctuations $\langle \dots \rangle_{\Theta}$ and deflection angles $\langle \dots \rangle_{\alpha}$ is permissible because their correlation, due to the iSW effect (cf. Section 7.4), is weak. It is interesting to note that the lensed correlation function (7.15) depends on the *difference* of the deflection angles involved, highlighting that absolute deflection angles are unobservable, as already mentioned in Section 3.2. The remaining average in equation (7.15) can be expressed in terms of the lensing potential power spectrum $C_{\ell}^{\phi\phi}$

$$\langle e^{i\boldsymbol{\ell} \cdot (\boldsymbol{\alpha} - \boldsymbol{\alpha}') } \rangle_{\alpha} = \exp\left(-\frac{1}{2}\ell^2 \left[\sigma^2(r) + \cos 2(\varphi_{\ell} - \varphi_r) C_{\text{gl},2}(r)\right]\right), \quad (7.16)$$

with $\sigma^2(r) = C_{\text{gl},0}(0) - C_{\text{gl},0}(r)$ and

$$C_{\text{gl},n}(r) = \frac{1}{2\pi} \int d\ell \ell^3 C_{\ell}^{\phi\phi} J_n(\ell r). \quad (7.17)$$

Equation (7.16) is exact only if the distribution of the deflection angles follows a Gaussian. The validity of this assumption was verified by Carbone et al. (2009) and Merkel & Schäfer (2011). Instead of using the full expression (7.16) in the evaluation of the lensed correlation function (7.15) an expansion in powers of $C_{\text{gl},2}(r)$, which is small in comparison to $\sigma^2(r)$, keeping quadratic terms, suffices (Challinor & Lewis, 2005)

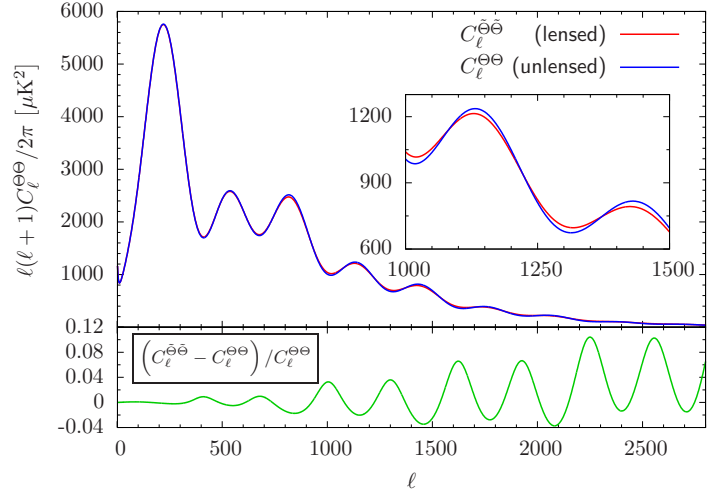
$$\tilde{\xi}(r) \approx \frac{1}{2\pi} \int d\ell \ell C_{\ell}^{\Theta\Theta} e^{-\ell^2 \sigma^2(r)/2} \left[\left(1 + \frac{1}{16} \ell^4 C_{\text{gl},2}^2(r)\right) J_0(\ell r) + \frac{1}{2} \ell^2 C_{\text{gl},2}(r) J_2(\ell r) + \frac{1}{16} \ell^4 C_{\text{gl},2}(r) J_4(\ell r) \right]. \quad (7.18)$$

As before, integrations over the polar angles $\varphi_{\ell,r}$ of the vectors $\boldsymbol{\ell}$ and \mathbf{r} , respectively, have been expressed by Bessel functions $J_n(z)$ of n th order (Abramowitz & Stegun, 1972). Analogous expressions for the lensed CMB polarization field and its cross-correlation with the temperature exist (Zaldarriaga & Seljak, 1998; Challinor & Lewis, 2005). The lensed power spectrum can then be obtained by equation (7.7) which becomes in the flat-sky limit

$$C_{\ell}^{\tilde{\Theta}\tilde{\Theta}} = 2\pi \int dr r \tilde{\xi}(r) J_0(\ell r). \quad (7.19)$$

In the upper panel of Figure 7.3 both, the fiducial and the lensed CMB temperature power spectrum, for the cosmological parameters in Table 2.1 are shown. The relative difference is plotted in the lower panel. Since gravitational lensing conserves surface brightness, it does not create additional structures in the power spectrum. In particular, lensing leaves the scale invariant Sachs-Wolfe plateau unchanged but it becomes observable by the acoustic peaks and the damping tail. The peaks are smoothed, whereas the power in the Silk damping part of the spectrum is increased.

Figure 7.3: Lensed and unlensed CMB temperature power spectrum (upper panel). The relative difference between these two spectra is shown in the lower panel.



7.4. The integrated Sachs-Wolfe effect

Section 7.2 showed that the CMB temperature power spectrum is almost scale-invariant on large scales. Now I would like to discuss the physical origin of this plateau more extensively. I thereby follow to some extent [Amendola & Tsujikawa \(2010\)](#).

Fluctuations in the CMB temperature, observed on the sky, are related to perturbations in the observed photon frequency via

$$\frac{\delta T}{T}\Big|_0 = \frac{\delta T}{T}\Big|_{\text{rec}} + \frac{\delta \langle k, u \rangle}{\langle k, u \rangle}\Big|_0 - \frac{\delta \langle k, u \rangle}{\langle k, u \rangle}\Big|_{\text{rec}}. \quad (7.20)$$

The measured photon frequency, or equivalently its energy, is determined by the projection of the photon four-momentum k onto the four-velocity of the observer u . Therefore, perturbations in both quantities have to be taken into account. The spatial part of the perturbed four-velocity is simply given by the (comoving) peculiar velocity $a\mathbf{u} = \mathbf{v}$, while the time component is proportional to the Newtonian potential, i.e. $\delta u^0 \sim \Phi$, reflecting the gravitational time delay. With this the relative perturbation in the observed frequency can be worked out to be

$$\frac{\delta \langle k, u \rangle}{\langle k, u \rangle} = \frac{\delta(k^\mu u_\mu)}{k^0 u_0} = \frac{\delta k^0}{k^0} + \frac{\Phi}{c^2} - \frac{k^i v_i}{k^0 c}. \quad (7.21)$$

The last term, the projection of the peculiar velocity onto the propagation direction of the photon, gives rise to a Doppler shift in the temperature. This is the source term of the previously discussed dipole anisotropy.

Below, it will be shown that the time-independent part of the relative shift in the photon energy $\delta k^0/k^0$ is given by $-2\Phi/c^2$. Since the Newtonian potential is independent of the photon direction, this term, along with the second term in equation (7.21), has to be accounted for only at the last scattering surface. The contributions of both to the CMB anisotropies were pointed out first by [Sachs & Wolfe \(1967\)](#). Due to the fact that the intrinsic large-scale temperature fluctuations are proportional to

the gravitational potential, too, one commonly refers to the combination of all three terms as (ordinary) *Sachs-Wolfe effect*

$$\left(\frac{\delta T}{T}\right)_{\text{SW}} = \frac{\delta T}{T}\Big|_{\text{rec}} + \frac{\Phi}{c^2}\Big|_{\text{rec}} = -\frac{2}{3}\frac{\Phi}{c^2}\Big|_{\text{rec}} + \frac{\Phi}{c^2}\Big|_{\text{rec}} = \frac{1}{3}\frac{\Phi}{c^2}\Big|_{\text{rec}}. \quad (7.22)$$

Furthermore, a discrimination between these two effects is rather artificial because they are gauge-dependent.

Finally, the relative shift in the photon energy $\delta k^0/k^0$ needs to be computed. The starting point is the perturbed geodesic equation (3.8). Inserting terms which are quadratic in the perturbation and which will therefore be automatically neglected later on, the fully simplified zeroth component reads

$$\frac{dk^0}{d\lambda} = -\frac{2}{c}\left(aH(a) + \frac{1}{c}\frac{\partial\Phi}{\partial\chi}\right)(k^0)^2. \quad (7.23)$$

Further progress can be achieved by rewriting the left-hand side of this equation as

$$c\frac{dk^0}{d\lambda} = \frac{k^0}{a^2}\frac{d(a^2k^0)}{d\eta} - 2(k^0)^2aH(a) = \hat{k}^0k^0\frac{d}{d\eta}\frac{\delta k^0}{k^0} - 2(k^0)^2aH(a). \quad (7.24)$$

To get the last equality it was used that $\hat{k}^0 = ca^{-2}$. Combining these elements one is left with

$$\frac{d}{d\eta}\frac{\delta k^0}{k^0} = -\frac{2}{c}\frac{\partial\Phi}{\partial\chi} \quad (7.25)$$

(at first order perturbation theory), which can be readily integrated by noting that

$$d\Phi = \left(\frac{\partial\Phi}{\partial\eta} + c\frac{\partial\Phi}{\partial\chi}\right)d\eta \quad (7.26)$$

because $cd\eta = d\chi$. Thus, the fractional shift in the photon energy is given by

$$\frac{\delta k^0}{k^0}\Big|_{\text{rec}}^0 = -2\frac{\Phi}{c^2}\Big|_{\text{rec}}^0 + \frac{2}{c^2}\int_{\eta_{\text{rec}}}^{\eta_0}d\eta\frac{\partial\Phi}{\partial\eta}. \quad (7.27)$$

In addition to the ordinary Sachs-Wolfe contribution anticipated before, the integral accounts for the red- or blueshift photons experience by evolving gravitational fields along their trajectory. This is the so-called *integrated Sachs-Wolfe (iSW) effect*. In case of an Einstein-de Sitter universe, where $\Omega_m = 1$, the linear Newtonian potential does not evolve in time and the iSW effect vanishes. Contributions from the iSW effect therefore arise only when the gravitational potential is still slightly decaying during the transition from radiation to matter domination shortly before decoupling (early time iSW effect) and when the dark energy component starts dominating at late times (late time iSW effect). The latter is thus a very important tool in the investigation of dark energy (cf. Chapter 9).

8

The interplay of CMB temperature lensing power reconstruction with primordial non-Gaussianity of local type

In the current era of high-precision CMB experiments, the imprint of gravitational lensing on the CMB temperature is exploited as a source of valuable information. Especially the reconstruction of the lensing potential power spectrum is of great interest. The reconstruction from the optimal quadratic estimator of the lensing potential, though, is biased. As long as the intrinsic CMB fluctuations are Gaussian this bias is well understood and controlled. In the presence of non-Gaussian primordial curvature perturbations, however, the CMB also acquires a non-Gaussian structure mimicking the lensing signal. Concentrating on primordial non-Gaussianity of local type, I address the resulting bias by extracting the lensing potential power spectrum from large samples of simulated lensed CMB temperature maps comprising different values of f_{NL} . I find that the bias is considerably larger than previous analytical calculations suggested. For current values of f_{NL} and a sensitivity like that of the *Planck* mission, however, the bias is completely negligible on all but the largest angular scales.

The contents of this chapter have been published in [Merkel & Schäfer \(2013c\)](#).

8.1. Introduction

As shown in Section 7.2 the cosmic microwave background (CMB) carries an incomparable content of cosmological information. After removing all foregrounds, its tiny temperature fluctuations observed today mirrors the physical conditions in the Universe approximately 400 000 years after the Big Bang. The primary tool to access this information is the CMB temperature power spectrum. Additionally, CMB polarization is an important diagnostic of gravitational waves. Gravitational lensing of the CMB by the intervening large-scale structure, however, alters the shape of the observed power spectra (see Section 7.3.2). In particular, it inevitably introduces *B*-modes confusing the imprint of primordial tensor perturbations. Therefore, in the context of parameter analysis and gravitational wave detection CMB lensing can be regarded as contaminant.

However, the unprecedented sensitivity of ongoing and future CMB experiments allows for a new perspective: The lensing signal in the CMB temperature itself contains valuable cosmological information. Precise knowledge of the lensed CMB power spectrum can be used to improve on parameter estimations from the primary CMB breaking several degeneracies ([Hu, 2002b](#); [Stompor & Efstathiou, 1999](#); [Smith et al., 2006](#)). Furthermore, lensing probes the (integrated) matter distribution from today's observer up to the last scattering surface. As the growth of the large-scale structure is sensitive to neutrino mass, so is the lensing signal, thereby tightening up the mass limits ([Lesgourgues et al.,](#)

2006). Besides these applications in cosmological parameter studies, direct reconstruction of the lensing effect is also of major importance. In order to access the primordial B -mode signal the lensing effect needs to be removed from the observed CMB, requiring the lensing potential (Knox & Song, 2002; Seljak & Hirata, 2004).

There are several approaches to extract the lensing potential from the observed CMB (Zaldarriaga & Seljak, 1999; Guzik et al., 2000; Hu, 2001b; Hirata & Seljak, 2003; Okamoto & Hu, 2003). The method of Okamoto & Hu (2003) is very well suited for the instrumental noise level of current experiments regarding precision and numerical complexity. As this estimator is quadratic in the lensed temperature field, it exploits the lensing induced non-diagonal elements of the CMB covariance matrix. In the next step the reconstructed lensing potential can be used to estimate its power spectrum. The resulting estimator, however, is biased. There are several contributions to this bias, which can be classified according to the order of the lensing potential involved. The zeroth-order contribution is dominant and given by the Gaussian variance of the estimator of the potential. Smaller, but substantial, contributions are of first and second order in the lensing potential and arise from the non-trivial part of the (lensing induced) CMB trispectrum. Up to date all relevant contributions to this so-called reconstruction bias are identified and under control (Kesden et al., 2003; Hanson et al., 2011).

Since not only the information about the lensing potential power spectrum itself, but in part also the reconstruction bias, originates from the connected part of the *lensing induced* CMB four-point function, any kurtosis present in the observed CMB will affect the power spectrum extraction, too. A non-trivial four-point function may arise from primordial non-Gaussian curvature perturbations, which are predicted by all inflationary models. Current observations suggest that the deviations from Gaussianity are quite small. Nevertheless, depending on the inflationary scenario, they can be rather sizeable.

In this chapter I extend the analytical work of Lesgourgues et al. (2005) to the full sky and investigate the impact of an intrinsic non-trivial CMB trispectrum on the lensing power spectrum reconstruction using numerical simulations.

The structure of this chapter is the following: Section 8.2 briefly reviews the key aspects of CMB lensing power extraction. Then, in Section 8.3, primordial non-Gaussian curvature perturbations of local type and their connection to a non-trivial CMB trispectrum are explained in detail. My method to determine the additional reconstruction bias in the presence of primordial non-Gaussianity is presented along with the results in Section 8.4. Finally, Section 8.5 is devoted to a short summary of the main findings of this chapter.

As reference cosmology I choose the parameters compiled in the *WMAP5*+BAO+SN data set. The matter content is described by $\Omega_{\text{CDM}} h^2 = 0.1143$ and $\Omega_{\text{b}} h^2 = 0.02256$, while the cosmological constant is given by $\Omega_{\Lambda} = 0.721$. Primordial perturbations are characterized by the scalar amplitude $\Delta_{\mathcal{R}}^2 = 2.457 \times 10^{-9}$ and spectral index $n_s = 0.96$. The value of the Hubble constant measured today is $H_0 = 100 h \text{ km s}^{-1} \text{ Mpc}^{-1}$ with $h = 0.701$ and the optical depth is assumed to be $\tau = 0.084$. The differences to the cosmology given in Table 2.1 are marginal.

8.2. CMB lensing power spectrum reconstruction

On their way from the last scattering surface to today's observer CMB photons are deflected by the intervening large-scale structure. This gravitational lensing effect on the CMB is well described by the simple remapping of the temperature contrast given in equation (7.13), which I now reformulate in terms of the lensing potential $\phi(\hat{n})$

$$\tilde{\Theta}(\hat{n}) = \Theta[\hat{n} + \nabla\phi(\hat{n})]. \quad (8.1)$$

In harmonic space and linear in the deflection field the effect of lensing can be expressed as (Hu,

2000)

$$\tilde{\Theta}_{\ell m} \approx \Theta_{\ell m} + \sum_{L, M, \ell_1, m_1} (-1)^m \phi_{LM} \Theta_{\ell_1 m_1} \begin{pmatrix} \ell & L & \ell_1 \\ -m & M & m_1 \end{pmatrix} F_{\ell L \ell_1} \quad (8.2)$$

with

$$F_{\ell_1 L \ell_2} = \frac{\Xi_L^2 - \Xi_{\ell_1}^2 + \Xi_{\ell_2}^2}{\sqrt{16\pi}} \Pi_{\ell_1 L \ell_2} \begin{pmatrix} \ell_1 & L & \ell_2 \\ 0 & 0 & 0 \end{pmatrix} \quad (8.3)$$

where

$$\Xi_{a \dots n} \equiv \sqrt{a(a+1) \dots n(n+1)}, \quad \Pi_{a \dots n} \equiv \sqrt{(2a+1) \dots (2n+1)}. \quad (8.4)$$

The sixfold indexed quantities in braces denote Wigner 3j-symbols (cf. equation 5.52).

Okamoto & Hu (2003) realized that it is possible to extract the lensing potential from equation (8.2) by taking the correlator of the lensed multipoles while keeping the realization of the lenses fixed. This procedure returns the multipoles of the lensing potential weighted by a function just depending on the intrinsic CMB power spectrum. Since lensing correlates temperature modes across a whole multipole band (whose width is given by the corresponding band power in the deflection field), one can construct an estimator of the lensing potential as weighted sum over lensed multipoles:

$$\hat{\phi}_{LM} = A_L \sum_{\ell_1, m_1, \ell_2, m_2} (-1)^M g_{\ell_1 \ell_2}(L) \begin{pmatrix} \ell_1 & \ell_2 & L \\ m_1 & m_2 & -M \end{pmatrix} \tilde{\Theta}_{\ell_1 m_1} \tilde{\Theta}_{\ell_2 m_2}. \quad (8.5)$$

Here I have slightly changed my notation. From now on multipoles with a tilde denote the *observed* temperature fluctuations containing the lensing signal, as well as all kinds of experimental noise. The weighted sum needs an appropriate normalization given by

$$A_L^{-1} = \frac{1}{\Pi_L^2} \sum_{\ell_1, \ell_2} f_{\ell_1 L \ell_2} g_{\ell_1 \ell_2}(L). \quad (8.6)$$

Under the assumption that both the intrinsic temperature fluctuations and the lensing potential are homogeneous and isotropic Gaussian random fields, i.e.

$$\langle X_{\ell m} X_{\ell' m'}^* \rangle = C_{\ell}^{XX} \delta_{\ell \ell'} \delta_{m m'}, \quad X \in \{\Theta, \phi\}, \quad (8.7)$$

Okamoto & Hu (2003) derived optimal weights

$$g_{\ell_1 \ell_2}(L) = \frac{f_{\ell_1 L \ell_2}}{2C_{\ell_1, \text{obs}}^{\Theta\Theta} C_{\ell_2, \text{obs}}^{\Theta\Theta}} = \frac{C_{\ell_1}^{\Theta\Theta} F_{\ell_2 L \ell_1} + C_{\ell_2}^{\Theta\Theta} F_{\ell_1 L \ell_2}}{2C_{\ell_1, \text{obs}}^{\Theta\Theta} C_{\ell_2, \text{obs}}^{\Theta\Theta}}, \quad (8.8)$$

where optimal means that they minimize the estimator's Gaussian variance. The spectrum $C_{\ell, \text{obs}}^{\Theta\Theta}$ denotes the observed one, i.e. it contains the lensing signal and all kinds of instrumental noise and foregrounds.

Given the estimated multipoles of the lensing potential field one can proceed to estimate the corresponding power spectrum via

$$C_L^{\hat{\phi}\hat{\phi}} = \frac{1}{2L+1} \sum_M \hat{\phi}_{LM} \hat{\phi}_{LM}^*. \quad (8.9)$$

Accordingly, the expectation value of the reconstructed lensing potential power spectrum involves the four-point function of the lensed temperature contrast

$$\begin{aligned} \langle C_L^{\hat{\phi}\hat{\phi}} \rangle &= \frac{A_L^2}{\Pi_L^2} \sum_{\substack{\ell_1, m_1, \ell_2, m_2, \\ \ell_3, m_3, \ell_4, m_4}} \sum_M (-1)^M \begin{pmatrix} \ell_1 & \ell_2 & L \\ m_1 & m_2 & -M \end{pmatrix} \begin{pmatrix} \ell_3 & \ell_4 & L \\ m_3 & m_4 & M \end{pmatrix} \\ &\times g_{\ell_1 \ell_2}(L) g_{\ell_3 \ell_4}(L) \langle \tilde{\Theta}_{\ell_1 m_1} \tilde{\Theta}_{\ell_2 m_2} \tilde{\Theta}_{\ell_3 m_3} \tilde{\Theta}_{\ell_4 m_4} \rangle. \end{aligned} \quad (8.10)$$

This estimator, however, is biased. While the connected part of the four-point function contains the information about the true lensing potential power spectrum, its Gaussian part gives the largest contribution to the bias which is identical with the normalization of the estimator, i.e. $N_L^{(0)} = A_L$. In addition, there are two more terms that need to be considered. The first one is linear in the lensing potential spectrum. It was first derived by Kesden et al. (2003). Since it is only substantial on small scales a treatment in the limit of a flat sky is well applicable

$$N_L^{(1)} = A^2(L) \int \frac{d^2\ell_1}{(2\pi)^2} \int \frac{d^2\ell_3}{(2\pi)^2} g(\ell_1, \ell_2) g(\ell_3, \ell_4) \times \left[C_{|\ell_1-\ell_3|}^{\phi\phi} f(-\ell_1, \ell_3) f(-\ell_2, \ell_4) + C_{|\ell_1-\ell_4|}^{\phi\phi} f(-\ell_1, \ell_4) f(-\ell_2, \ell_3) \right] \quad (8.11)$$

with the additional constraint $\ell_1 + \ell_2 = L = \ell_3 + \ell_4$. The explicit expressions for the flat-sky analogues of the normalization and weights are given in Appendix B.3.

Furthermore, on large scales Hanson et al. (2011) identified a negative bias which is quadratic in the lensing potential spectrum. Its approximative formula

$$N_L^{(2)} \approx 4C_L^{\phi\phi} \left(\frac{A_L}{\Pi_L^2} \right)^2 \left(\sum_{\ell_1, \ell_2} g_{\ell_1 \ell_2}(L) f_{\ell_1 L \ell_2} \right) \sum_{\ell_3, \ell_4} g_{\ell_3 \ell_4}(L) F_{\ell_4 L \ell_3} (C_{\ell_3}^{\Theta\Theta} - C_{\ell_3}^{\Theta\Theta}) \quad (8.12)$$

is in excellent agreement with results from numerical simulations. All three biases are shown in Figure 8.1.

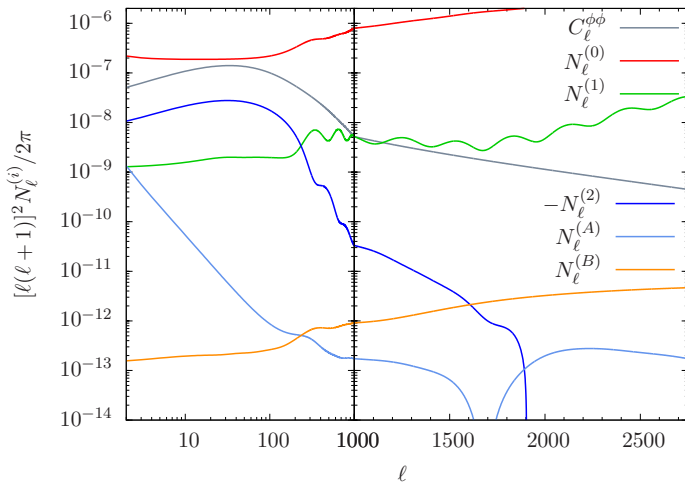


Figure 8.1: Biases involved in the reconstruction of the CMB lensing potential power spectrum $C_\ell^{\phi\phi}$, starting with the optimal quadratic estimator of the lensing potential defined in equation (8.5). The terms $N_\ell^{(A)}$ and $N_\ell^{(B)}$ are analytical estimates of the additional bias arising from primordial non-Gaussian curvature perturbations of local type where $f_{\text{NL}} = 100$ has been assumed.

8.3. Local non-Gaussianity

In the derivation of the optimal reconstruction weights and the three different biases of the estimated lensing potential power spectrum the intrinsic CMB fluctuations were always assumed to be Gaussian distributed. In this case, and under idealized experimental conditions, the non-Gaussian structure of the observed CMB solely arises from the lensing effect. Non-Gaussianity of the lensed CMB then manifests itself in the connected parts of the n -point correlation functions. Odd moments are not generated by lensing, as long as both fields are uncorrelated. Correlations, however, do arise on large scales due to the integrated Sachs-Wolfe (iSW) effect: In Section 7.4 it was shown that the cosmic large-scale structure does not only deflect the CMB photons but its late-time evolution also gives rise to an additional (large-scale) temperature anisotropy. On small scales there are correlations because of the nonlinear iSW (or Rees-Sciama) effect (see Chapter 9), as well as the Sunyaev-Zel'dovich effects discussed in Section 7.3.1. These correlations result in a non-vanishing bispectrum of the lensed CMB.

Thus, there are non-Gaussian signatures present in the lensed, i.e. observed, CMB; even when starting from Gaussian distributed temperature fluctuations.

Inflationary models, however, predict at least small deviations from pure Gaussian initial conditions. While simple inflationary scenarios generate a nearly Gaussian spectrum of the primordial curvature perturbations (Guth, 1981; Bardeen et al., 1983; Mukhanov et al., 1992), more involved models are expected to introduce a significant amount of non-Gaussianity. These models can be classified by the shape of their bispectrum: besides *equilateral* (Alishahiha et al., 2004; Arkani-Hamed et al., 2004; Silverstein & Tong, 2004; Seery & Lidsey, 2005; Chen et al., 2007; Cheung et al., 2008; Li et al., 2008) and *orthogonal* type (Senatore et al., 2010), *local* non-Gaussianity is an important category (Lyth et al., 2003; Dvali et al., 2004; Barnaby & Cline, 2008; Byrnes et al., 2008; Alabidi et al., 2010; Elliston et al., 2011).

Primordial non-Gaussian curvature perturbations of local type can be described starting from a Gaussian fluctuation field $\Phi_L(\mathbf{x})$ and setting

$$\Phi_{\text{NL}}(\mathbf{x}) = \Phi_L(\mathbf{x}) + f_{\text{NL}} \left(\Phi_L^2(\mathbf{x}) - \langle \Phi_L^2(\mathbf{x}) \rangle \right). \quad (8.13)$$

The amplitude of the non-Gaussianity observed is then set by the dimensionless parameter f_{NL} which, in this case, is assumed to be constant, although models with scale-dependent amplitude do exist (Byrnes et al., 2010).

The ansatz of equation (8.13) can be extended by adding a further term of the form $g_{\text{NL}}\Phi_L^3(\mathbf{x})$. I ignore this term in my analysis for simplicity and because g_{NL} is observationally almost completely unconstrained. However, in order to be competitive with the f_{NL} contributions, its value must be of the order $\sqrt{g_{\text{NL}}} \sim f_{\text{NL}}$ but is not constrained by theory; in fact it is possible to tune the inflationary model arbitrarily in these parameters (Sasaki et al., 2006). Likewise, terms proportional to τ_{NL} , which are similar in magnitude relative to f_{NL} because of the Suyama-Yamaguchi relation $\tau_{\text{NL}} \geq (6/5 f_{\text{NL}})^2$ (see, e.g. Suyama & Yamaguchi, 2008; Suyama et al., 2010; Sugiyama et al., 2011; Smith et al., 2011), are neglected. Neglecting these contributions should at most result in a slight underestimation of the impact of local primordial non-Gaussianity on the lensing power reconstruction.

By construction, the four-point function of the curvature perturbations acquires a non-trivial part. This is also true for the intrinsic CMB fluctuations since they are simply related to those in the curvature field via an integration over the corresponding radiation transfer function $\Delta_\ell(k)$

$$\Theta_{\ell m} = 4\pi (-i)^\ell \int \frac{d^3k}{(2\pi)^3} \Phi_{\text{NL}}(\mathbf{k}) \Delta_\ell(k) Y_{\ell m}^*(\hat{\mathbf{n}}_k) \quad (8.14)$$

with $\Phi_{\text{NL}}(\mathbf{k})$ being the Fourier transform of equation (8.13).

The non-trivial part of the angular trispectrum of the CMB temperature contrast is most conveniently expressed in its fully reduced form (at leading order in f_{NL})

$$\mathcal{T}_{\ell_3 \ell_4}^{\ell_1 \ell_2}(L) = \int r_1^2 dr_1 r_2^2 dr_2 F_L(r_1, r_2) \alpha_{\ell_1}(r_1) \beta_{\ell_2}(r_1) \alpha_{\ell_3}(r_2) \beta_{\ell_4}(r_2) h_{\ell_1 L \ell_2} h_{\ell_3 L \ell_4} \quad (8.15)$$

with

$$F_L(r_1, r_2) = \frac{2}{\pi} \int k^2 dk P_{\Phi\Phi}(k) j_L(kr_1) j_L(kr_2), \quad (8.16)$$

$$\alpha_\ell(r) = 2f_{\text{NL}} \frac{2}{\pi} \int k^2 dk \Delta_\ell(k) j_\ell(kr), \quad (8.17)$$

$$\beta_\ell(r) = \frac{2}{\pi} \int k^2 dk P_{\Phi\Phi}(k) \Delta_\ell(k) j_\ell(kr) \quad (8.18)$$

and

$$h_{\ell_1 L \ell_2} = \frac{\Pi_{\ell_1 L \ell_2}}{\sqrt{4\pi}} \begin{pmatrix} \ell_1 & L & \ell_2 \\ 0 & 0 & 0 \end{pmatrix} \quad (8.19)$$

(see [Okamoto & Hu, 2002](#), for details on this formalism). In the expressions above, $P_{\Phi\Phi}(k)$ is the power spectrum of the curvature perturbations and $j_\ell(x)$ denotes the ℓ th spherical Bessel function of the first kind (see [Abramowitz & Stegun, 1972](#)).

The computation of the trispectrum given in equation (8.15) is numerically quite cumbersome. [Okamoto & Hu \(2002\)](#) found a very useful approximation formula by extending the Sachs-Wolfe approximation, i.e.

$$\Delta_\ell(k) = \frac{1}{3} j_\ell [k(\eta_0 - \eta_{\text{rec}})], \quad (8.20)$$

valid at small ℓ into the acoustic regime

$$\mathcal{T}_{\ell_3\ell_4}^{\ell_1\ell_2}(L) \approx 36h_{\ell_1L\ell_2}h_{\ell_3L\ell_4}f_{\text{NL}}^2 C_L^{\text{SW}} C_{\ell_2}^{\Theta\Theta} C_{\ell_4}^{\Theta\Theta} \quad (8.21)$$

with

$$C_L^{\text{SW}} = \frac{2}{9\pi} \int k^2 dk P_{\Phi\Phi}(k) j_L^2 [k(\eta_0 - \eta_{\text{rec}})], \quad (8.22)$$

where $\eta_0 - \eta_{\text{rec}}$ is the conformal time spread between today and recombination. This approximation holds as long as the last scattering surface can be considered as thin and its temperature fluctuations only vary slowly.

8.4. Power reconstruction bias

8.4.1. Zeroth order calculation

Since the first and second order bias of the reconstructed lensing potential power spectrum arise from the connected part of the (lensing induced) CMB trispectrum, one expects that an intrinsic (non-trivial) trispectrum of the unlensed CMB also contributes an additional bias. This bias was first addressed by [Lesgourgues et al. \(2005\)](#). In their derivation they assumed that both of the effects leading to a connected part of the observed CMB four-point function are completely separable. Thus, they did not consider a so-to-speak lensed trispectrum but just added the connected part of the unlensed CMB trispectrum. In this approximation, and in the limit of a flat sky, the additional bias is given by

$$N^{(\text{NL},0)}(L) = A^2(L) \int \frac{d^2\ell_1}{(2\pi)^2} \int \frac{d^2\ell_3}{(2\pi)^2} g(\ell_1, \ell_2) g(\ell_3, \ell_4) \left(\mathcal{P}_{\ell_3\ell_4}^{\ell_1\ell_2}(L) + 2\mathcal{P}_{\ell_2\ell_4}^{\ell_1\ell_3}(|\ell_1 - \ell_3|) \right), \quad (8.23)$$

with the additional constraints $\ell_1 + \ell_2 = L$ and $\ell_3 + \ell_4 = L$. The functional form of the flat-sky expressions are relegated to Appendix B.3. [Lesgourgues et al. \(2005\)](#) also computed the bias contribution from the g_{NL} term which is not considered in this work.

Starting from equation (8.10), the all-sky generalization of equation (8.23) is

$$N_L^{(\text{NL},0)} = \left(\frac{4A_L^2}{\Pi_L^4} \right) \sum_{\ell_1, \ell_2, \ell_3, \ell_4} g_{\ell_1\ell_2}(L) g_{\ell_3\ell_4}(L) \left[\mathcal{T}_{\ell_3\ell_4}^{\ell_1\ell_2}(L) + \Pi_L^2 \sum_{L'} \begin{Bmatrix} \ell_1 & \ell_2 & L \\ \ell_4 & \ell_3 & L' \end{Bmatrix} \right. \\ \left. \times \left((-1)^{\ell_2+\ell_3} \mathcal{T}_{\ell_2\ell_4}^{-\ell_1\ell_3}(L') + (-1)^{L+L'} \mathcal{T}_{\ell_4\ell_2}^{-\ell_1\ell_3}(L') \right) \right]. \quad (8.24)$$

The quantity in curly brackets denotes a Wigner $6j$ -symbol (see [Abramowitz & Stegun, 1972](#)). Using the approximative formula for the trispectrum of unlensed temperature fluctuations given in equation (8.21) the similarity with the lensing induced CMB trispectrum ([Hu, 2001a](#))

$$\mathbb{T}_{\ell_3\ell_4}^{\ell_1\ell_2}(L) = C_L^{\phi\phi} C_{\ell_2}^{\Theta\Theta} C_{\ell_4}^{\Theta\Theta} F_{\ell_1L\ell_2} F_{\ell_3L\ell_4} \quad (8.25)$$

is striking. There are two important consequences. First, the term involving the Wigner $6j$ -symbol, hereafter denoted by $N_L^{(B)}$, should only contribute on small scales, it can therefore safely be treated in

the flat-sky limit, i.e. by using the second part of equation (8.23). Second, the other term, afterwards denoted by $N_L^{(A)}$, should be proportional to C_L^{SW} implying a scaling of the form

$$N_L^{(A)} \propto \frac{1}{L^3(L+1)^3} \quad (8.26)$$

due to the fact, that

$$C_L^{\text{SW}} = \frac{2}{9\pi} \int k^2 dk P_{\Phi\Phi}(k) j_L^2 [k(\eta_0 - \eta_{\text{rec}})] \propto \frac{1}{L(L+1)} \quad (8.27)$$

for a scale-invariant power spectrum (cf. [Liddle & Lyth, 2000](#)).

In Figure 8.1 the two additional bias contributions $N_L^{(A)}$ and $N_L^{(B)}$ are shown. The agreement with the results of [Lesgourgues et al. \(2005\)](#) is very good although they used the exact temperature transfer functions instead of the extended Sachs-Wolfe approximation applied in this work. Only in the acoustic regime the $N_L^{(A)}$ term shows substantial differences. There the bias is completely dominated by the $N_L^{(B)}$ term, which is accurately described by the extended Sachs-Wolfe approximation, even on smallest scales as the comparison with Figure 1 of [Lesgourgues et al. \(2005\)](#) shows. On large scales the full-sky calculation does not greatly improve the results [Lesgourgues et al. \(2005\)](#) obtained neglecting the curvature of the sky. For both methods one recovers the expected scaling relation with the multipole order (cf. again Figure 1 of [Lesgourgues et al., 2005](#)).

As already pointed out by [Lesgourgues et al. \(2005\)](#) for current values of f_{NL} , $-10 \leq f_{\text{NL}} \leq 74$ ([Komatsu, E. et al., 2011](#)), the additional bias is not a severe contaminant of the reconstructed power spectrum. On almost all scales the bias is more than four orders of magnitude smaller than the biases arising from the lensing induced trispectrum. Only on largest scales the contributions from the $N_L^{(A)}$ term can be substantial. Consequently, as long as a fully separate perturbative treatment of both, gravitational lensing, as well as primordial non-Gaussianity, is applicable, the additional bias is well controlled and for current f_{NL} parameters negligible.

However, the validity of this separation ansatz is not obvious. In the presence of primordial non-Gaussianity the mode coupling due to lensing is more involved since the perturbative expansions of the lensed temperature field in powers of the lensing potential on the one hand, and the unlensed temperature field in powers of the non-Gaussian curvature perturbations on the other hand, compete.

Furthermore, the analytical computation of the bias is only carried out at leading order in f_{NL} , i.e. only correlators in which the four multipoles are unlensed but two of them include non-Gaussian contributions are considered. Higher orders than f_{NL}^2 are neglected. Keeping in mind that the lensing induced bias receives substantial contributions from terms which are second order in the lensing potential power spectrum (namely the $N_L^{(2)}$ -term), it is not guaranteed that a leading order calculation is sufficient.

In order to circumvent the assumptions and limitations which are necessary for an analytical study of this problem I will resort to numerical simulations. Here, all the different effects involved, primordial non-Gaussianity, lensing, instrumental noise, can be incorporated in a consistent manner and to arbitrary order in f_{NL} .

8.4.2. Numerical simulations

The starting point of the simulations is the large sample of non-Gaussian CMB realizations provided by [Elsner & Wandelt \(2009\)](#). The non-Gaussian structure arises from primordial curvature perturbations of local type detailed in Section 8.3. The maps of [Elsner & Wandelt \(2009\)](#) are well suited for the analysis because they did not focus on the intrinsic CMB bispectrum but produced simulations with accurate non-Gaussian statistics to all correlation orders. Every realization consists of a set of Gaussian ($\Theta_{\ell m}^{\text{L}}$) and non-Gaussian ($\Theta_{\ell m}^{\text{NL}}$) multipoles, so that a CMB map containing the desired level of non-Gaussianity characterized by f_{NL} can be built via

$$\Theta_{\ell m} = \Theta_{\ell m}^{\text{L}} + f_{\text{NL}} \Theta_{\ell m}^{\text{NL}}. \quad (8.28)$$

The cosmological background of these simulations is adapted from the *WMAP5*+BAO+SN data as summarized at the end of Section 8.1.

Given a non-Gaussian CMB map, it can be lensed in the framework of `LENXPIX`⁵ (Lewis, 2005). The remapping technique implemented in `LENXPIX` assumes that the lensing potential is fully described by its power spectrum. Obviously, this is no longer true in the presence of primordial non-Gaussianity. However, for the reconstruction scheme detailed in Section 8.2 the CMB and the lensing potential are treated as statistically independent fields and higher order statistics of the lensing potential are not involved.

Since the map is already given in multipole space I use a slightly modified version of `LENXPIX`, which skips the simulation of a (Gaussian) CMB realization and starts directly from the temperature multipoles, constructed according to equation (8.28). In order to get a lensed CMB map at `HEALPIX` (Górski et al., 2005) resolution $N_{\text{side}} = 2048$, which is cosmically accurate up to $\ell_{\text{max}} = 2750$, one needs input multipoles up to $\ell_{\text{input}} = 3000$. The non-Gaussian maps of Elsner & Wandelt (2009), however, cover only a multipole range up to $\ell_{f_{\text{NL}}} = 1024$. I therefore extend the maps in the range $\ell_{f_{\text{NL}}} < \ell \leq 3000$ with pure Gaussian multipoles. Thus, equation (8.28) needs to be replaced by

$$\Theta_{\ell m} = \begin{cases} \Theta_{\ell m}^{\text{L}} + f_{\text{NL}} \Theta_{\ell m}^{\text{NL}}, & \text{if } \ell \leq 1024 \\ \Theta_{\ell m}^{\text{L}}, & \text{else.} \end{cases} \quad (8.29)$$

The power spectrum needed for the construction of Gaussian CMB realizations has been computed using `CAMB`⁶ (Lewis et al., 2000).

This method is not expected to crucially influence the main conclusion of this work. The non-Gaussianity of the maps constructed according to this prescription will be even milder due to the fact that scales smaller than about ten arcminutes are not affected by the primordial non-Gaussian curvature perturbations. Likewise, if there are serious concerns about this method, one can think of the resulting maps as not being subjected to primordial non-Gaussianity of the local type, but subjected to some intermediate type, which is scale-dependent. In any case, the influence of the resulting non-trivial intrinsic CMB trispectrum on the reconstructed lensing power needs to be studied.

Finally, the lensed maps are only exposed to instrumental noise. But neither any further secondary anisotropies nor foregrounds nor experimental complications, such as incomplete sky coverage, are included. Adapting the specification of the *Planck* satellite mission, the maps are first convolved with a Gaussian beam with $\sigma_{\text{FWHM}} = 7$ arcmin. Before deconvolution, white Gaussian pixel noise with standard deviation $\sigma_{\text{N}} = 27 \mu\text{K arcmin}$ is added. The power spectra of the final maps are well described by the analytic expression derived by Knox (1995)

$$C_{\ell, \text{obs}}^{\Theta\Theta} = C_{\ell}^{\Theta\Theta} + \left(\frac{\sigma_{\text{N}}}{T_{\text{CMB}}} \right)^2 e^{\ell(\ell+1)\sigma_{\text{FWHM}}^2/8 \log 2}. \quad (8.30)$$

8.4.3. Efficient estimator

For practical purposes, the estimator in the form of equation (8.5) is not suitable. One should use its angular space representation instead

$$\hat{\phi}_{LM} = A_L \int d\Omega Y_{LM}^*(\hat{n}) \nabla^i [V(\hat{n}) \nabla_i U(\hat{n})]. \quad (8.31)$$

Here, the spin-gradient derivative ∇ only acts on the spin part of the corresponding fields, the inverse weighted temperature map

$$V(\hat{n}) = \sum_{\ell, m} \frac{1}{C_{\ell, \text{obs}}^{\Theta\Theta}} \tilde{\Theta}_{\ell m} Y_{\ell m}(\hat{n}) \quad (8.32)$$

⁵<http://cosmologist.info/lenspix/>

⁶<http://camb.info/>

and the Wiener reconstruction of the unlensed temperature field

$$U(\hat{\mathbf{n}}) = \sum_{\ell, m} \frac{C_\ell^{\Theta\Theta}}{C_{\ell, \text{obs}}^{\Theta\Theta}} \tilde{\Theta}_{\ell m} Y_{\ell m}(\hat{\mathbf{n}}) \quad (8.33)$$

(Okamoto & Hu, 2003). This representation allows for the use of fast harmonic transform algorithms on the sphere.

8.4.4. Results

In order to determine the bias associated with the connected part of the trispectrum of the unlensed CMB, which is generated by primordial non-Gaussian curvature perturbations of local type, I proceeded as follows:

- (1) construct \mathcal{N} CMB maps following equation (8.29) setting $f_{\text{NL}} = 0$
- (2) use these maps to build a sample of lensed maps which contain the desired instrumental noise properties as detailed in Section 8.4.2
- (3) apply the efficient estimator of Section 8.4.3 to the sample and reconstruct the lensing potential power spectrum for each map according to

$$C_L^{\hat{\phi}\hat{\phi},(i)} = \frac{1}{2L+1} \sum_M \hat{\phi}_{LM}^{(i)} \hat{\phi}_{LM}^{*(i)} - N_L^{(0)} - N_L^{(1)} - N_L^{(2)}, \quad (8.34)$$

where the upper index runs from 1 to \mathcal{N} . The three bias contributions in the equation above have not been computed separately for each individual realization. Instead, the theoretical power spectrum of the lensed and unlensed CMB, as well as of the lensing potential, again computed with `CAMB`, were used. To illustrate that in this way the (purely lensing induced) biases are very well captured, the lensing potential power reconstruction for $f_{\text{NL}} = 0$ obtained from hundred CMB realizations is plotted in Figure 8.2. The boxes indicate the width of the multipole band and the one sigma error for one realization.

- (4) compute the sample mean

$$\bar{C}_L^{\hat{\phi}\hat{\phi}} = \frac{1}{\mathcal{N}} \sum_{i=1}^{\mathcal{N}} C_L^{\hat{\phi}\hat{\phi},(i)} \quad (8.35)$$

- (5) repeat steps (1) to (4) but now setting $f_{\text{NL}} = 100$ in the first step
- (6) repeat step (5) but now starting with $f_{\text{NL}} = 1000$
- (7) compute the bias for both values of f_{NL} according to

$$N_L^{(f_{\text{NL}})} = \bar{C}_L^{\hat{\phi}\hat{\phi}} \Big|_{f_{\text{NL}}} - \bar{C}_L^{\hat{\phi}\hat{\phi}} \Big|_{f_{\text{NL}}=0}. \quad (8.36)$$

It needs to be stressed that in steps (1) to (3) for all three values of f_{NL} the simulation conditions have been the same. In other words, I kept track of the different random seeds involved in the map making procedure. Thus, the i th map is always lensed by the same realization of the lensing potential and always contains the same realization of instrumental noise. This ensures that the differences in the reconstructed power spectra, i.e. the bias, are solely caused by the variations in f_{NL} . The numerical analysis of this work has been carried out setting $\mathcal{N} = 100$.

In Figure 8.2 the reconstructed power spectra for both values of f_{NL} are plotted, while Figures 8.3 and 8.4 show the corresponding biases. For comparison, also the bias derived by Lesgourgues et al.

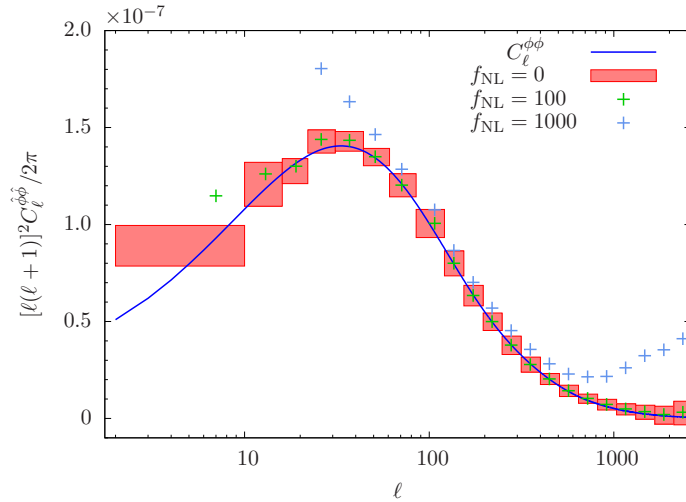


Figure 8.2: Illustration of the performance of the CMB lensing power reconstruction discussed in the text and condensed in equation (8.34). The red boxes indicate the width of the multipole band over which the extracted power spectrum has been binned, as well as the 1σ error for one realization. In addition, the reconstructions in presence of primordial non-Gaussianity for two different values of f_{NL} are shown. Note that on large angular scales the bias for $f_{\text{NL}} = 1000$ exceeds the range of the plot by far (cf. Figure 8.4) and is not shown for clarity.

(2005) (cf. equations 8.23 and 8.24) is plotted. While the functional form of the bias found in the simulations resembles that of the analytical zeroth order prediction, its amplitude is much larger. Interestingly, the disagreement in amplitude is different for the two parts of the analytic bias formula. For the smaller value of f_{NL} the $N_L^{(A)}$ part, which gives the relevant contribution on large scales, needs to be scaled by a factor of roughly 100 to reach the same level as the bias found in the simulations. Its small-scale counterpart, the $N_L^{(B)}$ term differs approximately by a factor of 125.

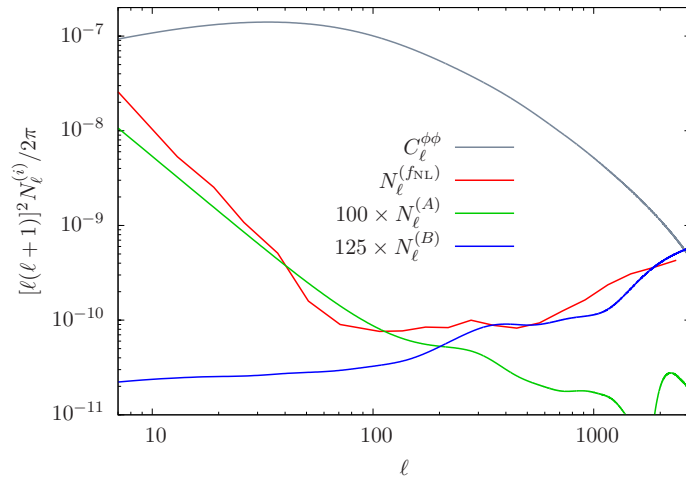
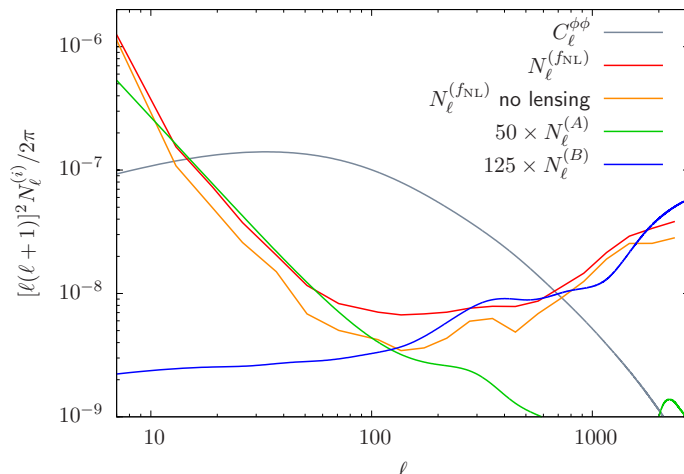


Figure 8.3: Additional bias associated with the presence of primordial non-Gaussian curvature perturbations. The bias (red curve) has been extracted from numerical simulations according to equation (8.36) with $f_{\text{NL}} = 100$. In addition, the analytical estimates of the bias (green and blue curve), phenomenologically amplified, are shown.

Looking at the bias obtained for $f_{\text{NL}} = 1000$ shown in Figure 8.4, one immediately realizes that, in contrast to the analytical formula of Lesgourgues et al. (2005), the bias extracted from numerical simulations does not scale quadratically with f_{NL} . This is particularly true for large angular scales. Here the agreement with the analytic expression, now phenomenologically amplified by a factor of 50, is much better than for $f_{\text{NL}} = 100$. Thus, there is no simple scaling relation with f_{NL} . To some extent the f_{NL} dependence of the bias qualitatively approaches a quadratic form in the acoustic regime and beyond.

I shall now address possible explanations for this enormous discrepancy between the analytical estimate of the bias and the results from numerical simulations. One can mainly think of three different sources: (1) the assumption that lensing induced and primordial non-Gaussianity completely separate does not hold. Thus, the discrepancy results from the lensing of the f_{NL} trispectrum; (2) a calculation of the bias at leading order in f_{NL} is not sufficient, i.e. the discrepancy results from terms which are higher order than f_{NL}^2 ; (3) the disconnected part of the trispectrum is changed in the presence of non-vanishing f_{NL} . In this case, the discrepancy results from changes in the $N_L^{(0)}$ term.

Figure 8.4: Same as Figure 8.3 but for another choice of the f_{NL} parameter, namely $f_{\text{NL}} = 1000$. Note that in this plot the $N_\ell^{(A)}$ term has been scaled differently highlighting, that the bias found in numerical simulations does not exhibit a simple scaling relation with f_{NL} in contrast to the analytical model. The orange line indicates the f_{NL} induced bias in the absence of lensing.



I start with the last of these three possibilities by recomputing the $N_L^{(0)}$ term. Now the average power spectrum of all the realizations is used instead of the theoretical one obtained from CAMB, which is in principle only valid in the case of $f_{\text{NL}} = 0$. However, there are no differences in the $N_L^{(0)}$ terms, indicating that the disconnected part of the trispectrum is unchanged.

In order to check whether explanation (1) or (2) applies, the reconstruction scheme detailed at the beginning of this section is repeated but this time without lensing. For clarity I focus on the case $f_{\text{NL}} = 1000$. The signal the estimator is now sensitive to is solely contained in the connected part of the trispectrum induced by the non-Gaussian primordial curvature perturbations. Since $N_L^{(1)}$ and $N_L^{(2)}$ identically vanish, subtracting $N_L^{(0)}$ from the reconstructed power spectrum then reveals the bias associated with non-vanishing f_{NL} . If explanation (1) is true the bias should be identical to the analytical one given in equation (8.24). As shown in Figure 8.4 this is not the case. The analysis without lensing reveals a deviation which has the same order of magnitude as before. In the absence of lensing, however, the f_{NL} bias is roughly one third smaller than with lensing. Again, the functional form of the bias resembles the one of the analytical leading order calculation to some extent.

Since the order of magnitude of the deviation does not change, it can be concluded that the discrepancy between the analytical expression for the f_{NL} bias and the results from numerical simulations is presumably due to contributions to the f_{NL} induced trispectrum which are of higher order than f_{NL}^2 . The influence of lensing of the f_{NL} induced trispectrum is subdominant. However, amounting to a factor of approximately two, it is not negligible.

It is important to keep in mind that these are just qualitative considerations. The actual discrepancy between the bias obtained from a rigorous simultaneous treatment of primordial, as well as lensing induced, non-Gaussianity via numerical simulations and its analytical lowest order estimate is tremendous. The analytical expression, even phenomenological amplified, is not suited for an accurate and consistent bias subtraction scheme. However, and this is the most important result, for intermediate values of f_{NL} , as suggested by current observational data, the bias associated with primordial non-Gaussianity of local type does not effect CMB lensing power reconstruction at all.

8.5. Summary

In this chapter the influence of primordial non-Gaussianity on CMB lensing power reconstruction was revisited. I determined the bias associated with the non-trivial structure of the CMB trispectrum generated by non-Gaussian curvature perturbations of local type. While the earlier work of [Lesgourgues et al. \(2005\)](#) addressed this issue analytically, I used numerical simulations. This allows to overcome the non-obvious hypothesis that both effects leading to a connected part of the CMB four-point func-

tion do completely separate. The results of this work can be summarized as follows:

- (i) The analytical expressions derived by [Lesgourgues et al. \(2005\)](#) in the limit of a flat sky have been extended to the all-sky formalism.
- (ii) In the case of non-Gaussian primordial curvature perturbations of local type the bias arising from a non-trivial trispectrum of the intrinsic CMB temperature contrast is substantially larger than so far expected.
- (iii) I presume that this discrepancy mainly arises from the parts of the f_{NL} induced trispectrum which are of higher order than f_{NL}^2 and which have not been considered in the analytical treatment. Lensing of the f_{NL} trispectrum itself amplifies the corresponding bias only by about 50%.
- (iv) The limitation of the simulated non-Gaussian CMB maps (discussed in Section 8.4.2) does not change the conclusion. Discarding the physical mechanism and thinking of the simulated maps as the simplest example of a scale-dependent form of non-Gaussian structure in the unlensed CMB, one finds that the associated connected part of the unlensed CMB is potentially a severe contaminant in lensing power reconstruction studies. This interpretation of the simulated data addresses another important aspect. In order to estimate the amplitude of the bias prior knowledge of the type of primordial non-Gaussianity is needed. For removing the bias this prior knowledge is even more important.
- (v) The strength of the contamination is obviously set by the amplitude of the non-Gaussian contributions. For current values of f_{NL} only smallest multipoles are affected, while the effect on intermediate and small scales is completely negligible. Low multipoles are anyway cosmic variance dominated and have therefore only small predictive power. Thus, even in the full-sky case, the bias arising from primordial non-Gaussianity of local type is not expected to compromise CMB lensing power reconstruction at all.

As this work focuses on the bias associated with primordial non-Gaussian curvature perturbations solely characterized by f_{NL} , an extension of this study including also the contributions from the g_{NL} -term is desirable. However, the simulation of accurate CMB maps containing the correct non-Gaussian structure arising from both, f_{NL} and g_{NL} , is challenging.

9

Contributions to the nonlinear integrated Sachs-Wolfe effect: Birkinshaw-Gull effect and gravitational self-energy density

In this chapter contributions to the spectrum of the nonlinear integrated Sachs-Wolfe (iSW)/Rees-Sciama effect in a dark energy cosmology are recomputed. Focusing on the moderate nonlinear regime, all dynamical fields involved are derived from the density contrast in Eulerian perturbation theory. Shape and amplitude of the resulting angular power spectrum are similar to that derived in previous work. With this purely analytical approach I identify two distinct contributions to the signal of the nonlinear iSW effect: the change of the gravitational self-energy density of the large-scale structure with (conformal) time and gravitational lenses moving with the large-scale matter stream. In the latter the Birkinshaw-Gull effect is recovered. As the nonlinear iSW effect itself is inherently hard to detect, observational discrimination between its individual contributions is almost excluded. This analysis, however, yields valuable insights into the theory of the nonlinear iSW effect as a post-Newtonian relativistic effect on propagating photons.

The contents of this chapter have been published in [Merkel & Schäfer \(2013a\)](#).

9.1. Introduction

In Chapter 7 several secondary anisotropies of the cosmic microwave background (CMB) temperature were discussed. Chief among these is the integrated Sachs-Wolfe (iSW) effect (see Section 7.4). The interaction of CMB photons with time-evolving gravitational potentials in the large-scale structure causes additional fluctuations in the CMB temperature. While being blueshifted when entering a potential well, the photons also experience a redshift on their way out of the potential. A net change in temperature results when blueshift and redshift do not compensate.

Being a secondary effect, the signal of the iSW effect is quite small in comparison to the CMB temperature itself. Its importance, however, arises from its dedicated sensitivity to cosmic fluids with non-vanishing equation of state ([Crittenden & Turok, 1996](#)), promoting it as a valuable tool in the investigation of dark energy and non-standard cosmologies ([Lue et al., 2004](#); [Zhang, 2006](#)), as well as the Universe's spatial curvature ([Kamionkowski & Spergel, 1994](#)).

Exploiting its strong correlation with the galaxy distribution the iSW effect has been detected with high significance by various groups ([Boughn & Crittenden, 2004](#); [Vielva et al., 2006](#); [McEwen et al., 2007](#); [Giannantonio et al., 2008](#)). The constraints they derive for the matter density Ω_m and the dark

energy equation of state w give support to the Λ CDM model.

The nonlinear iSW or Rees-Sciama (RS) effect (Rees & Sciama, 1968; Seljak, 1996b; Cooray, 2002; Schäfer & Bartelmann, 2006) refers to any temperature anisotropy caused by nonlinearly evolving gravitational potentials. In contrast to the linear iSW effect it is a small-scale phenomenon dominating the total iSW effect signal on multipoles $\ell \gtrsim 100$, but is nevertheless hard to detect because of the primary CMB (Cooray, 2002; Schäfer et al., 2011).

As it results from nonlinear structure formation, the statistics of the RS effect is necessarily non-Gaussian. The non-Gaussianities induced by the RS effect, however, are small. Spergel & Goldberg (1999) showed that the CMB bispectrum due to the RS effect is undetectable. Mixed polyspectra of the nonlinear iSW effect temperature perturbation and the tracer galaxy density field, as recently investigated by Jürgens & Schäfer (2013) in continuation of the work of Schäfer (2008), also do not reach sufficiently high signal-to-noise ratios. Therefore, stacking methods (Granett et al., 2008), as an alternative to a statistical detection of the iSW and RS effect, are of great interest.

Seljak (1996b) and Cooray (2002) provided two different perturbative descriptions of the nonlinear iSW effect yielding comparable results. In this work I take up the ansatz of Cooray (2002). While his results make extensive use of findings from the halo model in the deeply nonlinear regime, I am more interested in a perturbative treatment. Therefore, the analysis concentrates on the weakly nonlinear regime where the statistics of the underlying fields are not too far from being Gaussian and second order perturbation theory is well applicable. The nonlinear iSW effect is computed by solely using the density field and its derivatives. Although the applicability of this ansatz is naturally limited, it allows for deeper insights into the underlying physical processes. This approach is well suited for identifying the distinct contributions to the nonlinear iSW effect as well as elucidating their physical origin.

This chapter is structured in the following way: It begins with the computation of the spectrum of the nonlinear iSW effect in Section 9.2. Furthermore, the resulting two-point statistics are derived and the corresponding angular power spectrum are presented. The analysis is extended in Section 9.3, where I discriminate and interpret the different contributions to the nonlinear iSW effect. In Section 9.4 the physical interpretation is continued and deepened by pointing out analogies with classical field theory as well as the theory of gravitomagnetic potentials. Finally, I summarize the results in Section 9.5.

Throughout this chapter I choose a spatially flat w CDM cosmology as reference. The initial perturbations in the CDM component are assumed to be adiabatic and Gaussian distributed with variance $\sigma_8 = 0.8$, where the spectral index n_s is set to unity. The matter content is described by $\Omega_m = 0.25$ and $\Omega_b = 0.04$ while the value of the Hubble constant is set to $H_0 = 100 h \text{ km s}^{-1} \text{ Mpc}^{-1}$ with $h = 0.72$.

9.2. Nonlinear integrated Sachs-Wolfe effect

In Section 7.4 I derived the relative change in temperature CMB photons experience when they traverse time-evolving gravitational potentials on their way from the last scattering surface to today's observer. It is given by the line-of-sight integral (see the last term in equation 7.27)

$$\tau(\hat{n}) \equiv \frac{\Delta T_{\text{iSW}}(\hat{n})}{T_{\text{CMB}}} = \frac{2}{c^2} \int_0^{\eta_{\text{rec}}} d\eta \frac{\partial}{\partial \eta} \Phi(\hat{n}, \eta). \quad (9.1)$$

The gravitational potential is directly related to the density fluctuations via the (comoving) Poisson equation (2.33c). Its time derivative can be most easily accessed in Fourier space where the Poisson equation is readily inverted

$$\frac{\partial}{\partial \eta} \Phi(\mathbf{k}, \eta) = -\frac{3}{2} H_0^2 \Omega_m \frac{1}{k^2} \frac{\partial}{\partial \eta} \frac{\delta(\mathbf{k}, \eta)}{a}. \quad (9.2)$$

Here I expressed Newton's constant in terms of the critical density (2.11). In the derivation of the linear iSW effect one usually inserts $\delta(\mathbf{k}, a) = D_+(a) \delta_0(\mathbf{k})$, revealing that during matter domination where $D_+(a) = a$ the iSW effect vanishes. For the purposes of this work, however, it proves advantageous to

carry out the time derivative formally

$$\frac{\partial}{\partial \eta} \Phi(\mathbf{k}, \eta) = \frac{3}{2} H_0^2 \Omega_m \frac{1}{k^2} \left(H(\eta) \delta(\mathbf{k}, \eta) - \frac{1}{a} \frac{\partial}{\partial \eta} \delta(\mathbf{k}, \eta) \right). \quad (9.3)$$

Obviously, the time evolution of the potential is sourced by two different effects: on the one hand the scaling of structures by the Hubble expansion, represented by the first term, and on the other hand by the time varying structure growth. As mentioned before, in epochs dominated by a fluid with vanishing equation of state these two effects balance.

Since I am interested in nonlinear contributions to the iSW effect I express the time derivative of the density fluctuations by means of the continuity equation

$$\frac{\partial}{\partial \eta} \delta(\mathbf{x}, \eta) + \text{div } \mathbf{j}(\mathbf{x}, \eta) = 0. \quad (9.4)$$

Due to matter conservation, the change of the dark matter density in time needs to be compensated by the divergence of the corresponding flux

$$\mathbf{j}(\mathbf{x}, \eta) = [1 + \delta(\mathbf{x}, \eta)] \mathbf{v}(\mathbf{x}, \eta). \quad (9.5)$$

In the linear regime $\delta \ll 1$, thus the momentum density $\delta(\mathbf{x}, \eta) \mathbf{v}(\mathbf{x}, \eta)$ is negligible and one can immediately read off the familiar Fourier representation of the peculiar velocity field

$$\mathbf{v}(\mathbf{k}, \eta) = \int d^3 x \mathbf{v}(\mathbf{x}, \eta) e^{i\mathbf{k} \cdot \mathbf{x}} = -i \frac{\partial D_+(\eta)}{\partial \eta} \frac{\mathbf{k}}{k^2} \delta_0(\mathbf{k}). \quad (9.6)$$

In Fourier space, the dark matter current density becomes a convolution

$$\mathbf{j}(\mathbf{k}, \eta) = \mathbf{v}(\mathbf{k}, \eta) + \int \frac{d^3 k'}{(2\pi)^3} \mathbf{v}(\mathbf{k} - \mathbf{k}', \eta) \delta(\mathbf{k}', \eta), \quad (9.7)$$

so that the time evolution of the gravitational potential finally can be written as a function of density contrast and peculiar velocities

$$\frac{\partial}{\partial \eta} \Phi(\mathbf{k}, \eta) = \frac{3}{2} H_0^2 \Omega_m \frac{1}{k^2} \left[H(\eta) \delta(\mathbf{k}, \eta) - i \mathbf{k} \cdot \left(\mathbf{v}(\mathbf{k}, \eta) + \int \frac{d^3 k'}{(2\pi)^3} \mathbf{v}(\mathbf{k} - \mathbf{k}', \eta) \delta(\mathbf{k}', \eta) \right) \right]. \quad (9.8)$$

Due to the symmetry of the convolution the expression for the current density is not unique. For example, one could have explicitly symmetrized equation (9.7). However, for the purpose of this work, which aims at the different contributions to the RS effect, the form given above is most useful, which will become clear below.

So far, this derivation is essentially the same as the one presented by [Cooray \(2002\)](#). [Cooray \(2002\)](#), however, focused on the deeply nonlinear regime and proceeded by using approximations resulting from the halo model approach. In contrast to this, I am interested in an analytical description of the contributions to the nonlinear iSW effect which arise from dark matter currents. Therefore, this analysis is restricted to the moderate nonlinear regime. Obviously, in this regime the simple relation between peculiar velocities and density contrast, given in equation (9.6), is no longer strictly valid. The CDM particles cease to exclusively follow the gradients of the potential. However, in order to get an analytical estimate of the nonlinear contributions, it is still a useful approximation. Thus, nonlinear corrections to the continuity equation, manifest in the momentum density, are taken into account, but the linear properties of the underlying fields, density contrast and peculiar velocities, are maintained. Consequently, by virtue of equation (9.6), there is only one dynamical field, namely the density contrast, involved in the analysis. Equation (9.7) then may be written as

$$\mathbf{j}(\mathbf{k}, \eta) = -i \frac{\partial D_+(\eta)}{\partial \eta} \left[\frac{\mathbf{k}}{k^2} \delta_0(\mathbf{k}) + D_+(\eta) \int \frac{d^3 k'}{(2\pi)^3} \frac{\mathbf{k} - \mathbf{k}'}{|\mathbf{k} - \mathbf{k}'|^2} \delta_0(\mathbf{k} - \mathbf{k}') \delta_0(\mathbf{k}') \right]. \quad (9.9)$$

This expression for the current density has already been successfully used in the computation of the power spectrum of the Ostriker-Vishniac effect (Ostriker & Vishniac, 1986; Jaffe & Kamionkowski, 1998; Castro, 2003). Since in the framework presented here all nonlinear contributions to the iSW effect are solely sourced by the convolution part of the flux, it is convenient to define its rescaled divergence

$$\Theta(\mathbf{k}, \eta) \equiv -\frac{D_+(\eta)}{a} \frac{\partial D_+(\eta)}{\partial \eta} \int \frac{d^3 k'}{(2\pi)^3} \frac{\mathbf{k} \cdot (\mathbf{k} - \mathbf{k}')}{k^2 |\mathbf{k} - \mathbf{k}'|^2} \delta_0(\mathbf{k} - \mathbf{k}') \delta_0(\mathbf{k}'), \quad (9.10)$$

whereas the linear contributions are captured by

$$\tilde{\tau}(\mathbf{k}, \eta) \equiv \frac{\partial}{\partial \eta} \frac{D_+(\eta)}{a} \frac{\delta_0(\mathbf{k})}{k^2}. \quad (9.11)$$

With this the change of the gravitational potential takes the compact form

$$\frac{\partial}{\partial \eta} \Phi(\mathbf{k}, \eta) = -\frac{3}{2} H_0^2 \Omega_m [\tilde{\tau}(\mathbf{k}, \eta) - \Theta(\mathbf{k}, \eta)]. \quad (9.12)$$

In Ω_m/χ_H^2 one recognizes the gravitational coupling constant mediating between the evolving matter fields and the resulting change in the gravitational potential. Equations (9.10) and (9.11) underline the different time evolution of the linear and nonlinear iSW effect. For illustration the relevant combinations of the growth function and its derivative for three different equation of state parameters of the dark energy component (cf. equation 2.15) are plotted in Figure 9.1.

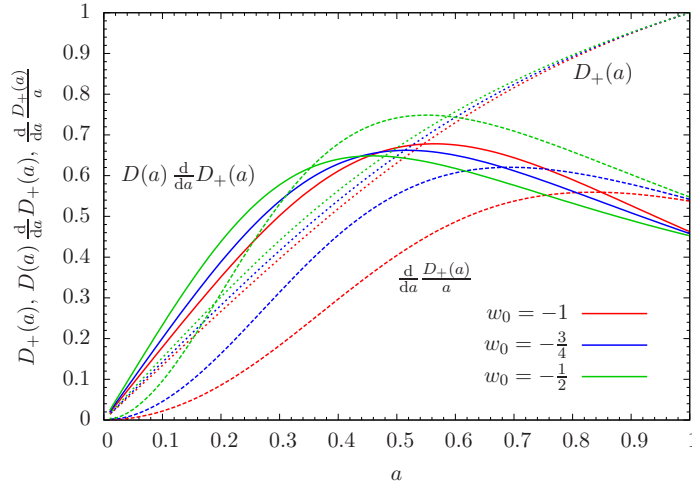


Figure 9.1: Growth function of the linear (dotted line) and nonlinear (solid line) iSW effect along with linear structure growth (dashed line), for varying equation of state parameters of the dark energy fluid.

In order to characterize the statistics of the source field $\tau(\mathbf{k}, \eta) \equiv \frac{\partial}{\partial \eta} \Phi(\mathbf{k}, \eta)$ its power spectrum is computed

$$\langle \tau(\mathbf{k}) \tau^*(\mathbf{k}') \rangle = (2\pi)^3 \delta_D(\mathbf{k} - \mathbf{k}') P_{\tau\tau}(k). \quad (9.13)$$

The cross term $P_{\tilde{\tau}\Theta}(k)$ involves the bispectrum of the density contrast. Since the density contrast is treated as a Gaussian random field its bispectrum vanishes identically. Thus, the power spectrum completely separates in its linear and first order nonlinear contributions

$$P_{\tau\tau}(k) = P_{\tilde{\tau}\tilde{\tau}}(k) + P_{\Theta\Theta}(k). \quad (9.14)$$

The linear contribution is given by $P_{\tilde{\tau}\tilde{\tau}}(k) = P_{\delta\delta}(k)/k^4$, while for the evaluation of the second term Wick's theorem (see Section A.2.1) is invoked, yielding

$$P_{\Theta\Theta}(k) = \int \frac{d^3 k'}{(2\pi)^3} \left[\frac{\mathbf{k} \cdot (\mathbf{k} - \mathbf{k}')}{k^2 |\mathbf{k} - \mathbf{k}'|^2} + \frac{\mathbf{k} \cdot \mathbf{k}'}{k^2 k'^2} \right] \frac{\mathbf{k} \cdot (\mathbf{k} - \mathbf{k}')}{k^2 |\mathbf{k} - \mathbf{k}'|^2} P_{\delta\delta}(|\mathbf{k} - \mathbf{k}'|) P_{\delta\delta}(k'). \quad (9.15)$$

At this point I would like to emphasize that in my approach the signal of the nonlinear iSW effect completely originates from the trispectrum of the density field representing velocity-density correlations. In contrast to this, contributions of this kind vanish entirely in the approach of Cooray (2002). Under the halo model, the trispectrum formed by velocity-density correlations does not contribute. In the deeply nonlinear regime it is independent of the wavevector configuration. Consequently, any anisotropic integration of this quantity cancels. Furthermore, Cooray (2002) argues that at small scales the density fluctuations are independent of the large-scale velocity field. Thus, in his approach there are no contributions from terms involving the cross-power spectra between density and velocity field. Another difference with respect to the work of Cooray (2002) results from correlations of the density field and its (conformal) time derivative. For describing these correlations Cooray (2002) borrows once more a result from the halo model assuming that for the fields involved the Cauchy-Schwarz inequality actually becomes an equality. In my approach, however, this far-reaching assumption is not necessary. At this level of approximation, correlations of this form do not contribute to the nonlinear iSW effect power spectrum because they involve the bispectrum of the (linear) density contrast which identically vanishes.

The computation of the convolution integral in equation (9.15) is most readily carried out in a coordinate system where the wavevector \mathbf{k} is aligned with the x -axis and by introducing spherical coordinates such that $\mathbf{k}' = \alpha k(\mu, \sin \vartheta \cos \phi, \sin \vartheta \sin \phi)$ with $\alpha \equiv k'/k$ and $\mu \equiv \cos \vartheta$. Expressing the CDM power spectrum in its dimensionless form, one finds

$$\Delta_{\Theta\Theta}^2(k) = \frac{1}{2} \int_0^\infty \frac{d\alpha}{\alpha^2} \int_{-1}^1 d\mu \frac{(\alpha\mu - 1) [\alpha(2\mu^2 - 1) - \mu]}{k^4 (\alpha^2 - 2\alpha\mu + 1)^{7/2}} \Delta_{\delta\delta}^2 \left(k \sqrt{\alpha^2 - 2\alpha\mu + 1} \right) \Delta_{\delta\delta}^2(\alpha k), \quad (9.16)$$

where I have defined $\Delta_{XX}^2(k) \equiv k^3 P_{XX}(k)/2\pi^2$. The corresponding angular power spectrum is obtained by Limber projection (Limber, 1953; Bartelmann & Schneider, 2001)

$$\frac{\ell(2\ell + 1)}{4\pi} C_\ell^{XX} = \frac{\pi}{\ell} \int_0^{\chi_H} \chi d\chi W_{XX}^2(\chi) \Delta_{XX}^2(k = \ell/\chi). \quad (9.17)$$

In case of the linear iSW effect, the weight function reads

$$W_{\tilde{\tau}\tilde{\tau}}(\chi) = 3\Omega_m H_0^2 \frac{\partial D_+(a)}{\partial \eta} \frac{1}{a}, \quad (9.18)$$

while for the first order nonlinear one it is given by

$$W_{\Theta\Theta}(\chi) = 3\Omega_m H_0^2 \frac{D_+(\eta)}{a} \frac{\partial}{\partial \eta} D_+(a). \quad (9.19)$$

In Figure 9.2 both weighting functions are plotted for varying equation of state parameter of the dark energy fluid. As expected, the weight function of the nonlinear iSW effect peaks at comoving distances where the one of the linear iSW effect has already started to decline rapidly. At high redshifts $\Omega_m(a)$ approaches unity so that here growth function and scale factor coincide. Consequently, the linear iSW effect vanishes identically (cf. equation 9.11).

The resulting power spectra are shown in Figure 9.3. Reflecting the additional fluctuation amplitude of the matter distribution on small spatial scales, the spectrum of the nonlinear iSW effect is much flatter than the linear one. In case of the Λ CDM model the nonlinear signal surpasses its linear counterpart at angular scales smaller than about one degree, i.e. $\ell \gtrsim 100$. For time evolving dark energy models this crossing has shifted to smaller scales. However, being of second order in the density contrast, the amplitude of the nonlinear spectrum is much less sensitive to the underlying dark energy equation of state than the linear one. Remarkably, the spectrum of the nonlinear iSW effect presented here is very similar to the result of Cooray (2002), regarding its shape and amplitude, even though Cooray (2002) worked in the deeply nonlinear regime while my analytical estimate is dedicated to the translinear

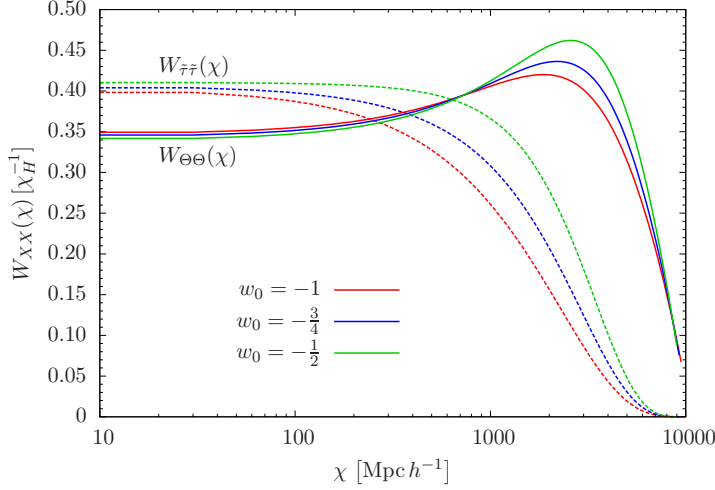


Figure 9.2: Weighting function of the linear (dashed line) and nonlinear (solid line) iSW effect, respectively, for three different values of the equation of state parameter of the dark energy component.

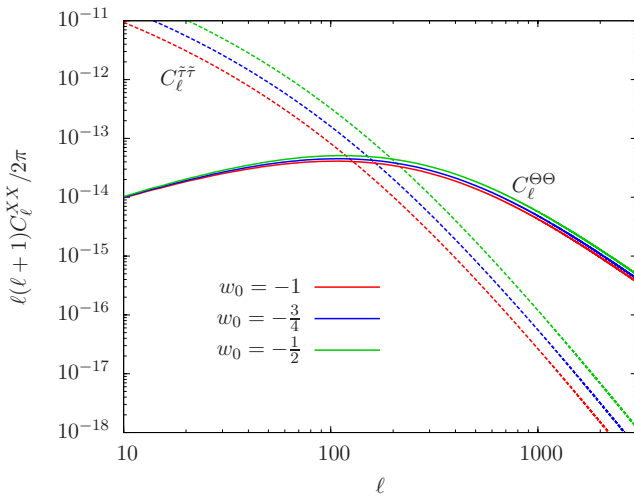


Figure 9.3: Angular power spectra of the linear (dashed line) and nonlinear (solid line) iSW effect, respectively, for three different values of the equation of state parameter of the dark energy fluid.

regime. The agreement with the angular power spectrum derived using N -body simulations (Smith et al., 2009; Cai et al., 2009, 2010) is also surprisingly good, suggesting that for a qualitative estimate of the spectrum the second order perturbative treatment presented in this chapter is already sufficient.

It is interesting to investigate the mass dependence of the nonlinear iSW effect. I focus on the Λ CDM model and smooth the power spectrum of the density contrast on different mass scales by introducing a Gaussian filter function

$$P_{\delta\delta}(k) \longrightarrow P_{\delta\delta}(k)S_R^2(k) \quad \text{with} \quad S_R(k) = \exp(-k^2R^2/2). \quad (9.20)$$

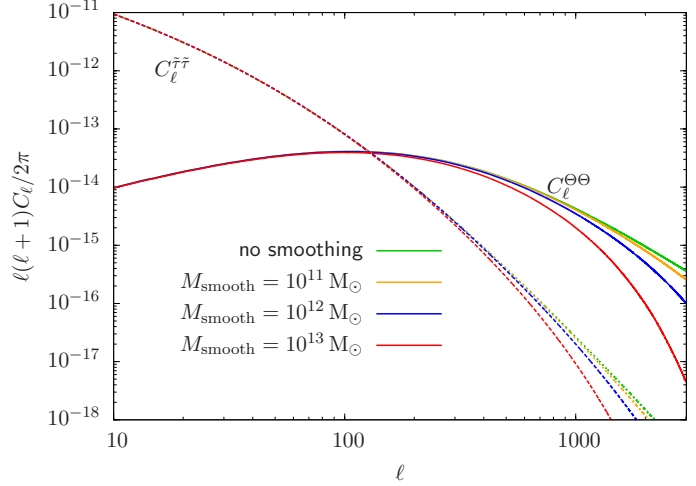
The smoothing scale R is set by the corresponding mass scale $M_{\text{smooth}} = \frac{4\pi}{3}\rho_{\text{crit}}\Omega_m R^3$. In Figure 9.4 the angular power spectra of the linear and nonlinear iSW effect are shown for three different masses, namely 10^{11} , 10^{12} and 10^{13} solar masses. Excluding objects with masses larger than 10^{13} solar masses, the power decreases considerably on small scales ($\ell \gtrsim 1000$), demonstrating that mostly cluster-size objects contribute to the signal.

9.3. Contributions to the nonlinear integrated Sachs-Wolfe effect

A deeper analysis of equation (9.10) reveals some physical insights into the origin of the nonlinear iSW effect. Mainly, one can identify two distinct sources. First, I rewrite equation (9.10) as the sum of two new fields

$$\Theta(\mathbf{k}, \eta) = \Theta_{\text{SG}}(\mathbf{k}, \eta) + \Theta_{\text{BG}}(\mathbf{k}, \eta), \quad (9.21)$$

Figure 9.4: Contributions of different mass scales to the angular power spectra of the linear (dashed line) and non-linear (solid line) iSW effect, respectively.



with

$$\Theta_{\text{SG}}(\mathbf{k}, \eta) \equiv -\frac{D_+(\eta)}{a} \frac{\partial D_+(\eta)}{\partial \eta} \int \frac{d^3 k'}{(2\pi)^3} \frac{\delta_0(\mathbf{k} - \mathbf{k}')}{|\mathbf{k} - \mathbf{k}'|^2} \delta_0(\mathbf{k}') \quad (9.22)$$

and

$$\Theta_{\text{BG}}(\mathbf{k}, \eta) \equiv \frac{D_+(\eta)}{a} \frac{\partial D_+(\eta)}{\partial \eta} \int \frac{d^3 k'}{(2\pi)^3} \frac{\mathbf{k} \cdot \mathbf{k}'}{k^2 |\mathbf{k} - \mathbf{k}'|^2} \delta_0(\mathbf{k} - \mathbf{k}') \delta_0(\mathbf{k}'). \quad (9.23)$$

Concentrating on the first term, I proceed by making use of the Poisson equation and obtain

$$\Theta_{\text{SG}}(\mathbf{k}, \eta) = \frac{H_0^{-2} \Omega_m^{-1}}{3} \frac{1}{a} \frac{\partial D_+(\eta)}{\partial \eta} \int \frac{d^3 k'}{(2\pi)^3} \Phi_0(\mathbf{k} - \mathbf{k}') \delta_0(\mathbf{k}') \quad (9.24)$$

$$= \frac{H_0^{-2} \Omega_m^{-1}}{3} \left[\frac{\partial}{\partial \eta} + H(a) \right] \int \frac{d^3 k'}{(2\pi)^3} \Phi(\mathbf{k} - \mathbf{k}', \eta) \delta(\mathbf{k}', \eta) \quad (9.25)$$

likewise in position space

$$\Theta_{\text{SG}}(\mathbf{x}, \eta) = \frac{H_0^{-2} \Omega_m^{-1}}{3} \left[\frac{\partial}{\partial \eta} + H(a) \right] \Phi(\mathbf{x}, \eta) \delta(\mathbf{x}, \eta). \quad (9.26)$$

Keeping in mind that the inverse of the prefactor has already been absorbed in the definition of the weighting function (cf. equation 9.19), the product $\Phi(\mathbf{x})\delta(\mathbf{x})$ can be interpreted as the gravitational self-energy density associated with the density contrast and its own gravitational potential. Consequently, the field Θ_{SG} may be interpreted as the (conformal) change of the gravitational self-energy density of the large-scale structure together with the variation arising from the homogeneous expansion of the background.

The interpretation of the second term is more involved. First, equation (9.23) is rewritten in a more suggestive form

$$\Theta_{\text{BG}}(\mathbf{k}, \eta) = \int \frac{d^3 k'}{(2\pi)^3} \mathbf{k}' \frac{D_+(\eta)}{a} \frac{\delta_0(\mathbf{k} - \mathbf{k}')}{|\mathbf{k} - \mathbf{k}'|^2} \cdot \frac{\partial D_+(\eta)}{\partial \eta} \frac{\mathbf{k}}{k^2} \delta_0(\mathbf{k}'). \quad (9.27)$$

By using the Poisson equation, one recognizes that the first term has the form of a gradient of the potential. The second term, however, resembles the velocity field (cf. equation 9.6). Thus, one is tempted to write

$$\Theta_{\text{BG}}(\mathbf{x}, \eta) \simeq -2\nabla\Phi(\mathbf{x}, \eta) \cdot \mathbf{v}(\mathbf{x}, \eta) \quad (9.28)$$

ignoring that equation (9.26) does not fully obey the structure of a convolution. Note that the prefactor contained in the weight function has also been restored. Although being rather symbolic, equation (9.28) has strong illustrative power. In the first term one recognizes the lensing deflection angle $\alpha = -2\nabla_\perp\Phi$ (Bartelmann & Schneider, 2001). Since the CMB temperature fluctuations are

measured along the line-of-sight, only the three-dimensional gradient perpendicular to the light ray is considered. Accordingly, the scalar product projects out the velocity components in the plane of the sky. Hence, one recovers the dipole-like temperature anisotropy pattern which is usually associated with moving gravitational lenses (Birkinshaw & Gull, 1983; Gurvits & Mitrofanov, 1986). The close relation between this effect and the nonlinear iSW effect has already been pointed out by Cooray (2002). However, neglecting the divergence part of the velocity field, Cooray (2002) does not account for the contributions of the gravitational self-energy density discussed before.

For the computation of the power spectra of the two different contributions to the nonlinear iSW effect I proceed in complete analogy to Section 9.2. In terms of the spectra of the two new fields Θ_{SG} and Θ_{BG} the power spectrum reads

$$\Delta_{\Theta\Theta}^2(k) = \Delta_{\text{SGSG}}^2(k) + \Delta_{\text{BGBG}}^2(k) + 2\Delta_{\text{SGBG}}^2(k). \quad (9.29)$$

The three different spectra involved can be jointly expressed as

$$\Delta_{XX}^2(k) = \frac{1}{2} \int_0^\infty d\alpha \int_{-1}^1 d\mu f_{XX}(k, \alpha, \mu) \Delta_{\delta\delta}^2(\alpha k) \frac{\Delta_{\delta\delta}^2(k \sqrt{\alpha^2 - 2\alpha\mu + 1})}{\alpha(\alpha^2 - 2\alpha\mu + 1)^{3/2}} \quad (9.30)$$

with

$$f_{\text{SGSG}}(k, \alpha, \mu) = \frac{2\alpha^2 - 2\alpha\mu + 1}{\alpha^2 k^4 (\alpha^2 - 2\alpha\mu + 1)^2}, \quad (9.31)$$

$$f_{\text{BGBG}}(k, \alpha, \mu) = \frac{\mu(2\alpha^2 + 2\alpha^2\mu^2 - \alpha^3\mu - 3\alpha\mu + 1)}{\alpha k^4 (\alpha^2 - 2\alpha\mu + 1)^2} \quad (9.32)$$

and the cross-spectrum

$$f_{\text{SGBG}}(k, \alpha, \mu) = -\frac{\alpha(2\alpha\mu^2 + \alpha - 3\mu) + 1}{\alpha^2 k^4 (\alpha^2 - 2\alpha\mu + 1)^2}. \quad (9.33)$$

In Figure 9.5 the three-dimensional power spectra of the gravitational self-energy density and the Birkinshaw-Gull term along with the cross-spectrum of both effects are plotted. In addition, the resulting power spectrum of the nonlinear iSW effect is shown, as well as, for comparison, the corresponding spectrum of the linear iSW effect. From scales $k \gtrsim 0.1 \text{ Mpc}^{-1} h$ on the spectra of the Θ_{SG} and Θ_{BG}

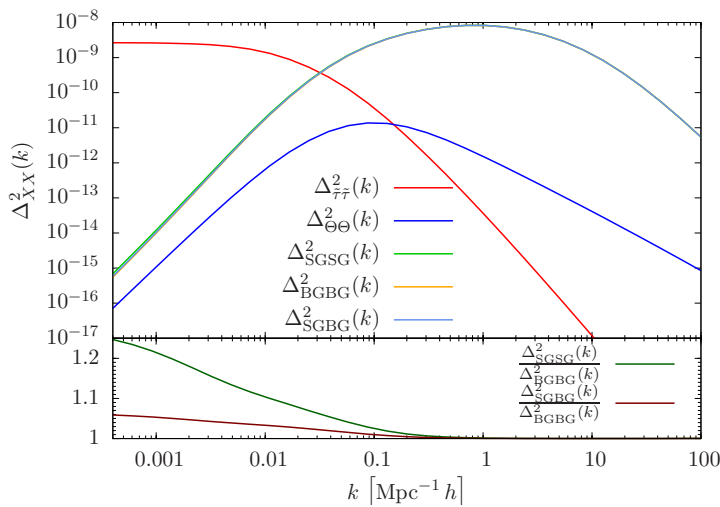
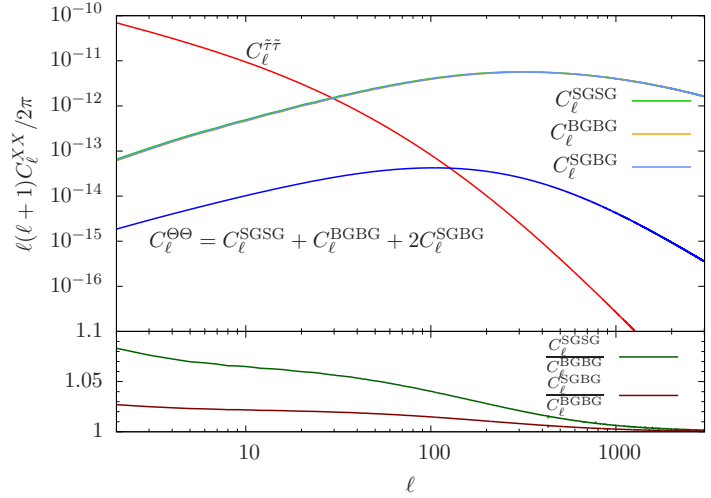


Figure 9.5: Three-dimensional power spectra of the gravitational self-energy density and Birkinshaw-Gull term comprising the nonlinear iSW effect as well as their cross-spectrum (upper panel). In the lower panel the relative strength of the signal in comparison to the Birkinshaw-Gull term is shown.

field, as well as their cross-correlation, exceed the linear signal by several orders of magnitude. However, all three spectra are almost identical, as is demonstrated in the lower panel of Figure 9.5. Only on largest scales does the relative difference amount to 10-20 per cent. Therefore, their combination

according to equation (9.29) results in the much lower signal of the nonlinear iSW effect, which starts to surpass the spectrum of the linear effect on scales $k \sim 0.2 \text{ Mpc}^{-1} h$. Furthermore, one recognizes that the three spectra peak at $k \sim 1 \text{ Mpc}^{-1} h$, whereas the maximum of their combination is shifted to larger scales ($k \sim 0.1 \text{ Mpc}^{-1} h$). Limber projection (cf. equation 9.17) of the three different spectra results in the corresponding angular power spectra shown at the top of Figure 9.6. Since the projection distributes the power of one mode over a wide multipole range the differences in the angular spectra are even smaller than in case of the three-dimensional power spectra (see lower panel of Figure 9.6). From multipoles $\ell \gtrsim 1000$ all three spectra are essentially indistinguishable.

Figure 9.6: Angular power spectra of the gravitational self-energy density and Birkinshaw-Gull term comprising the nonlinear iSW effect as well as their cross-spectrum (upper panel). The lower panel shows the relative strength of the signal in comparison to the Birkinshaw-Gull term.



9.4. Physical interpretation

To further motivate the interpretation of the contributions to the nonlinear iSW effect some analogies to the theory of gravitomagnetic potentials and classical field theory are now presented.

I start with the temperature anisotropy induced by a small lens moving with small (transverse) three-velocity \mathbf{v} . At lowest order one has (Birkinshaw & Gull, 1983; Gurvits & Mitrofanov, 1986)

$$\frac{\Delta T_{\text{BG}}}{T_{\text{CMB}}} = -2 \int d\chi \mathbf{v} \cdot \nabla \Phi, \quad (9.34)$$

where the integral is evaluated along the photon path. Albeit treating the involved fields in linear theory, the Birkinshaw-Gull effect is obviously nonlinear in the sense that the perturbed quantities enter as a product. In linear theory the velocity field can be obtained as the gradient of the potential (cf. equation 9.6). Consequently, the Birkinshaw-Gull effect is of order $O([\nabla\Phi]^2)$. In perturbation theory one can naturally construct one more term of this order, namely $\Phi\Delta\Phi$. By virtue of the Poisson equation this is exactly the gravitational self-energy density which was found in equation (9.26).

For simplicity any prefactors are dropped in the following. Then, both effects can be obtained from the auxiliary vector potential $\mathbf{A} \equiv \Phi\nabla\Phi$ by taking the divergence

$$\frac{\Delta T_{\text{RS}}}{T_{\text{CMB}}} = -2 \int d\chi \text{div } \mathbf{A} = -2 \int d\chi (\Phi\Delta\Phi + (\nabla\Phi)^2). \quad (9.35)$$

Rewriting the potential \mathbf{A} as

$$\mathbf{A}(\mathbf{x}) = \int_{\mathcal{V}} d^3x' \frac{\delta(\mathbf{x}')\nabla\Phi(\mathbf{x})}{|\mathbf{x} - \mathbf{x}'|} \quad (9.36)$$

one immediately recognizes its similarity to the gravitomagnetic potential

$$\mathbf{A}_{\text{GM}}(\mathbf{x}) \equiv \int_{\mathcal{V}} d^3x' \frac{\mathbf{j}(\mathbf{x}')}{|\mathbf{x} - \mathbf{x}'|} \simeq \int_{\mathcal{V}} d^3x' \frac{\delta(\mathbf{x}')\nabla\Phi(\mathbf{x}')}{|\mathbf{x} - \mathbf{x}'|}. \quad (9.37)$$

The vector potentials can be identified when the change of the gravitational potential may be considered to be constant over the volume of integration \mathcal{V} . As long as both vector potentials coincide, the nonlinear iSW effect is completely described by the Birkinshaw-Gull effect, as well as the gravitational self-energy term (at the corresponding order in Φ) since Schäfer & Bartelmann (2006) showed that $\Delta T_{RS}/T_{CMB} = 2 \int d\chi \operatorname{div} A_{GM}$.

There is an important difference with respect to the theory of electromagnetism. In general, the vector potential describing the magnetic field is not fully determined by the scalar potential of the electric field. The scalar potential only enters implicitly via the charge density. At the level of approximation employed in this work, however, not only the mass density ($\delta \sim \Delta\Phi$) enters the gravitomagnetic potential but the velocity field is derived from the scalar potential, too ($v \sim \nabla\Phi$). Thus, given the scalar gravitational potential, the gravitomagnetic vector potential is already completely fixed.

It is interesting to note that the contribution of the self-energy density is independent of the assumption $\nabla\Phi \simeq \text{const.}$ for $\mathbf{x} \in \mathcal{V}$. This can be seen as

$$\nabla \cdot \int_{\mathcal{V}} d^3x' \frac{\delta(\mathbf{x}') \nabla' \Phi(\mathbf{x}')}{|\mathbf{x} - \mathbf{x}'|} = \nabla \cdot \int_{\mathcal{V}} d^3x' \left(\Phi(\mathbf{x}') \nabla \frac{1}{|\mathbf{x} - \mathbf{x}'|} + \delta(\mathbf{x}') \nabla' \frac{\Phi(\mathbf{x}')}{|\mathbf{x} - \mathbf{x}'|} \right) \quad (9.38)$$

$$= -4\pi\delta(\mathbf{x}) \Phi(\mathbf{x}) + \nabla \cdot \int_{\mathcal{V}} d^3x' \delta(\mathbf{x}') \nabla' \frac{\Phi(\mathbf{x}')}{|\mathbf{x} - \mathbf{x}'|}, \quad (9.39)$$

which was first integrated by parts and subsequently the order of differentiation and integration was interchanged.

The strong similarity to the potential A also indicates why the statistics of the Birkinshaw-Gull and the self-energy density term are almost identical (cf. Figures 9.5 and 9.6). Integrated over a large volume, one expects the divergence of A to vanish due to Gauss's theorem. Accordingly, both terms, considered over a large volume, must cancel. Thus, one expects that they reveal the same statistical properties, whereas the small deviations point to the actual differences in the two vector potentials A and A_{GM} .

Finally, it is worth mentioning an analogy with the theory of massless scalar fields. Interpreting the potential Φ as scalar field interacting with an additional scalar field δ one readily computes its energy momentum tensor (cf. Liddle & Lyth, 2000)

$$T_{\mu\nu} = \partial_\mu \Phi \partial_\nu \Phi - \left(\frac{1}{2} \partial_\lambda \Phi \partial^\lambda \Phi + \delta \Phi \right) \eta_{\mu\nu} \quad (9.40)$$

where $\eta_{\mu\nu} = \text{diag}(-1, 1, 1, 1)$. Then the so-called *mechanical pressure* P of the field Φ is given by one third of the trace of the spatial part of the energy momentum tensor, i.e.

$$P \equiv \frac{1}{3} T^i_i = \frac{1}{2} \dot{\Phi}^2 - \frac{1}{6} (\nabla\Phi)^2 - \delta \Phi. \quad (9.41)$$

One now sees that, at the level of approximation used in this work, the nonlinear iSW effect measures to some extent the mechanical pressure of the gravitational potential without the contribution arising from its variation in time. That the term including time derivatives does not contribute is somewhat expected since in this derivation of the nonlinear iSW effect the continuity equation was used to express the time variation of the gravitational potential by its variation in space. The analogy with the mechanical pressure once more shows that the nonlinear iSW effect is naturally constituted by both the Birkinshaw-Gull effect, as well as the gravitational self-energy density. The halo model approach of Cooray (2002), however, cannot resolve this close relationship between these two contributions.

At the end of this section I shall comment on the apparent weakness of the presented approach. Major concerns may arise from the fact that a nonlinear effect was analysed starting from linear theory. I exploit the commonly used ansatz in perturbation theory that a product of first order fields yields a second order perturbative, i.e. nonlinear quantity. This approach, however, at the same time reveals one of the main problems of perturbation theory: it is not clear how to generalize this ansatz to

higher order. On the other hand, this disadvantage is compensated for by the extreme simplification provided by this ansatz. It allows for the reduction to one single dynamical field, the density contrast or likewise the gravitational potential. One can then easily identify the terms which contribute at the same order in the perturbative field. Furthermore, the statistical properties may be derived most conveniently by tracing back higher order correlators to the matter power spectrum (cf. Section 9.3). Thus, this approach facilitates a fully analytical treatment, which in turn offers some direct physical interpretations of the origin of the nonlinear iSW effect. These interpretations are widely inspired by analogies and always prefer the illustrative power of physical reasoning.

9.5. Summary

In this chapter the theory of the nonlinear iSW effect was revisited. I used the continuity equation to express the time evolution of the gravitational potential in terms of the divergence of the dark matter flux density. The momentum density, being the product of density and velocity field, can then be interpreted as source field of the nonlinear iSW effect.

- (i) This ansatz treats both dynamical fields, density contrast and velocity, in linear theory. Consequently, the velocity field is completely determined by the density contrast, leaving the latter as the only dynamical quantity involved in my analysis. This simplification allows for a fully analytical treatment in contrast to the previous work of [Cooray \(2002\)](#) which substantially relies on results from the halo model.
- (ii) Exploiting Wick's theorem I derived the angular power spectrum of the nonlinear iSW effect. I confirmed the shape and amplitude found by other authors using different approaches ([Seljak, 1996b](#); [Cooray, 2002](#)). Especially, I verified that the nonlinear signal surpasses that of the linear iSW effect at multipoles $\ell \gtrsim 100$.
- (iii) This analytical ansatz allowed to reveal two contributions to the nonlinear iSW effect: the Birkinshaw-Gull effect (as already pointed out by [Cooray, 2002](#)) and the conformal change of the gravitational self-energy density of the cosmic large-scale structure.
- (iv) Computing the three-dimensional power spectra and the corresponding angular power spectra of the individual contributions, it was found that they are almost identical, except on large scales, and their individual detection is certainly impossible for ongoing CMB experiments.
- (v) I showed, with simple arguments from perturbation theory, that it is natural that the Birkinshaw-Gull term is accompanied by the gravitational self-energy density term. Furthermore, I pointed out several analogies with the theory of gravitomagnetic potentials and scalar fields to highlight the physical meaning of the different contributions to the nonlinear iSW effect.

Despite its confinement to linear theory my ansatz allows for a deeper understanding of the physical processes underneath the nonlinear iSW effect, especially regarding its relation to other phenomena like the Birkinshaw-Gull effect.

10

Chapter 10

Summary and conclusions

In this thesis I investigated several aspects of the interplay between light and the large-scale structure of the Universe. The first part was concerned with the intrinsic alignment of galaxies and its impact on weak gravitational lensing measurements. Intrinsic ellipticity correlations are expected to be the most important systematic in future weak lensing analyses. Therefore, a deep understanding of intrinsic alignments is a key requirement in order to extract unbiased cosmological parameters from observations. In particular, the physical mechanisms from which they arise and their statistics, which contaminate the lensing signal, are of major interest. On the way to refined parameter constraints, weak lensing measurement techniques became more and more elaborate, culminating in tomographic and three-dimensional methods.

As a main result of my thesis I developed the fundamental formalism to consistently incorporate intrinsic alignments into the framework of $3d$ weak gravitational lensing. My method allows for the direct usage of physical alignment models and avoids any empirical parametrization common to previous work. Specifically, I employed two different models, which are linear and quadratic in the cosmic tidal field, respectively. My approach for the first time facilitated to formulate the covariance matrix of the intrinsic ellipticity field (II -alignments), as well as that of GI -alignments (the cross-correlation between the intrinsic and lensing induced ellipticity field). The latter only arise in case of the linear alignment model provided that the distribution of the underlying cosmic density perturbations is Gaussian which is a well justified assumption.

In order to compare the different alignment signals to the actual lensing signal the covariance matrices were evaluated numerically. The numerical efforts for the covariance matrices resulting from the linear alignment model are as demanding as those of the cosmic shear field itself. The enhanced numerical complexity of $3d$ cosmic shear, with respect to conventional lensing studies, mainly stems from the fact that the three-dimensional analysis invokes a basis set the radial part of which is given by spherical Bessel functions. Their highly oscillatory behaviour complicates any harmonic space integration. The complexity of the quadratic model is then further aggravated by the internal mode coupling, which results from the products of tidal tensors. This mode coupling contains numerous slowly converging sums in multipole space, leaving a direct numerical evaluation impossible.

For this reason I concentrated the numerical efforts on the linear alignment model. I found that for a shallow redshift survey with median redshift $z_{\text{median}} = 0.3$ II -alignments dominate the total covariance matrix for large multipoles, which underlines the fact that intrinsic alignments are a small-scale phenomenon. The situation is different for the forthcoming *Euclid* mission, which is much more extended in redshift ($z_{\text{median}} = 0.9$). Here the lensing signal contributes most for all multipoles. In comparison to lensing the II -alignment contamination is more than one order of magnitude smaller. Comparing the two alignment types, I found that, opposed to two-dimensional lensing studies, the GI -signal is only slightly enhanced, if at all, with respect to the II -contributions. They are the dominant contaminant on almost all scales for both survey specifications under consideration.

Concerning the three-dimensional shape of the covariance matrices in the k - k' -plane I showed that

there is a fundamental difference between cosmic shear on the one hand and intrinsic alignments on the other hand. Assuming a *Euclid*-like survey, the lensing covariance matrix adopts a rather circular shape, whereas those of the *II*- and *GI*-alignments are strongly elongated along the diagonal $k = k'$. In particular, for large multipoles ($\ell \sim 100$) the covariance matrices of both alignment types tend to almost completely concentrate along this diagonal.

These results stimulate the demand for a numerical evaluation of the quadratic model, too. One possibility might be to resort to a hybrid approach, interpolating between pure $3d$ cosmic shear and conventional tomographic methods, which allows to speed up $3d$ weak lensing computations (Kitching et al., 2011). However, one has to be careful that such an approach is not too coarse for an accurate description of intrinsic alignments. It needs to be assured that it does not accidentally remove parts of the alignment signal. A reliable numerical implementation of the quadratic model therefore has to be considered as a long-term goal. But in the meantime my findings for the linear alignment model may serve as the starting point for a detailed quantitative study of the parameter estimation bias in $3d$ cosmic shear measurements due to the presence of intrinsic alignments.

In the conventional two-dimensional lensing formalism numerous studies of this kind have already successfully been carried out. In contrast to its formulation in the framework of $3d$ cosmic shear, the quadratic alignment model can be used without any numerical difficulties in such analyses. Nevertheless, previous efforts in this field have exclusively addressed the linear alignment model. In order to bridge this gap I computed the biases associated with the quadratic alignment model for a minimal set of cosmological parameters. In my analysis I took a two-dimensional non-tomographic weak lensing measurement as a basis. I found that the matter density Ω_m and the normalization of the linearly evolved matter power spectrum σ_8 are most strongly affected. The equation of state parameter of the dark energy component, however, turns out to be rather insensitive to the presence of intrinsic ellipticity correlations derived from the quadratic model. This is opposed to findings from studies which have been carried out for the linear alignment model. The parameter describing the time evolution of the dark energy fluid is severely biased here.

These differences underline the importance of the investigation of different models to gradually improve the understanding of intrinsic alignments and their impact on cosmic shear measurements. It seems that both models comprise complementary properties, as they apply to distinct galaxy morphologies. Future work should therefore address a combined analysis aiming at a realistic morphological mix of source galaxies. In addition, an extension to tomographic methods would be desirable and is in fact one of the subjects of my current research.

The great advantage of the quadratic alignment model, in comparison to its linear counterpart, is that its free parameters do not need to be inferred from galaxy shape measurements which are the main weak lensing observable. Since in this model intrinsic shape correlations result from correlations in the angular momenta of neighbouring galaxies, all model parameters are in principle accessible in appropriate structure formation simulations. The close relationship between intrinsic alignments and galactic angular momentum couplings motivated my investigation of the latter in the course of this thesis. In my analysis angular momentum acquisition was described in the framework of tidal torque theory. This mechanism has recently been questioned by results from numerical simulations and its applicability is subjected to certain restrictions. These limitations, however, are compensated for by the fact that tidal torque theory allows for a fully analytical treatment, which comprises the most important properties of galactic angular momenta. In particular, it is well suited for a statistical description where the formation process of individual galaxies is of minor importance.

I focused on the two-point correlation function of galactic angular momenta. According to tidal torque theory in the Zel'dovich approximation, the angular momentum vector of a galaxy may be described by 15 Gaussian variates; the covariance of which is given in terms of the linear matter power spectrum. Since galaxy formation is assumed to only take place at peaks in the cosmic density field the underlying random process is discrete. The peak restriction reduces the dimensionality of the probability distribution to 12. Hence, the joint distribution function describing angular momentum

correlations is 24-dimensional. This high dimensionality was the main difficulty in the computation of the correlation function. In fact, its evaluation has been considered to be impossible only a decade ago. In this thesis, however, I showed that an improved sampling strategy does allow for a numerical evaluation. It can be carried out on a standard personal computer within a reasonable amount of time. Applying this new evaluation scheme, I verified the fundamental scaling relation between specific angular momentum and halo mass, as predicted by tidal torque theory. Finally, I estimated the typical correlation length of galactic angular momenta for Milky Way-sized objects to be about $1 \text{ Mpc } h^{-1}$. This is in excellent agreement with previous studies carried out for less involved angular momentum models. In the perspective of intrinsic alignments, my findings support the fact that intrinsic shape correlations, i.e. *II*-alignments, only arise between physically close-by galaxies.

In the second part of my thesis I considered two important secondary anisotropies of the cosmic microwave background: weak gravitational lensing and the nonlinear integrated Sachs-Wolfe effect. CMB lensing has become directly accessible by the unprecedented precision of the ongoing *Planck* mission, and is exploited as a precious source of additional information (Planck Collaboration, 2013a,b). The reconstruction of the CMB lensing potential power spectrum in particular allows to break parameter degeneracies in the primary temperature anisotropies, revealing valuable insight into the late-time Universe. As in the case of cosmic shear analyses, a reliable control of systematics is essential in order to take full advantage of the constraining power of the observations. For the CMB lensing potential power reconstruction primordial non-Gaussianities are one of these systematic effects. In my thesis I investigated the reconstruction bias due to the presence of primordial non-Gaussianity of local type, the amplitude of which is characterized by the so-called f_{NL} parameter.

Since the reconstruction scheme is based on the connected part of the CMB temperature trispectrum, any of its contributions other than lensing necessarily affects the reconstructed power. I improved upon earlier work by leaving the flat-sky approximation behind and providing analytical expressions for the reconstruction bias on the full sky. This is particularly important as in high-precision CMB experiments like *Planck* the curvature of the sky may not be neglected any more.

The analytical predictions of the bias associated with local non-Gaussianity were confronted with results from numerical simulations. In these simulations I could consistently model both contributions to the CMB trispectrum, lensing and primordial non-Gaussianity, as well as experimental noise. It turned out that the bias found from the simulations is about two orders of magnitude larger than the leading order calculations suggested. Treating the lensing effect separately from primordial non-Gaussianity revealed that lensing of the f_{NL} trispectrum amplifies the corresponding bias only by roughly 50 per cent. Thus, the major extent of the discrepancy found from the simulations is presumably due to those parts of the f_{NL} induced trispectrum, which are of higher order than f_{NL}^2 , and have not been considered in the analytical treatment. The overall strength of the bias is set by the amplitude of the non-Gaussian contributions. This, however, is quite small, $f_{\text{NL}} \sim \mathcal{O}(10)$. Therefore, the bias does not compromise the *Planck* data analysis at all.

From a theoretical point of view it would be interesting to further disentangle the distinct contributions to the bias to at least the next higher order in f_{NL} . These calculations, however, become quite involved and the complex structure of the resulting mode coupling faces the same numerical challenges encountered in the evaluation of the quadratic alignment model discussed before. The feasibility of an extension of the analytical results presented in this work is therefore rather questionable, especially with respect to the efforts required by its numerical implementation.

Regarding the four-momentum of a photon, the lensing effect may be interpreted as the rotation of the photons's (three-dimensional) wavevector by the spatial gradient of the gravitational potential, leaving the photon's energy unchanged. This is contrary to the time variation of the Newtonian potential which does change the photon's frequency and therefore the effective CMB temperature. Integrated along the line-of-sight, the corresponding (secondary) CMB anisotropy is known as the integrated Sachs-Wolfe effect. In this thesis I proposed a novel, fully analytical, description of the nonlinear iSW or Rees-Sciama effect, which is sourced by the nonlinear time evolution of the gravita-

tional potential.

The main purpose of this ansatz was to gain further insights into the theory of the nonlinear iSW effect as a post-Newtonian relativistic effect on propagating photons. First and foremost, I aimed at revealing the different contributions to the signal, rather than at its precise calculation. The fully analytical treatment of a nonlinear effect inevitably requires a number of simplifications. I chose a perturbative ansatz which includes second order contributions but keeps the linear time evolution of the individual constituents. These constituents were the (linear) cosmic density contrast and the peculiar velocity field, which are directly related to each other in linear theory. One of the advantages of this ansatz is that all terms of the very same perturbative order may be readily identified and their individual contributions to the total signal become transparent. By construction, the applicability of my approach is naturally restricted to the translinear regime. Nonetheless, the qualitative agreement of the resulting angular power spectrum in comparison to results of both, alternative analytical descriptions and numerical simulations, is surprisingly good.

I was able to identify two distinct sources: the change of the gravitational self-energy density with conformal time and gravitational lenses moving with the large-scale matter stream. The latter is also known as Birkinshaw-Gull effect. These contributions, in particular their lucid physical interpretation, remain hidden in the standard derivation of the nonlinear iSW effect. An observational discrimination between the two contributions is practically excluded, not only because the detection of the nonlinear iSW effect itself is extremely difficult but mostly due to the fact that the (two-point) statistics of both contributions is almost identical on all, but the largest angular scales. There, however, the signal of the linear iSW effect is largely dominating.

A

Appendix A

Mathematical details

In this appendix I compile several mathematical details which have been excluded from the main part of this thesis. The first part is devoted to some key concepts of differential geometry, while the second contains the statistical supplement. Most of the contents presented in Section A.1 can be found in much more detail in [Nakahara \(2003\)](#) and [Wald \(2005\)](#).

A.1. Riemannian geometry

A.1.1. Levi-Civita connection

The most basic definition of an n -dimensional *manifold* might be given as a topological space which locally looks like \mathbb{R}^n . The existence of smooth coordinate systems ensures calculus on it. If a manifold is additionally endowed with a metric tensor, there exists a generalization of the inner product of two vectors in \mathbb{R}^n . Such a structure is essential for the notion of both lengths of and angles between vectors, which belong to the same tangent space. Furthermore, the metric can be used to define a *connection*. It allows to compare vectors which belong to different tangent spaces. The transport from one tangent space to the other must not change the vector. Parallel transport of a vector field W along a vector field V thus requires that the directional or *covariant derivative* of W along V

$$\nabla_V W = V^\mu \underbrace{\left(\frac{\partial W^\lambda}{\partial x^\mu} + W^\nu \Gamma_{\mu\nu}^\lambda \right)}_{\equiv \nabla_\mu W^\lambda} \frac{\partial}{\partial x^\lambda} \quad (\text{A.1})$$

vanishes, i.e. $\nabla_V W = 0$. On a (pseudo-) Riemannian manifold the *connection coefficients* or *Christoffel symbols* $\Gamma_{\mu\nu}^\lambda$ are uniquely defined in terms of the (inverse) metric and its derivatives

$$\Gamma_{\mu\nu}^\lambda = \frac{1}{2} g^{\kappa\lambda} \left(\frac{\partial g_{\kappa\nu}}{\partial x^\mu} + \frac{\partial g_{\kappa\mu}}{\partial x^\nu} - \frac{\partial g_{\mu\nu}}{\partial x^\kappa} \right). \quad (\text{A.2})$$

This so-called Levi-Civita connection is torsion-free, i.e. $\Gamma_{\mu\nu}^\lambda = \Gamma_{\nu\mu}^\lambda$, and metric-compatible, i.e. $(\nabla_\kappa g)_{\mu\nu} = 0$.

Christoffel symbols for scalar perturbations of the FLRW metric

Equation (A.2) can now be used to compute the connection obtained from the perturbed FLRW metric (3.6). I assume $\hat{\gamma}_{ij} = \delta_{ij}$ in equation (3.6) for convenience. The resulting non-vanishing Christoffel symbols are compiled in Table A.1. Both the contributions from the homogeneous and isotropic background $\hat{\Gamma}_{\mu\nu}^\lambda$, and those of the perturbations $\delta\Gamma_{\mu\nu}^\lambda$ (to first order in the Newtonian potential), are listed, i.e. $\Gamma_{\mu\nu}^\lambda = \hat{\Gamma}_{\mu\nu}^\lambda + \delta\Gamma_{\mu\nu}^\lambda$. The speed of light has been set equal to one for clarity.

Table A.1.: Christoffel symbols of the perturbed FLRW metric.

Christoffel symbol $\Gamma_{\mu\nu}^\lambda$	background $\hat{\Gamma}_{\mu\nu}^\lambda$	perturbation $\delta\Gamma_{\mu\nu}^\lambda$
Γ_{00}^0	$aH(a)$	$\frac{\partial\Phi}{\partial\eta}$
Γ_{00}^i	0	$\frac{\partial\Phi}{\partial x^i}$
$\Gamma_{0i}^0 = \Gamma_{i0}^0$	0	$\frac{\partial\Phi}{\partial x^i}$
$\Gamma_{0j}^i = \Gamma_{j0}^i$	$aH(a)$	$\Phi\delta_j^i$
$\Gamma_{ij}^0 = \Gamma_{ji}^0$	$aH(a)$	$-\left(2aH(a)\Phi + \frac{\partial\Phi}{\partial\eta}\right)\delta_{ij}$

A.1.2. Riemann curvature tensor

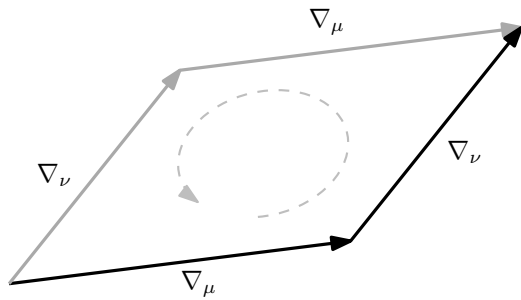
Albeit a two-dimensional plane is obviously flat, the corresponding connection coefficients are non-zero if for example polar coordinates are employed. Therefore, the connection coefficients cannot serve as measure of the intrinsic curvature of a manifold. In fact, for any point on a manifold there always exists a transformation to *normal coordinates* in which the Christoffel symbols vanish. From the view point of General Relativity this is just a manifestation of Einstein's equivalence principle (Will, 2001). The connection, however, can be used to define the *Riemann tensor* $R(X, Y)Z$, which does characterize the curvature of the manifold

$$R(X, Y)Z \equiv \nabla_X \nabla_Y Z - \nabla_Y \nabla_X Z - \nabla_{[X, Y]} Z, \quad (\text{A.3})$$

where X, Y and Z are vector fields. The geometrical meaning of this tensor becomes obvious if one computes the commutator of the covariant derivative in the coordinate basis

$$[\nabla_\mu, \nabla_\nu] V^\lambda \equiv \nabla_\mu \nabla_\nu V^\lambda - \nabla_\nu \nabla_\mu V^\lambda = R^\lambda{}_{\sigma\mu\nu} V^\sigma. \quad (\text{A.4})$$

While equation (A.3) is valid for any connection, equation (A.4) does only hold true for a torsion free connection like the Levi-Civita connection (A.2). Since the covariant derivative of a vector


Figure A.1.: Geometrical meaning of the Riemann curvature tensor.

measures its difference with respect to a vector which would have been parallel transported along the same direction one can think of the commutator (A.4) as the difference which results from moving a vector along an infinitesimal closed loop (cf. Figure A.1). This difference obviously depends on the intrinsic curvature of the manifold.

The Riemann tensor constructed from the Levi-Civita connection obeys several symmetries, reducing the number of its independent components considerably. There are only $n^2(n^2 - 1)/12$ independent components. A further consequence of these symmetries is that there is only one independent contraction of the Riemann tensor, the *Ricci tensor* $R_{\mu\nu} = g^{\alpha\beta} R_{\beta\mu\alpha\nu} = R^\alpha{}_{\mu\alpha\nu}$. Its trace is the *Ricci scalar* (or *curvature scalar*) $R = g^{\mu\nu} R_{\mu\nu} = R^\nu{}_\nu$. Their appropriate combination fulfils the *contracted Bianchi identity* $\nabla^\mu \left(R_{\mu\nu} - \frac{1}{2} R g_{\mu\nu} \right) = 0$, ensuring that the energy momentum tensor which enters Einstein field equations (2.3) is divergence free.

A.1.3. Killing vectors and maximally symmetric spaces

A Killing vector k singles out a special direction in space in the sense that the local geometry does not change along this direction. Formally, this is expressed by the vanishing *Lie derivative* of the metric along k , i.e. $\mathcal{L}_k g = 0$. In components the *Killing equation* reads

$$(\mathcal{L}_k g)_{\mu\nu} = \nabla_\mu k_\nu + \nabla_\nu k_\mu = 0. \quad (\text{A.5})$$

While the covariant derivative of the metric vanishes for any vector field by construction, the Lie derivative is defined independently of the metric. Therefore, the existence of a Killing vector field indicates a certain *symmetry* of the manifold.

Spaces which admit $n(n+1)/2$ linear independent Killing vector fields, i.e. the maximal number possible, are called *maximally symmetric spaces*. Those spaces are spaces of constant curvature in the sense that the Ricci scalar is constant. In case of the Robertson-Walker metric (2.5) the spatial hypersurfaces are maximally symmetric spaces and the corresponding Ricci scalar is proportional to the (constant) curvature parameter K .

A.2. Statistics

A.2.1. Wick theorem

Since most inflationary models predict Gaussian or almost Gaussian initial conditions (see Section 2.4.3) higher order correlators, for example of the cosmic density field, can be expressed in terms of the correlation function or equivalently in terms of the power spectrum by virtue of *Wick's theorem*:

For even n the n -point correlator of a collection of Gaussian variables $X_{i_1}, X_{i_2}, \dots, X_{i_n}$ can be obtained by summing all the possible products of two-point correlators made from the variables $\{X_{i_n}\}$,

$$\langle X_{i_1} \dots X_{i_{2n}} \rangle = \sum_{\{j_1, \dots, j_{2n}\} = \{i_1, \dots, i_{2n}\}} \langle X_{j_1} X_{j_2} \rangle \times \dots \times \langle X_{j_{2n-1}} X_{j_{2n}} \rangle, \quad (\text{A.6})$$

where the sum is to be taken over all permutations which give rise to different pairs.

A proof of this important theorem is provided by [Durrer \(2008\)](#).

A.2.2. Characteristic function

Finally, I would like to introduce the *characteristic function* φ_X of the random variable X

$$\varphi_X(t) \equiv \langle e^{iXt} \rangle = \int dX \rho(X) e^{iXt}. \quad (\text{A.7})$$

Being related by Fourier transformation, the characteristic function is dual to the probability density function ρ ; it conveys all information about its properties and behaviour. Due to this duality the probability density function may be reconstructed from measurements of the moments $\langle X^n \rangle$. For a random variable with zero mean the characteristic function can be written as

$$\varphi_X(t) = \sum_{n=0}^{\infty} \frac{(it)^n}{n!} \langle X^n \rangle. \quad (\text{A.8})$$

Subsequent Fourier transformation yields the probability density function.

B

Appendix B

Calculational details

This appendix gathers additional material to the Chapters 5, 6 and 8.

B.1. Derivation of the covariance matrix of the quadratic model

In this appendix the missing steps in the derivation of of the covariance matrix of the quadratic intrinsic ellipticity model used in Chapter 5 (see equation 5.53) are given. In order to simplify the notation I denote multipoles with a bar $\bar{\ell}$ when I refer to ℓ and m at the same time. I begin with the computation of $\langle \epsilon_{\ell m}(k) \epsilon_{\ell' m'}^*(k') \rangle$. Denoting the trispectrum of the Newtonian gravitational potential evaluated today by

$$\mathbb{T}_{\bar{\ell}'_1 \bar{\ell}'_2}^{\bar{\ell}_1 \bar{\ell}_2}(k_1, k_2, k'_1, k'_2) \equiv \left\langle \Phi_{\ell_1 m_1}^{S,0}(k_1) \Phi_{\ell_2 m_2}^{S,0}(k_2) \Phi_{\ell'_1 m'_1}^{S,0*}(k'_1) \Phi_{\ell'_2 m'_2}^{S,0*}(k'_2) \right\rangle \quad (\text{B.1})$$

one has

$$\langle \epsilon_{\ell m}(k) \epsilon_{\ell' m'}^*(k') \rangle = C_2^2 \sum_{\bar{\ell}_1, \bar{\ell}_2, \bar{\ell}'_1, \bar{\ell}'_2} \bar{Q}_{\bar{\ell}_1 \bar{\ell}_2 \bar{\ell}}^k(k_1, k_2) \bar{Q}_{\bar{\ell}'_1 \bar{\ell}'_2 \bar{\ell}'}^{k'}(k'_1, k'_2) \mathbb{T}_{\bar{\ell}'_1 \bar{\ell}'_2}^{\bar{\ell}_1 \bar{\ell}_2}(k_1, k_2, k'_1, k'_2). \quad (\text{B.2})$$

In the last equation I have defined

$$\bar{Q}_{\bar{\ell}_1 \bar{\ell}_2 \bar{\ell}}^k(k_1, k_2) \equiv (-1)^{m+1} \sqrt{\frac{2}{\pi^3}} \ell_1 (\ell_1 + 1) \sqrt{\frac{(\ell_2 + 2)!}{(\ell_2 - 2)!}} \mathcal{W}_{m_1 m_2 m}^{\ell_1 \ell_2 \ell} \mathcal{I}_{\ell_1 \ell_2 \ell}(k_3, k_4, k) \tilde{\eta}_{\ell_1}(k_3, k_1) \tilde{\eta}_{\ell_2}(k_4, k_2). \quad (\text{B.3})$$

Exploiting the orthogonality of the spherical Bessel functions

$$\int k^2 dk j_{\ell}(k\chi) j_{\ell}(k\chi') = \frac{\pi}{2\chi^2} \delta_{\text{D}}(\chi - \chi') \quad (\text{B.4})$$

(Abramowitz & Stegun, 1972) the matrix product in equation (B.3) can be simplified considerably.

Introducing

$$\tilde{\mathcal{I}}_{\ell_1 \ell_2 \ell}(k_1, k_2, k) \equiv \frac{\pi}{2} \int \frac{d\chi}{\chi^2} j_{\ell_1}(k_1 \chi) j_{\ell_2}(k_2 \chi) j_{\ell}(k \chi) \quad (\text{B.5})$$

one is left with

$$\bar{Q}_{\bar{\ell}_1 \bar{\ell}_2 \bar{\ell}}^k(k_1, k_2) \equiv (-1)^{m+1} \sqrt{\frac{2}{\pi^3}} \ell_1 (\ell_1 + 1) \sqrt{\frac{(\ell_2 + 2)!}{(\ell_2 - 2)!}} \mathcal{W}_{m_1 m_2 m}^{\ell_1 \ell_2 \ell} \tilde{\mathcal{I}}_{\ell_1 \ell_2 \ell}(k_1, k_2, k). \quad (\text{B.6})$$

As explained in Section 5.3.2, the trispectrum is evaluated via Wick's theorem given in Appendix A.2.1. The trispectrum is then diagonal in the respective combinations of k_i and $\bar{\ell}_i$. Therefore, the sums over $\bar{\ell}'_{1,2}$ collapse. The remaining sums over $m_{1,2}$ trivializes due to the fact that

$$\sum_{m_1, m_2} \begin{pmatrix} \ell_1 & \ell_2 & \ell \\ m_1 & m_2 & m \end{pmatrix} \begin{pmatrix} \ell_1 & \ell_2 & \ell' \\ m_1 & m_2 & m' \end{pmatrix} = \frac{1}{2\ell + 1} \delta_{\ell \ell'} \delta_{m m'}. \quad (\text{B.7})$$

Having removed the entire $m_{1,2}$ dependence I now set

$$\mathcal{Q}_{\ell_1 \ell_2 \ell}^k(k_1, k_2) \equiv \sqrt{\frac{2}{\pi^3}} \ell_1 (\ell_1 + 1) \sqrt{\frac{(\ell_2 + 2)!}{(\ell_2 - 2)!}} \begin{pmatrix} \ell_1 & \ell_2 & \ell \\ 0 & -2 & 2 \end{pmatrix} \Pi_{\ell_1 \ell_2 \ell} \tilde{\mathcal{I}}_{\ell_1 \ell_2 \ell}(k_1, k_2, k) \quad (\text{B.8})$$

and exploit another property of the Wigner 3j-symbols, namely

$$\begin{pmatrix} \ell_1 & \ell_2 & \ell \\ m_1 & m_2 & m \end{pmatrix} = (-1)^{\ell_1 + \ell_2 + \ell} \begin{pmatrix} \ell_2 & \ell_1 & \ell \\ m_2 & m_1 & m \end{pmatrix}, \quad (\text{B.9})$$

to arrive at

$$\langle \epsilon_{\ell m}(k) \epsilon_{\ell' m'}^*(k') \rangle = \frac{A^4 C_2^2}{2\ell + 1} \sum_{\ell_1, \ell_2} \mathcal{Q}_{\ell_1 \ell_2 \ell}^k(k_3, k_4) \frac{P_{\delta\delta}(k_3)}{k_3^4} \frac{P_{\delta\delta}(k_4)}{k_4^4} \left(\mathcal{Q}_{\ell_1 \ell_2 \ell}^{k'}(k_3, k_4) + (-1)^{\ell_1 + \ell_2 + \ell} \mathcal{Q}_{\ell_2 \ell_1 \ell}^{k'}(k_3, k_4) \right). \quad (\text{B.10})$$

Equation (5.53) may then be recovered by setting

$$\mathcal{B}_{\ell \ell_1 \ell_2}^k(k_3, k_4) \equiv \mathcal{Z}_\ell(k, k'') \mathcal{M}_\ell(k'', k''') \mathcal{Q}_{\ell_1 \ell_2 \ell}^{k'''}(k_3, k_4). \quad (\text{B.11})$$

B.2. Mode coupling functions

In Fourier space the quadratic alignment model of Chapter 6 becomes a convolution. This appendix provides the explicit form of the resulting mode coupling functions. In case of the gradient or E -mode it reads

$$\begin{aligned} f_E(\mathbf{a}, \mathbf{b}, c) &= \frac{1}{2} (2c^2 - a^2) [b^4 + (\mathbf{a} \cdot \mathbf{b})^2 - (\mathbf{a} \times \mathbf{b})^2 + 2b^2(\mathbf{a} \cdot \mathbf{b})] \\ &\quad + \frac{1}{2} (2c^2 - b^2) [a^4 + (\mathbf{a} \cdot \mathbf{b})^2 - (\mathbf{a} \times \mathbf{b})^2 + 2a^2(\mathbf{a} \cdot \mathbf{b})] \\ &\quad + 3c^2 [(\mathbf{a} + \mathbf{b})^2(\mathbf{a} \cdot \mathbf{b}) + 2(\mathbf{a} \times \mathbf{b})^2], \end{aligned} \quad (\text{B.12})$$

while one finds for the curl or B -mode

$$f_B(\mathbf{a}, \mathbf{b}, c) = (c^2 - \mathbf{a} \cdot \mathbf{b})(a^2 - b^2)(\mathbf{a} \times \mathbf{b}) \quad (\text{B.13})$$

(Mackey et al., 2002). Here \mathbf{a} and \mathbf{b} denote two-dimensional vectors and c is a real number. Obviously, f_E is a true scalar, whereas f_B is a pseudo scalar. The coupling functions obey the following symmetries

$$f_{E,B}(\mathbf{a}, \mathbf{b}, c) = f_{E,B}(\mathbf{a}, \mathbf{b}, -c) = f_{E,B}(\mathbf{b}, \mathbf{a}, c). \quad (\text{B.14})$$

B.3. Some flat-sky expressions

Here the flat-sky expressions used in Chapter 8 are compiled. Starting with the lensing reconstruction bias linear in the lensing potential (cf. equation 8.11), the normalization reads

$$A^{-1}(L) = \int \frac{d^2 \ell_1}{(2\pi)^2} f(\ell_1, \ell_2) g(\ell_1, \ell_2), \quad (\text{B.15})$$

while the optimal weights are given by

$$g(\ell_1, \ell_2) = \frac{f(\ell_1, \ell_2)}{2C_{\ell_1, \text{obs}}^{\Theta\Theta} C_{\ell_2, \text{obs}}^{\Theta\Theta}} = \frac{\ell_1 \cdot \mathbf{L} C_{\ell_1}^{\Theta\Theta} + \ell_2 \cdot \mathbf{L} C_{\ell_2}^{\Theta\Theta}}{2C_{\ell_1, \text{obs}}^{\Theta\Theta} C_{\ell_2, \text{obs}}^{\Theta\Theta}} \quad (\text{B.16})$$

with the additional condition $\ell_1 + \ell_2 = L$ imposed.

Finally, the expression for the intermediate quantities $\mathcal{P}_{\ell_3\ell_4}^{\ell_1\ell_2}(L)$, which build up the flat-sky fully reduced CMB trispectrum associated with primordial non-Gaussianity of local type (cf. equation 8.23), reads

$$\mathcal{P}_{\ell_3\ell_4}^{\ell_1\ell_2}(L) = \int r_1^2 dr_1 \int r_2^2 dr_2 F_L(r_1, r_2) [\alpha_{\ell_1}(r_1)\beta_{\ell_2}(r_1) + \alpha_{\ell_2}(r_1)\beta_{\ell_1}(r_1)] [\alpha_{\ell_3}(r_2)\beta_{\ell_4}(r_2) + \alpha_{\ell_4}(r_2)\beta_{\ell_3}(r_2)] \quad (\text{B.17})$$

with $F_L(r_1, r_2)$, $\alpha_{\ell}(r)$ and $\beta_{\ell}(r)$ defined in equations (8.16) - (8.18).

Bibliography

- Abdalla F. B., Amara A., Capak P., Cypriano E. S., Lahav O., Rhodes J., 2008, *MNRAS*, 387, 969
- Abramowitz M., Stegun I. A., 1972, *Handbook of Mathematical Functions*. Dover, New York
- Abramowitz M., Stegun I. A., Romer R. H., 1988, *American Journal of Physics*, 56, 958
- Adler R. J., 1981, *The Geometry of Random Fields*. Wiley, Chichester
- Aghanim N., Majumdar S., Silk J., 2008, *Reports on Progress in Physics*, 71, 066902
- Alabidi L., Malik K., Byrnes C. T., Choi K.-Y., 2010, *J. Cosmology Astropart. Phys.*, 11, 37
- Alishahiha M., Silverstein E., Tong D., 2004, *Phys. Rev. D*, 70, 123505
- Amendola L., Tsujikawa S., 2010, *Dark Energy: Theory and Observations*. Cambridge Univ. Press, Cambridge
- Amendola, L. et al., 2012, preprint (arXiv:1206.1225)
- Anselmi S., Matarrese S., Pietroni M., 2011, *J. Cosmology Astropart. Phys.*, 6, 15
- Anselmi S., Pietroni M., 2012, *J. Cosmology Astropart. Phys.*, 12, 13
- Arfken G. B., Weber H. J., 2005, *Mathematical methods for physicists*. Elsevier Academic Press, Amsterdam
- Arkani-Hamed N., Creminelli P., Mukohyama S., Zaldarriaga M., 2004, *J. Cosmology Astropart. Phys.*, 4, 1
- Ayaita Y., Schäfer B. M., Weber M., 2012, *MNRAS*, 422, 3056
- Bacon D. J., Goldberg D. M., Rowe B. T. P., Taylor A. N., 2006, *MNRAS*, 365, 414
- Bardeen J. M., Bond J. R., Kaiser N., Szalay A. S., 1986, *ApJ*, 304, 15
- Bardeen J. M., Steinhardt P. J., Turner M. S., 1983, *Phys. Rev. D*, 28, 679
- Barnaby N., Cline J. M., 2008, *J. Cosmology Astropart. Phys.*, 6, 30
- Bartelmann M., 2010a, *Reviews of Modern Physics*, 82, 331
- Bartelmann M., 2010b, *Classical and Quantum Gravity*, 27, 233001
- Bartelmann M., Schneider P., 2001, *Physics Reports*, 340, 291
- Bennett, C. L. et al., 2012, *ApJS*, in press (arXiv:1212.5225)
- Bernstein G. M., 2009, *ApJ*, 695, 652
- Bersanelli M., Bensadoun M., de Amici G., Levin S., Limon M., Smoot G. F., Vinje W., 1994, *ApJ*, 424, 517

- Birkinshaw M., Gull S. F., 1983, *Nature*, 302, 315
- Blandford R. D., Saust A. B., Brainerd T. G., Villumsen J. V., 1991, *MNRAS*, 251, 600
- Bond J. R., Myers S. T., 1996a, *ApJS*, 103, 1
- Bond J. R., Myers S. T., 1996b, *ApJS*, 103, 41
- Bond J. R., Myers S. T., 1996c, *ApJS*, 103, 63
- Bonvin C., 2008, *Phys. Rev. D*, 78, 123530
- Boughn S., Crittenden R., 2004, *Nature*, 427, 45
- Boylan-Kolchin M., Springel V., White S. D. M., Jenkins A., Lemson G., 2009, *MNRAS*, 398, 1150
- Bridle S., King L., 2007, *New Journal of Physics*, 9, 444
- Bridle, S. et al., 2009, *Annals of Applied Statistics*, 3, 6
- Brown M. L., Taylor A. N., Hambly N. C., Dye S., 2002, *MNRAS*, 333, 501
- Byrnes C. T., Choi K.-Y., Hall L. M. H., 2008, *J. Cosmology Astropart. Phys.*, 10, 8
- Byrnes C. T., Gerstenlauer M., Nurmi S., Tasinato G., Wands D., 2010, *J. Cosmology Astropart. Phys.*, 10, 4
- Cai Y.-C., Cole S., Jenkins A., Frenk C., 2009, *MNRAS*, 396, 772
- Cai Y.-C., Cole S., Jenkins A., Frenk C. S., 2010, *MNRAS*, 407, 201
- Caldwell R. R., Dave R., Steinhardt P. J., 1998, *Physical Review Letters*, 80, 1582
- Capranico F., Merkel P., Schäfer B. M., 2013, *MNRAS*, in press (arXiv:1207.5939)
- Carbone C., Baccigalupi C., Bartelmann M., Matarrese S., Springel V., 2009, *MNRAS*, 396, 668
- Carron J., Amara A., Lilly S. J., 2011, *MNRAS*, 417, 1938
- Castro P. G., 2003, *Phys. Rev. D*, 67, 123001
- Castro P. G., Heavens A. F., Kitching T. D., 2005, *Phys. Rev. D*, 72, 023516
- Catelan P., Kamionkowski M., Blandford R. D., 2001, *MNRAS*, 320, L7
- Catelan P., Porciani C., 2001, *MNRAS*, 323, 713
- Catelan P., Theuns T., 1996a, *MNRAS*, 282, 436
- Catelan P., Theuns T., 1996b, *MNRAS*, 282, 455
- Catelan P., Theuns T., 1997, *MNRAS*, 292, 225
- Challinor A., Lewis A., 2005, *Phys. Rev. D*, 71, 103010
- Chandrasekhar S., 1931, *ApJ*, 74, 81
- Chen X., Huang M.-x., Kachru S., Shiu G., 2007, *J. Cosmology Astropart. Phys.*, 1, 2
- Cheung C., Fitzpatrick A. L., Kaplan J., Senatore L., Creminelli P., 2008, *Journal of High Energy Physics*, 3, 14

- Chevallier M., Polarski D., 2001, *International Journal of Modern Physics D*, 10, 213
- Cooray A., 2002, *Phys. Rev. D*, 65, 083518
- Cooray A., Hu W., 2002, *ApJ*, 574, 19
- Crittenden R. G., Natarajan P., Pen U.-L., Theuns T., 2001, *ApJ*, 559, 552
- Crittenden R. G., Natarajan P., Pen U.-L., Theuns T., 2002, *ApJ*, 568, 20
- Crittenden R. G., Turok N., 1996, *Physical Review Letters*, 76, 575
- Crocce M., Scoccimarro R., 2006, *Phys. Rev. D*, 73, 063519
- Desjacques V., 2008, *MNRAS*, 388, 638
- Dodson S., 2007, *Modern cosmology*. Academic Press, Amsterdam
- Dodson S., Kolb E. W., Matarrese S., Riotto A., Zhang P., 2005, *Phys. Rev. D*, 72, 103004
- Doroshkevich A. G., 1970, *Astrophysics*, 6, 320
- Durrer R., 2008, *The Cosmic Microwave Background*. Cambridge Univ. Press, Cambridge
- Dvali G., Gruzinov A., Zaldarriaga M., 2004, *Phys. Rev. D*, 69, 023505
- Einstein A., 1915, *Sitzungsberichte der Königlich Preußischen Akademie der Wissenschaften (Berlin)*, 844
- Einstein A., 1916, *Annalen der Physik*, 354, 769
- Eisenstein D. J., Hu W., 1998, *ApJ*, 496, 605
- Eisenstein D. J., Hu W., 1999, *ApJ*, 511, 5
- Elliston J., Mulryne D. J., Seery D., Tavakol R., 2011, *J. Cosmology Astropart. Phys.*, 11, 5
- Elsner F., Wandelt B. D., 2009, *ApJS*, 184, 264
- Fixsen D. J., 2009, *ApJ*, 707, 916
- Fixsen D. J., Cheng E. S., Gales J. M., Mather J. C., Shafer R. A., Wright E. L., 1996, *ApJ*, 473, 576
- Fixsen D. J., Mather J. C., 2002, *ApJ*, 581, 817
- Friedmann A., 1922, *Zeitschrift für Physik*, 10, 377
- Friedmann A., 1924, *Zeitschrift für Physik*, 21, 326
- Giahi A., Schäfer B. M., 2013a, *MNRAS*, 428, 1312
- Giahi A., Schäfer B. M., 2013b, *MNRAS*, submitted (arXiv:1302.2607)
- Giannantonio T., Scranton R., Crittenden R. G., Nichol R. C., Boughn S. P., Myers A. D., Richards G. T., 2008, *Phys. Rev. D*, 77, 123520
- Goldberg D. M., Bacon D. J., 2005, *ApJ*, 619, 741
- Goldberg J. N., Macfarlane A. J., Newman E. T., Rohrlich F., Sudarshan E. C. G., 1967, *Journal of Mathematical Physics*, 8, 2155

BIBLIOGRAPHY

- Górski K. M., Hivon E., Banday A. J., Wandelt B. D., Hansen F. K., Reinecke M., Bartelmann M., 2005, *ApJ*, 622, 759
- Granett B. R., Neyrinck M. C., Szapudi I., 2008, *ApJ*, 683, L99
- Gurvits L. I., Mitrofanov I. G., 1986, *Nature*, 324, 349
- Guth A. H., 1981, *Phys. Rev. D*, 23, 347
- Guzik J., Seljak U., Zaldarriaga M., 2000, *Phys. Rev. D*, 62, 043517
- Hahn O., Carollo C. M., Porciani C., Dekel A., 2007, *MNRAS*, 381, 41
- Hahn O., Teyssier R., Carollo C. M., 2010, *MNRAS*, 405, 274
- Haiman Z., Loeb A., 1997, *ApJ*, 483, 21
- Hannestad S., Tu H., Wong Y. Y., 2006, *J. Cosmology Astropart. Phys.*, 6, 25
- Hanson D., Challinor A., Efstathiou G., Bielewicz P., 2011, *Phys. Rev. D*, 83, 043005
- Heavens A., 2003, *MNRAS*, 343, 1327
- Heavens A., Peacock J., 1988, *MNRAS*, 232, 339
- Heavens A., Refregier A., Heymans C., 2000, *MNRAS*, 319, 649
- Heavens A. F., Kitching T. D., Taylor A. N., 2006, *MNRAS*, 373, 105
- Heavens A. F., Sheth R. K., 1999, *MNRAS*, 310, 1062
- Heymans C., Heavens A., 2003, *MNRAS*, 339, 711
- Heymans C., White M., Heavens A., Vale C., van Waerbeke L., 2006, *MNRAS*, 371, 750
- Heymans, C. et al., 2013, *MNRAS*, 432, 2433
- Hilbert S., Hartlap J., White S. D. M., Schneider P., 2009, *A&A*, 499, 31
- Hirata C. M., Mandelbaum R., Ishak M., Seljak U., Nichol R., Pimbblet K. A., Ross N. P., Wake D., 2007, *MNRAS*, 381, 1197
- Hirata C. M., Seljak U., 2003, *Phys. Rev. D*, 68, 083002
- Hirata C. M., Seljak U., 2004, *Phys. Rev. D*, 70, 063526
- Hoyle F., 1949, *MNRAS*, 109, 365
- Hu W., 1999, *ApJ*, 522, L21
- Hu W., 2000, *Phys. Rev. D*, 62, 043007
- Hu W., 2001a, *Phys. Rev. D*, 64, 083005
- Hu W., 2001b, *ApJ*, 557, L79
- Hu W., 2002a, *Phys. Rev. D*, 66, 083515
- Hu W., 2002b, *Phys. Rev. D*, 65, 023003
- Jaffe A. H., Kamionkowski M., 1998, *Phys. Rev. D*, 58, 043001

- Jain B., Seljak U., 1997, *ApJ*, 484, 560
- Jing Y. P., 2002, *MNRAS*, 335, L89
- Joachimi B., Bridle S. L., 2010, *A&A*, 523, A1
- Joachimi B., Mandelbaum R., Abdalla F. B., Bridle S. L., 2011, *A&A*, 527, A26
- Joachimi B., Schneider P., 2008, *A&A*, 488, 829
- Joachimi B., Schneider P., 2009, *A&A*, 507, 105
- Jürgens G., Schäfer B. M., 2013, *MNRAS*, 430, 797
- Kaiser N., 1992, *ApJ*, 388, 272
- Kaiser N., Squires G., Broadhurst T., 1995, *ApJ*, 449, 460
- Kamionkowski M., Babul A., Cress C. M., Refregier A., 1998, *MNRAS*, 301, 1064
- Kamionkowski M., Kosowsky A., Stebbins A., 1997, *Phys. Rev. D*, 55, 7368
- Kamionkowski M., Spergel D. N., 1994, *ApJ*, 432, 7
- Kesden M., Cooray A., Kamionkowski M., 2003, *Phys. Rev. D*, 67, 123507
- King L., Schneider P., 2002, *A&A*, 396, 411
- King L. J., 2005, *A&A*, 441, 47
- King L. J., Schneider P., 2003, *A&A*, 398, 23
- Kirk D., Bridle S., Schneider M., 2010, *MNRAS*, 408, 1502
- Kirk D., Laszlo I., Bridle S., Bean R., 2011, preprint (arXiv:1109.4536)
- Kirk D., Rassat A., Host O., Bridle S., 2012, *MNRAS*, 424, 1647
- Kitching T. D., Heavens A. F., Miller L., 2011, *MNRAS*, 413, 2923
- Kitching T. D., Miller L., Heymans C. E., van Waerbeke L., Heavens A. F., 2008, *MNRAS*, 390, 149
- Kitching T. D., Taylor A. N., Heavens A. F., 2008, *MNRAS*, 389, 173
- Kitching, T. et al., 2010, *Annals Appl. Stat.*, 5, 2231
- Knox L., 1995, *Phys. Rev. D*, 52, 4307
- Knox L., Song Y.-S., 2002, *Physical Review Letters*, 89, 011303
- Komatsu, E. et al., 2011, *ApJS*, 192, 18
- Krause E., Hirata C. M., 2010, *A&A*, 523, A28
- Krause E., Hirata C. M., 2011, *MNRAS*, 410, 2730
- Kuhlen M., Diemand J., Madau P., 2007, *ApJ*, 671, 1135
- Landau L. D., Lifšic E. M., 1975, *The classical theory of fields*. Pergamon Press, Oxford
- Langlois D., 2010, *Lect. Notes Phys.*, 800, 1

BIBLIOGRAPHY

- Larson, D. et al., 2011, *ApJS*, 192, 16
- Lee J., 2006, *ApJ*, 644, L5
- Lee J., Park D., 2006, *ApJ*, 652, 1
- Lee J., Pen U., 2000, *ApJ*, 532, L5
- Lee J., Pen U.-L., 2001, *ApJ*, 555, 106
- Lee J., Pen U.-L., 2008, *ApJ*, 681, 798
- Lemaître G., 1927, *Annales de la Societe Scietifique de Bruxelles*, 47, 49
- Lesgourgues J., Liguori M., Matarrese S., Riotto A., 2005, *Phys. Rev. D*, 71, 103514
- Lesgourgues J., Perotto L., Pastor S., Piat M., 2006, *Phys. Rev. D*, 73, 045021
- Lewis A., 2005, *Physical Review D*, 71, 083008
- Lewis A., Challinor A., 2006, *Physics Reports*, 429, 1
- Lewis A., Challinor A., Lasenby A., 2000, *ApJ*, 538, 473
- Li M., Wang T., Wang Y., 2008, *J. Cosmology Astropart. Phys.*, 3, 28
- Libeskind N. I., Hoffman Y., Steinmetz M., Gottlöber S., Knebe A., Hess S., 2013, *ApJ*, 766, L15
- Liddle A. R., 1999, preprint (arXiv:9901124)
- Liddle A. R., Lyth D. H., 1992, *Physics Letters B*, 291, 391
- Liddle A. R., Lyth D. H., 2000, *Cosmological Inflation and Large-Scale Structure*. Cambridge Univ. Press, Cambridge
- Limber D. N., 1953, *ApJ*, 117, 134
- Linder E. V., 2003, *Physical Review Letters*, 90, 091301
- Linder E. V., Jenkins A., 2003, *MNRAS*, 346, 573
- Lovelock D., 1971, *Journal of Mathematical Physics*, 12, 498
- Lovelock D., 1972, *Journal of Mathematical Physics*, 13, 874
- Ludlow A. D., Porciani C., 2011a, *MNRAS*, submitted (arXiv:1107.5808)
- Ludlow A. D., Porciani C., 2011b, *MNRAS*, 413, 1961
- Lue A., Scoccimarro R., Starkman G. D., 2004, *Phys. Rev. D*, 69, 124015
- Lyth D. H., Ungarelli C., Wands D., 2003, *Phys. Rev. D*, 67, 023503
- Mackey J., White M., Kamionkowski M., 2002, *MNRAS*, 332, 788
- Mandelbaum R., Hirata C. M., Ishak M., Seljak U., Brinkmann J., 2006, *MNRAS*, 367, 611
- Mandelbaum, R. et al., 2011, *MNRAS*, 410, 844
- Marinucci D., Peccati G., 2010, *Journal of Mathematical Physics*, 51, 043301

- Marsaglia G., Tsang W. W., 2000, *Journal of Statistical Software*, 5
- McEwen J. D., Vielva P., Hobson M. P., Martínez-González E., Lasenby A. N., 2007, *MNRAS*, 376, 1211
- Mehrem R., Hohenegger A., 2010, *Journal of Physics A Mathematical General*, 43, 5204
- Mehrem R., Londergan J. T., Macfarlane M. H., 1991, *Journal of Physics A Mathematical General*, 24, 1435
- Melchior P., Viola M., Schäfer B. M., Bartelmann M., 2011, *MNRAS*, 412, 1552
- Merkel P. M., Schäfer B. M., 2011, *MNRAS*, 411, 1067
- Merkel P. M., Schäfer B. M., 2013a, *MNRAS*, 431, 2433
- Merkel P. M., Schäfer B. M., 2013b, *MNRAS*, in press (arXiv:1306.6466)
- Merkel P. M., Schäfer B. M., 2013c, *MNRAS*, 429, 444
- Messiah A., 1962, *Quantum mechanics*. North-Holland, Amsterdam
- Meszaros P., 1974, *A&A*, 37, 225
- Miller L., Kitching T. D., Heymans C., Heavens A. F., van Waerbeke L., 2007, *MNRAS*, 382, 315
- Mukhanov V., 2005, *Physical Foundations of Cosmology*. Cambridge Univ. Press, Cambridge
- Mukhanov V. F., Feldman H. A., Brandenberger R. H., 1992, *Phys. Rep.*, 215, 203
- Nakahara M., 2003, *Geometry, Topology and Physics*. Taylor & Francis, New York
- Newman E. T., Penrose R., 1966, *Journal of Mathematical Physics*, 7, 863
- Okamoto T., Hu W., 2002, *Phys. Rev. D*, 66, 063008
- Okamoto T., Hu W., 2003, *Phys. Rev. D*, 67, 083002
- Okumura T., Jing Y. P., Li C., 2009, *ApJ*, 694, 214
- Ostriker J. P., Vishniac E. T., 1986, *ApJ*, 306, L51
- Peacock J. A., 2003, *Cosmological physics*. Cambridge Univ. Press, Cambridge
- Peebles P. J. E., 1969, *ApJ*, 155, 393
- Peirani S., Mohayaee R., de Freitas Pacheco J. A., 2004, *MNRAS*, 348, 921
- Penzias A. A., Wilson R. W., 1965, *ApJ*, 142, 419
- Perlmutter, S. et al., 1999, *ApJ*, 517, 565
- Pietroni M., 2008, *J. Cosmology Astropart. Phys.*, 10, 36
- Planck Collaboration 2013a, *A&A*, submitted (arXiv:1303.5076)
- Planck Collaboration 2013b, *A&A*, submitted (arXiv:1303.5077)
- Porciani C., Dekel A., Hoffman Y., 2002a, *MNRAS*, 332, 325
- Porciani C., Dekel A., Hoffman Y., 2002b, *MNRAS*, 332, 339

- Pratten G., Munshi D., 2013, MNRAS, submitted (arXiv:1301.3673)
- Ratra B., Peebles P. J. E., 1988, Phys. Rev. D, 37, 3406
- Rees M. J., Sciama D. W., 1968, Nature, 217, 511
- Refregier A., 2003, MNRAS, 338, 35
- Refregier A., Bacon D., 2003, MNRAS, 338, 48
- Regos E., Szalay A. S., 1995, MNRAS, 272, 447
- Riess, A. G. et al., 1998, AJ, 116, 1009
- Robertson H. P., 1935, ApJ, 82, 284
- Rybicki G. B., Lightman A. P., 2004, Radiative processes in astrophysics. Wiley-VCH, Weinheim
- Sachs R. K., Wolfe A. M., 1967, ApJ, 147, 73
- Sasaki M., Väliviiita J., Wands D., 2006, Phys. Rev. D, 74, 103003
- Sato M., Nishimichi T., 2013, Phys. Rev. D, 87, 123538
- Schäfer B. M., 2008, MNRAS, 388, 1394
- Schäfer B. M., 2009, International Journal of Modern Physics D, 18, 173
- Schäfer B. M., Bartelmann M., 2006, MNRAS, 369, 425
- Schäfer B. M., Heisenberg L., 2012, MNRAS, 423, 3445
- Schäfer B. M., Heisenberg L., Kalovidouris A. F., Bacon D. J., 2012, MNRAS, 420, 455
- Schäfer B. M., Kalovidouris A. F., Heisenberg L., 2011, MNRAS, 416, 1302
- Schäfer B. M., Merkel P. M., 2012, MNRAS, 421, 2751
- Schneider P., Kilbinger M., Lombardi M., 2005, A&A, 431, 9
- Schneider P., Kochanek C. S., Wambsganß J., 2006, in Meylan G. H., Jetzer P. H., North P. H., eds, Gravitational lensing: strong, weak and micro. Springer, Heidelberg
- Schneider P., van Waerbeke L., Jain B., Kruse G., 1998, MNRAS, 296, 873
- Schneider P., van Waerbeke L., Kilbinger M., Mellier Y., 2002, A&A, 396, 1
- Schneider P., van Waerbeke L., Mellier Y., 2002, A&A, 389, 729
- Sciama D. W., 1955, MNRAS, 115, 2
- Seery D., Lidsey J. E., 2005, J. Cosmology Astropart. Phys., 6, 3
- Seiffert M., et al., 2011, ApJ, 734, 6
- Seitz C., Schneider P., 1997, A&A, 318, 687
- Seitz S., Schneider P., Ehlers J., 1994, Classical and Quantum Gravity, 11, 2345
- Seljak U., 1996a, ApJ, 463, 1

- Seljak U., 1996b, *ApJ*, 460, 549
- Seljak U., Hirata C. M., 2004, *Phys. Rev. D*, 69, 043005
- Seljak U., Zaldarriaga M., 1996, *ApJ*, 469, 437
- Senatore L., Smith K. M., Zaldarriaga M., 2010, *J. Cosmology Astropart. Phys.*, 1, 28
- Shapiro C., Cooray A., 2006, *J. Cosmology Astropart. Phys.*, 3, 7
- Silverstein E., Tong D., 2004, *Phys. Rev. D*, 70, 103505
- Smith K. M., Hu W., Kaplinghat M., 2006, *Phys. Rev. D*, 74, 123002
- Smith K. M., Loverde M., Zaldarriaga M., 2011, *Physical Review Letters*, 107, 191301
- Smith R. E., Hernández-Montegudo C., Seljak U., 2009, *Phys. Rev. D*, 80, 063528
- Smith, R. E. et al., 2003, *MNRAS*, 341, 1311
- Song H., Lee J., 2012, *ApJ*, 748, 98
- Spergel D. N., Goldberg D. M., 1999, *Phys. Rev. D*, 59, 103001
- Springel, V. et al., 2005, *Nature*, 435, 629
- Stebbins A., 1996, preprint (arXiv:9609149)
- Stompor R., Efstathiou G., 1999, *MNRAS*, 302, 735
- Sugerman B., Summers F. J., Kamionkowski M., 2000, *MNRAS*, 311, 762
- Sugiyama N., 1995, *ApJS*, 100, 281
- Sugiyama N. S., Komatsu E., Futamase T., 2011, *Phys. Rev. Lett.*, 106, 251301
- Sunyaev R. A., Zel'dovich Y. B., 1972, *Comments on Astrophysics and Space Physics*, 4, 173
- Suyama T., Takahashi T., Yamaguchi M., Yokoyama S., 2010, *J. Cosmology Astropart. Phys.*, 12, 30
- Suyama T., Yamaguchi M., 2008, *Phys. Rev. D*, 77, 023505
- Taburet N., Aghanim N., Douspis M., Langer M., 2009, *MNRAS*, 392, 1153
- Taburet N., Douspis M., Aghanim N., 2010, *MNRAS*, 404, 1197
- Takada M., Hu W., 2013, *Phys. Rev. D*, 87, 123504
- Takada M., Jain B., 2004, *MNRAS*, 348, 897
- Takada M., Jain B., 2009, *MNRAS*, 395, 2065
- Takada M., White M., 2004, *ApJ*, 601, L1
- Tegmark M., Taylor A. N., Heavens A. F., 1997, *ApJ*, 480, 22
- Troxel M. A., Ishak M., 2012, *MNRAS*, 423, 1663
- Turner M. S., White M., 1997, *Phys. Rev. D*, 56, 4439
- Vielva P., Martínez-González E., Tucci M., 2006, *MNRAS*, 365, 891

BIBLIOGRAPHY

- Wald R. M., 2005, *General Relativity*. Univ. of Chicago Press, Chicago
- Walker A. G., 1935, *The Quarterly Journal of Mathematics*, 6, 81
- Wang L., Steinhardt P. J., 1998, *ApJ*, 508, 483
- Weinberg S., 1976, *Gravitation and cosmology*. Wiley, New York
- Wetterich C., 1988, *Nuclear Physics B*, 302, 668
- White M., Hu W., 2000, *ApJ*, 537, 1
- White S. D. M., 1984, *ApJ*, 286, 38
- Will C., 2001, *Living Reviews in Relativity*, 4, 4
- Wolz L., Kilbinger M., Weller J., Giannantonio T., 2012, *J. Cosmology Astropart. Phys.*, 9, 9
- Zaldarriaga M., Seljak U., 1998, *Phys. Rev. D*, 58, 023003
- Zaldarriaga M., Seljak U., 1999, *Phys. Rev. D*, 59, 123507
- Zel'dovich Y. B., 1970, *A&A*, 5, 84
- Zhang P., 2006, *Phys. Rev. D*, 73, 123504

Acknowledgements

Now follows the part of this thesis which will probably withstand longest. First and foremost I wish to deeply thank Björn Malte Schäfer. He is, needless to say, an outstanding researcher, but above all Björn is an outstanding supervisor. That I am now writing the final page of my PhD thesis is almost exclusively due to his continuous and endless encouragement and support. Björn taught me everything I know about cosmology and most importantly, he taught me not to give up, even in personally difficult times.

I also want to thank Matthias Bartelmann for tolerating me in his group at the Institute of Theoretical Astrophysics (ITA), although we manage to disagree on almost everything one can think of. Unfortunately, the situation worsened during the last two years, which I cordially regret.

I am particularly grateful to Prof. Dr. Volker Springel for issuing the second referee report of my thesis and Prof. Dr. Stephanie Hansmann-Menzemer and Prof. Dr. Tilman Plehn for completing my thesis committee.

I express my gratitude to Martin Reinecke who never hesitated to share his impressive knowledge about HEALPIX and the *Planck* software package whenever I encountered an “unsolvable” problem.

I would also like to thank all the inhabitants of the Geistesvernichtungsanstalt which Christian unfailingly translated into “intelligence truncation agency”, or in short: ITA. I am in particular thankful to my “long-term” officemates Britta Zieser, Christoph “Eduard” Kommer and Charles Majer. I should not forget to mention Elena Sellentin, Christian Angrick, Alexander Gelsin, Gero Jürgens, Sven Meyer, Francesco Pace and Matthias Redlich. They all contribute, tough sometimes in a more than extraordinary way, to the heart and soul of the ITA cosmology group. I am very thankful to Christian and Gero for providing the L^AT_EX template I used for writing this thesis.

A PhD thesis is accompanied by a tremendous amount of bureaucracy. Gesine Heinzemann and Elisabeth Miller, the secretaries of the HGSFP, helped me not to get lost in the jungle of forms and deadlines. I am very thankful to them, as well as to Christian Fendt, the antagonist of any bureaucracy and lover of handy solutions. Whenever I think of the IMPRS-HD Christian comes to my mind. I would also like to thank ITA’s secretary Anna Zacheus.

Since idealism may be sufficient to carry out a PhD thesis, but does not suffice to still hunger, I am especially grateful for the stipend according to the Landesgraduiertenförderung (LGFG) granted by the Graduate Academy Heidelberg.

It is also time to express my gratitude to my friends Tina Gauch, Michael Baum, Alexander Bien and Simon Schettler. They all influenced my work in many, many different ways – most probably without ever noting.

Before I ultimately close this thesis I wish to thank the innermost circle of my life. I am deeply grateful to my parents, my sister and Sandra.

